Computational Studies of Oxygen Reduction Catalysts

Björn Kirchhoff

Faculty of Physical Sciences
University of Iceland
2021

Computational Studies of Oxygen Reduction Catalysts

Björn Kirchhoff

Dissertation submitted in partial fulfillment of a
Philosophiae Doctor degree in Chemistry

Advisor
Prof. Dr. Hannes Jónsson

PhD Committee
Prof. Dr. Hannes Jónsson
Prof. Dr. Egill Skúlason
Prof. Dr. Timo Jacob

Opponents
Prof. Dr. Felix Studt
Prof. Dr. Andrei Manolescu

Faculty of Physical Sciences
School of Engineering and Natural Sciences
University of Iceland
Reykjavik, May 2021

Computational Studies of Oxygen Reduction Catalysts

Dissertation submitted in partial fulfillment of a *Philosophiae Doctor* degree in Chemistry

Faculty of Physical Sciences
School of Engineering and Natural Sciences
University of Iceland
VR-III, Hjarðarhagi 2
107, Reykjavík, Reykjavik
Iceland

Telephone: 525-4000

Bibliographic information:
Björn Kirchhoff, 2021, *Computational Studies of Oxygen Reduction Catalysts*, PhD dissertation, Faculty of Physical Sciences, University of Iceland, 178 pp.

ISBN 978-9935-9564-5-3

Printing: Háskólaprent
Reykjavik, Iceland, May 2021

Abstract

The oxygen reduction reaction (ORR) is of central importance in the development of more efficient and durable fuel cells and computer simulations can be used to help explain and predict properties of ORR catalysts. In this thesis, various simulation methods are used, their accuracy tested, and some new tools developed for simulations of different types of ORR catalysts. The first part of the thesis presents a ReaxFF reactive force field study of the oxidation of platinum nanoparticles, the catalyst currently used in most fuel cells. The simulations make use of a grand-canonical Monte Carlo simulation approach to study the mechanism of oxidative nanoparticle degradation. Electrochemical oxidation phase diagrams are constructed and they show that stable surface oxides can form under fuel cell operating conditions. Furthermore, clusters of Pt_6O_8 stoichiometry are identified as the primary oxidation product and this provides a detailed, atomic scale mechanism for the degradation of platinum nanoparticle ORR catalysts.

In the second part of the thesis, metal-free ORR catalysts are studied, namely nitrogen-doped graphene (NG). There, electron density functional theory calculations are used to estimate the thermodynamics of possible reaction paths and provide an estimate of the overpotential. Various density functional approximations are tested against high level diffusion Monte Carlo calculations on the binding and migration of an *O adatom on graphene, an important intermediate in the ORR. It is found that generalized-gradient approximation (GGA) functionals have low accuracy while some hybrid functionals and a self-interaction corrected GGA functional give good agreement with the reference calculation. A hybrid functional is then used to calculate the free energy of ORR intermediates to estimate the overpotential for various catalyst structures and compositions. While overpotentials are initially found to be unfavorable, the presence of water molecules at the catalyst surface is estimated to reduce the calculated overpotentials significantly. This shows that proper inclusion of the aqueous electrolyte is important. From this conclusion, a significant challenge arises as inclusion of many solvent molecules makes the simulated system too large for electronic structure calculations.

In the third part of the thesis, a new methodology is developed to make it possible to include the aqueous electrolyte in simulations by using a hybrid simulation approach where part of the system — the catalyst as well as the reacting species and nearby water molecules — are included in the electronic structure calculation, while the rest of the aqueous electrolyte is described using a potential energy function. The separation between the two regions is made to lie through the aqueous phase in order to make it easier to describe the interaction between atoms on opposite sides of the boundary. Therein, the challenge is to enforce the boundary in such a way that atoms and molecules

do not wander from one region to another. A new method referred to as scattering-adapted flexible inner region ensemble separator (SAFIRES) is developed for this purpose. It represents an improvement on a previous algorithm called FIRES. With SAFIRES, the boundary between the two regions is flexible and adjusts automatically but particles cannot move between the regions. It is demonstrated that using SAFIRES, the energy, atomic forces, and probability distribution for the location of atoms are reproduced accurately compared to results of simulations where where no boundary is present. The SAFIRES algorithm dynamically changes the time step in the iterative algorithm for time evolution to identify and enforce elastic collisions of atoms with the boundary separating the two regions. A new propagator is introduced to simulate the time evolution of the system with or without a connection to a heat bath. Tests are carried out by simulating a Lennard-Jones liquid, a Lennard-Jones liquid/solid interface, and water described using a potential energy function. With the SAFIRES method, along with the recently developed, self-consistent polarizable hybrid simulation methodology, the stage is set for proper inclusion of the aqueous phase at the electrode surface in future electrochemistry simulations.

Útdráttur

Aukin virkni í afoxun súrefnis í rafefnahvörfum (oxygen reduction reaction, ORR) er mikilvægur liður í þróun á hagkvæmari og endingarbetri efnarafölum. Tölvureikninga er hægt að nota til að hjálpa til við að skilja og spá fyrir um betri ORR efnahvata. Í þessari ritgerð eru ýmsar reikniaðferðir notaðar, nákvæmni þeirra prófuð og nýjar aðferðir þróaðar í reikningum á ýmsum ORR hvötum. Í fyrsta hluta ritgerðarinnar er greint frá ransóknum á oxun platínu nanóklasa þar sem ReaxFF mættisfall er notað, en þetta er sá hvati sem nú er mest notaður í efnarafölum. Reikningarnir byggja á stórkanónsku Monte Carlo aðferðinni til að líkja eftir því hvernig nanóagnirnar oxast og eyðast. Fasagröf fyrir rafefnaoxun eru sett fram og þau sýna að stöðug yfirborðsoxíð geta myndast þegar efnarafalar eru í notkun. Jafnframt er sýnt fram á að klasar með samsetninguna Pt_6O_8 myndast einkum við oxunina og þannig er fengin atóm skala mynd af því hvað veldur hrörnun platínu nanóklasanna.

Í öðrum hluta ritgerðarinnar eru málmlausir ORR hvatar rannsakaðir, nefnilega nitur-íbætt grafín (N-doped graphene, NG). Þar eru reikningar byggðir á þétnifellafræði rafeinda notaðir til að meta varmafræðilega eiginleika mismunandi hvarfganga og meta yfirspennuna. Ýmsar nálganir fyrir þéttnifellið eru prófaðar með samanburði við Monte Carlo rafeindareikninga á ásogi og sveimi *O atóms á grafíni, en það er mikilvægt stig í ORR. Niðurstöðurnar sýna að felli af GGA gerð eru ekki nægjanlega nákvæm en sum hýbríð felli og GGA felli með sjálfsvíxlverkunarleiðréttingu gefa útkomu sem er í góðu samræmi við Monte Carlo reikningana. Hýbríð felli er svo notað til að meta yfirspennuna fyrir ýmsar gerðir efnahvata. Útreiknuð yfirspenna bendir til að efnahvatar af þessari gerð séu ekki virkir, en þegar leiðrétt er fyrir víxlverkun við vatnssameindir lækkar útreiknuð yfirspenna verulega. Þessi niðurstaða leiðir til mikillar áskorunar því kerfi þar sem margar vatnssameindir eru einnig til staðar eru of stór fyrir rafeindareikningana.

Í þriðja hluta ritgerðarinnar er þróuð ný aðferðafræði sem gerir það kleift að taka vatnsraflausn með í reikninginn. Þar er hluti kerfisins - hvatinn sem og sameindir sem hvarfast og nærliggjandi vatnssameindir - tekinn með í rafeindareikningana á meðan hinn hluti kerfisins, þ.e. restin af raflausninni er lýst með mættisfalli. Mörkin milli svæðanna tveggja eru valin þannig að þau liggja í gegnum lausnina til að gera það auðveldara að lýsa víxlverkuninni milli atóma sitt hvorru megin við skilin. Þar með verður áskorunin sú að innleiða skilin þannig að atóm og sameindir fari ekki frá einu svæði yfir í annað. Ný aðferð sem byggð er á endurvarpi frá skilfletinum og kallast SAFIRES er þróuð í þessum tilgangi. Hún byggir á eldri aðferð sem nefnd er FIRES. Með SAFIRES aðferðinni er skilflöturinn milli svæðanna færanlegur og finnur sjálfkrafa réttan stað, en agnir geta ekki farst í gegnum skilflötinn. Sýnt er fram á að með SAFIRES aðferðinni er orka, kraftar á atómin og líkindadreifingin fyrir

staðsetningu atómanna í góðu samræmi við reikninga þar sem enginn skilflötur er til staðar. Í SAFIRES aðferðinni er tímaskrefið í reikningum á tímaframvindu aðlagað sjálfkrafa til að finna þann tímapunkt þar sem árekstur á sér stað við skilflötinn og atómin endurvarpast frá skilfletinum án orkubreytingar. Nýtt reiknirit fyrir tímaframvinduna er innleitt með og án tengingar við hitabað. Þetta er prófað með því að reikna út Lennard-Jones vökva, mót vökva og fastefnis Lennard-Jones atóma og vatn þar sem mættisföll lýsa víxlverkuninni. Með þessari SAFIRES aðferð ásamt nýlegri aðferð til að gera hýbríð reikninga með skautanlegum sameindum er lagður grunnurinn að leið til að taka vatnsraflausn með í reikninginn í kennilegum rannsóknum á rafefnafræði í framtíðinni.

Table of Contents

List of Figures

List of Original Articles

Included in this work

2019:

Kirchhoff, B., Braunwarth, L., Jung, C., Jónsson, H., Fantauzzi, D., and Jacob, T. (2019). Simulations of the Oxidation and Degradation of Platinum Electrocatalysts. *Small*, 16(5):1905159

2021:

Kirchhoff, B., Ivanov, A., Skúlason, E., Jacob, T., Fantauzzi, D., and Jónsson, H. (2021a). Assessment of the Accuracy of Density Functionals for Calculations of the Oxygen Reduction Reaction on Nitrogen Doped Graphene. Submitted to *J. Chem. Theory Comput.*

Kirchhoff, B., Jónsson, E. O., Dohn, A. O., Jacob, T., and Jónsson, H. (2021b). Elastic Collision Based Dynamic Partitioning Scheme for Hybrid Simulations. *arXiv:2103.16342 [physics]*. Submitted to *J. Chem. Theory Comput.*

Not included in this work

2021:

Kirchhoff, B., Jung, C., Jónsson, H., Fantauzzi, D., and Jacob, T. (2021d). Comparison of the Electrocatalytic Oxidation of Different Platinum Nanoparticle Structures from Simulations. In preparation.

Kirchhoff, B., Skúlason, E., Jacob, T., Fantauzzi, D., and Jónsson, H. (2021e). Calculations of Oxygen Reduction Thermochemistry for Boron-Doped Graphene using a Hybrid Density Functional. In preparation.

Kirchhoff, B., Jung, C., Gaissmeier, D., Braunwarth, L., Jónsson, H., and Jacob, T. (2021c). In-Silico Characterization of Nanoparticle Catalysts. In preparation.

Abbreviations

2PT	two-phase thermodynamics
BG	boron-doped graphene
BO	bond order
BSSE	basis set superposition error
CCSD(T)	coupled-cluster singles doubles and pertubative triples
CVD	chemical vapor deposition
DFT	density functional theory
DLPNO	domain-based local pair natural orbital approximation
DMC	Diffusion Monte Carlo
EAITD	extended *ab initio* thermodynamics
FF	force field
GCMC	grand canonical Monte Carlo
GCN	generalized coordination number
GEA	gradient expansion approximation
GGA	general gradient approximation
GTO	Gaussian-type orbital
HF	Hartree-Fock
HOR	hydrogen oxidation reaction
LCAO	linear combination of atomic orbitals
LDA	local density approximation
LJ	Lennard-Jones
LSDA	local spin-density approximation
MD	molecular dynamics
NAP	near-ambient pressure
NG	nitrogen-doped graphene
NP	nanoparticle
OER	oxygen evolution reaction
ORR	oxygen reduction reaction
PEMFC	proton-exchange membrane fuel cell
QM	quantum-mechanics / -mechanical
RDF	radial distribution function

SE	Schrödinger equation
STM	scanning tunneling microscopy
UHV	ultra high vacuum
XC	exchange-correlation
XPS	X-ray photoelectron spectroscopy

Acknowledgments

Prof. Dr. Hannes Jónsson is acknowledged as the main supervisor of my thesis. Hannes, I am deeply grateful for your invaluable advice, patience, and support over the course of my PhD. Thank you for the knowledge you shared and the opportunities you created for me along the way.

Furthermore, I'd like to thank my PhD committee, Prof. Dr. Timo Jacob and Prof. Dr. Egill Skúlasson, for additional supervision and support. Timo, thank you for intermittently hosting me at Ulm University.

Dr. Elvar Jónsson and Dr. Asmus Dohn are acknowledged for additional supervision of the SAFIRES project. Thank you for introducing me to the fascinating world of method development and for helping me out whenever I got stuck.

Further thanks go to:

Dr. Donato Fantauzzi: Donato offered me the opportunity to come to Iceland and was an important mentor during my Master's project and early in my PhD. Dr. Maxime van den Bossche: Maxime found [62], which became a central element in my work on graphene. Dr. Aleksei Ivanov: Aleksei helped with the mathematical proof presented in section 4.5. Dr. Marcos Tacca: Marcos partly translated [32] to English. Nico Bevilacqua, Nicola Jobst, Barði Benediktsson, Daniel Gaissmeier, and Matthias van den Borg: thank you for inspiring discussions over the years and for the good times we shared.

Finally, to my family and my partner Felicitas: thank you for your tireless emotional support, patience, and love. I could not have done this without you.

This work was supported by a PhD fellowship from the University of Iceland Research Fund.

1 Theoretical Background

The following sections discuss the fundamentals of Density Functional Theory (DFT), force field methods, and the grand-canonical Monte Carlo (GCMC) approach. This brief introduction is based on textbook chapters by Koch,[88] Jensen,[69] and Cramer.[28]

1.1 Density Functional Theory

The Schrödinger Equation

Quantum mechanical (QM) electronic structure calculation methods such as Density Functional Theory (DFT) and Hartree-Fock (HF) theory are derived from the Schrödinger equation (SE). In its time-independent form, the SE is given as

$$\hat{H}\,\Psi(r_i,R_I) = E\,\Psi(r_i,R_I) \tag{1}$$

with the Hamiltonian $\hat{H}$, the wave function Ψ, the total energy E, as well as coordinates of nuclei and electrons, R_I and r_i.

$\hat{H}$ contains the kinetic components of nuclei and electrons ($\hat{T}_\mathrm{N}$ and $\hat{T}_\mathrm{e}$) as well as repulsive electrostatic contributions between subatomic particles of the same charge ($\hat{V}_\mathrm{N\text{-}N}$ and $\hat{V}_\mathrm{e\text{-}e}$) and attractive contributions between those of opposite charge ($\hat{V}_\mathrm{e\text{-}N}$),

$$\hat{H} = \hat{T}_\mathrm{N} + \hat{T}_\mathrm{e} + \hat{V}_\mathrm{N\text{-}N} + \hat{V}_\mathrm{e\text{-}e} + \hat{V}_\mathrm{e\text{-}N}. \tag{2}$$

Since the movements of electrons and nuclei occur at different time scales, $\hat{H}$ can be separated into contributions from the nuclei and electrons in the context of the Born-Oppenheimer approximation.[13] $\hat{T}_\mathrm{N}$ is treated using classical equations of motion and $\hat{V}_\mathrm{N\text{-}N}$ is treated using a classical Coulomb term,

$$E_\mathrm{N} = \sum_{A=1}^{M}\sum_{B>A}^{M}\frac{Z_A Z_B}{r_{AB}}, \tag{3}$$

while $\hat{T}_\mathrm{e}$, $\hat{V}_\mathrm{e\text{-}N}$, and $\hat{V}_\mathrm{e\text{-}e}$ are treated quantum-mechanically as

$$\hat{H}_\mathrm{e} = -\frac{1}{2}\sum_{i=1}^{n}\nabla_i^2 - \sum_{i=1}^{n}\sum_{A=1}^{M}\frac{Z_A}{r_{iA}} + \sum_{i=1}^{n}\sum_{j>i}^{n}\frac{1}{r_{ij}}. \tag{4}$$

Here, $\nabla_i = \frac{\partial}{\partial x_i} + \frac{\partial}{\partial y_i} + \frac{\partial}{\partial z_i}$ is the Nabla operator, M and n are the total number of nuclei and electrons, and Z represent the nuclear charges.

Electron Density, Pair Density, and Exchange-Correlation Hole

Because no analytical solution has been found yet for the SE with more than one interacting electron, further approximations are required to bring it into a computationally useful form. To this end, DFT builds on the eponymous electron density

$$\rho(\vec{r}) = n \int \dots \int |\Psi(\vec{x}_1, \vec{x}_2, \dots, \vec{x}_n)|^2 \, d\vec{s}_1, d\vec{x}_2, \dots, d\vec{x}_n. \tag{5}$$

The interaction between electrons is governed by two main contributions: electrostatic Coulomb repulsion and the Pauli exchange principle. To account for these properties, the pair density

$$\rho(\vec{x}_1, \vec{x}_2) = n(n-1) \int \dots \int |\Psi(\vec{x}_1, \vec{x}_2, \dots, \vec{x}_n)|^2 \, d\vec{x}_3 \dots d\vec{x}_n \tag{6}$$

can be formulated. Bringing equation (6) into matrix form results in several desirable properties, such as exchange of $\vec{x}_1$ and $\vec{x}_2$ resulting in a sign change (non-commutability of fermions), as well as the pair density vanishing for $\vec{x}_1 = \vec{x}_2$ which ensures that two electrons can never occupy the same volume segment.

Integrating over equation (6) will yield n, the total number of electrons. However, since equation (6) is a pair density, only $n-1$ combinations of pairs of (different) electrons should exist. This means that there is a contribution of an electron interacting with itself. This contribution is referred to as the self-interaction error.

Normalizing equation (6) gives the conditional probability

$$\Omega(\vec{x}_1, \vec{x}_2) = \frac{\rho(\vec{x}_1, \vec{x}_2)}{\rho(\vec{x}_1)}. \tag{7}$$

The energy difference between equation (6) including self-interaction and the corrected case in equation (7) is referred to as the exchange-correlation (XC) hole

$$h_{\mathrm{XC}}(\vec{x}_1, \vec{x}_2) = \Omega(\vec{x}_1, \vec{x}_2) - \rho(\vec{x}_2). \tag{8}$$

The XC hole represents a spherical area of negative density around each electron resulting from electrostatic repulsion and the exchange principle. The XC hole integrates to one electron (sum rule), *i.e.* it accounts for the surplus contribution resulting from self-interaction.

Exchange-Correlation Functionals

Local (Spin-) Density Approximation The unknown component in DFT is the XC energy E_{XC}. The historically first approximation to this quantity is known as the local density approximation (LDA). In LDA, E_{XC} is derived based on the properties of the simple Jellium model for electrons in solids, *i.e.* a homogeneous electron gas with a smeared positive background charge representing the nuclei:

$$E_{\mathrm{XC}}^{\mathrm{LDA}}[\rho] = \int \rho(\vec{r}) \, \varepsilon_{\mathrm{XC}}(\rho(\vec{r})) \, d\vec{r}. \tag{9}$$

Here, $\rho(\vec{r})$ is the density of Jellium and $\varepsilon_{\mathrm{XC}}(\rho(\vec{r}))$ is the per-particle XC energy. The exchange component can be calculated explicitly while the correlation part was sampled numerically using a quantum Monte Carlo method.[22].

Unrestricted LDA (local spin-density approximation, LSDA) treats spin explicitly. The XC contribution in LSDA is defined as

$$E_{\mathrm{XC}}^{\mathrm{LSDA}}[\rho_\alpha, \rho_\beta] = \int \rho(\vec{r})\ \varepsilon_{\mathrm{XC}}(\rho_\alpha(\vec{r}), \rho_\beta(\vec{r}))\ d\vec{r}, \tag{10}$$

where α and β refer to spin states.

While a homogeneous electron gas can serve as a reasonable approximation for the delocalized electron clouds of metals, it is less suited as a model for localized covalent and ionic bonds. LDA is known to give significant overbinding for molecular systems[36] due to overestimation of the atomization energy. The XC hole in LDA is spherical and negative at all points. This desirable property however is not a result of correct treatment of self-interaction but results from the isotropic nature of Jellium's properties.

Generalized Gradient Approximation The gradient expansion approximation (GEA) is obtained by introducing the density gradient $\nabla\rho(\vec{r})$ to equation (10) in a Taylor-series-like expansion step. The XC energy term in GEA is given as

$$E_{\mathrm{XC}}^{\mathrm{GEA}}[\rho_\alpha, \rho_\beta] = \int f(\rho_\alpha, \rho_\beta, \nabla\rho_\alpha, \nabla\rho_\beta)\ d\vec{r}. \tag{11}$$

Unlike for L(S)DA, the XC hole in GEA fails to be negative at all points. It is therefore necessary to correct the shape of the XC hole, resulting in the expression for the XC energy

$$E_{\mathrm{XC}}^{\mathrm{GGA}} = E_{\mathrm{XC}}^{\mathrm{LDA}} - \sum_\sigma \int F(s_\sigma)\ \rho_\sigma^{\frac{4}{3}}(\vec{r})\ d\vec{r}. \tag{12}$$

Here, F is a correction function, σ is the spin and s_σ constitutes the reduced density gradient used to level local inhomogenities. Equation (12) is typically referred to as the generalized gradient approximation (GGA) functional. Various approximations for F exist. The popular definition developed by Becke in 1988 [9] gave rise to the B88 family of density functionals. Another popular approximation is the PBE functional developed by Perdew, Burke, and Ernzerhof in 1996, [120] which defines F as a rational function of the reduced density gradient.

GGA functionals show smaller errors compared to L(S)DA for calculations of molecules or when treating non-metallic adspecies on periodic metal surface models. However, GGA functionals still have a tendency to over-delocalize electrons; errors for molecules in particular are often still significant. A well known case is that of triplet oxygen, for which the atomization energy is erroneous by more than 1 eV using the PBE functional.[87]

Hybrid DFT Hybrid DFT was developed to improve the accuracy of density functionals for systems with predominantly localized electron density dominated by

the self-interaction error. Assuming completely non-interacting single-particles (*i.e.* no electron correlation), the DFT wave function can be formulated as a Slater determinant of Kohn-Sham orbitals. Solving the Slater determinant using HF theory will yield the exact exchange energy component since HF theory does not give rise to self-interaction. Exact exchange is mixed with L(S)DA and GGA exchange and correlation to obtain the hybrid XC energy term. The DFT correlation energy component is used exclusively because HF theory does not yield the correlation energy without additional post-processing. For the PBE0 functional, for example, the XC energy is defined as[121; 1]

$$E_{\mathrm{XC}}^{\mathrm{PBE0}} = \frac{1}{4}E_{\mathrm{X}}^{\mathrm{HF}} + \frac{3}{4}E_{\mathrm{X}}^{\mathrm{PBE}} + E_{\mathrm{C}}^{\mathrm{PBE}}\,, \tag{13}$$

resulting in 25 % exact exchange. The amount of exact exchange varies between functionals and is chosen to fit a certain set of chemical problems. Increasing the relative amount of exact exchange can sometimes improve results for systems with highly localized electron densities. In many cases the exchange and correlation mixing coefficients are fitted to experimental data sets. B3LYP is an example of an empirically-fitted functional. Care must be taken when using fitted functionals to calculate problems outside the scope of their training data.

Calculating $E_{\mathrm{X}}^{\mathrm{HF}}$ increases the computational effort significantly, especially when sampling periodic models with dense Brillouin zone grids (see section 1.1). Screened hybrids such as the HSE family of functionals[56] restrict how much of the long range exact exchange is being sampled by implementing a screening parameter ω. This approximation not only counteracts the additional computational cost of hybrid functionals but has also been found to improve results for periodic metallic model systems where long range exact exchange interactions can lead to unphysical contributions.[56] Good results for a large number of systems are obtained for $\omega = 0.2$, which is referred to as the HSE06 functional.[89]

Implementation of DFT

Basis Sets Within the Kohn-Sham approximation to DFT, the Hamiltonian is described as a Slater determinant of non-interacting electrons. These Kohn-Sham orbitals φ_i can be approximated as a linear combination of pre-calculated base functions η_μ,

$$\varphi_i = \sum_{\mu=1}^{L} c_{\mu i}\,\eta_\mu\,. \tag{14}$$

Computation of the $c_{\mu i}$ coefficients is a linear computational problem whereas the original Kohn-Sham operator contains both derivative and integral components, making this approximation a key factor for the computationally efficient implementation of DFT.

This methodology is derived from the linear combination of atomic orbitals (LCAO) ansatz developed by Rothaan in the 1950s for the construction of molecular orbitals as a linear combination of individual atomic orbitals for HF methods.[132] Historically, base functions therefore resembled atomic orbitals. Modern basis functions are constructed according to mathematical requirements and have no analogue in reality.

Gaussian-type orbitals (GTOs) of the form

$$\eta^{\mathrm{GTO}} = N x^1 y^m z^n e^{-\alpha r^2} \tag{15}$$

are used prominently. $L = 1 + m + n$ denotes the orbital type (s, p, d, f for L = 0, 1, 2, 3), N is a normalization factor, and diffuseness is controlled by α. Another type of base function are Slater-type orbitals (STOs), which are more costly to integrate but require less functions for accurate fitting. Contracted Guassian functions aim to combine the favorable properties of GTOs and STOs by merging three GTOs into one STO-like basis function.

The size of a basis set is indicated via the ζ notation. *Single-*ζ or *minimal* basis sets contain one basis function per atomic orbital. *Double-*, *triple-*, *quadruple-*ζ basis sets contain two, three, four, *etc.* basis functions to represent each orbital. Basis sets can be augmented using diffuse basis functions which can improve description of anions and long-range interactions.

The fit quality for the KS orbitals improves with increasing number of base functions. While in theory, an infinite number of functions would be required to represent a KS orbital exactly, results from DFT calculations rarely improve for basis sets larger than *triple-*ζ. Increasing the basis set also increases the potential number of functions available for basis set superposition errors (BSSE). The BSSE occurs when two atomic centers with incomplete basis sets come into contact and use the basis functions of the other respective atom to complete their own basis set. This can lead to an artificially lower total energy of the compound material. Since basis functions have finite size, the BSSE also fluctuates with interatomic distance. Corrective approaches for the BSSE are available, such as the counterpoise correction[164] and the chemical Hamiltonian approach.[105]

Basis sets are constructed to systematically approach the complete basis set limit with increasing size. Because the general function by which electronic energy results obtained from a specific basis set family converge to the basis set limit is known, results for the complete basis set limit can be extrapolated by fitting this function using results from two calculations with basis sets of increasing size.[55; 196; 111] In practice, basis set extrapolation is expected to give results that roughly correspond to the next-larger basis set in the family. *I.e.* extrapolation based on results from calculations using a double- and a triple-ζ basis set are expected to yield quadruple-ζ results. This can be worth the effort because the computational costs of doing the extrapolation calculations can be smaller than using a more complete basis set. HF methods in particular profit from extrapolation methods due to more pronounced basis set dependency compared to DFT.

Another approach to basis functions is to use plane waves instead of GTOs or STOs. They take the general form of

$$\phi(r) = e^{i\mathbf{k}r}\,, \tag{16}$$

where $\mathbf{k}$ is the wave vector, which is limited by the dimensions of the simulation cell t. Equation (16) gives possible $\mathbf{k}$ values of $\mathbf{k} = 2\pi m t^{-1}$, where m is a positive integer. $\mathbf{k}$ therefore determines the basis set size in plane wave calculations and is linked to the total energy as $E = \frac{1}{2}\,\mathbf{k}^2$. Due to the quadratic dependence on $\mathbf{k}$, the impact on the total energy for large m diminishes rapidly. The number of plane waves included in a calculation can thus be limited by a cut-off criterion to reduce the computational effort.

The plane wave approach is used in DFT codes geared towards solid-state calculations with periodic model systems. Plane wave basis sets lend themselves to modeling the delocalized electron clouds of metallic systems. Plane wave calculations give rise to energy bands instead of dedicated orbital energy levels.

Pseudopotentials Effective core potentials or pseudopotentials can be used to replace the core electrons of atoms to improve computational performance. This approximation has negligible impact on the accuracy as long as correct description of the core electrons is not required (*cf.* simulations of core-level X-ray photon spectroscopy (XPS) spectra). Pseudopotentials are generated for each element separately and can include lesser relativistic contributions for the core electrons of heavy elements. The computational speedup from pseudopotentials is particularly significant in case of plane wave calculations. Without pseudopotentials, a large cut-off criterion is required to properly describe the electron density singularity at each nucleus.

Bloch's Theorem and Periodicity Periodic boundary conditions (PBCs) are used to study periodically-repeating systems such as crystals. Bloch's theorem says that if the Kohn-Sham orbital $\varphi^{n}_{\vec{k}}(\vec{r})$ of the smallest repeating reciprocal unit cell is known, all other states can be calculated by expansion of the wave vector $\vec{k}$ and band index n:

$$\Psi^{n}_{\vec{k}}(\vec{r}) = \varphi^{n}_{\vec{k}}(\vec{r})\, e^{i\vec{k}\vec{r}}. \tag{17}$$

In reciprocal space, the primitive unit cell is referred to as the first Brillouin zone. Equation (14) can thus be made periodic by equation (17) such that

$$\varphi_j(\vec{r}+\vec{R}) = \varphi^{n}_{\vec{k}}(\vec{r})\, e^{i\vec{k}\vec{r}} \tag{18}$$

$$\Rightarrow \varphi_{j,n_\mathrm{r},L,\vec{k}}(\vec{r}) = \sum_{\vec{R}} c_{\mu\, j}\; \eta_{j,n_\mathrm{r},L(\vec{r}-\vec{R})}\; e^{i\vec{k}\vec{R}}. \tag{19}$$

Here, n_r is the radial quantum number and $L = (l,m)$ is the quantum number of the base function.

Brillouin Zone Sampling Integrating over the first Brillouin zone yields the electron density. However, complete integration is computationally unfeasible. Therefore, sampling schemes are used to sum over special nodes in the first Brillouin zone called $\boldsymbol{k}$-points. The number of $\boldsymbol{k}$-points can be further reduced by combining symmetry-equivalent points into "stars", $f_{\boldsymbol{k}_i}(\vec{r})$, weighed by a factor ω_i:

$$\rho(\vec{r}) = \sum_{\boldsymbol{k}} \sum_{i} |\varphi_{\boldsymbol{k},i}(\vec{r})|^2 \rightarrow \sum_{i} \omega_i\, f_{\boldsymbol{k}_i}(\vec{r}) \tag{20}$$

The widely-used sampling scheme by Monkhorst and Pack[108] generates a uniform, unbiased distribution of $\boldsymbol{k}$-points in the Brillouin zone.

1.2 Force Field Methods

Classic Force Fields

Force field (FF) methods use a potential energy term rooted in classical mechanics to compute the energy of a system. While the size of model systems in electronic structure calculations is typically limited to a few dozen atoms, FF methods are able to treat tens of thousands of particles. Notably, FFs do not compute electrons explicitly and require fitting to an experimental or higher-level computational training data set. These limitations results in overall lower accuracy compared to electronic structure methods and limited transferability to chemical problems not represented in the training data set.

The potential energy term can be infinitely complex and depends on the desired application. However, certain common terms are found in most potential functions. A typical FF might contain

$$V_{\text{tot}} = V_{\text{stretch}} + V_{\text{bend}} + V_{\text{tors}} + V_{\text{vdW}} + V_{\text{Coulomb}} + V_{\text{HX}} + V_{\text{cross}} \dots \tag{21}$$

With the bond stretching energy V_{stretch}, bond bending energy V_{bend}, torsional energy V_{tors}, van der Waals (non-bonding) energy V_{vdW}, the electrostatic Coulomb term V_{Coulomb}, hydrogen bonding energy V_{HX}, and the cross terms V_{cross} which make two or more FF terms interdependent.

The Lennard-Jones Model

The Lennard-Jones (LJ) model is a simple pair potential used to calculate non-bonding attractive and repulsive interactions. It is used to model V_{vdW} (see equation (21)) in many FF potential functions. It can also be used to approximate the interactions between monoatomic chemical species that only interact through van der Waals interactions. The LJ potential can be formulated as

$$V_{\text{LJ}}(r_{ij}) = \frac{A_{ij}}{r_{ij}^{12}} - \frac{C_{ij}}{r_{ij}^{6}}, \tag{22}$$

where A and C are atom-specific constants and r_{ij} is the inter-particle distance.

The TIP4P Water Model

The TIP4P pair potential was developed to describe the interactions between water molecules at low computational cost.[74] Even though flexible implementations of TIP4P exist, bond lengths and bond angles of the water molecules are often kept rigid using constraints such as RATTLE[6] in order to allow for room temperature dynamics simulations with larger time steps; otherwise, time steps as low as 0.1–0.2 fs are required to accurately sample O – H stretching and bending vibrational modes. The electrostatic distribution on each water molecule is governed by 4 point charges: one on each atomic center and one on an additional virtual position to improve the overall distribution. The TIP4P potential relies on non-bonded interactions; it contains a Coulomb term to treat electrostatic interactions and a Lennard-Jones term (see equation (22)) to treat van der

Waals interactions. For two molecules m and n, the potential follows the general form

$$E_{mn}^{\mathrm{TIP4P}} = \sum_{i}^{\text{on } m} \sum_{j}^{\text{on } n} \frac{q_i\, q_j\, e^2}{r_{ij}} + \frac{A}{r_{\mathrm{O\text{-}O}}^{12}} - \frac{C}{r_{\mathrm{O\text{-}O}}^{6}} \,. \tag{23}$$

With the elementary charge e, indices i and j of the point charges q on molecules m and n, respectively, distance between point charges r_{ij}, and the Lennard-Jones parameters A and C. The parameters are chosen to reproduce the bulk properties of water.

Reactive Force Fields

Classical FFs are unable to describe the formation or breaking of chemical bonds during the runtime of a simulation. Attempts were made to describe chemical reactions with FFs by introducing potential terms that depend on the bond order (BO), which itself is a function of interatomic distance.[117; 73] Thus, reactive FFs do not use fixed binding tables but re-calculate bonding partners at each iteration. Notable reactive FF approaches are the Brenner[16], Tersoff[157], and ReaxFF[165] potential functions.

ReaxFF

The ReaxFF reactive force field was first published in 2001 by van Duin and Goddard.[165] Like other reactive potentials, ReaxFF assumes that the bond order BO_{ij} between two atoms i and j is a function of the bond length r_{ij}. Compared to equation (21), the ReaxFF potential,

$$V_{\mathrm{tot}} = V_{\mathrm{stretch}} + V_{\mathrm{over}} + V_{\mathrm{under}} + V_{\mathrm{angle}} + V_{\mathrm{tors}} + V_{\mathrm{vdW}} + V_{\mathrm{Coulomb}} \cdots , \tag{24}$$

introduces the BO-dependent V_{over} and V_{under} terms. BO_{ij} is determined as

$$BO'_{ij} = \exp\left[\rho_{\mathrm{bo},1}\left(\frac{r_{ij}}{r_0}\right)^{\rho_{\mathrm{bo},2}}\right] + \exp\left[\rho_{\mathrm{bo},3}\left(\frac{r_{ij}^{\pi}}{r_0}\right)^{\rho_{\mathrm{bo},4}}\right] + \exp\left[\rho_{\mathrm{bo},5}\left(\frac{r_{ij}^{\pi\pi}}{r_0}\right)^{\rho_{\mathrm{bo},6}}\right] . \tag{25}$$

The exponential terms correspond to the σ bond ($\rho_{\mathrm{bo},1}$ and $\rho_{\mathrm{bo},2}$), the first π bond ($\rho_{\mathrm{bo},3}$ and $\rho_{\mathrm{bo},4}$) and the second $\pi\pi$ bond ($\rho_{\mathrm{bo},5}$ and $\rho_{\mathrm{bo},6}$). The interdependence of the bond length and BO for each bond type is tuned via the parameters $\rho_{\mathrm{bo},1-6}$. Fig. 1.1 illustrates the dependence of BO_{ij} on the bond distance of a C−C bond.

Without additional correction, this approach can lead to overcoordination. In an ethane molecule, for example, the C atoms are close enough that the hydrogen atoms will contribute to the BO of both C atoms. Therefore, corrective factors f are introduced so that

$$BO_{ij} = BO'_{ij}\, f_1(\Delta'_i, \Delta'_j)\, f_4(\Delta'_i, BO'_{ij})\, f_5(\Delta'_j, BO'_{ij}) \tag{26}$$

$$\Delta'_i = \sum_{j=1}^{n_{\mathrm{bond}}} BO'_{ij} - Val_i \,. \tag{27}$$

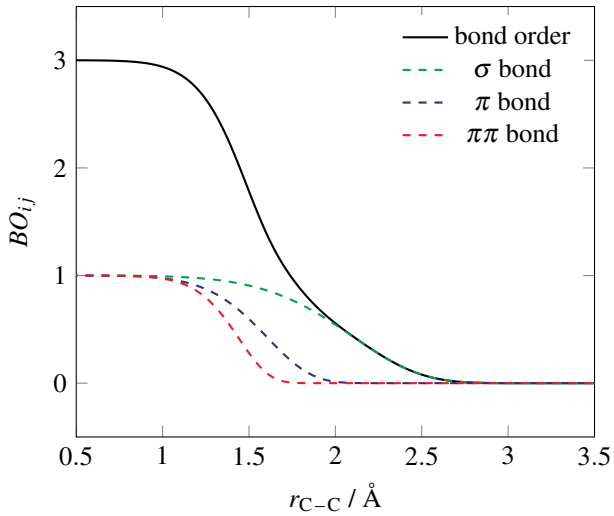

Figure 1.1. Illustration of the relationship between the C−C interatomic distance r_{C-C} and the bond order BO_{ij} in the ReaxFF potential. Adapted from [165].

Here, Δ'_i measures how much the uncorrected bond order BO'_{ij} differs from the maximum valency Val_i of atom i. n_{bond} indicates the number of bonding partners.

This correction gives rise to the overcoordination energy penalty V_{over} which ensures that maximum valencies are not exceeded. Like any other potential term, V_{over} requires careful fitting for each new atomic species. For example, introducing excessive overcoordination penalty for hydrogen atoms would lead to incorrect description of H−X bonds and transition states. The V_{under} term in equation (24) is obtained in an analogous way in order to penalize undercoordination.

To illustrate how ReaxFF introduces BO dependency into classical FF terms, consider the ReaxFF V_{vdW} term, which is derived from a Morse potential function:

$$\begin{aligned} V_{\text{vdW}} &= D_{ij}\left\{\exp\left[\alpha_{ij}\left(1-\frac{f_{13}(r_{ij})}{r_{\text{vdW}}}\right)\right]\right. \\ &\quad \left. -2\,\exp\left[\frac{1}{2}\,\alpha_{ij}\left(1-\frac{f_{13}(r_{ij})}{r_{\text{vdW}}}\right)\right]\right\}. \end{aligned} \tag{28}$$

Here, D_{ij} is the bond dissociation energy, r_{vdW} are the atomic van der Waals radii, and α_{ij} is the stiffness of the potential. This term is modified by a BO-dependent correction term (f_{13}) which ensures that the contributions vanish for $r_{ij} \to \infty$. Note that the van der Waals and Coulomb terms in ReaxFF use fixed, finite repulsive forces for small r_{ij} to avoid discontinuities.

1.3 Thermodynamic Ensembles

Microcanonical Ensemble (*NVE*) Adiabatic conditions, isolated model system. Constant number of particles N, volume V, and energy E. Because of the conservation of energy, NVE ensembles are ergodic.

Canonical Ensemble Closed model system in contact with a heat bath (thermostat). Constant number of particles N, volume V, and temperature T. Different thermostats exist, ReaxFF uses the *Nosé-Hoover* variant.[114; 60]

Grand Canonical Ensemble Open model system in contact with a heat bath. Constant chemical potential μ, volume V, and temperature T. Particles can be added to or subtracted from the model system until equilibrium is reached based on the μ of the particle reservoir.

1.4 Grand Canonical Monte Carlo Simulations

Introduction

The grand canonical Monte Carlo (GCMC) algorithm was introduced by Senftle *et al.* in 2013.[137] The GCMC algorithm randomly adds, moves, and subtracts particles (atoms or molecules) from a simulation box until equilibrium is reached with a reservoir, which is defined by the chemical potential μ of the particles. ReaxFF energy minimization steps after each Monte Carlo move allow the system to relax and accommodate the new atomic configuration. As a result, the model system can rearrange significantly over the course of the simulation.

The GCMC Algorithm

In the beginning of every iteration of the GCMC algorithm, one of the following moves is performed at random:

1. Insertion of a particle at a random position,
2. removal of a random particle, or
3. movement of a particle to a new, random position.

ReaxFF subsequently optimizes the new configuration. If the optimization fails, the move is rejected. Otherwise, the Boltzmann probabilities

$$P_{\text{insert}} = \min\left(1, \frac{V}{\Lambda^3(N+1)} \exp\left[-\beta(E_{\text{new}} - E_{\text{old}} - \mu_{\text{res}})\right]\right), \tag{29}$$

$$P_{\text{delete}} = \min\left(1, \frac{N\Lambda^3}{V} \exp\left[-\beta(E_{\text{new}} - E_{\text{old}} + \mu_{\text{res}})\right]\right), \tag{30}$$

$$\text{and } P_{\text{move}} = \min\left(1, \exp\left[-\beta(E_{\text{new}} - E_{\text{old}})\right]\right) \tag{31}$$

are calculated to evaluate the new configuration. Here, N are the number of particles allowed to exchange before the GCMC iteration, Λ is the thermal de Broglie wavelength of the exchanged particle, V is the constant volume of the system, $\beta = (k_B T)^{-1}$ is a Boltzmann factor, E_{old} and E_{new} are ReaxFF total energy results for the system before and after the GCMC step, and μ_{res} is the chemical potential of the particle reservoir.

Note however that the energy minimization steps introduce a bias into the acceptance criteria.[15] To compensate for this bias, the total volume of the system in equations (29)–(31) must be replaced with the volume V_{acc} that the active reservoir species can access during MC moves. V_{acc} is approximated as the difference between the occupied space and the total cell volume V. Assuming x as the active species and the only species in the simulation, the accessible volume is given as

$$V_{acc} = V - N_x \frac{4}{3} \pi r_x^3 , \tag{32}$$

where r_x indicates the atomic radius of species x. Figure 1.2 presents a flow chart of the GCMC algorithm.

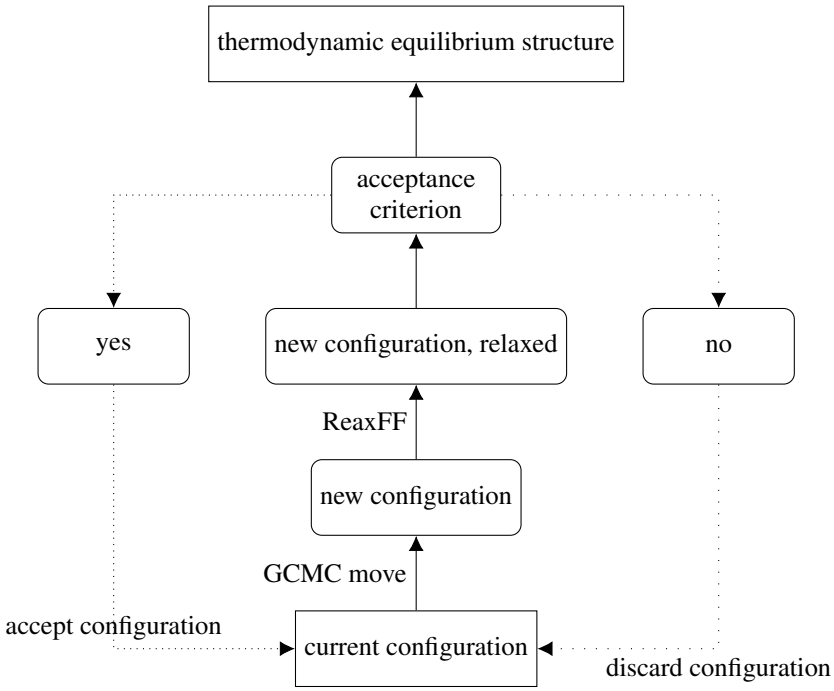

Figure 1.2. Flow chart of the GCMC algorithm. Adapted from Gai et al.[44]

1.5 The Free Energy Method

The free energy method can be used to estimate the stability of reaction intermediates on an electrocatalyst as a function of the electrode potential.[113; 95; 143] Standard hydrogen electrode (SHE) conditions are assumed, *i.e.* pH 0, $p_{H_2} = 1$ bar, and $T = 298$ K. Under these conditions, equation (33) is in equilibrium:

$$H_{2(g)} \longleftrightarrow 2\,(H^+_{(aq)} + e^-) \tag{33}$$

For the ORR in particular, reactions (34)–(36) can therefore be defined to be in equilibrium at $U = 0$ V:

$$2\,H_2O + {}^* \quad \longleftrightarrow \quad {}^*OOH + \frac{3}{2}\,H_2 \tag{34}$$

$$H_2O + {}^* \quad \longleftrightarrow \quad {}^*OH + \frac{1}{2}\,H_2 \tag{35}$$

$$H_2O + {}^* \quad \longleftrightarrow \quad {}^*O + H_2\,, \tag{36}$$

where * denotes a favorable adsorption position on the studied electrocatalyst model.

Assuming the associative pathway and concerted proton-coupled electron transfer steps throughout, the individual steps of the catalytic $4\,e^-$ ORR mechanism can therefore be defined, given in equations (37) to (40), as

$$O_2 + {}^* + H^+ + e^- \quad \longrightarrow \quad {}^*OOH \tag{37}$$

$${}^*OOH + H^+ + e^- \quad \longrightarrow \quad {}^*O + H_2O \tag{38}$$

$${}^*O + H^+ + e^- \quad \longrightarrow \quad {}^*OH \tag{39}$$

$${}^*OH + H^+ + e^- \quad \longrightarrow \quad H_2O + {}^* \tag{40}$$

By introducing an $e\,U$ term, where e is the elementary charge of an electron and U is the electrode potential, the potential-dependent Gibbs free energy changes $\Delta G(U)$ for all reaction steps can be calculated as

$$\Delta G_{OOH}(U) = (G_{OOH} + 2\,G_{H_2O}) - (G_{clean} + 3\,G_{H^+}) - 3\,eU \tag{41}$$

$$\Delta G_{O}(U) = (G_{O} + G_{H_2O}) - (G_{clean} + 2\,G_{H^+}) - 2\,eU \tag{42}$$

$$\Delta G_{OH}(U) = (G_{OH} + G_{H_2O}) - (G_{clean} + G_{H^+}) - eU \tag{43}$$

$$\tag{44}$$

where $G_{H^+} = \frac{1}{2} G_{H_2}$. The Gibbs free energy for each component x (x = O, OH, OOH, H_2, H_2O) is calculated as

$$G_x = E_x + E_{ZPE} + T \cdot S_{vib,x} \tag{45}$$

with the total SCF energy from DFT calculations E_x as well as contributions from the zero-point energy E_{ZPE} and entropy $T \cdot S_{vib,x}$ at room temperature $T = 298$ K.

The onset potential U_{onset} of the electrocatalytic ORR process can be estimated by setting U to the value where equations (41)–(43) first become exergonic. The overpotential η_{TCM} can then be obtained as the difference between the ideal thermodynamic

potential of the ORR, 1.23 V, and U_{onset}. The index "TCM" indicates that this thermochemical model neglects other contributions besides free energy changes that affect the overpotential in experiments, such as reaction kinetics and mass transport of educts and products.

Different pH conditions can be accounted for by modifying the Gibbs free energy of the proton, $G_{\mathrm{H^+}} = \frac{1}{2} G_{\mathrm{H_2}} - k_{\mathrm{B}}\, T \ln(10)\ \mathrm{pH}$, where k_{B} is the Boltzmann constant.

2 Simulations of the Oxidation of Platinum Nanoparticles Using Reactive Force Fields

2.1 Motivation

Climate change and global warming are major threats to public safety. A recent report by the United Nations Office for Disaster Risk Reduction estimates that extreme weather events between 2000 and 2019 have claimed over 1 million lives and generated close to 3 trillion USD in economic damages.[162] Compared to the previous 20 year time span, the number of floodings has doubled and the incidence of serious storms grew by 50 %.

The scientific community has reached an overwhelming consensus that our way of living accelerates natural climate change processes.[110; 26] Thus, research into sustainable energy sources with low or zero carbon footprint has become a major point of interest across many fields, from chemistry to surface science to engineering.

A promising technology emerging from these efforts is the proton-exchange membrane fuel cell (PEMFC). Fuel cells generate electricity by reacting hydrogen and oxygen under controlled, electrocatalytic conditions. Although the technology itself is not new as alkaline fuel cells have been used in the US space program since the 1950s, commercial use of PEMFCs in personal transport and stationary applications has only received mainstream attention in the new millennium.

2.2 Proton-Exchange Membrane Fuel Cells

A PEMFC is made up of two coupled electrochemical half cells, as illustrated in Fig. 2.3. In a PEMFC, the simple reaction

$$2\,H_2 + O_2 \longrightarrow 2\,H_2O \tag{46}$$

occurs as two half-reactions in physically separated environments:

$$2\,H_2 \longrightarrow 4\,H^+ + 4\,e^- \tag{47}$$

$$O_2 + 4\,e^- + 4\,H^+ \longrightarrow 2\,H_2O \tag{48}$$

The first half cell reaction, hydrogen oxidation, occurs at the anode of the fuel cell. Here, H_2 is oxidized in the presence of an electrocatalyst. This reaction yields 4 electrons which are transported to an external load where work is accomplished. The protons

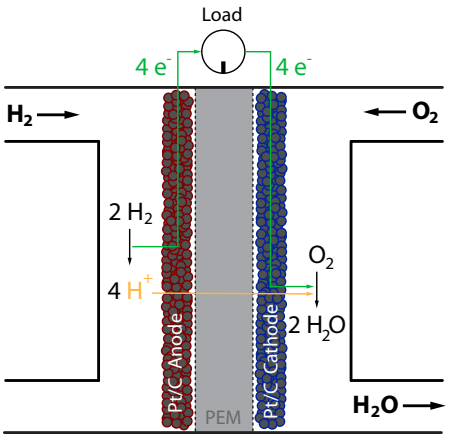

Figure 2.3. Schematic representation of the electrochemical processes in a PEMFC using a carbon-supported Pt catalyst (Pt/C).

generated during this step can pass through the PEM into the other half cell. On the cathodic side, molecular oxygen reacts to water in the presence of an electrocatalyst using protons and electrons from the anodic half cell reaction.

Typically, carbon-supported platinum nanoparticles (Pt/C) are used as electrocatalysts for both half cell reactions. The anodic hydrogen oxidation reaction (HOR), however, is much faster than the cathodic oxygen reduction reaction (ORR), making the ORR the bottleneck step of this process.

2.3 The Oxygen Reduction Reaction

Being the bottleneck step for fuel cell performance, the mechanism of the ORR on Pt-based electrocatalysts has been studied extensively, both in experiments and in computational works. There are two mechanisms for the desirable $4\,e^-$ ORR pathway which are prominently discussed: the associative ORR mechanism

$$O_2 + {}^* \longrightarrow {}^*O_2 \tag{49}$$

$${}^*O_2 + H^+ + e^- \longrightarrow {}^*OOH \tag{50}$$

$${}^*OOH + H^+ + e^- \xrightarrow[-H_2O]{} {}^*O \tag{51}$$

$${}^*O + H^+ + e^- \longrightarrow {}^*OH \tag{52}$$

$${}^*OH + H^+ + e^- \xrightarrow[-H_2O]{} {}^* \tag{53}$$

and the dissociative ORR mechanism

$$O_2 + {}^* \longrightarrow {}^*O_2 \tag{54}$$

$${}^*O_2 \longrightarrow 2\,{}^*O \tag{55}$$

$$2\,{}^*O + 2e^- + 2H^+ \longrightarrow 2\,{}^*OH \tag{56}$$

$$2\,{}^*OH + 2H^+ + 2e^- \xrightarrow[-\,2H_2O]{} 2\,{}^* . \tag{57}$$

Here, * denotes an active adsorption site on the catalyst. The associative mechanism can branch off into a competing process, referred to as the $2e^-$ pathway, which leads to the formation of H_2O_2. Starting from equation (51), adsorbed *OOH can further react according to

$${}^*OOH + H^+ + e^- \longrightarrow {}^*O_2H_2 . \tag{58}$$

This product can further dissociate into 2 *OH or it can desorb. Desorbed H_2O_2 can potentially react to H_2O in what is referred to as the $2 + 2e^-$ pathway. For fuel cell applications, the $2 + 2e^-$ pathway is generally undesirable; not only is it slower than the direct $4e^-$ pathway as it involves potential desorption and re-adsorption of H_2O_2, but there is a chance that the desorbed H_2O_2, which is a strong oxidant, can damage the cell components.

Using the B3LYP hybrid DFT functional and a Pt(111) cluster model catalyst, Keith and Jacob have shown that all of the mentioned mechanisms are competitive from a thermodynamic perspective.[76] However, they also found that the H_2O_2-producing pathways become unfavorable when the influence of water molecules on the stability of the ORR intermediates is taken into account.[77]

2.4 The Role of Oxides in the ORR on Pt Catalysts

There is a consensus that the oxygen evolution reaction (OER) takes place on an oxidized Pt catalyst, which is reflected in the computational literature on this topic (see for example the DFT study by Rossmeisl and co-workers[134]). The review by Suen *et al.* is also suggested for further information on the OER.[154] The mechanism of the ORR, on the other hand, has predominantly been researched on non-oxidized Pt surfaces in computational studies.

Notably, several computational and experimental reports suggest that surface oxides may be present on Pt catalysts at typical fuel cell operating conditions. In 2007, Jacob used DFT calculations and the extended *ab initio* thermodynamics (EAITD) approach, which is conceptually related to the free energy method presented in section 1.5, to determine that surface oxides have a window of stability under these conditions.[67] More recently, Fantauzzi *et al.* first predicted the presence of stable surface oxides on a Pt(111) single crystal model at near-ambient pressure (NAP) using the ReaxFF-GCMC simulation strategy and then experimentally confirmed their predictions using NAP-XPS.[39] A recent review by Farkas *et al.* summarizes these and further theoretical and experimental efforts of the group on this topic.[41]

A DFT study by Holby *et al.*[58] as well as DFT and ReaxFF studies by Fantauzzi *et al.*[38; 39] find low barriers for place exchange processes of oxygen on Pt(111),

which can lead to the formation of buckled surface oxide structures. These buckled structures can be described as rows of elevated Pt atoms lined by oxygen on both sides in a pattern resembling bulk α-PtO_2. Such α-PtO_2-like patterns were also observed by Zhu *et al.* in scanning tunneling microscopy (STM) and XPS measurements.[197] The group finds that from these patterns, PtO clusters will readily form on the stepedge sites of a Pt(557) surface and will even grow to nanometer size at room temperature and elevated oxygen pressure. A recent STM study by van Spronsen and co-workers comes to similar conclusions, observing formation of α-PtO_2-like stripes on a Pt(111) single crystal in O_2, NO, and CO atmospheres.[167] Hanselman *et al.* studied the α-PtO_2-like stripes found by van Spronsen *et al.* using DFT and conclude that they are likely stable under electrochemical conditions.[53]

The suggestion that stable surface oxides are present on Pt-based oxygen reduction electrocatalysts under operating conditions has far reaching consequences. Mechanistic insights obtained from simulations with non-oxidized Pt model systems may have to be re-investigated in light of this premise. Notably, platinum oxides are known to be catalytically active outside the context of the ORR. For example, Li *et al.* report high experimental photocatalytic HER activity of small supported PtO clusters.[94] In a DFT study, Seriani and co-workers report a Pt_3O_4 surface to be surprisingly active for the oxidation of carbon compounds.[140] They however also report that the Pt_3O_4 phase has only a small window of stability.[139] The review by Gómez-Marín *et al.*, which focuses on computational studies, is pointed out as a resource for more detailed information on how different oxygen-containing species can affect the ORR on Pt-based catalysts.[51]

It can be summarized that significant evidence points towards the active involvement of oxides in the catalytic cycle of the ORR on Pt catalysts. However, the studies discussed in this section relied on single crystals to study the oxidation of Pt, both in experiments and in computational works. So far, to the best of the authors knowledge, no computational studies explicitly used nanoparticle model systems to research oxidation trends of Pt electrocatalysts. This observation in part motivates the present study. Furthermore, while oxidation of Pt fuel cell catalysts is hypothesized to be a prerequisite for the ORR to take place, oxidative degradation of the catalyst is learly an undesirable process. Disagreement exists in literature over the mechanism of oxidative degradation as well as the chemical nature of oxides on platinum catalysts in general.[174; 139; 125; 155] This study, therefore, aims to simulate complete oxidation of the model systems with the goal to improve understanding of the mechanisms underlying oxidative degradation processes.

2.5 Pt Nanoparticles as ORR Catalysts

With few exceptions, most theoretical works studying the ORR on Pt catalysts are performed using single-crystal model surfaces. However, Pt catalysts in PEMFCs are applied in nanoparticle (NP) form. Using high-indexed surface models to mimic the behavior of NPs cannot cover all factors that lend NPs their unique catalytic properties, as was recently emphasized in a publication by Calle-Vallejo and co-workers.[20] The

group notes that, for example, stepped surface models contain both convex and concave surface sites while typical NPs only contain one type. Therefore, the present work will explicitly make use of NP model systems to study the oxidation behavior of Pt catalysts as close to real applications as possible. In the following, the relationship between structural parameters of NPs and their catalytic activity for the ORR is discussed.

Nanoparticle Shape

The shape of a NP is linked to the Miller indices of its facets and the overall ratio between edge and facet sites. Fig. 2.4 illustrates the NP shapes used in this work. Analogous to single crystal surfaces,[101] NPs show different oxygen binding strength

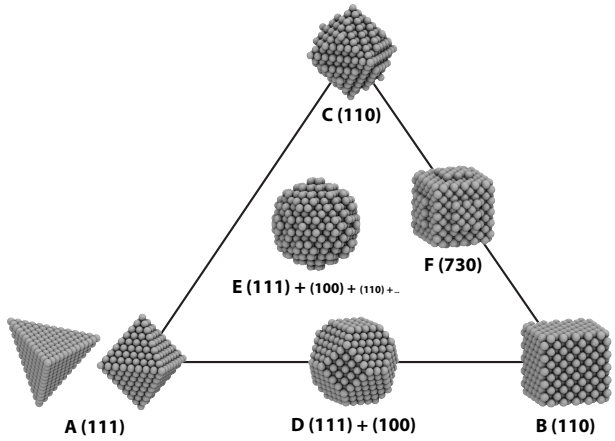

Figure 2.4. Shapes and associated facet Miller indices of the 3 nm NPs used in this work. ***A*** *Tetrahedron (left) and octahedron (right),* ***B*** *cube,* ***C*** *dodecahedron,* ***D*** *cuboctahedron,* ***E*** *sphere, and* ***F*** *tetrahexahedron. Adapted from [159].*

and different ORR activity depending on the nature of their surface facets. Even though calculations find the thermodynamic stability sequence Pt(111) > Pt(100) > Pt(110) in vacuum,[38] the cuboctahedral shape, which consists of (111) and (100) facets, is found to be thermodynamically most stable in simulations,[185; 63] likely due to its more favorable surface-to-volume ratio compared to the purely (111)-indexed octahedra and tetrahedra. Calculations also showed that the per-atom formation energy of spherical NPs is higher than of cuboctahedral NPs,[185; 63] which indicates that at some point, is is energetically more favorable for particles to form low-indexed surface facets rather than to fully maximize roundness (*i.e.* to further reduce the surface-to-volume ratio). It can therefore be assumed that commercial, non-shape-controlled Pt NP catalysts are of (disordered) cuboctahedral shape.

As research into NP catalysts intensified in the new millennium, it quickly became clear that synthesizing shapes other than the cuboctahedron is a productive way to fine-tune their catalytic activity. Some of the most active ORR catalysts reported to date have octahedral shape, as summarized in a 2019 review by Zhao and co-workers.[195] In 2013, Cui and co-workers presented an octahedral Pt-Ni alloy NP with thus far

unprecedented mass activity and stability.[31; 30] Huang *et al.* iterated on this theme and introduced additional Mo doping to an octahedral Pt-Ni catalyst, leading to one of the most active known Pt-based NP catalysts to date.[64] Wang and co-workers furthermore synthesized an octahedral core-shell Pt-Co catalyst with similarly exceptional qualities for the ORR.[175] Other highly active catalysts are based on nanowires and nanoframeworks;[195] however, these types of catalyst structures are beyond the scope of this work. Within the realm of non-alloyed Pt catalysts, the tetrahexahedral particles introduced by Tian and co-workers are noteworthy.[160] The rough facets of this NP family have a high ratio of undercoordinated sites, making them interesting candidates for catalysis.

Experimental studies comparing the ORR activity of various NP shapes have been inconclusive. For example, Wang *et al.* compared the ORR activity of 3–7 nm Pt polyhedra, truncated cubes, and cubes and found the cube to outperform all other tested materials.[173] Another study by Narayanan *et al.* reports ORR activities for 5–7 nm tetrahedral, cubic, and near-spherical nanoparticles and found the tetrahedral NP to be most active.[109]

Nanoparticle Size

Size impacts NP reactivity significantly. For example, assuming that the generalized coordination numbers (GCNs)[19] of facet atoms of a NP are a reasonable first indicator for reactivity, a certain size of the facet is required before the facet atoms' GCNs reach the value of the corresponding single crystal surface. According to a study by Kleis *et al.*, NPs sized larger than *ca.* 2.8 nm are required before adsorption properties on cuboctahedral Au NPs converge to values produced by infinite-surface models.[86] This result is in agreement with GCN based analysis which indicates that GCNs of facet atoms of NPs sized *ca.* 3 nm have converge to the value of the corresponding single crystal surface.

In case of Pt NPs, catalytic activity and stability present a trade off. Meier *et al.*[106] and Yu *et al.*[188] find that Pt NPs smaller than 5 nm have higher measured ORR activity but degrade much more quickly than larger particles. An experimental study by Shao *et al.* investigates Pt NP catalysts in the 1–5 nm range in particular and finds that the specific activity increases exponentially from 1 to 3 nm and then reaches a plateau, resulting in the highest mass activity for 2.2 nm particles.[144] The group links this result to the abundance of undercoordinated sites on small NPs. Similarly, an experimental study by Wang and Yeh shows correlation between particle size and heat of formation when oxidizing Pt NPs at temperatures between 200 and 1000 K.[174]

2.6 This Work in the Context of Similar Literature

Studies simulating oxidation of Pt NPs of this size are rare because DFT-based studies typically employ periodic surface models[58; 140; 139] or small clusters.[187] Using the ReaxFF-GCMC approach also employed in the present work, Senftle *et al.* published several studies on H, C, and O uptake in Pd NPs.[137; 138] Fantauzzi *et al.* used the

ReaxFF-GCMC approach to predict conditions under which stable surface oxides will form on a Pt single crystal surface.[38] Their prediction was confirmed experimentally using NAP-XPS.

To the best of the author's knowledge, only one other publication specifically tackles oxidation of Pt NPs at this scale: Gai *et al.* combine the ReaxFF-GCMC approach with reactive molecular dynamics (MD) to study O and H uptake in a stepped Pt(321) surface and octahedral, cuboctahedral, and cubic Pt NPs.[44] While the main focus of their study is the development of a new Pt/O/H ReaxFF FF, they calculated adsorption isotherms and make general observations about the relationship between the number of available edge and vertex sites for each NP shape and the resulting proclivity towards oxidation. Bulk oxidation is not studied. Notably, for the Pt(321) surface they show formation of a surface cluster resembling the Pt_6O_8 motif, which is one of the key results in the present work, but do not explore this observation any further.

2.7 Project Summary and Outlook

The oxidation of the various 3 nm NPs presented in Fig. 2.4 as well as of 2 and 4 nm cuboctahedral NPs is simulated using the ReaxFF-GCMC methodology. The present work will focus on results for the 2, 3, and 4 nm cuboctahedral particles. This size range is representative of commercial Pt/C catalysts used in fuel cells.[106] Results for the other particles shapes will be briefly touched on but will be published outside the context of this thesis at a later date.[83]

Oxidation of the cuboctahedral particles is studied at 200–1200 K and oxygen partial pressures of $p_O = 1$ mbar (NAP) and $p_O = 10^{10}$ mbar (ultra high vacuum, UHV). The Pt/O ReaxFF FF developed by Fantauzzi and co-workers is used.[38] Temperature and pressure conditions are dialed in by varying the chemical potential μ_{res} of the oxygen reservoir. The resulting chemical potential of oxygen is

$$\begin{aligned} \mu_O(T,p) &= \frac{1}{2}\,\mu_{O_2}(T,p) \\ &= \frac{1}{2}\left[\mu_{res}(T,p^0) + k_B\,T\,\ln\left(\frac{p}{p^0}\right) - (E_d + E_{ZPE})\right], \end{aligned} \tag{59}$$

where $(E_d + E_{ZPE})$ is the zero-point energy corrected bond dissociation energy of O_2. Note that the training set for this particular FF is based on GGA DFT data. Due to self-interaction, DFT significantly overestimates the bond strength of O_2.[35; 87] This error can affect the boundary temperatures in these simulations. Fantauzzi *et al.* showed that the boundary temperatures obtained using this FF deviate from experiments by *ca.* 50 K.[40]

The per-atom formation energy of various NP shapes over a large size range is calculated and the FF, which had originally been trained on periodic surface model systems, is found to reproduce published stability trends. Adsorption isobars are constructed from the obtained data set. The general oxidation trends in these simulations (*e.g.* initial oxidation of undercoordinated sites) are found to be in agreement with other published studies.

Unlike in the aforementioned ReaxFF-GCMC study on Pt NP catalysts by Gai and co-workers, simulations in this work are continued until particles are completely oxidized. At strongly oxidizing conditions, simulations predict degradation of the NPs into amorphous agglomerates of smaller clusters of Pt_6O_8 stoichiometry. Note that α-PtO_2 (*i.e.* fully oxidized Pt(IV)) is expected to be the thermodynamic end point for the oxidation of Pt. However, given the molecular nature of the used model systems, rearrangement into the sheet-like α-PtO_2 structure is unfavorable and thus, the simulation does not proceed beyond $[Pt_6O_8]_n$. The Pt_6O_8 structure can be interpreted as a variant of Pt_3O_4; Vegas notes that a bulk Pt_3O_4 crystal consisting of icosahedral Pt_6O_8 units like those observed in the present simulations is most likely a mixed-valence oxide with a Pt(IV) to Pt(II) ratio of 2:1.[170] As noted earlier, Gai *et al.* obtained a single cluster reminiscent of this Pt_6O_8 motif in a ReaxFF-GCMC-driven oxidation simulation of a Pt(321) surface using a different FF but did not investigate this structure any further further.[44]

To the best of the author's knowledge, existence of the Pt_6O_8 species is only corroborated in one other work, a PhD thesis by Dimas Rivera. They report interlayer distances corresponding to Pt_6O_8 based on high-resolution transmission electron microscopy experiments of a Pt-Fe compound catalyst.[32]

DFT results indicate that formation of Pt_6O_8 clusters is thermodynamically favorable. Further DFT calculations not presented in Publication **I** (but using the same methodology) also indicate that there is a driving force for these clusters to form linear chains, in particular when negatively charged. Partial charge distribution analysis using the EEM method implemented in ReaxFF suggests that the Pt_6O_8 cluster is likely negatively charged. An argument based on the electronic structure of the solid state icosahedral Pt_3O_4 structure presented by Vegas suggests that the cluster carries 4 negative charges.[170] However, the exact charge state of the cluster remains unclear and is subject to future research.

Additional research is also needed to investigate if Pt_6O_8 is in fact a stable primary degradation product of oxidized Pt catalysts or just a transient species. Furthermore, while the used FF has proven its predictive capabilities in the past regarding formation of stable surface oxides on Pt(111) single crystals,[38] and despite encouraging DFT results, it cannot be completely ruled out that formation of the Pt_6O_8 motif is a result of an artificial bias introduced by the training data set or during fitting of the potential function.

Ultimately, experimental confirmation of Pt_6O_8 is needed, ideally in the electrolyte of a PEMFC during or shortly after operation. To this end, time-resolved X-ray scattering measurements could prove useful.[52] Results from this experiment can be correlated with radial pair distribution functions (RDFs) obtained from constant-temperature MD simulations which could provide indirect evidence of the species.[33] To this end, simulations of Pt_6O_8 in (explicit) water solvent would be required. Due to the size of the cluster, many thousand H_2O molecules would be necessary to properly sample the solvent response. The FF used in this work contains parameters for H_2O and its interactions with Pt, which was exploited to simulate the influence of solvation on the particle stability in Publication **I**. However, it would be advantageous to study the solvation of the Pt_6O_8 cluster using an electronic structure method in order to accurately take into account its charge state (once conclusively established). Section 4 presents the

development of a methodology intended to be used in hybrid QM/MM simulations that will make such simulations computationally feasible in the future.

Finally, the obtained ReaxFF-GCMC data set is used to construct electrochemical oxidation phase diagrams for the various NPs. Publication **I** summarizes work on cuboctahedral NPs. The phase diagram of the 3 nm cuboctahedral particle is refined by calculations of the stabilization energy due to interaction with water molecules as well as entropic contributions from the two-phase thermodynamics (2PT) method.[97] Results suggest that stable surface oxides are likely present on the particle at typical fuel cell operating potentials. The $[Pt_6O_8]_n$ structure is expected to form between 1.1–1.2 V *vs.* SHE. Above 1.2 V, formation of α-PtO_2 is expected based on DFT predictions.[67] The onset potential for complete oxidation is found to depend on the particle size, rising from 2 to 3 to 4 nm, in agreement with general chemical intuition.

Results for various other NP shapes will be published outside the context of this thesis.[83] While similar general trends as for the cuboctahedron are found for the other particles, such as favored oxidation of undercoordinated sites under mildly oxidizing conditions, electrochemical phase diagrams reveal that, notably, the onset potential of surface oxidation depends on the particle shape.

To summarize, the ReaxFF-GCMC simulation approach is shown to be a powerful predictive tool for structure-activity relationships of NP catalysts. While the present work focuses on oxidation exclusively, this methodology could be transferred to other chemical processes of interest. Finally, since Pt_3O_4 surfaces were shown to catalyze small molecule oxidation,[140] investigations of the catalytic activity of Pt_6O_8 clusters should be considered in the future.

2.8 Addendum I: SCM ADF Suite Version Conflict

The results in this work are obtained using ReaxFF implemented in the SCM ADF suite version 2017.103.[166] All data presented in this work and in the associated publications use this version of ADF for consistency. In trying to reproduce the ReaxFF-GCMC simulations with newer versions of the ADF suite, the author noticed that it was impossible to obtain the completely oxidized structures. Using the same input parameters as before, simulations stop after surface oxidation. However, when using the completely oxidized structures obtained using version 2017.103 as input structures for single point or geometry optimization calculations with newer version, the same total energy values are obtained as with version 2017.103 (last tested version: 2019.301). This result confirms that the obtained fully oxidized structures are indeed lower in energy under aggressive conditions and that the obtained trends and phase diagrams hold true.

However, this also indicates that the GCMC routine was changed after version 2017.103. SCM were informed of the issue. This disparity between versions should be kept in mind when attempting to reproduce results from this work.

2.9 Addendum II: Disclaimer

This project was started in 2017 as an industrial collaboration with the Volkswagen Group (VW) in Wolfsburg, Germany (main contact: Dr. Jonathan Mueller, jonathan.edward.mueller@volkswagen.de). The collaboration with VW extended between February 2017 and January 2019 and involved regular progress meetings and two workshops in Wolfsburg. The project was then continued without further involvement of VW.

3 The Thermochemistry of the Oxygen Reduction Reaction on N-Doped Graphene from DFT Calculations

3.1 Motivation

Pt-based materials constitute the most active class of electrocatalysts for PEMFCs to date. However, Pt is scarce and expensive, and significant ethical concerns revolve around Pt mining conditions.[21; 5]

Understanding-driven material optimization strategies such as the study presented in part 2 can help to reduce the overall amount of Pt necessary to operate PEMFCs. Also, alloying platinum with more abundant elements like Cu[112] or Ni[31] can reduce costs and even increase catalytic performance. However, for fuel cell technology to become one of the main pillars in a new mix of sustainable technologies that have the potential to supersede fossil fuels, precious metals in ORR electrocatalysts will ultimately need to be replaced outright.

Enter the discovery of graphene by Novoselov, Geim, and co-workers in 2004 which changed material science over night and was recognized with the physics Nobel Prize in 2010.[115] Due to its unusual electronic properties such as being a zero band gap semiconductor graphene was, among many other applications, also explored as an electrocatalyst over the past decade. At first glance, however, graphene does not seem to possess the necessary properties that would make an efficient ORR catalyst in particular. In experiments, the ORR on pure graphene follows a $2e^-$ mechanism, has a high overpotential, and mainly produces the unwanted byproduct H_2O_2.[102]

The view on graphenes as ORR catalysts changed in 2010 when Qu *et al.* published the first report on nitrogen-doped graphene (NG).[126] The material was synthesized via chemical vapor deposition (CVD) on a Ni substrate. Qu's NG catalyzed the $4e^-$ ORR under alkaline conditions and produced 3 times higher steady state currents than a reference Pt/C catalyst. Qu's NG also showed exceptional resistance to the catalyst poisons methanol and CO. In 2011, a first report by Sheng *et al.* on the alkaline ORR on boron-doped graphene (BG) emerged.[145] Several other first- and second-row doped graphenes followed. The review articles by Sturala *et al.*,[153] Hou *et al.*,[61] Agnoli and Favaro,[2] Mamtami and Ozkan,[99] and Wang *et al.*[176] are recommended as an overview over experimental studies in this highly active field of research. The present work will focus on NG in particular.

Fundamentals of fuel cells and the ORR are introduced in sections 2.2 and 2.3, respectively. The following sections will focus on introducing the specific challenges

that researchers face when attempting to use NG as an ORR electrocatalyst.

3.2 The Role of Transition Metal Impurities

A notable number of experimental studies claim that the high experimental ORR activity of doped graphenes stems from transition metal impurities rather than from inherent material properties. For example, several groups note that if natural graphite is used as a precursor for the synthesis of NG, significant amounts of Fe impurities remain in the product.[4; 177] This observation is significant because NGs that are explicitly functionalized with Fe are well known to be active ORR catalysts.[141; 96; 179] In case of Fe-NG catalysts, experiments have conclusively shown that the Fe centers and not the N moieties constitute the active sites for the ORR.[180; 59] Masa and co-workers synthesized NG under ideal, metal-free conditions and then added increasing amounts of an Fe-containing precursor into subsequent batches.[102] They found that a truly metal-free NG sample showed similar behavior to pure graphene, inefficiently catalyzing the $2e^-$ ORR pathway with H_2O_2 as the main product. However, as soon as Fe contaminants were introduced during synthesis, ORR activity increased significantly and the $4e^-$ process was found to be prevalent.

Furthermore, one of the most popular ways of synthesizing graphene oxide, which is a precursor to NG in some synthetic strategies, is the Hummers method. This method uses molar equivalents of $KMnO_4$ for the oxidation.[65; 100] Wang and co-workers report that large quantities of Mn remain in NG synthesized using Hummers method.[177] Note that manganese oxides are known to catalyze the ORR under alkaline conditions.[161]

Ambrosi and co-workers found that both naturally occurring transition metal impurities and residues from the synthetic method cannot be easily removed from the product.[4] They found that wet-chemical methods are nearly useless and that aggressive conditions (Cl_2 atmosphere, 1000 °C) are required to see a substantial amount of reduction. However, they also found that such aggressive treatment partly destroys the material.

In 2020, Wang and co-workers published the sensationally-titled study "Will Any Crap We Put Into Graphene Increase Its Electrocatalytic Effect?".[178] The group synthesized doped graphene using guano, an excrement of certain bird and bat species which is rich in the elements N, P, and S. They report significantly increased electrocatalytic activity of the guano-doped graphene compared to undoped graphene and raise the question if the chemical nature of the dopant matters at all.

It can thus be summarized that the exact source of catalytic activity of formally metal-free doped-graphene-based ORR electrocatalysts remains an open question.

3.3 Computational Studies of the ORR on NG

Computational studies on NG are motivated by the open questions on the nature of the ORR mechanism and the involved active site(s). Experiments that tried to pinpoint the

active site have been inconclusive (see for example Qu,[127] Geng,[46] and Vazquez-Arenas[169]) and the debate about the influence of transition metal impurities splits the community. The strength of theory in this context is that computational methods can provide activity estimates that are truly unaffected by unwanted impurities and can thus help to provide additional context for the experiments. Computational studies on NG relevant for this work will be discussed in the following.

Active Site and Reaction Mechanism

One of the earliest computational studies important for the field was published by Ikeda and co-workers.[66] In a Car-Parrinello MD simulation using the HCTH functional, they find that zig-zag edges of an N-doped graphite model are most active for O_2 adsorption. They also note that presence of water is integral to stabilizing the various ORR intermediates. This publication and a later, PBE-based MD study by Yu *et al.*,[189] which also considered the presence of explicit solvent molecules, are typically cited as having established the *associative* ORR mechanism to be prevalent for NG and doped graphenes in general. Okamoto studied a periodic NG model system in contact with explicit water molecules in a PBE-based MD simulation.[116] They identified possible reaction pathways for both the $4e^-$ and for the competing, less desirable $2e^-$ ORR pathway. They also suggest a potential catalyst poisoning mechanism resulting from strong binding of the *O intermediate at high surface coverage. This study furthermore corroborates findings by Ikeda *et al.* with regards to presence of water molecules significantly changing adsorption strength of the ORR intermediates. A recent publication by Reda and co-workers, in which the authors evaluate the influence of an ice-like layer of water molecules on the ORR intermediates in calculations using the BEEF-vdW functional, arrives at the same conclusion.[128]

Several studies find that NG edge sites should be most active for the ORR. Both Okamoto[116] and Choi *et al.*[25], however, point out that it is unlikely that the high measured ORR activity of NGs stems exclusively from the relatively few edge sites of NG sheets. The latter group therefore proposed a long-range electron transfer mechanism from PBE-based simulations which does not require the otherwise critical O_2 adsorption step, suggesting that basal-plane graphitic dopant atoms can serve as viable active sites as well.[25] Using the PBE functional, Kim *et al.* reconcile contradicting experimental reports regarding the active site by postulating a ring opening mechanism on an NG nanoribbon during which a graphitic N site at the edge of the ribbon is converted into a pyridinic site.[78] Using the PBE functional, Chai and co-workers report an ionic $2e^-$ pathway involving direct reaction of O_2 with an adsorbed H^+ species.[23] This mechanism, too, does not require energetically favorable adsorption of O_2.

Studies by Chai *et al.*[24] (HCTH functional) and Xie *et al.*[186] (PW91 functional) suggest that Stone-Wales defects and other lattice deformations can induce ORR activity. The PBE studies by Zhao *et al.*[194] and Jia *et al.*[70] go even further and suggest that the lattice defects themselves are responsible for the ORR activity of these materials, suggesting that heteroatom doping may not be required at all. While these studies on lattice defects are outside the scope of the present work, they emphasize that the computational community, too, has not reached a consensus yet with regards to the

active site and the mechanism of the ORR on NG.

Computational Estimates of the ORR Overpotential

Many computational studies use the free energy approach (see section 1.5) to calculate estimates of the overpotential of the ORR on doped graphenes.[113] The overpotentials obtained using the free energy approach are herein referred to as η_{TCM} (TCM: thermochemical model) to indicate that η_{TCM} is a thermodynamic descriptor exclusively and neglects other factors such as reaction kinetics or mass transport phenomena which affect experimentally measured overpotentials.

Studies that apply the free energy approach to computational NG models typically assume the associative $4\,e^-$ ORR pathway. In the first publication of this kind, Studt estimates an η_{TCM} of 0.72 V for a periodic model system with 6.2 % graphitic N dopants.[152] They use the BEEF-vdW functional but do not consider solvation effects. For reference, typical overpotentials measured for Pt/C electrocatalysts are in the range of 0.3–0.4 eV.[171] Using the BEEF-vdW functional, Reda *et al.* predict an η_{TCM} range of 0.7–0.9 V for different N dopant concentrations and varying coverage of spectating (unreactive) *O adatoms in the presence of one layer of water molecules in ice-like configuration.[128] The group considered graphitic active sites exclusively. The studies by Reda *et al.* and Studt both find overbinding of the *O intermediate to be responsible for the comparatively high η_{TCM} results, in agreement with the study by Okamoto discussed earlier.[116] For a model system similar to the one used by Studt, Gíslason and Skúlason calculate an η_{TCM} of 0.57 V using RPBE.[50] PBE studies by Li *et al.*[92] and Sinthika *et al.*[150] and a B3LYP study Jiao *et al.*[72] calculate η_{TCM} values in the range of 0.4–0.5 V. To summarize, with few exceptions, most studies predict low overpotentials and thus, high ORR activity for the employed metal-free NG model systems.

The combined computational and experimental study by Jiao and co-workers[72] is noteworthy for several reasons. Firstly, they used the hybrid B3LYP functional while all other studies referenced so far used GGA functionals. Secondly, the group employed a molecular flake model system while the majority of studies in this field used periodic sheet or ribbon model systems. Finally, their study included not only N-doped graphene but also B-doped graphene and several other dopant elements. Notably, they find that NG and BG show the best and very similar ORR activity in experiments, and they also estimate similar η_{TCM} values for NG and BG in calculations using the free energy approach. Solvation contributions were accounted for in their calculations via an implicit solvation approach.

In case of the Jiao model system, the N dopant is located at the center of the flake. This result is corroborated in a study by Sidik and co-workers who used a similar flake model system and the B3LYP functional to calculate free energy results.[149] A study by Zhang and Xia used a molecular NG model system in combination with B3LYP as well.[193] They predict that the $4\,e^-$ ORR pathway on the studied NG flake model should take place spontaneously. The group also investigated spin and charge densities at the B3LYP level and found that clustering N atoms at the active site will not increase the ORR activity beyond a cluster size of 2.[192] In contrast to the Jiao and Sidik studies, the latter two publications find that edge dopant sites are most active for the

ORR. Notably, all four referenced studies used flake models of different size and shape to study the ORR on NG.

To summarize, reviewing the computational literature on NG reveals two important aspects: i) there is no consensus with regards to the active site (pyrrolic, pyridinic, graphitic, defects, *etc.*) and ii) η_{TCM} predictions for NGs are typically favorable even though fundamentally different model systems (infinite-sheets, ribbons, molecular flake models) and methodological approaches (different GGA and hybrid DFT functionals) are used. This is a surprising analysis. One might be inclined to therefore conclude that graphene, despite its complex electronic and structural properties, is well-described at all rungs of DFT and that computational results support those experiments which suggest that metal-free NGs are *inherently* active electrocatalysts for the ORR. Unfortunately, benchmark studies suggest that many of the DFT functionals used in the reviewed studies introduce large errors into adsorption energy calculations for this material class, which will be discussed in the following section.

3.4 Accuracy of DFT Functionals for Adsorption Energy Calculations on Graphene

Based on the computational works on NG reviewed in the preceding sections, a noteworthy trends emerges. The studies can be divided into two groups: group 1 used periodic model systems and GGA functionals while group 2 used molecular flake model systems and the B3LYP functional. Despite employing a variety of fundamentally different model systems (sheets, ribbons, molecular flakes) and despite the disagreements regarding mechanisms and active sites, most publications ultimately agree that NG possesses reasonably favorable thermodynamic properties for the ORR based on η_{TCM} estimates within the free energy approach. Notable exceptions are the more pessimistic BEEF-vdW-based studies by Studt[152] and Reda *et al.*[128]

The consensus with regards to low computational η_{TCM} results is not only surprising because of the wide range of density functionals and model systems used throughout literature. The mentioned studies also contradict experimental results that link transition metal impurities to high experimental ORR activity of NG. It is therefore important to establish that the level of theory and the model systems used in these calculations are appropriate for this chemical problem.

To the best of the author's knowledge, only two benchmark studies exist that test the accuracy of DFT methods for adsorption energy calculations of graphene-based model systems. In 2012, Hsing and co-workers published tests of the accuracy of LDA and typical GGA functionals for adsorption energy calculations of H, O, and Li on undoped graphene.[62] An accurate Diffusion Monte Carlo (DMC) simulation is used as the benchmark value in their study. GGA functionals are found to reproduce H adsorption energy values reasonably well but are found to introduce errors of up to 0.5 eV into adsorption energy calculations of *O, which is one of the reaction intermediates in the ORR catalytic cycle. The poor accuracy of GGA functionals in these tests is concerning even though this study considered pure graphene exclusively and only a single $\boldsymbol{k}$ point was sampled as a limitation of the DMC approach.

A follow-up study was published by Janesko and co-workers one year later.[68] The group reused the DMC values reported by Hsing *et al.* as a reference and calculated O adsorption energy results and approximate O diffusion barriers on undoped graphene using GGA, meta-GGA, and hybrid functionals. They find that the hybrid functionals PBE0 and HSE06 reproduce the DMC reference value most closely. GGA, meta-GGA, and the B3LYP hybrid functionals are found to produce significant deviations from the reference value.

Although these benchmark studies used undoped graphene to study the influence of different density functionals, they serve as a warning that GGA functionals and certain hybrids like B3LYP potentially fail to reproduce accurate binding energy results and diffusion barriers for oxygen-containing species on graphene-based model systems in general. Note that several groups[116; 152; 128] for example find that overbinding of the *O intermediate in particular is a poisoning mechanism for NG ORR catalysts. The present work therefore sets out to re-investigate adsorption energy trends shown in earlier computational works using a simulation strategy based on the accurate PBE0 and HSE06 functionals.

3.5 Project Summary and Outlook

The present work aims to further build on the benchmark works by Hsing *et al.*[62] and Janesko *et al.*[68], relate the benchmark results to free energy calculations of the ORR intermediates on NG, and finally derive a reliable simulation approach for this chemical problem. Using this reliable simulation approach, dopant concentration is studied as a parameter that can be used to tune the thermodynamic properties of NG model systems. Furthermore, solvation is found to be a key factor that significantly affects predictions of the ORR activity of the tested NG model systems.

Firstly, the aforementioned benchmark calculations for O adsorption on undoped graphene are reproduced; the set of tested density functionals is however expanded by the BEEF-vdW and SCAN functionals. Note that the present work compares the energy difference ΔE between the top and bridge adsorption geometry to avoid calculations of the free ^3O and $^3O_2$ species which are known to be erroneous in LDA and GGA DFT due to self-interaction.[87] The benchmark results obtained in this work are in agreement with the Hsing and Janesko studies, showing that PBE0 and HSE06 reproduce the DMC reference value most closely with 5 and 6 % deviation, respectively. GGA and meta-GGA functionals as well as the hybrid B3LYP are found to underestimate ΔE by and least 27 % (B3LYP) and up to 40 % (BEEF-vdW). A PBE functional with explicit self-interaction correction as proposed by Perdew and Zunger (PZ-SIC)[122] is found to overestimate ΔE by 8 % compared to the reference value.

Further benchmark calculations are performed for molecular flake models. Hybrid DFT calculations using the PBE0 functional reveal that these models can give erratic adsorption energy results depending on the exact shape and size of the flakes. The accuracy of the PBE0 functional is validated against coupled-cluster singles doubles and perturbative triples (CCSD(T)) electronic structure calculations using the domain-based local pair natural orbital (DLPNO) approximation to reduce the computational

effort.[124; 129; 49; 119; 118] Contrary to periodic model systems, the flake models are found to deform strongly when oxygen-containing species adsorb on them (see also [14]). This deformation is significant because curvature effects have been found to break the scaling relations for calculated adsorption energy results on NG.[186] The results presented in this part therefore indicate that molecular flake models do not reliably represent the properties of sheet-like, extended doped graphene ORR electrocatalysts but should only be used to study actual nanomaterials such as quantum dots.[93]

Subsequently, thermochemical overpotentials η_{TCM} are calculated for NG using various density functionals, assuming the associative $4\,e^-$ mechanism. An infinite-sheet model with 3.1 % dopant concentration and one graphitic dopant per cell is used. The size of this model is converged with respect to the adsorption energy of the ORR intermediates, indicating that no interaction between dopants across periodic images occurs (dilute limit). This model is chosen deliberately for benchmarking because of its low complexity. By showing the obtained η_{TCM} as a function of the benchmark ΔE result for each functional, a noteworthy trend emerges. Fig. 3.5 illustrates this relationship for BG, the corresponding results for an NG model can be found in Publication **II**.[1] The

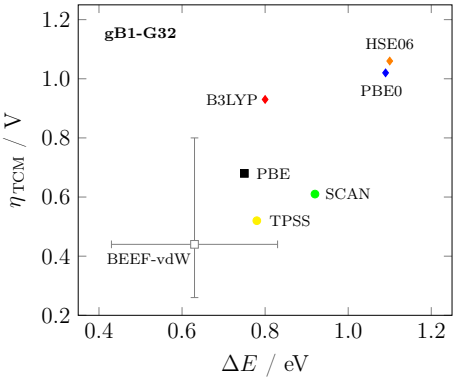

Figure 3.5. The thermochemical overpotential η_{TCM} obtained for a 32-atomic (3.1 % doping) BG model system is shown as a function of the benchmark result ($\Delta E = E_{tot}^{top} - E_{tot}^{bridge}$) for oxygen adsorption on undoped graphene for various density functionals.

DMC benchmark result is not shown in this Fig. 3.5 because the ΔE and η_{TCM} values were obtained using a fully converged $\boldsymbol{k}$ grid while the DMC ΔE value from Hsing *et al.* was obtained by sampling a single $\boldsymbol{k}$ point.[62] However, by calculating the average difference between ΔE values for all DFT functionals obtained using the same single $\boldsymbol{k}$ point and using a converged $\boldsymbol{k}$ grid ($\Delta\Delta E = -0.186$ eV, standard deviation: ± 0.009 eV), the ΔE value for DMC using a converged-k-grid can be estimated to be 1.174 eV.

Fig. 3.5 suggests that better performance in the benchmark for oxygen adsorption on undoped graphene is roughly correlated with a higher η_{TCM} on BG. The same

[1] More in-depth results on the ORR on BG will be published outside the context of this thesis in the future. Fig. 3.5 is shown as an illustration of the data analysis approach. Results for NG published in Publication **II** give rise to the same conclusions.

trend is obtained for NG, see Publication **II**. Fig. 3.5 illustrates that depending on the choice of functional, this particular model system is predicted to be either highly active (BEEF-vdW) or completely inactive (hybrids). According to the preceding benchmark, the η_{TCM} results obtained using PBE0 and HSE06 constitute the most reliable estimate.

BEEF-vdW allows users to calculate standard deviations for relative energy results based on Bayesian error estimation. To this end, BEEF-vdW generates an ensemble of GGA functionals (here: 2000) with varying functional parameters. This error estimation approach is therefore expected to reflect the general accuracy of GGA-DFT for this particular application. The maximum and minimum values for ΔE and η_{TCM} obtained this way constitute the extreme points of the error bars in Fig. 3.5. This analysis indicates that the uncertainty is significant, with $\Delta\Delta E \approx \pm 0.2$ eV and $\Delta\eta_{\mathrm{TCM}} \approx \pm 0.25$ V for BG. Error estimates for NG are similar, see Publication **II**. Note that ΔE results for HSE06 and PBE0 are not within the error range of BEEF-vdW, which could indicate that GGA functionals fundamentally lack contributions — most likely exact exchange — that are necessary to accurately describe this particular chemistry.

Using the HSE06 hybrid functional, the influence of dopant concentration is studied in more detail. To this end, the number of dopant atoms is doubled, resulting in a material with 6.2 % dopant concentration.[2] The resulting NG model is the same as a model used by Studt.[152] Using the HSE06 functional, η_{TCM} is found to reduce from 0.97 V at 3.1 % to 0.72 V at 6.2 % doping. Using the BEEF-vdW functional, on the other hand, η_{TCM} is found to increase from 0.59 V at 3.1 % to 0.72 V at 6.2 % doping. This result is noteworthy because it highlights that for this application, GGA functionals not only produce wrong quantitative results, they also likely predict wrong qualitative trends.

To estimate the influence of water molecules on the adsorption energy of the ORR intermediates on NG, two sets of published solvation stabilization energy ($\Delta E_{\mathrm{solv}} = \Delta E_{\mathrm{ads}} - \Delta E_{\mathrm{ads}}^{\mathrm{solv}}$) results are applied to HSE06 total energy results from this work. The first set of ΔE_{solv} results was calculated by Reda *et al.* using a periodic infinite-sheet NG model in contact with an ice-like layer of 5 H_2O molecules.[128] The BEEF-vdW functional was used to obtain adsorption energy results. Using these ΔE_{solv} results, the η_{TCM} for the 3.1 % NG model used in this work reduces from 0.97 V to 0.79 V. For the model with 6.1 % doping, η_{TCM} reduces even further to 0.54 V. Note that calculations of ΔE_{solv} for the ORR intermediates on NG using the HSE06 functional shown in the Supplementary Information to Publication **II** are similar to the ΔE_{solv} results published by Reda *et al.* obtained using the BEEF-vdW functional. This good agreement indicates that calculations of ΔE_{solv} are less sensitive to the choice of functional than adsorption energy calculations of the ORR intermediates.

The second set of ΔE_{solv} results was published by Yu *et al.* who performed MD simulations using the PBE density functional to sample structures of the ORR intermediates on a periodic infinite-sheet NG model in contact with 41 H_2O molecules.[189] The energetically most favorable snapshots from these MD simulations were then used to calculate ΔE_{solv}. Using these ΔE_{solv} results, η_{TCM} of the 3.1 % doped model system reduces from 0.97 V to 0.48 V but η_{TCM} for the the 6.1 %-doped model only reduces from 0.72 V to 0.66 V. This observed change in overall trends when using ΔE_{solv}

[2] Note that calculating η_{TCM} for lower dopant concentrations is not necessary since the 3.1 % model already constitutes the dilute dopant limit (see Supplementary Information of Publication **II**).

corrections based on different simulation approaches highlights how critical a robust description of solvation is when attempting to calculate accurate adsorption energetics of the ORR intermediates on NG.

To summarize, benchmark calculations have shown that typical GGA functionals will underestimate the η_{TCM} on NG models by up to 40 % compared to the accurate hybrid PBE0 and HSE06 functionals. Using the HSE06 functionals, η_{TCM} calculations of different NG models give high η_{TCM} results, suggesting that these models posses unfavorable properties for the ORR. However, first tests using published data indicate that solvation can affect η_{TCM} trends significantly.

Treatment of solvation is the part of this work with the largest potential for improvement. The published ΔE_{solv} datasets for NG by Reda *et al.* and Yu *et al.* are in disagreement, likely due to differences in methodology, and there is no easy way to establish which results are more trustworthy. A rigorous approach to sampling ΔE_{solv} as a thermodynamic average from MD simulations using a large number of explicit water molecules would be required to obtain more reliable results. Section 4 details the development of a method that will enable such simulations in the future. While this work can suggest a consistent simulation approach to obtain high quality electronic structure results, more rigorous ΔE_{solv} data and inclusion of the explicit electrode potential are required before decisive contributions can be made to the ongoing debate about the nature of the ORR activity of doped graphene electrocatalysts.

4 Development of a Flexible Boundary Algorithm for Hybrid Simulations

4.1 Motivation

Despite using fundamentally different computational methodologies, the studies presented in sections 2 and 3 arrived at a similar end point where accurate solvation calculations using a large number of explicit water molecules constitute the next milestone in these projects. In fact, the importance of correctly describing solvent interactions cannot be overstated in general.

Water, in particular, actively participates in many reaction mechanisms. The field of organic synthesis has experienced what Kitanosono *et al.* describe as a "watershed" moment in a recent review: after efforts were increased to reduce the use of organic solvents for environmental concerns and to redesign industrial processes in the context of water-based chemistry, studies emerged detailing how presence of water would alter reaction mechanisms and selectivities, oftentimes in positive ways.[85] For example, Rossin *et al.* report that water takes an active role in the regioselective hydrogenation of aldehydes via a Ru-based catalyst.[133] Water-based solvents can be combined with organic solvents in two-phase reactions, where different reaction steps occur in different solvents or where the product of the reaction transfers into a different solvent.[131] Introduction of water is also known to improve reactions that rely on acid-base catalysts.[107; 47]

As highlighted in parts 2 and 3, solvation plays an important role in heterogeneous catalysis as well. In computational studies, accurate description of the solid-liquid interface is critical. For example, solvation can significantly change the binding energy of ORR intermediates on a fuel cell catalyst and therefore change predicted activity trends.[66; 116; 128] In battery research, the solid-electrolyte interface (SEI) has been the focus of many studies. The SEI is suspected to affect dendrite growth in Li-ion batteries[190] and is found to be one of the major contributors to capacity fading.[91] Understanding and ultimately fine-tuning SEI growth will help to maximize battery lifetime and performance.[3]

To attempt a comprehensive review of current research efforts in this highly active and multidisciplinary field would be futile. Hopefully, these exemplary studies serve to illustrate that researchers from widely different backgrounds are invested in improving our understanding of solvation phenomena.

4.2 Solvation in Electronic Structure Calculations

Introducing hundreds or thousands of solvent molecules into DFT or HF electronic structure calculations is prohibitively expensive. Various strategies have therefore been developed to ease the computational effort. Therein, implicit solvation methods constitute the most common approach due to their widespread availability in most modern DFT codes. Implicit solvation methods represent the solvent as a homogeneous medium defined by bulk properties such as the permittivity.[29; 142] Since no actual molecules are added to the simulation box, this approach fails to capture many important interactions such as hydrogen bonding and charge transfer processes. As a result, several studies find that use of implicit solvation models rarely improve results compared to calculations without any solvation and typically cannot reproduce experimental measurements.[37; 191; 48; 54]

The embedded solvation approach constitutes the next rung in the hierarchy of solvation methods. Here, a small number of explicit solvent molecules is included in the calculations while the rest of the solvent is represented using an implicit solvent method. This way, contributions such as hydrogen bonding or charge transfer can be properly represented at reasonable computational cost. Garcia *et al.* for example used this approach to study the influence of water on the decomposition of methanol on transition metal surfaces.[45] Moreover, embedded solvation can be combined with a Poisson-Boltzmann-based approach to model the influence of the electrode potential at the interface by placing virtual counter charges in the implicit solvent region. This simulation strategy was used to good effect recently by Van den Bossche *et al.* who successfully reproduced HER barriers on Pt(111) from elaborate extrapolation methods[135; 151] at a fraction of the computational cost.[163] Basdogan *et al.* however point out an important limitation of the embedded solvation approach: introducing too many explicit molecules can introduce a significant error into the electronic energy.[7] The number of explicit solvent molecules used in an embedded solvation simulation strategy therefore requires careful optimization.

Hybrid methods constitute the most sophisticated approach to modeling solvation. The QM/MM approach, for which Karplus, Levitt, and Warshel received the Nobel Prize in 2013, is the most prominent example of a hybrid method.[181; 158; 43] In hybrid simulations, the model system is divided into subsystems which are calculated using different computational methods. Typically, the region of a model where a process of interest occurs is confined to one subsystem and is calculated using a higher accuracy method. The remaining chemical environment makes up another, larger subsystem which is calculated at lower accuracy and interacts with the first subsystem electrostatically.

Hybrid methods can be broadly categorized into two classes. The first class of methods are adaptive hybrid methods. In adaptive hybrid simulations, particles (atoms or molecules) can pass from one subsystem into another. This freedom of movement introduces energetic discontinuities if the potential description of a particle is switched abruptly, thereby breaking conservation of energy and forces.[183] To counteract this source of error, state-of-the-art adaptive hybrid methods[172; 11; 57; 123; 17; 42; 184; 182; 183] make use of a scheme referred to as adaptive partitioning.[57] In adaptive partitioning, a buffer region around the boundary is defined. The potential energy and/or

forces of particles in the buffer region are evaluated using both computational methods used in the hybrid simulation. It was found that ideally, all possible permutations of describing each particle with one computational method or the other should be calculated and weighted. The results from this so-called multi-partitioning approach then enable smooth interpolation of the potential energy and force terms between the two regions.

The multi-partitioning approach can resolve most (but not all[183]) errors introduced by switching the potential description of particles during the simulation. However, the computational cost of multi-partitioning simulations is greatly increased due to the large number of calculations required to evaluate all permutations of particles in the buffer region. Current implementations of adaptive hybrid methods therefore focus on reducing the number of permutations needed to accurately conserve the energy and forces.

The second class of hybrid methods, restrictive hybrid methods, are the focus of the present work and will be discussed in more detail in the following section.

4.3 Restrictive Hybrid Methods

Unlike in case of adaptive hybrid methods, particles cannot pass from one subsystem into another when using a restrictive hybrid method. An impenetrable boundary confines particles within the subsystem they were originally assigned to. Restrictive methods therefore sacrifice the correct description of microscopic trajectories but instead aim to implement the formally unphysical boundary in a way that preserves correct average thermodynamic properties of the simulation. Unlike in adaptive hybrid methods, particles never leave their initial potential energy surface. Restrictive hybrid methods therefore remain computationally efficient since they, in principle, do not require additional sets of calculations to ensure conservation of energy and forces around the boundary.

The most straightforward way of implementing the boundary is to partition the simulation box into a static inner and outer region. While this approach can be used to good effect in hybrid simulations of entirely rigid systems such as a proteins, it is less useful if mobile species are present in simulations. Firstly, hard sphere boundaries can lead to an erroneous particle density around the boundary.[18] Secondly, in order to obtain correct thermodynamic solvation free energy results, the number of water molecules in the inner region needs to be varied and the resulting configurations require statistical analysis within the quasi-chemical theory (QCT) approach.[8] Not only does this increase the computational effort significantly but each configuration of n solvent particles in the inner region also needs to be weighted by (entirely system-dependent) probability factors $P(n)$ which Rogers and Beck report to be challenging to obtain.[130]

Some of these limitations can be alleviated by having a dynamic boundary instead of a static one. The Flexible Inner Region Ensemble Separator (FIRES) method was introduced by Rowley and Roux in 2012 and features a non-static definition of the boundary.[136] FIRES assumes that three components are present in a simulation: a solute, an inner region that expands around the solute, and an outer region that expands

around the inner region. Particles in the inner and outer region must be of the same chemical species while the solute can be of arbitrary chemical composition. The boundary is then defined by the distance between the solute and the outermost particle in the inner region. Given that the intended use case for FIRES is to study solvated systems, the position of the boundary is therefore dynamic because the inner and outer region (solvent) particles are mobile.

Rowley and Roux showed that this approach gives correct average thermodynamic properties, without the need for an elaborate QCT scheme. Their justification is based on an earlier work by Beglov and Roux on the spherical solvent boundary potential method[10] in which the outer region is represented by an implicit solvation method. Consider the configurational integral Z of the system,

$$Z = \int dr_{\mathrm{sol}} \, \frac{1}{N!} \int dr_1 \int dr_2 \, \ldots \int dr_N \, e^{-U/k_{\mathrm{B}}\,T} \, . \tag{60}$$

Here, $r_{\mathrm{sol,\,1,\,2,\,\ldots,\,N}}$ are the solute and solvent particle degrees of freedom, N is the total number of solvent particles, and U is the total potential energy (assuming a canonical ensemble). The factor $\frac{1}{N!}$ accounts for equivalent configurations that can emerge from the N identical particles in the simulation.

The configurational integral can now be separated into n inner region and $N-n$ outer region particles,

$$\begin{aligned} Z' = \quad & \int dr_{\mathrm{sol}} \, \frac{1}{n!} \int dr_1 \int dr_2 \, \ldots \int dr_n \\ & \frac{1}{(N-n)!} \int' dr_{n+1} \int' dr_{n+2} \, \ldots \int' dr_N \, e^{-U/k_{\mathrm{B}}\,T} \, , \end{aligned} \tag{61}$$

where the prime indicates integration over the spatially restricted outer region. As long as inner and outer region particles are identical and are not allowed to cross into the respective other region, the average thermodynamic quantities obtained from equation (61) will be correct. Section 4.5 (Addendum) contains a proof that $Z = Z'$ for an exemplary one-dimensional system of non-interacting particles.

In case of FIRES, the crossover of particles between regions is restricted using a Hookean potential,

$$E_{\mathrm{FIRES}} = \frac{1}{2} \sum k_{\mathrm{FIRES}} (r_j - \max(R_{\mathrm{i}}))^2 \, . \tag{62}$$

Here, k_{FIRES} is a spring force constant, r_j is the distance from an outer region particle j to the solute, and $\max(R_{\mathrm{i}})$ is the distance to the solute of the inner region particle that is farthest away from the solute. The potential is zero as long as $r_j > \max(R_{\mathrm{i}})$ and is scaled by how far particle j has penetrated into the inner region when $r_j < \max(R_{\mathrm{i}})$. The FIRES penalty potential therefore results in a gradual separation process.

Applications of FIRES include, for example, benchmark calculations of Zn and Mg in chemical and biological contexts to obtain training data for DFTB3 parameterization[98] and calculations of solvation effects for the transition state in a nucleophilic carbonyl reaction.[12]

In their 2013 review, Bulo *et al.* find that FIRES produces unphysical structural artifacts.[18] Studying RDFs of simulations using FIRES, they report erroneous accumulation of particles around the location of the boundary, similar to what is observed in

simulations using a static sphere boundary. A possible explanation for this erroneous particle density is that FIRES does not, as implied by the original premise, instantaneously redirect particles at the boundary but rather approximates this process using a Hookean constraint. This hypothesis is the main motivator for the present work and will be elucidated in more detail in section 4.4. Another issue pointed out by Bulo *et al.* is that coupling sufficiently different potential functions can lead to large deviations of the RDFs from ideal behavior. However, this limitation is inherent to all coupling schemes[183] and can be ameliorated by using matched potentials.[71]

Other restrictive hybrid methods have followed in the footsteps of FIRES. The BEST (Boundary based on Exchange Symmetry Theory) method by Shiga and Masia aims to find a generalized form of the separation potential, which makes FIRES a specific case of BEST.[146; 147] The BEST separation potential is constructed by calculating a penalty function for each pair of inner and outer region particles in a system. The penalty function is unity for separated pairs and approaches zero as particles travel outside the region that they were assigned to. The separation potential is the product of all penalty functions. Shiga and Masia find that taking into account only those few particle pairs with penalty functions closest to zero usually suffices to obtain consistent results, which reduces the additional computational effort required when using BEST.

The main drawback of BEST is that the separation potential makes it impossible to study dynamic properties of a system. In 2015, Shiga and Masia introduced an improved version of BEST, entitled QUEST (QUasi-boundary based on Exchange Symmetry Theory), which aims to restore correct dynamics.[148] However, QUEST requires additional calculations of the exchange partners to offset the influence of the separating potential, thereby increasing computational demands again.

In 2018, Takahashi *et al.* introduced the BCC (Boundary Constraint with Correction) method.[156] Similar to BEST, BCC uses a Fermi-type separating potential to restrict exchange of particles between regions. Because instantaneous redirection at the boundary cannot be achieved with any penalty potential, BCC requires additional sets of calculations of configurations at the boundary in order to remove the statistical error caused by this approach. BCC conserves energy and forces.

Both the BEST/QUEST and BCC methods seek to alleviate the shortcomings of the original FIRES method. However, in attempting to do so, they introduce additional layers of complexity on top of the original, relatively straightforward FIRES premise. This increases the computational overhead of all of these methods, thereby somewhat offsetting FIRES biggest advantage over more accurate but much more costly adaptive coupling methods. In the following, a new method will be introduced which aims to address the issue of non-instantaneous boundary conflict resolution in restrictive hybrid methods on a fundamental level while retaining computational efficiency.

4.4 Project Summary and Outlook

A restrictive boundary method for hybrid MD simulations called Scattering-Adapted Flexible Inner Region Ensemble Separator (SAFIRES) is developed withing the Python-based open-source simulation framework ASE (Atomic Simulation Environment)[90].

The following requirements were defined for SAFIRES from the outset and are met by the implementation presented in Publication **III**:

1. The simulation box contains a solute, an inner region, and an outer region.
2. Molecules in the inner and outer regions are indistinguishable so that the system's configurational integral is separable. The solute can be of arbitrary chemical composition.
3. Both molecular solutes and periodic surface models can be employed.
4. The boundary is dynamically determined by the inner region particle that is farthest away from the origin point, which can — but is not required to — coincide with the solute or surface model.
5. Boundary conflicts are resolved instantaneously. This requirement is hypothesized to overcome the erroneous density around the boundary reported for hybrid simulations using the FIRES boundary method.
6. Energy and momenta are conserved so that constant-energy calculations can be performed.

The SAFIRES algorithm operates as follows. After a successful iteration of the superordinate MD integrator, SAFIRES checks if any outer region particles have propagated into the inner region. If this is the case, the iteration is rejected and SAFIRES restores the atomic configurations (including all associated properties such as momenta and forces) of the previous iteration while remembering which pair of inner and outer region particles triggered the event. SAFIRES then extrapolates the time step that is required to propagate the conflicting particle pair to the same distance from the origin so that both particles are located exactly on the boundary. This time step will always be smaller than or equal to the default time step. A partial propagation step using this extrapolated smaller time step is then executed using a new propagator which is based on the Vanden-Eijnden / Ciccotti implementation of the Langevin algorithm.[168] The SAFIRES propagator reduces to the Langevin algorithm for constant time steps and reduces to the Velocity Verlet algorithm for constant time steps and no friction.

Once the conflicting particle pair is located on the boundary, an elastic collision is performed between them. The boundary serves as a mediator for the collision; technically, a spherical coordinate transformation is applied to the outer region particle to rotate it "on top" of the inner region particle before the collision and to rotate it back to its original position after the elastic collision has been carried out. Rotation is unnecessary if a periodic surface model is used but the outer region particle may have to be flipped to the opposite side of the surface if a symmetric surface model with solvent particles on both sides of the slab is used.

Finally, the SAFIRES propagator evolves the system by the remaining time necessary to complete one default time step. This two-step propagation process cannot be handled by the regular propagator because forces should only be evaluated after the SAFIRES process — and, therefore, a full default time step — has been completed. If forces were evaluated after each partial propagation step, SAFIRES would not satisfy the requirement of time-reversibility of the Taylor expressions that the propagator is

derived from. All velocity updates in SAFIRES therefore are based on the default time step, as outlined in Publication **III**.

Within the ASE framework, SAFIRES is first tested on an argon Lennard-Jones (LJ) liquid model system, using the same potential description for the inner and outer regions and without any electrostatic coupling of the regions. SAFIRES is found to reproduce the RDF of a simulation without a separation algorithm without significant deviations. An analogous simulation using FIRES is found to produce an erroneous particle density around the statistical location of the boundary, analogous to reports from Bulo *et al.*[18]

SAFIRES is then tested using a LJ liquid which is in contact with a frozen Ar(111) surface generated from an *fcc* Ar crystal. SAFIRES is found to reproduce a reference calculation without separation without significant deviations in this case as well.

Finally, MD simulations of water using the SAFIRES and FIRES separators as well as a reference simulation without separation are performed. The TIP4P potential function is used to describe the interactions. Since SAFIRES resolves boundary conflicts via elastic collisions, an additional layer of complexity is introduced when molecules are involved in the collision instead of monoatomic particles. Using water as an example, if an elastic collision is performed at the boundary between a hydrogen atom of molecule 1 and an oxygen atom of molecule 2, the hydrogen atom will violently change its trajectory while the oxygen atom will barely be affected. Thus, performing elastic collisions based on individual atoms of a molecule cannot guarantee that SAFIRES instantaneously redirects the entire molecules so that the outer region remains contained. To this end, molecules are reduced to pseudoparticles with cumulative mass and effective velocity and force located at the center of mass of the original molecule. The time step extrapolation and elastic collision routines are performed on the basis of these pseudoparticles. The redistribution of the pseudoparticles' velocities to the individual atoms after the collision is performed so that rotational degrees of freedom are not quenched during the SAFIRES procedure.

At the time of writing, simulations with SAFIRES that use a periodic surface as the solute require that the surface is parallel to the *xy* plane. Stepped or non-orthogonal surfaces cannot be used at the moment. This limitation can be resolved by implementing an approach that identifies the geometry of the surface on-the-fly and constructs the boundary plane accordingly. Furthermore, SAFIRES currently requires molecular solutes to be fixed; an implementation that allows for moving solutes is in development.

SAFIRES will be used in the near future to study the effect of water molecules on the stability of the ORR intermediates on NG and BG as outlined in chapter 3. To this end, a polarizable water force field[34; 75] will be used for the outer region and DFT calculations will be used for the inner region. Furthermore, tests will be performed to determine if dynamic properties like diffusion constants can be sampled using SAFIRES if the processes occur sufficiently deep inside the QM region. In case of FIRES, it was found that dynamics could be studied in this fashion, so SAFIRES will likely succeed at this task as well.[18]

Long term development plans for SAFIRES involve extension of the methodology to include the explicit electrode potential for simulations with periodic surface models. The Poisson-Boltzmann-based approach implemented in JDFTx and VASPsol could therein serve as a template.[104; 103] Another promising direction to this end is the mass-zero constrained molecular dynamics for electrode charges method recently introduced by

Coretti and co-workers.[27]

4.5 Addendum: Equivalency of the Separated and Non-Separated Configurational Integrals

Assume a one-dimensional simulation box of two identical non-interacting particles ($U = 0$) as illustrated in Figure 4.6.

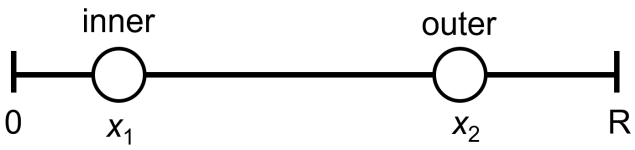

Figure 4.6. Illustration of a one-dimensional simulation box of length R. "Inner" and "outer" denote two identical non-interacting ($U = 0$) particles with coordinates x_1 and x_2, respectively. The solute is implied to be located at $x = 0$ in this simple model.

The regular, non-separated configurational integral Z from equation (60) can thus be formulated for this system as

$$Z = \int dr_{\mathrm{sol}} \frac{1}{N!} \int dr_1 \int dr_2 \ \ldots \ \int dr_N \, e^{-U/k_{\mathrm{B}}T} \tag{63}$$

$$= \int dr_{\mathrm{sol}} \frac{1}{2!} \int_0^R dx_1 \int_0^R dx_2 \, e^0 \tag{64}$$

$$= \int dr_{\mathrm{sol}} \frac{R^2}{2}. \tag{65}$$

The separated configurational integral Z' from equation (61) can be formulated accordingly as

$$
\begin{aligned}
Z' = \quad & \int dr_{\mathrm{sol}} \, \frac{1}{n!} \int dr_1 \int dr_2 \, \ldots \int dr_n \\
& \frac{1}{(N-n)!} \int' dr_{n+1} \int' dr_{n+2} \, \ldots \int' dr_N \, e^{-U/k_{\mathrm{B}}\,T} && (66) \\
= \quad & \int dr_{\mathrm{sol}} \, \frac{1}{1!} \int_0^R dx_1 \, \frac{1}{1!} \int_{x_1}^R dx_2 \, e^0 && (67) \\
= \quad & \int dr_{\mathrm{sol}} \int_0^R (R - x_1) \, dx_1 && (68) \\
= \quad & \int dr_{\mathrm{sol}} \, \frac{R^2}{2} && (69)
\end{aligned}
$$

Hence, $Z = Z'$. Note the dependence of the outer region integration limits on x_1 in Z'.

References

[1] Adamo, C. and Barone, V. (1999). Toward reliable density functional methods without adjustable parameters: The PBE0 model. *J. Chem. Phys.*, 110(13):6158–6170.

[2] Agnoli, S. and Favaro, M. (2016). Doping graphene with boron: a review of synthesis methods, physicochemical characterization, and emerging applications. *J. Mater. Chem. A*, 4(14):5002–5025.

[3] Agubra, V. A. and Fergus, J. W. (2014). The formation and stability of the solid electrolyte interface on the graphite anode. *J. Power Sources*, 268:153–162.

[4] Ambrosi, A., Chua, C. K., Khezri, B., Sofer, Z., Webster, R. D., and Pumera, M. (2012). Chemically reduced graphene contains inherent metallic impurities present in parent natural and synthetic graphite. *Proc. Natl. Acad. Sci. USA*, 109(32):12899–12904.

[5] Amnesty International (2021). South Africa: Mining gathering must confront human rights violations. https://www.amnesty.org/en/latest/news/2020/02/south-africa-mining-gathering-must-confront-human-rights-violations/. Accessed 2021-02-04.

[6] Andersen, H. C. (1983). Rattle: A "velocity" version of the shake algorithm for molecular dynamics calculations. *J. Comput. Phys.*, 52(1):24–34.

[7] Basdogan, Y., Groenenboom, M. C., Henderson, E., De, S., Rempe, S. B., and Keith, J. A. (2020). Machine Learning-Guided Approach for Studying Solvation Environments. *J. Chem. Theory Comput.*, 16(1):633–642.

[8] Beck, T. L., Paulaitis, M. E., and Pratt, L. R. (2006). *The Potential Distribution Theorem and Models of Molecular Solutions*. Cambridge University Press.

[9] Becke, A. D. (1988). Density-functional exchange-energy approximation with correct asymptotic behavior. *Phys. Rev. A*, 38(6):3098.

[10] Beglov, D. and Roux, B. (1994). Finite representation of an infinite bulk system: Solvent boundary potential for computer simulations. *J. Chem. Phys.*, 100(12):9050–9063.

[11] Bernstein, N., Várnai, C., Solt, I., Winfield, S. A., Payne, M. C., Simon, I., Fuxreiter, M., and Csányi, G. (2012). Qm/mm simulation of liquid water with an adaptive quantum region. *Phys. Chem. Chem. Phys.*, 14:646–656.

[12] Boereboom, J. M., Fleurat-Lessard, P., and Bulo, R. E. (2018). Explicit Solvation Matters: Performance of QM/MM Solvation Models in Nucleophilic Addition. *J. Chem. Theory Comput.*, 14(4):1841–1852.

[13] Born, M. and Oppenheimer, R. (1927). Zur quantentheorie der molekeln. *Ann. Phys.*, 389(20):457–484.

[14] Boukhvalov, D. (2013). DFT modeling of the covalent functionalization of

graphene : from ideal to realistic models. *RSC Adv.*, 3(20):7150–7159.

[15] Boutin, A., Tavitian, B., Fuchs, A. H., et al. (1997). Grand canonical monte carlo simulations of adsorption of mixtures of xylene molecules in faujasite zeolites. *Faraday Discuss.*, 106:307–323.

[16] Brenner, D. W. (1990). Empirical potential for hydrocarbons for use in simulating the chemical vapor deposition of diamond films. *Phys. Rev. B*, 42(15):9458.

[17] Bulo, R. E., Ensing, B., Sikkema, J., and Visscher, L. (2009). Toward a practical method for adaptive qm/mm simulations. *J. Chem. Theory Comput.*, 5(9):2212–2221.

[18] Bulo, R. E., Michel, C., Fleurat-Lessard, P., and Sautet, P. (2013). Multiscale Modeling of Chemistry in Water: Are We There Yet? *J. Chem. Theory Comput.*, 9(12):5567–5577.

[19] Calle-Vallejo, F., Martinez, J. I., Garcia-Lastra, J. M., Sautet, P., and Loffreda, D. (2014). Fast prediction of adsorption properties for platinum nanocatalysts with generalized coordination numbers. *Angew. Chem. Int. Ed.*, 53(32):8316–8319.

[20] Calle-Vallejo, F., Pohl, M. D., Reinisch, D., Loffreda, D., Sautet, P., and Bandarenka, A. S. (2017). Why conclusions from platinum model surfaces do not necessarily lead to enhanced nanoparticle catalysts for the oxygen reduction reaction. *Chem. Sci.*, 8(3):2283–2289.

[21] Capps, G. (2015). Labour in the time of platinum. *Rev. Afr. Political Econ.*, 42(146):497–507.

[22] Ceperley, D. M. and Alder, B. (1980). Ground state of the electron gas by a stochastic method. *Phys. Rev. Lett.*, 45(7):566.

[23] Chai, G.-L., Hou, Z., Ikeda, T., and Terakura, K. (2017). Two-electron oxygen reduction on carbon materials catalysts: Mechanisms and active sites. *J. Phys. Chem. C*, 121(27):14524–14533.

[24] Chai, G.-L., Hou, Z., Shu, D.-J., Ikeda, T., and Terakura, K. (2014). Active sites and mechanisms for oxygen reduction reaction on nitrogen-doped carbon alloy catalysts: Stone-wales defect and curvature effect. *J. Am. Chem. Soc.*, 136(39):13629–13640.

[25] Choi, C. H., Lim, H.-K., Chung, M. W., Park, J. C., Shin, H., Kim, H., and Woo, S. I. (2014). Long-range electron transfer over graphene-based catalyst for high-performing oxygen reduction reactions: Importance of size, n-doping, and metallic impurities. *J. Am. Chem. Soc.*, 136(25):9070–9077.

[26] Cook, J., Oreskes, N., Doran, P. T., Anderegg, W. R. L., Verheggen, B., Maibach, E. W., Carlton, J. S., Lewandowsky, S., Skuce, A. G., Green, S. A., Nuccitelli, D., Jacobs, P., Mark Richardson, Winkler, B., Painting, R., and Rice, K. (2016). Consensus on consensus: a synthesis of consensus estimates on human-caused global warming. *Environ. Res. Lett.*, 11(4):048002.

[27] Coretti, A., Scalfi, L., Bacon, C., Rotenberg, B., Vuilleumier, R., Ciccotti, G., Salanne, M., and Bonella, S. (2020). Mass-zero constrained molecular dynamics for electrode charges in simulations of electrochemical systems. *J. Chem. Phys.*, 152:10.

[28] Cramer, C. J. (2004). *Essentials of computational chemistry: theories and models*. Wiley, 2nd ed edition.

[29] Cramer, C. J. and Truhlar, D. G. (1999). Implicit solvation models: Equilibria, structure, spectra, and dynamics. *Chem. Rev.*, 99(8):2161–2200.

[30] Cui, C., Gan, L., Heggen, M., Rudi, S., and Strasser, P. (2013). Compositional

segregation in shaped pt alloy nanoparticles and their structural behaviour during electrocatalysis. *Nat. Mat.*, 12(8):765–771.

[31] Cui, C., Gan, L., Li, H.-H., Yu, S.-H., Heggen, M., and Strasser, P. (2012). Octahedral PtNi Nanoparticle Catalysts: Exceptional Oxygen Reduction Activity by Tuning the Alloy Particle Surface Composition. *Nano Lett.*, 12(11):5885–5889.

[32] Dimas Rivera, G. L. (2015). *Síntesis y aplicación de catalizadores bimetálicos Pt y Pd con Fe sobre alúmina en la desorción del furfural y la hidrogenación del 2-metilfurano*. phd, Universidad Autónoma de Nuevo León.

[33] Dohn, A. O., Biasin, E., Haldrup, K., Nielsen, M. M., Henriksen, N. E., and Møller, K. B. (2015). On the calculation of x-ray scattering signals from pairwise radial distribution functions. *J. Phys. B: At. Mol. Opt. Phys.*, 48(24):244010.

[34] Dohn, A. O., Jónsson, E. Ö., and Jónsson, H. (2019). Polarizable Embedding with a Transferable H2O Potential Function II: Application to (H2O)n Clusters and Liquid Water. *J. Chem. Theory Comput.*, 15(12):6578–6587.

[35] Droghetti, A., Pemmaraju, C., and Sanvito, S. (2008). Predicting d 0 magnetism: Self-interaction correction scheme. *Phys. Rev. B*, 78(14):140404.

[36] Ernzerhof, M., Perdew, J. P., and Burke, K. (1997). Coupling-constant dependence of atomization energies. *Int. J. Quantum Chem.*, 64(3):285–295.

[37] E. Skyner, R., L. McDonagh, J., R. Groom, C., Mourik, T. v., and O. Mitchell, J. B. (2015). A review of methods for the calculation of solution free energies and the modelling of systems in solution. *Phys. Chem. Chem. Phys.*, 17(9):6174–6191.

[38] Fantauzzi, D., Bandlow, J., Sabo, L., Mueller, J. E., van Duin, A. C., and Jacob, T. (2014). Development of a reaxff potential for pt–o systems describing the energetics and dynamics of pt-oxide formation. *Phys. Chem. Chem. Phys.*, 16(42):23118–23133.

[39] Fantauzzi, D., Krick Calderón, S., Mueller, J. E., Grabau, M., Papp, C., Steinrück, H.-P., Senftle, T. P., van Duin, A. C., and Jacob, T. (2017). Growth of stable surface oxides on pt (111) at near-ambient pressures. *Angew. Chem. Int. Ed.*, 56(10):2594–2598.

[40] Fantauzzi, D., Mueller, J. E., Sabo, L., van Duin, A. C. T., and Jacob, T. (2015). Surface buckling and subsurface oxygen: Atomistic insights into the surface oxidation of pt(111). *ChemPhysChem*, 16(13):2797–2802.

[41] Farkas, A., Fantauzzi, D., Mueller, J. E., Zhu, T., Papp, C., Steinrück, H.-P., and Jacob, T. (2017). On the platinum-oxide formation under gas-phase and electrochemical conditions. *J. Electron Spectrosc. Relat. Phenom.*, 221:44–57.

[42] Field, M. J. (2017). An algorithm for adaptive qc/mm simulations. *J. Chem. Theory Comput.*, 13(5):2342–2351.

[43] Field, M. J., Bash, P. A., and Karplus, M. (1990). A combined quantum mechanical and molecular mechanical potential for molecular dynamics simulations. *J. Comp. Chem.*, 11(6):700–733.

[44] Gai, L., Shin, Y. K., Raju, M., van Duin, A. C., and Raman, S. (2016). Atomistic adsorption of oxygen and hydrogen on platinum catalysts by hybrid grand canonical monte carlo/reactive molecular dynamics. *J. Phys. Chem. C*, 120(18):9780–9793.

[45] Garcia-Ratés, M., García-Muelas, R., and López, N. (2017). Solvation effects on methanol decomposition on pd(111), pt(111), and ru(0001). *J. Phys. Chem. C*, 121(25):13803–13809.

[46] Geng, D., Chen, Y., Chen, Y., Li, Y., Li, R., Sun, X., Ye, S., and Knights, S. (2011). High oxygen - reduction activity and durability of nitrogen -doped graphene. *Energ. Environ. Sci.*, 4(3):760–764.

[47] Gould, N. S., Li, S., Cho, H. J., Landfield, H., Caratzoulas, S., Vlachos, D., Bai, P., and Xu, B. (2020). Understanding solvent effects on adsorption and protonation in porous catalysts. *Nat. Commun.*, 11(1):1060.

[48] Gray, C. M., Saravanan, K., Wang, G., and Keith, J. A. (2017). Quantifying solvation energies at solid/liquid interfaces using continuum solvation methods. *Mol. Simul.*, 43(5-6):420–427.

[49] Guo, Y., Sivalingam, K., Valeev, E. F., and Neese, F. (2016). SparseMaps—A systematic infrastructure for reduced-scaling electronic structure methods. III. Linear-scaling multireference domain-based pair natural orbital N-electron valence perturbation theory. *J. Chem. Phys.*, 144(9):094111.

[50] Gíslason, P. M. and Skúlason, E. (2019). Catalytic trends of nitrogen doped carbon nanotubes for oxygen reduction reaction. *Nanoscale*, 11(40):18683–18690.

[51] Gómez-Marín, A. M., Rizo, R., and Feliu, J. M. (2014). Oxygen reduction reaction at Pt single crystals: a critical overview. *Catal. Sci. Technol.*, 4(6):1685–1698.

[52] Haldrup, K., Levi, G., Biasin, E., Vester, P., Laursen, M. G., Beyer, F., Kjær, K. S., Brandt van Driel, T., Harlang, T., Dohn, A. O., Hartsock, R. J., Nelson, S., Glownia, J. M., Lemke, H. T., Christensen, M., Gaffney, K. J., Henriksen, N. E., Møller, K. B., and Nielsen, M. M. (2019). Ultrafast X-Ray Scattering Measurements of Coherent Structural Dynamics on the Ground-State Potential Energy Surface of a Diplatinum Molecule. *Phys. Rev. Lett.*, 122(6):063001.

[53] Hanselman, S., McCrum, I. T., Rost, M. J., and Koper, M. T. M. (2019). Thermodynamics of the formation of surface PtO2 stripes on Pt(111) in the absence of subsurface oxygen. *Phys. Chem. Chem. Phys.*

[54] Heenen, H. H., Gauthier, J. A., Kristoffersen, H. H., Ludwig, T., and Chan, K. (2020). Solvation at metal/water interfaces: An ab initio molecular dynamics benchmark of common computational approaches. *J. Chem. Phys.*, 152(14):144703.

[55] Helgaker, T., Klopper, W., Koch, H., and Noga, J. (1997). Basis-set convergence of correlated calculations on water. *J. Chem. Phys.*, 106(23):9639–9646.

[56] Heyd, J., Scuseria, G. E., and Ernzerhof, M. (2003). Hybrid functionals based on a screened Coulomb potential. *J. Chem. Phys.*, 118(18):8207–8215.

[57] Heyden, A., Lin, H., and Truhlar, D. G. (2007). Adaptive partitioning in combined quantum mechanical and molecular mechanical calculations of potential energy functions for multiscale simulations. *J. Phys. Chem. B*, 111(9):2231–2241.

[58] Holby, E. F., Greeley, J., and Morgan, D. (2012). Thermodynamics and Hysteresis of Oxide Formation and Removal on Platinum (111) Surfaces. *J. Phys. Chem. C*, 116(18):9942–9946.

[59] Holby, E. F., Wu, G., Zelenay, P., and Taylor, C. D. (2014). Structure of Fe–N $_x$ –C Defects in Oxygen Reduction Reaction Catalysts from First-Principles Modeling. *J. Phys. Chem. C*, 118(26):14388–14393.

[60] Hoover, W. G. (1985). Canonical dynamics: equilibrium phase-space distributions. *Phys. Rev. A*, 31(3):1695.

[61] Hou, Y., Zhuang, X., and Feng, X. (2017). Recent Advances in Earth-Abundant Heterogeneous Electrocatalysts for Photoelectrochemical Water Splitting. *Small*

Methods, 1(6):11498–11503.

[62] Hsing, C. R., Wei, C. M., and Chou, M. Y. (2012). Quantum monte carlo investigations of adsorption energetics on graphene. *J. Phys. Condens. Matter*, 24(39):395002.

[63] Huang, R., Wen, Y.-H., Zhu, Z.-Z., and Sun, S.-G. (2011). Structure and stability of platinum nanocrystals: from low-index to high-index facets. *J. Mater. Chem.*, 21(31):11578–11584.

[64] Huang, X., Zhao, Z., Cao, L., Chen, Y., Zhu, E., Lin, Z., Li, M., Yan, A., Zettl, A., Wang, Y. M., et al. (2015). High-performance transition metal–doped pt3ni octahedra for oxygen reduction reaction. *Science*, 348(6240):1230–1234.

[65] Hummers, W. S. and Offeman, R. E. (1958). Preparation of Graphitic Oxide. *J. Am. Chem. Soc.*, 80(6):1339–1339.

[66] Ikeda, T., Boero, M., Huang, S.-F., Terakura, K., Oshima, M., and Ozaki, J.-i. (2008). Carbon alloy catalysts: Active sites for oxygen reduction reaction. *J. Phys. Chem. C*, 112(38):14706–14709.

[67] Jacob, T. (2007). Theoretical investigations on the potential-induced formation of Pt-oxide surfaces. *J. Electroanal. Chem.*, 607(1):158–166.

[68] Janesko, B. G., Barone, V., and Brothers, E. N. (2013). Accurate surface chemistry beyond the generalized gradient approximation: Illustrations for graphene adatoms. *J. Chem. Theory Comput.*, 9(11):4853–4859.

[69] Jensen, F. (2007). *Introduction to computational chemistry*. John Wiley & Sons, 2nd ed edition.

[70] Jia, Y., Zhang, L., Du, A., Gao, G., Chen, J., Yan, X., Brown, C. L., and Yao, X. (2016). Defect graphene as a trifunctional catalyst for electrochemical reactions. *Adv. Mater.*, 28(43):9532–9538.

[71] Jiang, T., Simko, S., and Bulo, R. E. (2018). Accurate Quantum Mechanics/Molecular Mechanics Simulation of Aqueous Solutions with Tailored Molecular Mechanics Models. *J. Chem. Theory Comput.*, 14(8):3943–3954.

[72] Jiao, Y., Zheng, Y., Jaroniec, M., and Qiao, S. Z. (2014). Origin of the electrocatalytic oxygen reduction activity of graphene-based catalysts: A roadmap to achieve the best performance. *J. Am. Chem. Soc.*, 136(11):4394–4403.

[73] Johnston, H. S. and Parr, C. (1963). Activation energies from bond energies. i. hydrogen transfer reactions. *J. Am. Chem. Soc.*, 85(17):2544–2551.

[74] Jorgensen, W. L., Chandrasekhar, J., Madura, J. D., Impey, R. W., and Klein, M. L. (1983). Comparison of simple potential functions for simulating liquid water. *J. Chem. Phys.*, 79(2):926–935.

[75] Jónsson, E. Ö., Dohn, A. O., and Jónsson, H. (2019). Polarizable Embedding with a Transferable H2O Potential Function I: Formulation and Tests on Dimer. *J. Chem. Theory Comput.*, 15(12):6562–6577.

[76] Keith, J. A. and Jacob, T. (2010). Theoretical Studies of Potential-Dependent and Competing Mechanisms of the Electrocatalytic Oxygen Reduction Reaction on Pt(111). *Angew. Chem. Int. Ed.*, 49(49):9521–9525.

[77] Keith, J. A., Jerkiewicz, G., and Jacob, T. (2010). Theoretical Investigations of the Oxygen Reduction Reaction on Pt(111). *ChemPhysChem*, 11(13):2779–2794.

[78] Kim, H., Lee, K., Ihl Woo, S., and Jung, Y. (2011). On the mechanism of enhanced oxygen reduction reaction in nitrogen -doped graphene nanoribbons. *Phys. Chem. Chem. Phys.*, 13(39):17505–17510.

[79] Kirchhoff, B., Braunwarth, L., Jung, C., Jónsson, H., Fantauzzi, D., and Jacob, T. (2019). Simulations of the Oxidation and Degradation of Platinum Electrocatalysts. *Small*, 16(5):1905159.

[80] Kirchhoff, B., Ivanov, A., Skúlason, E., Jacob, T., Fantauzzi, D., and Jónsson, H. (2021a). Assessment of the Accuracy of Density Functionals for Calculations of the Oxygen Reduction Reaction on Nitrogen Doped Graphene. Submitted to *J. Chem. Theory Comput.*

[81] Kirchhoff, B., Jónsson, E. O., Dohn, A. O., Jacob, T., and Jónsson, H. (2021b). Elastic Collision Based Dynamic Partitioning Scheme for Hybrid Simulations. *arXiv:2103.16342 [physics]*. Submitted to *J. Chem. Theory Comput.*

[82] Kirchhoff, B., Jung, C., Gaissmeier, D., Braunwarth, L., Jónsson, H., and Jacob, T. (2021c). In-Silico Characterization of Nanoparticle Catalysts. In preparation.

[83] Kirchhoff, B., Jung, C., Jónsson, H., Fantauzzi, D., and Jacob, T. (2021d). Comparison of the Electrocatalytic Oxidation of Different Platinum Nanoparticle Structures from Simulations. In preparation.

[84] Kirchhoff, B., Skúlason, E., Jacob, T., Fantauzzi, D., and Jónsson, H. (2021e). Calculations of Oxygen Reduction Thermochemistry for Boron-Doped Graphene using a Hybrid Density Functional. In preparation.

[85] Kitanosono, T., Masuda, K., Xu, P., and Kobayashi, S. (2018). Catalytic Organic Reactions in Water toward Sustainable Society. *Chem. Rev.*, 118(2):679–746.

[86] Kleis, J., Greeley, J., Romero, N. A., Morozov, V. A., Falsig, H., Larsen, A. H., Lu, J., Mortensen, J. J., Dułak, M., Thygesen, K. S., Nørskov, J. K., and Jacobsen, K. W. (2011). Finite Size Effects in Chemical Bonding: From Small Clusters to Solids. *Catal. Lett.*, 141(8):1067–1071.

[87] Klüpfel, S., Klüpfel, P., and Jónsson, H. (2012). The effect of the Perdew-Zunger self-interaction correction to density functionals on the energetics of small molecules. *J. Chem. Phys.*, 137(12):124102.

[88] Koch, W., Holthausen, M. C., and Wiley InterScience (Online service) (2001). *A chemist's guide to density functional theory*. Wiley-VCH.

[89] Krukau, A. V., Vydrov, O. A., Izmaylov, A. F., and Scuseria, G. E. (2006). Influence of the exchange screening parameter on the performance of screened hybrid functionals. *J. Chem. Phys.*, 125(22):224106.

[90] Larsen, A. H., Mortensen, J. J., Blomqvist, J., Castelli, I. E., Christensen, R., Dulak, M., Friis, J., Groves, M. N., Hammer, B., Hargus, C., Hermes, E. D., Jennings, P. C., Jensen, P. B., Kermode, J., Kitchin, J. R., Kolsbjerg, E. L., Kubal, J., Kaasbjerg, K., Lysgaard, S., Maronsson, J. B., Maxson, T., Olsen, T., Pastewka, L., Peterson, A., Rostgaard, C., Schiøtz, J., Schütt, O., Strange, M., Thygesen, K. S., Vegge, T., Vilhelmsen, L., Walter, M., Zeng, Z., and Jacobsen, K. W. (2017). The atomic simulation environment—a Python library for working with atoms. *J. Phys.: Condens. Matter*, 29(27):273002.

[91] Lei, Y., Han, D., Dong, J., Qin, L., Li, X., Zhai, D., Li, B., Wu, Y., and Kang, F. (2020). Unveiling the influence of electrode/electrolyte interface on the capacity fading for typical graphite-based potassium-ion batteries. *Energy Storage Mater.*, 24:319–328.

[92] Li, M., Zhang, L., Xu, Q., Niu, J., and Xia, Z. (2014a). N-doped graphene as catalysts for oxygen reduction and oxygen evolution reactions: Theoretical consider-

ations. *J. Catal.*, 314:66–72.

[93] Li, Y., Zhao, Y., Cheng, H., Hu, Y., Shi, G., Dai, L., and Qu, L. (2012). Nitrogen-doped graphene quantum dots with oxygen-rich functional groups. *J. Am. Chem. Soc.*, 134(1):15–18.

[94] Li, Y. H., Xing, J., Yang, X. H., and Yang, H. G. (2014b). Cluster Size Effects of Platinum Oxide as Active Sites in Hydrogen Evolution Reactions. *Chem. Eur. J.*, 20(39):12377–12380.

[95] Lima, F. H. B., Zhang, J., Shao, M. H., Sasaki, K., Vukmirovic, M. B., Ticianelli, E. A., and Adzic, R. R. (2007). Catalytic activity-d-band center correlation for the o2 reduction reaction on platinum in alkaline solutions. *J. Phys. Chem. C*, 111(1):404–410.

[96] Lin, L., Zhu, Q., and Xu, A.-W. (2014). Noble-Metal-Free Fe–N/C Catalyst for Highly Efficient Oxygen Reduction Reaction under Both Alkaline and Acidic Conditions. *J. Am. Chem. Soc.*, 136(31):11027–11033.

[97] Lin, S.-T., Blanco, M., and Goddard, W. A. (2003). The two-phase model for calculating thermodynamic properties of liquids from molecular dynamics: Validation for the phase diagram of Lennard-Jones fluids. *J. Chem. Phys.*, 119(22):11792–11805.

[98] Lu, X., Gaus, M., Elstner, M., and Cui, Q. (2015). Parametrization of DFTB3/3OB for Magnesium and Zinc for Chemical and Biological Applications. *J. Phys. Chem. B*, 119(3):1062–1082.

[99] Mamtani, K. and Ozkan, U. S. (2015). Heteroatom-Doped Carbon Nanostructures as Oxygen Reduction Reaction Catalysts in Acidic Media: An Overview. *Catal. Lett.*, 145(1):436–450.

[100] Marcano, D. C., Kosynkin, D. V., Berlin, J. M., Sinitskii, A., Sun, Z., Slesarev, A., Alemany, L. B., Lu, W., and Tour, J. M. (2010). Improved Synthesis of Graphene Oxide. *ACS Nano*, 4(8):4806–4814.

[101] Marković, N. M., Adžić, R. R., Cahan, B. D., and Yeager, E. B. (1994). Structural effects in electrocatalysis: oxygen reduction on platinum low index single-crystal surfaces in perchloric acid solutions. *J. Electroanal. Chem.*, 377(1):249–259.

[102] Masa, J., Zhao, A., Xia, W., Sun, Z., Mei, B., Muhler, M., and Schuhmann, W. (2013). Trace metal residues promote the activity of supposedly metal-free nitrogen-modified carbon catalysts for the oxygen reduction reaction. *Electrochem. Commun.*, 34:113–116.

[103] Mathew, K., Kolluru, V. S. C., Mula, S., Steinmann, S. N., and Hennig, R. G. (2019). Implicit self-consistent electrolyte model in plane-wave density-functional theory. *J. Chem. Phys.*, 151:234101.

[104] Mathew, K., Sundararaman, R., Letchworth-Weaver, K., Arias, T. A., and Hennig, R. G. (2014). Implicit solvation model for density-functional study of nanocrystal surfaces and reaction pathways. *J. Chem. Phys.*, 140:084106.

[105] Mayer, I. and Valiron, P. (1998). Second order møller–plesset perturbation theory without basis set superposition error. *J. Chem. Phys.*, 109(9):3360–3373.

[106] Meier, J. C., Galeano, C., Katsounaros, I., Witte, J., Bongard, H. J., Topalov, A. A., Baldizzone, C., Mezzavilla, S., Schüth, F., and Mayrhofer, K. J. J. (2014). Design criteria for stable Pt/C fuel cell catalysts. *Beilstein J. Nanotechnol.*, 5:44–67.

[107] Mellmer, M. A., Sanpitakseree, C., Demir, B., Bai, P., Ma, K., Neurock, M., and Dumesic, J. A. (2018). Solvent-enabled control of reactivity for liquid-phase

reactions of biomass-derived compounds. *Nat. Catal.*, 1(3):199–207.
[108] Monkhorst, H. J. and Pack, J. D. (1976). Special points for brillouin-zone integrations. *Phys. Rev. B*, 13(12):5188.
[109] Narayanan, R. and El-Sayed, M. A. (2004). Shape-Dependent Catalytic Activity of Platinum Nanoparticles in Colloidal Solution. *Nano Lett.*, 4(7):1343–1348.
[110] NASA (2016). Scientific consensus: Earth's climate is warming. https://climate.nasa.gov/scientific-consensus. Accessed: 2021-02-01.
[111] Neese, F. and Valeev, E. F. (2011). Revisiting the Atomic Natural Orbital Approach for Basis Sets: Robust Systematic Basis Sets for Explicitly Correlated and Conventional Correlated ab initio Methods? *J. Chem. Theory Comput.*, 7(1):33–43.
[112] Neyerlin, K., Srivastava, R., Yu, C., and Strasser, P. (2009). Electrochemical activity and stability of dealloyed pt–cu and pt–cu–co electrocatalysts for the oxygen reduction reaction (orr). *J. Power Sources*, 186(2):261–267.
[113] Nørskov, J. K., Rossmeisl, J., Logadottir, A., Lindqvist, L., Kitchin, J. R., Bligaard, T., and Jónsson, H. (2004). Origin of the overpotential for oxygen reduction at a fuel-cell cathode. *J. Phys. Chem. B*, 108(46):17886–17892.
[114] Nosé, S. (1984). A unified formulation of the constant temperature molecular dynamics methods. *J. Chem. Phys.*, 81(1):511–519.
[115] Novoselov, K. S., Geim, A. K., Morozov, S. V., Jiang, D., Zhang, Y., Dubonos, S. V., Grigorieva, I. V., and Firsov, A. A. (2004). Electric Field Effect in Atomically Thin Carbon Films. *Science*, 306(5696):666–669.
[116] Okamoto, Y. (2009). First-principles molecular dynamics simulation of o2 reduction on nitrogen-doped carbon. *Appl. Surf. Sci.*, 256(1):335–341.
[117] Pauling, L. (1947). Atomic radii and interatomic distances in metals. *J. Am. Chem. Soc.*, 69(3):542–553.
[118] Pavošević, F., Peng, C., Pinski, P., Riplinger, C., Neese, F., and Valeev, E. F. (2017). SparseMaps—A systematic infrastructure for reduced scaling electronic structure methods. V. Linear scaling explicitly correlated coupled-cluster method with pair natural orbitals. *J. Chem. Phys.*, 146(17):174108.
[119] Pavošević, F., Pinski, P., Riplinger, C., Neese, F., and Valeev, E. F. (2016). SparseMaps—A systematic infrastructure for reduced-scaling electronic structure methods. IV. Linear-scaling second-order explicitly correlated energy with pair natural orbitals. *J. Chem. Phys.*, 144(14):144109.
[120] Perdew, J. P., Burke, K., and Ernzerhof, M. (1996a). Generalized gradient approximation made simple. *Phys. Rev. Lett.*, 77(18):3865.
[121] Perdew, J. P., Ernzerhof, M., and Burke, K. (1996b). Rationale for mixing exact exchange with density functional approximations. *J. Chem. Phys.*, 105(22):9982–9985.
[122] Perdew, J. P. and Zunger, A. (1981). Self-interaction correction to density-functional approximations for many-electron systems. *Phys. Rev. B*, 23(10):5048–5079.
[123] Pezeshki, S. and Lin, H. (2015). Adaptive-partitioning qm/mm for molecular dynamics simulations: 4. proton hopping in bulk water. *J. Chem. Theory Comput.*, 11(6):2398–2411.
[124] Pinski, P., Riplinger, C., Valeev, E. F., and Neese, F. (2015). Sparse maps—A systematic infrastructure for reduced-scaling electronic structure methods. I. An

efficient and simple linear scaling local MP2 method that uses an intermediate basis of pair natural orbitals. *J. Chem. Phys.*, 143(3):034108.

[125] Porsgaard, S., Merte, L. R., Ono, L. K., Behafarid, F., Matos, J., Helveg, S., Salmeron, M., Roldan Cuenya, B., and Besenbacher, F. (2012). Stability of platinum nanoparticles supported on sio2/si (111): a high-pressure x-ray photoelectron spectroscopy study. *ACS nano*, 6(12):10743–10749.

[126] Qu, L., Liu, Y., Baek, J.-B., and Dai, L. (2010a). Nitrogen-Doped Graphene as Efficient Metal-Free Electrocatalyst for Oxygen Reduction in Fuel Cells. *ACS Nano*, 4(3):1321–1326.

[127] Qu, L., Liu, Y., Baek, J.-B., and Dai, L. (2010b). Nitrogen-doped graphene as efficient metal-free electrocatalyst for oxygen reduction in fuel cells. *ACS Nano*, 4(3):1321–1326.

[128] Reda, M., Hansen, H. A., and Vegge, T. (2018). DFT study of stabilization effects on N-doped graphene for ORR catalysis. *Catal. Today*, 312:118–125.

[129] Riplinger, C., Pinski, P., Becker, U., Valeev, E. F., and Neese, F. (2016). Sparse maps—A systematic infrastructure for reduced-scaling electronic structure methods. II. Linear scaling domain based pair natural orbital coupled cluster theory. *J. Chem. Phys.*, 144(2):024109.

[130] Rogers, D. M. and Beck, T. L. (2008). Modeling molecular and ionic absolute solvation free energies with quasichemical theory bounds. *J.Chem. Phys.*, 129(13):134505.

[131] Román-Leshkov, Y., Chheda, J. N., and Dumesic, J. A. (2006). Phase Modifiers Promote Efficient Production of Hydroxymethylfurfural from Fructose. *Science*, 312(5782):1933–1937.

[132] Roothaan, C. C. J. (1951). New developments in molecular orbital theory. *Rev. Mod. Phys.*, 23(2):69.

[133] Rossin, A., Kovács, G., Ujaque, G., Lledós, A., and Joó, F. (2006). The Active Role of the Water Solvent in the Regioselective CO Hydrogenation of Unsaturated Aldehydes by [RuH2(mtppms)x] in Basic Media. *Organometallics*, 25(21):5010–5023.

[134] Rossmeisl, J., Karlberg, G. S., Jaramillo, T., and Nørskov, J. K. (2009). Steady state oxygen reduction and cyclic voltammetry. *Faraday Discuss.*, 140:337–346.

[135] Rossmeisl, J., Skúlason, E., Björketun, M. E., Tripkovic, V., and Nørskov, J. K. (2008). Modeling the electrified solid–liquid interface. *Chem. Phys. Lett.*, 466(1):68–71.

[136] Rowley, C. N. and Roux, B. (2012). The Solvation Structure of Na^+ and K^+ in Liquid Water Determined from High Level *ab Initio* Molecular Dynamics Simulations. *J. Chem. Theory Comput.*, 8(10):3526–3535.

[137] Senftle, T. P., Meyer, R. J., Janik, M. J., and Van Duin, A. C. (2013). Development of a reaxff potential for pd/o and application to palladium oxide formation. *J. Chem. Phys.*, 139(4):044109.

[138] Senftle, T. P., van Duin, A. C., and Janik, M. J. (2014). Determining in situ phases of a nanoparticle catalyst via grand canonical monte carlo simulations with the reaxff potential. *Catal. Commun.*, 52:72–77.

[139] Seriani, N., Jin, Z., Pompe, W., and Ciacchi, L. C. (2007). Density functional theory study of platinum oxides: From infinite crystals to nanoscopic particles. *Phys.*

Rev. B, 76(15):155421.

[140] Seriani, N., Pompe, W., and Ciacchi, L. C. (2006). Catalytic oxidation activity of pt3o4 surfaces and thin films. *J. Phys. Chem. B*, 110(30):14860–14869.

[141] Serov, A., Robson, M. H., Halevi, B., Artyushkova, K., and Atanassov, P. (2012). Highly active and durable templated non-PGM cathode catalysts derived from iron and aminoantipyrine. *Electrochem. Commun.*, 22:53–56.

[142] Sha, Y., Yu, T. H., Liu, Y., Merinov, B. V., and Goddard, W. A. (2010). Theoretical study of solvent effects on the platinum-catalyzed oxygen reduction reaction. *J. Phys. Chem. Lett.*, 1(5):856–861.

[143] Shao, M., Liu, P., Zhang, J., and Adzic, R. (2007). Origin of enhanced activity in palladium alloy electrocatalysts for oxygen reduction reaction. *J. Phys. Chem. B*, 111(24):6772–6775.

[144] Shao, M., Peles, A., and Shoemaker, K. (2011). Electrocatalysis on platinum nanoparticles: particle size effect on oxygen reduction reaction activity. *Nano Lett.*, 11(9):3714–3719.

[145] Sheng, Z.-H., Gao, H.-L., Bao, W.-J., Wang, F.-B., and Xia, X.-H. (2011). Synthesis of boron doped graphene for oxygen reduction reaction in fuel cells. *J. Mater. Chem.*, 22(2):390–395.

[146] Shiga, M. and Masia, M. (2013a). Boundary based on exchange symmetry theory for multilevel simulations. I. Basic theory. *J. Chem. Phys.*, 139(4):044120.

[147] Shiga, M. and Masia, M. (2013b). Erratum: "Boundary based on exchange symmetry theory for multilevel simulations. I. Basic theory" [J. Chem. Phys. 139, 044120 (2013)]. *J. Chem. Phys.*, 139(11):119901.

[148] Shiga, M. and Masia, M. (2015). Quasi-boundary based on exchange symmetry theory for multilevel simulations. *Mol. Simul.*, 41(10-12):827–831.

[149] Sidik, R. A., Anderson, A. B., Subramanian, N. P., Kumaraguru, S. P., and Popov, B. N. (2006). O $_2$ reduction on graphite and nitrogen-doped graphite: Experiment and theory. *J. Phys. Chem. B*, 110(4):1787–1793.

[150] Sinthika, S., Waghmare, U. V., and Thapa, R. (2018). Structural and electronic descriptors of catalytic activity of graphene-based materials: First-principles theoretical analysis. *Small*, 14(10):1703609.

[151] Skúlason, E., Tripkovic, V., Björketun, M. E., Gudmundsdóttir, S., Karlberg, G., Rossmeisl, J., Bligaard, T., Jónsson, H., and Nørskov, J. K. (2010). Modeling the Electrochemical Hydrogen Oxidation and Evolution Reactions on the Basis of Density Functional Theory Calculations. *J. Phys. Chem. C*, 114(42):18182–18197.

[152] Studt, F. (2013). The oxygen reduction reaction on nitrogen-doped graphene. *Catal. Lett.*, 143(1):58–60.

[153] Sturala, J., Luxa, J., Pumera, M., and Sofer, Z. (2018). Chemistry of Graphene Derivatives: Synthesis, Applications, and Perspectives. *Chem. Eur. J.*, 24(23):5992–6006.

[154] Suen, N.-T., Hung, S.-F., Quan, Q., Zhang, N., Xu, Y.-J., and Chen, H. M. (2017). Electrocatalysis for the oxygen evolution reaction: recent development and future perspectives. *Chem. Soc. Rev.*, 46(2):337–365.

[155] Takagi, Y., Wang, H., Uemura, Y., Nakamura, T., Yu, L., Sekizawa, O., Uruga, T., Tada, M., Samjeské, G., Iwasawa, Y., and Yokoyama, T. (2017). In situ study of oxidation states of platinum nanoparticles on a polymer electrolyte fuel cell electrode

by near ambient pressure hard x-ray photoelectron spectroscopy. *Phys. Chem. Chem. Phys.*, 19(8):6013–6021.

[156] Takahashi, H., Kambe, H., and Morita, A. (2018). A simple and effective solution to the constrained QM/MM simulations. *J. Chem. Phys.*, 148(13):134119.

[157] Tersoff, J. (1988). New empirical approach for the structure and energy of covalent systems. *Phys. Rev. B*, 37(12):6991.

[158] Thole, B. T. and van Duijnen, P. T. (1980). On the quantum mechanical treatment of solvent effects. *Theor. Chim. Acta*, 55(4):307–318.

[159] Tian, N., Zhou, Z.-Y., and Sun, S.-G. (2008). Platinum metal catalysts of high-index surfaces: From single-crystal planes to electrochemically shape-controlled nanoparticles. *J. Phys. Chem. C*, 112(50):19801–19817.

[160] Tian, N., Zhou, Z.-Y., Sun, S.-G., Ding, Y., and Wang, Z. L. (2007). Synthesis of tetrahexahedral platinum nanocrystals with high-index facets and high electro-oxidation activity. *Science*, 316(5825):732–735.

[161] Toh, R. J., Sofer, Z., and Pumera, M. (2015). Transition Metal Oxides for the Oxygen Reduction Reaction: Influence of the Oxidation States of the Metal and its Position on the Periodic Table. *ChemPhysChem*, 16(16):3527–3531.

[162] UN (2019). Human Cost of Disasters 2000-2019. https://www.undrr.org/publication/human-cost-disasters-2000-2019. Accessed 2021-02-01.

[163] Van den Bossche, M., Skúlason, E., Rose-Petruck, C., and Jónsson, H. (2019). Assessment of Constant-Potential Implicit Solvation Calculations of Electrochemical Energy Barriers for H2 Evolution on Pt. *J. Phys. Chem. C*, 123(7):4116–4124.

[164] Van Duijneveldt, F. B., van Duijneveldt-van de Rijdt, J. G. C. M., and van Lenthe, J. H. (1994). State of the art in counterpoise theory. *Chem. Rev.*, 94(7):1873–1885.

[165] Van Duin, A. C. T., Dasgupta, S., Lorant, F., and Goddard, W. A. (2001). ReaxFF: A reactive force field for hydrocarbons. *J. Phys. Chem. A*, 105(41):9396–9409.

[166] Van Duin, A. C. T., Goddard III, W. A., Islam, M. M., van Schoot, H., and Yakovlev, A. L. (2017). Adf 2017. http://www.scm.com/. Accessed: 2017-06-12.

[167] Van Spronsen, M. A., Frenken, J. W. M., and Groot, I. M. N. (2017). Observing the oxidation of platinum. *Nat. Commun.*, 8(1):429.

[168] Vanden-Eijnden, E. and Ciccotti, G. (2006). Second-order integrators for Langevin equations with holonomic constraints. *Chem. Phys. Lett.*, 429(1):310–316.

[169] Vazquez-Arenas, J., Galano, A., U. Lee, D., Higgins, D., Guevara-García, A., and Chen, Z. (2016). Theoretical and experimental studies of highly active graphene nanosheets to determine catalytic nitrogen sites responsible for the oxygen reduction reaction in alkaline media. *J. Mater. Chem. A*, 4(3):976–990.

[170] Vegas, A. (2011). *Inorganic 3D Structures*. Springer Science & Business Media.

[171] Vielstich, W., Lamm, A., and Gasteiger, H., editors (2003). *Handbook of fuel cells: fundamentals, technology and applications*. Wiley, Chichester.

[172] Waller, M. P., Kumbhar, S., and Yang, J. (2014). A density-based adaptive quantum mechanical/molecular mechanical method. *ChemPhysChem*, 15(15):3218–3225.

[173] Wang, C., Daimon, H., Onodera, T., Koda, T., and Sun, S. (2008). A General Approach to the Size- and Shape-Controlled Synthesis of Platinum Nanoparticles and

Their Catalytic Reduction of Oxygen. *Angew. Chem. Int. Ed.*, 47(19):3588–3591.

[174] Wang, C.-B. and Yeh, C.-T. (1998). Effects of particle size on the progressive oxidation of nanometer platinum by dioxygen. *J. Catal.*, 178(2):450–456.

[175] Wang, D., Xin, H. L., Hovden, R., Wang, H., Yu, Y., Muller, D. A., DiSalvo, F. J., and Abruña, H. D. (2013a). Structurally ordered intermetallic platinum–cobalt core–shell nanoparticles with enhanced activity and stability as oxygen reduction electrocatalysts. *Nat. Mater.*, 12(1):81–87.

[176] Wang, H., Maiyalagan, T., and Wang, X. (2012). Review on recent progress in nitrogen-doped graphene: Synthesis, characterization, and its potential applications. *ACS Catal.*, 2(5):781–794.

[177] Wang, L., Ambrosi, A., and Pumera, M. (2013b). "Metal-Free" Catalytic Oxygen Reduction Reaction on Heteroatom-Doped Graphene is Caused by Trace Metal Impurities. *Angew. Chem. Int. Ed.*, 52(51):13818–13821.

[178] Wang, L., Sofer, Z., and Pumera, M. (2020). Will Any Crap We Put into Graphene Increase Its Electrocatalytic Effect? *ACS Nano*, 14(1):21–25.

[179] Wang, M.-Q., Yang, W.-H., Wang, H.-H., Chen, C., Zhou, Z.-Y., and Sun, S.-G. (2014a). Pyrolyzed Fe–N–C Composite as an Efficient Non-precious Metal Catalyst for Oxygen Reduction Reaction in Acidic Medium. *ACS Catal.*, 4(11):3928–3936.

[180] Wang, Q., Zhou, Z.-Y., Lai, Y.-J., You, Y., Liu, J.-G., Wu, X.-L., Terefe, E., Chen, C., Song, L., Rauf, M., Tian, N., and Sun, S.-G. (2014b). Phenylenediamine-Based FeN_x/C Catalyst with High Activity for Oxygen Reduction in Acid Medium and Its Active-Site Probing. *J. Am. Chem. Soc.*, 136(31):10882–10885.

[181] Warshel, A. and Levitt, M. (1976). Theoretical studies of enzymic reactions: Dielectric, electrostatic and steric stabilization of the carbonium ion in the reaction of lysozyme. *J. Mol. Biol.*, 103(2):227–249.

[182] Watanabe, H. C. (2018). Improvement of performance, stability and continuity by modified size-consistent multipartitioning quantum mechanical/molecular mechanical method. *Molecules*, 23(8):1882.

[183] Watanabe, H. C. and Cui, Q. (2019). Quantitative analysis of qm/mm boundary artifacts and correction in adaptive qm/mm simulations. *J. Chem. Theory Comput.*, 15(7):3917–3928.

[184] Watanabe, H. C., Kubař, T., and Elstner, M. (2014). Size-consistent multipartitioning qm/mm: A stable and efficient adaptive qm/mm method. *J. Chem. Theory Comput.*, 10(10):4242–4252.

[185] Wen, Y., Fang, H., Zhu, Z., and Sun, S. (2009). Molecular dynamics investigation of shape effects on thermal characteristics of platinum nanoparticles. *Phys. Lett. A*, 373(2):272–276.

[186] Xie, Y., Wang, Z.-W., Zhu, T.-Y., Shu, D.-J., Hou, Z.-F., and Terakura, K. (2018). Breaking the scaling relations for oxygen reduction reaction on nitrogen-doped graphene by tensile strain. *Carbon*, 139:129–136.

[187] Xu, Y., Shelton, W. A., and Schneider, W. F. (2006). Effect of Particle Size on the Oxidizability of Platinum Clusters. *J. Phys. Chem. A*, 110(17):5839–5846.

[188] Yu, K., Groom, D. J., Wang, X., Yang, Z., Gummalla, M., Ball, S. C., Myers, D. J., and Ferreira, P. J. (2014). Degradation Mechanisms of Platinum Nanoparticle Catalysts in Proton Exchange Membrane Fuel Cells: The Role of Particle Size. *Chem. Mater.*, 26(19):5540–5548.

[189] Yu, L., Pan, X., Cao, X., Hu, P., and Bao, X. (2011). Oxygen reduction reaction mechanism on nitrogen-doped graphene: A density functional theory study. *J. Catal.*, 282(1):183–190.

[190] Yurkiv, V., Foroozan, T., Ramasubramanian, A., Shahbazian-Yassar, R., and Mashayek, F. (2018). Phase-field modeling of solid electrolyte interface (SEI) influence on Li dendritic behavior. *Electrochim. Acta*, 265:609–619.

[191] Zhang, J., Zhang, H., Wu, T., Wang, Q., and van der Spoel, D. (2017). Comparison of Implicit and Explicit Solvent Models for the Calculation of Solvation Free Energy in Organic Solvents. *J. Chem. Theory Comput.*, 13(3):1034–1043.

[192] Zhang, L., Niu, J., Dai, L., and Xia, Z. (2012). Effect of microstructure of nitrogen-doped graphene on oxygen reduction activity in fuel cells. *Langmuir*, 28(19):7542–7550.

[193] Zhang, L. and Xia, Z. (2011). Mechanisms of oxygen reduction reaction on nitrogen-doped graphene for fuel cells. *J. Phys. Chem. C*, 115(22):11170–11176.

[194] Zhao, H., Sun, C., Jin, Z., Wang, D.-W., Yan, X., Chen, Z., Zhu, G., and Yao, X. (2015). Carbon for the oxygen reduction reaction: a defect mechanism. *J. Mater. Chem. A*, 3(22):11736–11739.

[195] Zhao, Z., Chen, C., Liu, Z., Huang, J., Wu, M., Liu, H., Li, Y., and Huang, Y. (2019). Pt-Based Nanocrystal for Electrocatalytic Oxygen Reduction. *Adv. Mater.*, 31(31):1808115.

[196] Zhong, S., Barnes, E. C., and Petersson, G. A. (2008). Uniformly convergent n-tuple-zeta augmented polarized (nZaP) basis sets for complete basis set extrapolations. I. Self-consistent field energies. *J. Chem. Phys.*, 129(18):184116.

[197] Zhu, Z., Tao, F. F., Zheng, F., Chang, R., Li, Y., Heinke, L., Liu, Z., Salmeron, M., and Somorjai, G. A. (2012). Formation of Nanometer-Sized Surface Platinum Oxide Clusters on a Stepped Pt(557) Single Crystal Surface Induced by Oxygen: A High-Pressure STM and Ambient-Pressure XPS Study. *Nano Lett.*, 12(3):1491–1497.

Publication I

Simulations of the Oxidation and Degradation of Platinum Electrocatalysts

B. Kirchhoff, L. Braunwarth, C. Jung, H. Jónsson, D. Fantauzzi*, T. Jacob*

Small, **2019**, *16*, 1905159.

Author contributions: Björn Kirchhoff performed calculations of various clean clusters shown in Figure 1, GCMC calculations of the cuboctahedral particle shown in Figure 2, data analysis using the *ab initio* thermodynamics approach shown in Figure 4, and wrote the initial manuscript draft. Laura Braunwarth performed solvation simulations shown in Figures 3 and 5 and calculated solvation energy contributions in Table 1. Christoph Jung contributed data analysis using the 2PT method shown in Table 1. Hannes Jónsson, Donato Fantauzzi, and Timo Jacob supervised the project and contributed writing revisions.

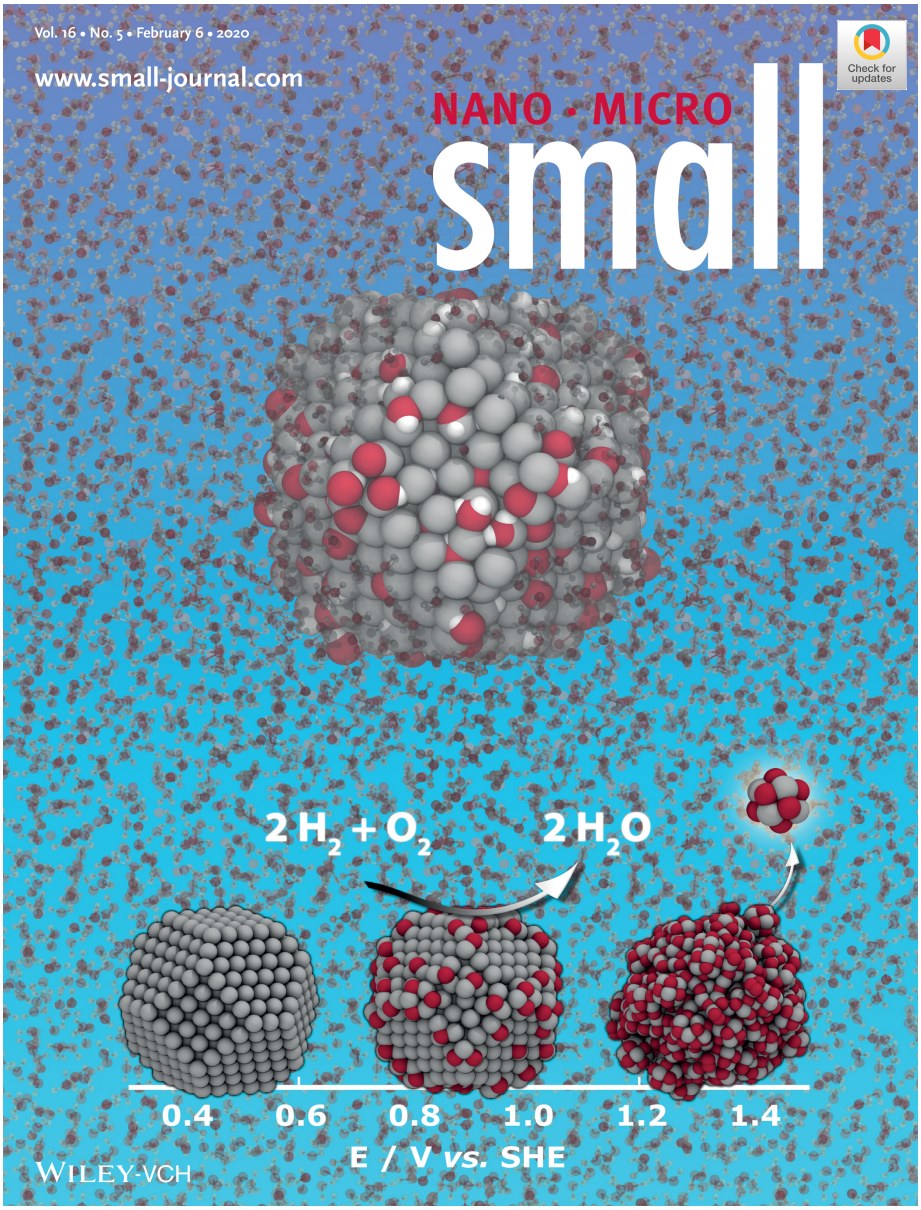
Vol. 16 • No. 5 • February 6 • 2020
www.small-journal.com
NANO · MICRO
small
Check for updates
2 H2 + O2
2 H2O
0.4
0.6
0.8
1.0
1.2
1.4
E / V vs. SHE
WILEY-VCH

FULL PAPER

NANO · MICRO small
www.small-journal.com

Simulations of the Oxidation and Degradation of Platinum Electrocatalysts

Björn Kirchhoff, Laura Braunwarth, Christoph Jung, Hannes Jónsson, Donato Fantauzzi, and Timo Jacob**

Improved understanding of the fundamental processes leading to degradation of platinum nanoparticle electrocatalysts is essential to the continued advancement of their catalytic activity and stability. To this end, the oxidation of platinum nanoparticles is simulated using a ReaxFF reactive force field within a grand-canonical Monte Carlo scheme. 2–4 nm cuboctahedral particles serve as model systems, for which electrochemical potential-dependent phase diagrams are constructed from the thermodynamically most stable oxide structures, including solvation and thermochemical contributions. Calculations in this study suggest that surface oxide structures should become thermodynamically stable at voltages around 0.80–0.85 V versus standard hydrogen electrode, which corresponds to typical fuel cell operating conditions. The potential presence of a surface oxide during catalysis is usually not accounted for in theoretical studies of Pt electrocatalysts. Beyond 1.1 V, fragmentation of the catalyst particles into $[Pt_6O_8]^{4-}$ clusters is observed. Density functional theory calculations confirm that $[Pt_6O_8]^{4-}$ is indeed stable and hydrophilic. These results suggest that the formation of $[Pt_6O_8]^{4-}$ may play an important role in platinum catalyst degradation as well as the electromotoric transport of $Pt^{2+/4+}$ ions in fuel cells.

1. Introduction

Platinum-based nanoparticulate electrocatalysts are currently the most widely used oxygen reduction catalysts in various fields of application, for example, metal–air batteries,[1] plasma catalysis,[2] or polymer–electrolyte membrane fuel cells.[3] Given the socioeconomic implications of precious metal mining, it is necessary to optimize the performance of these materials as much as possible if widespread deployment of fuel cell technology is to become reality. To this end, extending the lifetime of Pt electrocatalysts by minimizing material degradation[4] and Pt loading[5] as well as increasing their activity toward the cathodic oxygen reduction reaction (ORR) are paramount objectives. Alloying with nonplatinum-group metals has proved to be a successful avenue.[6] Similarly, varying the shape of the nanoparticle (NP) catalyst can expose different types of surface facets, edges, kinks, and other lower coordinated sites, which govern reactivity and selectivity.[7–11] Computational methods have played an integral part in these efforts for predicting catalysts with improved ORR performance. For instance, the density functional theory (DFT)–based screening approach utilized by Nørskov et al. has, in particular, turned out to be useful.[12–14] There, trends for free energy changes of the ORR intermediates are investigated on pristine, infinite surface model systems with the goal of identifying bottleneck steps and to suggest chemical or structural modifications to overcome them. However, some studies have called into question whether such model systems are in fact representative of the structure of fuel cell catalysts under working conditions.[15,16] In a combined theoretical–experimental study, our group has recently shown that stable surface oxides do exist on single-crystalline Pt(111) at near-ambient pressure and have potential impact on its electrocatalytic behavior.[16] Similarly, a DFT study by Seriani et al. has indicated that a few layers of Pt_3O_4 are thermodynamically stable on a Pt(100) surface and are catalytically active toward methane dissociation.[15] Clearly, more research into the influence of surface oxides on catalysis is needed to improve the catalytic activity of these materials.

In the present work, a grand-canonical Monte Carlo (GCMC)[17,18] algorithm is used in combination with a ReaxFF[19] reactive force field to investigate the oxidation of Pt

B. Kirchhoff, Prof. H. Jónsson, Dr. D. Fantauzzi
Science Institute and Faculty of Physical Sciences
University of Iceland
107 Reykjavík, Iceland
E-mail: donato@hi.is
B. Kirchhoff, L. Braunwarth, Prof. T. Jacob
Institute of Electrochemistry
Ulm University
Albert-Einstein-Allee 47, 89081 Ulm, Germany
E-mail: timo.jacob@uni-ulm.de
C. Jung, Dr. D. Fantauzzi, Prof. T. Jacob
Helmholtz Institute Ulm (HIU) Electrochemical Energy Storage
Helmholtz-Straße 16, 89081 Ulm, Germany
C. Jung, Dr. D. Fantauzzi, Prof. T. Jacob
Karlsruhe Institute of Technology (KIT)
P.O. Box 3640, 76021 Karlsruhe, Germany
The ORCID identification number(s) for the author(s) of this article can be found under https://doi.org/10.1002/smll.201905159.

DOI: 10.1002/smll.201905159

ADVANCED SCIENCE NEWS
www.advancedsciencenews.com

NANO · MICRO small
www.small-journal.com

nanoparticles. The computational models are 2–4 nm cuboctahedral particles, corresponding to the typical size range of catalysts used experimentally in fuel cells.[5] Note that particles larger than 4 nm become computationally too expensive to simulate within this scheme, and smaller particles could potentially be outside the confidence region of the force field description, as will be discussed in the following text. The thermodynamically most stable oxide structures are identified and energetics are further refined by considering stabilization through explicit solvation and thermochemical contributions obtained with the two-phase thermochemistry (2PT)[20] method. A potential-dependent phase diagram is constructed using the extended ab initio thermodynamics (EAITD)[21] approach. We find that oxidation of Pt NP catalysts starts at edges and vertices of the nanoparticle, with (111) facets showing surprising resistance toward oxidation. Surface oxide structures are predicted to be stable between ≈0.8 and 1.1 V versus standard hydrogen electrode (SHE), which coincides with typical fuel cell operating conditions. This result suggests that clean metal surfaces might not be appropriate model systems for Pt oxidation catalysts, for instance, ORR electrocatalysts under steady-state conditions. Upon complete oxidation, we observe dismemberment of the particle into subunits of Pt_6O_8 stoichiometry. DFT calculations confirm the high stability and hydrophilicity of these $[Pt_6O_8]^{4-}$ units. Thus, we propose that $[Pt_6O_8]^{4-}$ could be responsible for the transport of ionic Pt species through the fuel cell and thereby plays an important role in fuel cell catalyst degradation.

2. Results and Discussion

The reactive force field developed in-house used in this study was initially trained for surface science applications.[22] Focusing on oxidation processes on Pt(111), it was successfully employed to reveal the importance of surface-buckled and subsurface oxide structures[23] and to predict the growth of stable surface oxides under near-ambient pressure, which was then validated by in situ X-ray photoelectron spectroscopy (XPS).[16] However, transferability of the force field to nanoparticulate systems needs to be confirmed. To this end, two tests are performed. First, we examine the stability of octahedral (only (111) facets), cubic (only (100) facets), dodecahedral (only (110) facets), cuboctahedral (both (111) and (100) facets), and spherical (mixed facets) particles in the catalytically relevant size range between ≈1 and 10 nm. **Figure 1** depicts the dependence of the energy per atom, E_{atom}, on the number of atoms in the particle. The stability sequence resulting from Figure 1 is cuboctahedron > octahedron > sphere > dodecahedron > cube, with the spherical particle somewhat increasing in stability above 3 nm. This sequence is in good agreement with results from studies using quantum-corrected Sutton–Chen type potentials[24–26] and is consistent with DFT calculations for single crystal surfaces of the same Miller indices (constituting the corresponding NPs).[22] Note that for increasing particle sizes, E_{atom} values converge toward the fcc-Pt cohesive energy obtained with the present force field (E_C = 5.77 eV per atom; experimental: 5.84 eV per atom[27]). In a second test, the force field's performance for smaller particles is explored. To this end, we reproduce a recently published DFT study on the formation energy of Pt clusters by Lambie et al.[28] with our force field.

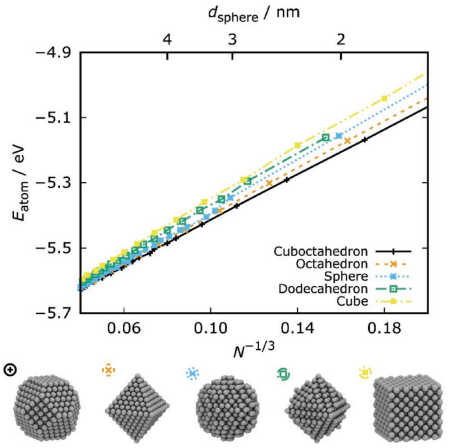

Figure 1. Stability of cuboctahedral, octahedral, spherical, dodecahedral, and cubic NPs as a function of particle size. *N*: number of atoms in a particle. The key diameter of the spherical particle, d_{sphere}, is given on top. Bottom: illustration of NP structures of ≈3 nm size.

The results are shown and discussed in more detail in Figure S1 (Supporting Information). Combining this finding with results for nanoparticles with extended facets (see Figure 1), we can conclude that the force field is appropriate for simulations of small (<100 atoms) and larger nanoparticles (≳3 nm).[5] For the intermediate particle size range, the comparison shows an error in the formation energy in the range of 0.1–0.3 eV per atom. Therefore, emphasis is placed on the 3 nm particle (711 atoms, see Figure 1).

An in-depth description of the GCMC algorithm can be found in refs. [14] and [15]. Conditions are chosen by adjusting the chemical potential μ_O of the oxygen reservoir, which is a function of temperature T and oxygen partial pressure p_O. In the present study, isobaric oxidation is investigated at ultra-high vacuum (UHV, $p_O = 10^{-10}$ mbar) and near-ambient pressure (NAP, $p_O = 1$ mbar) in the temperature range between 200 and 1400 K. NAP conditions are considered following our recent combined theoretical–experimental effort that made use of NAP–XPS spectroscopy to investigate oxidation of Pt(111).[16]

Figure 2 illustrates examples of the most stable structures obtained with the ReaxFF–GCMC approach under NAP conditions. The oxygen-to-platinum ratio, x_O, is used to quantify the degree of oxidation.[18,29] At 1250 K and beyond, an adsorbate-free state is thermodynamically favored. As the temperature decreases, oxidation starts at vertices and edges of the NP while the overall shape is still retained. x_O increases slowly in this regime, which will be referred to as surface adsorption. The first significant jump in coverage is observed at 950 K. At this temperature and below, edges and vertices are densely covered and oxidation proceeds to the (100) facets of the cuboctahedral particle. Notably, oxygen coverage on (111) facets remains low during this stage. Cross-sections of structures at this temperature reveal that oxidation

ADVANCED SCIENCE NEWS
www.advancedsciencenews.com

NANO · MICRO small
www.small-journal.com

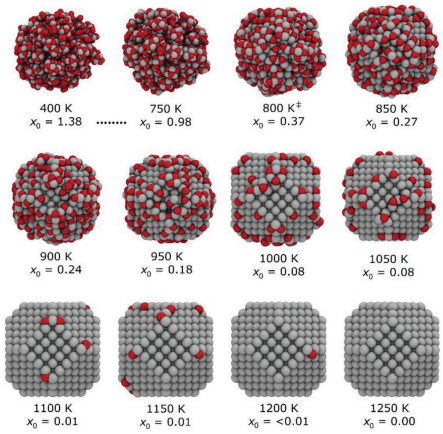

Figure 2. Overview of the oxidation process. Thermodynamic equilibrium structures from the isobaric oxidation process of a 3 nm cuboctahedral particle at p_O = 1 mbar. x_O: oxygen-to-platinum ratio. ‡ Below 800 K, complete oxidation of the particle is observed.

has not proceeded to the core of the particle but is confined to only a few surface layers, analogous to our recent observations for Pt(111).[16] This regime will therefore be referred to as surface oxide. Complete oxidation of the particle is first observed at 750 K, indicated by a jump of x_O to ≈1.0. Notably, these fully oxidized structures are dominated by a motif of smaller subunits of Pt_6O_8 stoichiometry. To the best of our knowledge, this observation is unprecedented and will be discussed in more detail below. As temperature decreases further, x_O increases up to ≈1.4 at 400 K. The same Pt_6O_8 motif is observed throughout, however, an additional motif appears where particles are decorated with dioxygen species. Under UHV conditions, similar structures are generated, albeit shifted to lower temperature with respect to NAP (see Figure S2 in the Supporting Information). This indicates that thermodynamic equilibrium was reached in all cases.

To develop a better understanding of the electrochemical stability of these different oxide structures, potential-dependent phase diagrams are constructed using the EAITD approach.[21] To represent the adsorbate-free system, we consider two models: i) the perfectly ordered cuboctahedral nanoparticle ("pristine"), which was also the input structure for our GCMC simulations, and ii) a slightly disordered particle ("rearranged") generated by removing O atoms from a surface-oxidized structure and subsequent structural relaxation. The rearranged system is expected to be a more realistic representation of the catalyst's structure than the pristine (perfect) system considering the stresses acting on the particle due to repeated reductive jumps and the thermal discharge generated by the ORR on the particle surface. The latter can cause local surface melting which was recently observed for Cu NPs to occur significantly below the actual melting temperature.[30] To lend more significance to the rearranged model, in the following text, all values are averaged over 5 different particles, generated from initially oxidized structures with x_O = 0.1–0.5. Note that particles with x_O > 0.5 typically contain the Pt_6O_8 motif and will lead to highly disordered structures that are significantly less stable in comparison to the pristine cluster. To identify the most stable oxidized structures, all particles generated during GCMC sampling are first grouped based on their x_O. Bins of Δx_O = 0.1 and 0.01 were tested and it was found that no important information is lost in case of the coarser division. From within each of these groups, the structure with the lowest formation energy (E_F) is determined. The structures found this way are then introduced into a simulation box filled with water molecules at a density of ρ_{H_2O} = 1.0 g cm^{-3}. Afterward, reactive molecular dynamics (MD) simulations are run at 300 K (*NVT* ensemble) for 500 000 iterations (Δt = 0.25 fs). E_{solv} is then obtained by averaging over the latter 250 000 iterations. Results are summarized in **Table 1**.

Several noteworthy trends are observed for E_{solv}. First, the solvation energy for the pristine system is larger than for surface-oxidized structures (x_O = 0.1–0.4). This trend likely results from oxygen atoms at the surface breaking up the regular ordering of solvent molecules in comparison to the pristine particle. **Figure 3**a,b illustrates the first solvation shell around the pristine particle. The arrangement of water molecules observed here is akin to reports of a hydrophobic water monolayer on Pt(111).[31] Note that additionally to H_2O, a small amount of H and OH adspecies are formed during these simulations. While the rearranged particle is also slightly more stabilized by the water environment than the surface-oxidized systems, the calculated solvation stabilization is considerably lower (≈25%) than for the pristine system. The ordering of H_2O molecules on its surface is more irregular than in the case of the pristine particle, see Figure 3c. At larger x_O, solvation stabilization is larger than for the clean system. This can be attributed to the increased hydrophilicity of these structures. Entropic contributions *S* are obtained using the 2PT.[20] To this end, *NVE*-ensemble MD simulations are carried out at an initial temperature of 300 K starting with the structures without solvent for

Table 1. Summary of solvation energy values (E_{solv}), entropic (*S*) corrections, and final formation free energy values (ΔG_F). "Pristine" and "rearranged" refer to a perfect cuboctahedron and a slightly rearranged particle, see Figure 4. Values for the rearranged cluster are an average over 5 systems (see text).

Structure	E_{solv}[a)] [eV]	TS[b)] [eV]	ΔG_F [eV]@0 V[c)]
Pristine	−94.18	−83.61	0.00(reference)
Rearranged	−76.04	−84.51	13.26
x_O = 0.1	−66.19	−91.63	90.79
x_O = 0.2	−68.82	−96.01	219.42
x_O = 0.4	−86.34	−33.53	514.93
x_O = 1.1	−128.16	−133.94	1659.04

[a)]Obtained from MD simulations (*NVT* ensemble) at 300 K and a density of explicit solvent molecules of ρ_{H_2O} = 1.0 g cm^{-3}; [b)]2PT results from MD simulations (*NVE* ensemble) with a starting temperature of 300 K; [c)]All values calculated against H_2/H_2O at standard conditions (pH 0, T = 298 K, p = 1 bar) and the pristine cluster as reference.

ADVANCED SCIENCE NEWS
www.advancedsciencenews.com

NANO · MICRO small
www.small-journal.com

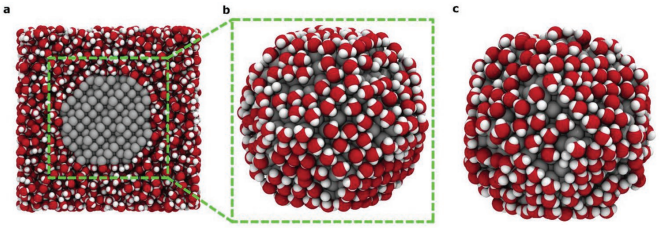

Figure 3. Solvated particles. a) Solvated pristine particle in water (shown is a cut through the simulation box). b,c) First layer of H_2O solvent molecules on the pristine (b) and rearranged particle (c). All snapshots from MD simulations.

13.8 ps from which the last 1.3 ps are used to evaluate entropy contributions with the 2PT approach. As summarized in Table 1, *S* is found to increase as particles become more disordered either due to rearrangement or oxidation of the particle. Formation free energy values of the most stable structures that entered the phase diagram are also summarized in Table 1.

Figure 4 shows the calculated oxidation phase diagrams for the 3 nm cuboctahedral particle. This phase diagram includes the solvation energy and entropic contributions discussed earlier; phase diagrams without solvation or entropic contributions data are shown in Figure S3 (Supporting Information). Approximately 500 000 structures were generated using GCMC simulations, and they were grouped with respect to x_O ($x_O = 0.1$–1.5, $\Delta x_O = 0.1$). For clarity, only the most stable structures—i.e., the enveloping, lowest-energy lines that define the phases by their intersections—are shown. In Figure 4, the stability of the oxidized structures is referenced against the rearranged particle and not the ideal, defect-free system since the latter are unlikely to exist under experimental conditions and after repeated oxidation and reduction cycles. Three overall regions can be distinguished. First, in the range between 0.00 and 0.80 V versus SHE, the adsorbate-free system is thermodynamically favored. From 0.80 to 0.85 V onward, which corresponds to typical fuel cell operating conditions, surface oxide structures are starting to become the thermodynamically preferred phase. This also coincides well with the experimentally observed onset of platinum oxidation in nonadsorbing solvents in cyclic voltammograms.[32] Without solvation and entropic contributions, this phase transition is shifted to slightly lower potentials, see Figure S3 in the Supporting Information. Beyond 1.15 V, the simulations predict full oxidation of the particle. Note that for 2 and 4 nm particles, the onset of full oxidation is shifted by −270 and +100 mV, respectively, indicating that this process is size-dependent (see Figure S3 in the Supporting Information). On the other hand, the onset of surface oxide formation is found to be shifted by −100 mV for the 2 nm particle but is identical for the larger 4 nm particle. Generally, the surface oxide window becomes larger with particle size. Finally, a comparison of phase diagrams without (Figure S3, Supporting Information) and with thermochemical corrections (Figure 4) of the 3 nm particle shows that inclusion of entropy and solvation leads to a slight shrinkage of the surface oxide phase. This is likely a result of solvation stabilizing the clean and fully oxidized systems more strongly than the surface-oxidized structures.

The second major observation in this work concerns the Pt_6O_8 units present in fully oxidized structures. Pt_6O_8 can be described as Pt icosahedron inside a cube of oxygen atoms.[33] Stoichiometrically, this structure should be derived from the Pt_3O_4 phase. However, some key differences can be observed when comparing the two structures as presented in Table S1 (Supporting Information). Most notably, only one type of

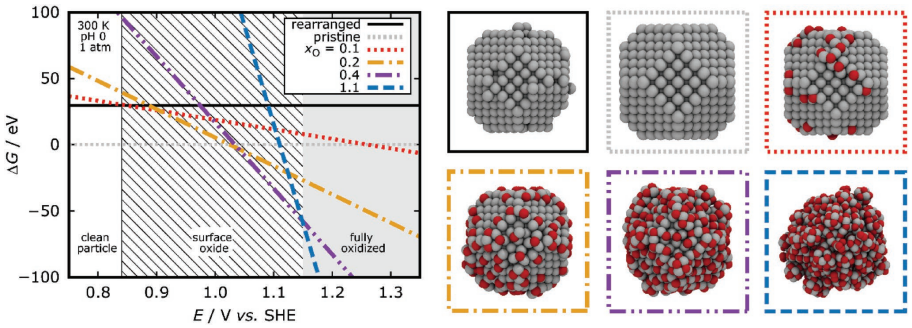

Figure 4. Potential-dependent phase diagram for a 3 nm cuboctahedron and illustration of the thermodynamically most stable structures therein.

ADVANCED SCIENCE NEWS
www.advancedsciencenews.com

NANO · MICRO small
www.small-journal.com

Pt—O bond is found in Pt_6O_8, while Pt_3O_4 features two types of inequivalent Pt—O bonds. This assessment is supported by a comparison of calculated partial charge distributions of a fully oxidized nanoparticle from GCMC and spherical particles cut from PtO, α-PtO_2, β-PtO_2, and Pt_3O_4 crystals (see Figures S4 and S5 in the Supporting Information). Pt_6O_8 has been discussed by Vegas to most likely correspond to a mixed-valence compound of 4 Pt(IV) and 2 Pt(II) with four net negative charges in the context of explaining the crystal structure of Pt_3O_4.[33] We will thus refer to it as $[Pt_6O_8]^{4-}$. To the best of our knowledge, so far the only experimental report mentioning this species is a thesis work by Dimas Rivera, who observed an interlattice distance corresponding to the (012) plane of Pt_6O_8 using high-resolution transmission electron microscopy on a composite Pt–Fe/Al_2O_3 hydrogenation catalyst.[34] It is unsurprising that $[Pt_6O_8]^{4-}$ has so far not been observed in experiments due to the necessity for intricate operando studies and because this kind of degradation product has simply not been considered and expected so far. While experimental confirmation is needed to establish $[Pt_6O_8]^{4-}$ as a primary degradation product of Pt-based electrocatalysts, theoretical evidence will now be presented in favor of the significance of this observation. As a first clue, note that although our force field had not been trained to directly reproduce the Pt_3O_4 phase, the formation of these Pt_6O_8 units could still be observed, indicating a remarkably high driving force for its formation.

Afterward, the $[Pt_6O_8]^{4-}$ cluster is studied more closely by DFT. Molecular DFT calculations of $[Pt_6O_8]^n$ (n = 0, −2, −4, −6) in various spin states are summarized in Table S2 (Supporting Information); they reveal that $^1[Pt_6O_8]^{4-}$ is indeed, as suggested by Vegas, the most stable combination of spin and charge state when a stabilizing water environment is taken into account. The formation energy from the elements is exothermic. A similar result is obtained in periodic DFT calculations. DFT results are therefore in good agreement with ReaxFF calculations regarding the stability and ease of formation of the $[Pt_6O_8]^{4-}$ cluster. See the Experimental Section and Supporting Information for more information on these calculations.

Finally, in order to evaluate their influence on particle degradation, we study the detachment of Pt_6O_8 clusters from a fully oxidized particle using ReaxFF. There is an endothermic energy difference of ≈1.6 eV between the particle with an attached Pt_6O_8 cluster and the cluster dissociated from the nanoparticle. This result is unsurprising due to the instability of anions in the gas phase.[35] It is therefore important to take into account the influence of the solvent on this process. To this end, we perform MD calculations of the nanoparticle in the solvent, see Figure S6 (Supporting Information). The initial state of this simulation, showing the solvated nanoparticle with the Pt_6O_8 motif, is illustrated in **Figure 5**. We find that when being solvated, detachment of the Pt_6O_8 cluster is now exothermic by ≈11–12 eV, which is in good agreement with the high stabilization computed using DFT with implicit solvent models.

Based on these results, we offer the hypothesis that $[Pt_6O_8]^{4-}$ could not only be involved in the catalyst's degradation process but also in the transport of $Pt^{2+/4+}$ ions through the fuel cell. The mechanism of propagation would be similar to what was proposed by Guilminot et al.,[36] who analyzed a proton exchange membrane fuel cell using a Pt/C catalyst after 529 h of continuous operation and reported the presence of Pt^{2+} and Pt^{4+} in the electrolyte. They argue that these ions form anionic complexes with halide impurities that originate from catalyst synthesis and experience electromotoric drag that moves them throughout the cell. However, we suggest that $[Pt_6O_8]^{4-}$ is the active species in this mechanism based on the calculated properties of this cluster. Certainly, more experimental evidence is required to assess this hypothesis. It must also be stressed that, given the nature of the GCMC approach, all results presented here describe the thermodynamic behavior, while kinetic aspects—as for instance, activation barriers related to the formation of the Pt_6O_8 units—are not included. However, the presented studies provide an important basis for further studies on these interesting effects.

3. Conclusion

To summarize, a potential-dependent electrochemical phase diagram is constructed from the thermodynamically most stable oxide structures found for 2–4 nm cuboctahedral nanoparticles using the ReaxFF–GCMC approach. Gas-phase formation energy values from GCMC are further refined by considering explicit water solvation and entropic corrections. The resulting phase diagram predicts the existence of stable surface oxides at electrochemical potentials between ≈0.8 and 1.1 V versus SHE. Additionally, a degradation mechanism involving anionic units of Pt_6O_8 stoichiometry is reported. Formation of $[Pt_6O_8]^{4-}$ is found to be exothermic both in DFT and ReaxFF calculations and the molecule appears to be hydrophilic. Detachment of a Pt_6O_8 cluster from the oxidized particle is found to be exothermic under aqueous conditions. We propose this structure to be a primary and important oxidation product of Pt NP electrocatalysts and to be involved in Pt nanoparticle degradation as well as the electromotoric transport of $Pt^{2+/4+}$ ions in fuel cells.

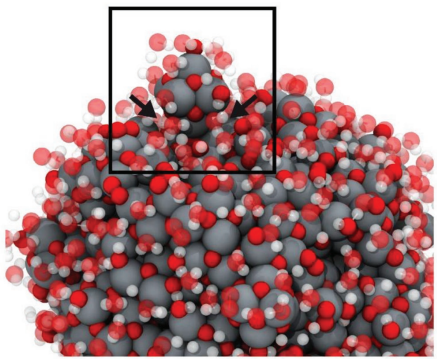

Figure 5. Fully oxidized Pt nanoparticle containing the Pt_6O_8 motif shown with a selection of solvent molecules. The rectangular box highlights a Pt_6O_8 unit where arrows indicated the "attack" by solvent molecules, potentially assisting detachment of solvated $[Pt_6O_8]^{4-}$.

ADVANCED SCIENCE NEWS
www.advancedsciencenews.com

NANO · MICRO small
www.small-journal.com

4. Computational Section

The freeware python 3 program nanocut[37] was used to cut nanoparticles from a fcc-Pt crystal. Lattice parameters for fcc-Pt as well as for the tested Pt oxides optimized using ReaxFF are listed in Table S3 (Supporting Information). ReaxFF–GCMC calculations were performed using the implementation of ReaxFF by software for chemistry & materials (SCM) in the Amsterdam Density Functional Suite Version 2017.106[19,38,39] and the GCMC algorithm by Senftle et al.[17,18] In short, the algorithm would randomly choose to insert, delete, or move an oxygen atom in the simulation box while the number Pt atoms was kept constant ($\mu_O N_{Pt} VT$ ensemble, where μ_O is the chemical potential of the oxygen reservoir). The geometry of the newly generated structure was then relaxed within the ReaxFF framework and accepted or dismissed based on the energy criterion. As ReaxFF followed a bond-order representation of the energy terms, it allowed for bond formation or breakage, thereby enabling structural rearrangement during relaxation cycles. Formally, this process was repeated until equilibrium with the gas phase reservoir reached. In practice, however, the GCMC algorithm was implemented with a forward bias, which pushed the simulation beyond the point of equilibrium in order to facilitate sampling of local minima. Careful postanalysis of all structures generated along the way was therefore required to find the minimum energy structure under the given simulation conditions. The Pt−O−H force field developed in the group was used.[22] Initial geometry optimizations of the nanoparticle structures used a convergence criterion of 0.05 kcal mol^{-1}. Up to 1000 energy relaxation steps were performed in between the GCMC steps, using a convergence criterion of 0.5 kcal mol^{-1}. A bond order cutoff of 0.0075 was employed, as well as full system electronegativity equalization method (EEM) charge equilibration. GCMC simulations usually achieved convergence within ≈30 000 iterations. Solvation energy calculations were carried out by placing the NP in a simulation box filled with explicit water molecules (≈5000 molecules, depending on the system), maintaining a density of ρ_{H_2O} = 1.0 g cm^{-3}. Simulations were carried out for 500 000 iterations using a time step of 0.25 fs and a temperature damping constant of 100 fs with the Velocity–Verlet algorithm and Berendsen thermostat (*NVT* ensemble). E_{solv}^{system} was obtained from the latter 250 000 iterations and was calculated according to Equation (1) as

$$E_{solv}^{system} = E^{system}(aq) - E^{system} - N_{H_2O} \cdot E_{tot}^{H_2O} \quad (1)$$

where $E^{system}(aq)$ is the total energy of the solvated particle, E^{system} is the total energy of the particle from GCMC calculations, N_{H_2O} is the number of H_2O molecules in the simulation box, and $E_{tot}^{H_2O}$ is the averaged total energy of a water molecule. The water density (not the number of water molecules) was kept constant at ρ_{H_2O} = 1.0 g cm^{-3}. For the 2PT analysis, particles were equilibrated for 55 000 iterations in an *NVE* ensemble with a starting temperature of T = 300 K and the same time step as before. The last 5000 iterations were used for the analysis. Enthalpy and entropy corrections for the oxygen molecule corrections (obtained from the thermochemical tables of the National Institute of Standards and Technology and the Joint Army-Navy-NASA-Air Force Interagency Propulsion Committee (NIST-JANAF)) were used to obtain chemical potentials of O, H_2, and H_2O. Free energy G^{system} and potential-dependent formation free energy values $\Delta G_F^{system}(\Delta\phi)$ of the system under investigation were calculated according to Equations (2) and ((3)) as

$$G^{system} = E_{tot}^{system} + E_{solv}^{system} - TS^{system} \quad (2)$$

$$\Delta G_F^{system}(\Delta\phi) = G^{system} - G^{ref} - N_O\,\mu_O + 2e\Delta\phi \quad (3)$$

where E_{tot}^{system} is the total ReaxFF energy of the system from GCMC calculations, E_{solv}^{system} is the solvation correction obtained from MD simulations, T is the temperature, S^{system} is the entropic contribution obtained with the 2PT method, G^{ref} is the total free energy of the pristine cuboctahedral particle used as reference, N_O is the number of oxygen atoms in the system, μ_O is the chemical potential of oxygen (where $\mu_O = \mu_{H_2O} - \mu_{H_2}$), and e is the elementary charge. The last term of Equation (3) implied that in the electrochemical system all oxygen that was used for the Pt oxidation originated from a water splitting reaction. Detachment of the Pt_6O_8 cluster in a water environment was investigated using ReaxFF constrained-MD calculations; see the Supporting Information for detailed simulation procedure.

Periodic DFT calculations were performed with the Vienna Ab Initio Simulation Package (VASP)[40–43] using the projector-augmented wave method[44] to represent the basis set. The exchange-correlation functional by Perdew, Burke, and Ernzerhof (PBE) was used.[45] Plane waves were cut off at 350 eV. Wave functions were optimized to an accuracy of 10^{-6} eV, while forces were relaxed to below 10^{-2} eV Å^{-1}. Gaussian smearing with a smearing parameter of 0.001 eV was used. For implicit solvation calculations, the GLSSA13 solvent model[46] implemented in VASPsol was invoked[47–49] with the empirical bulk dielectric constant of water at room temperature (ε_{bulk} = 78.4). VASPsol implicitly located counterions in the double layer in a Poisson–Boltzmann-based approach. For this charge screening, a Debye length κ of 3.0 Å, which corresponded to a 1:1 electrolyte at pH 0 and concentration 1 M, was used. Molecular DFT calculations were performed using the ORCA software[50] using the same PBE exchange-correlation functional. Here, triple-ζ def2-TZVP basis sets[51] and def2/J auxiliary basis[52] in order to profit from the computational speedup provided by the resolution-of-identity approximation were used. Further, effective core potentials by Andrae et al. were employed for Pt.[53] Wave functions were optimized using the "TightSCF" setting. The conductor-like polarizable continuum solvation model (CPCM) used in conjuction with the solvent model based on density (SMD)[54] with standard settings for the water solvent was used in ORCA. The program *VMD* was used to visualize structures.[55]

Supporting Information

Supporting Information is available from the Wiley Online Library or from the author.

Acknowledgements

B.K. thanks the University of Iceland Research Fund for support through a PhD fellowship, Dr. Anna Garden for access to nanoparticle DFT structures, and Marcos Tacca for translation help of Spanish primary literature. Andrey Sinyavskiy is acknowledged for implementing the 2PT method. This work was supported by the German Federal Ministry of Education and Research through the BMBF-project "GEP – Grundlagen elektrochemischer Phasengrenzen" (Grant No. 13XP5023D), the Deutsche Forschungsgemeinschaft (DFG) through Grant No. SFB-1316 (collaborative research center), as well as through the Icelandic Research Fund under Grant No. 174582-052. Computational resources were provided by the state of Baden–Württemberg through bwHPC and the German Science Foundation (DFG) under Grant No. INST 40/467-1 FUGG. The Volkswagen Group, Wolfsburg, Germany is acknowledged for partial funding of this project.

Conflict of Interest

The authors declare no conflict of interest.

Keywords

electrocatalysis, fuel cells, oxidation, platinum catalysts, ReaxFF

Received: September 10, 2019
Revised: November 17, 2019
Published online:

[1] F. Cheng, J. Chen, *Chem. Soc. Rev.* **2012**, *41*, 2172.
[2] H. Puliyalil, D. Lašič Jurković, V. D. B. C. Dasireddy, B. Likozar, *RSC Adv.* **2018**, *8*, 27481.
[3] J. Wu, H. Yang, *Acc. Chem. Res.* **2013**, *46*, 1848.
[4] S. Zhang, X.-Z. Yuan, J. N. C. Hin, H. Wang, K. A. Friedrich, M. Schulze, *J. Power Sources* **2009**, *194*, 588.
[5] J. C. Meier, C. Galeano, I. Katsounaros, J. Witte, H. J. Bongard, A. A. Topalov, C. Baldizzone, S. Mezzavilla, F. Schüth, K. J. J. Mayrhofer, *Beilstein J. Nanotechnol.* **2014**, *5*, 44.
[6] A. Morozan, B. Jousselme, S. Palacin, *Energy Environ. Sci.* **2011**, *4*, 1238.
[7] N. Tian, Z.-Y. Zhou, S.-G. Sun, *J. Phys. Chem. C* **2008**, *112*, 19801.
[8] E. Skúlason, A. A. Faraj, L. Kristinsdóttir, J. Hussain, A. L. Garden, H. Jónsson, *Top. Catal.* **2014**, *57*, 273.
[9] G. A. Tritsaris, J. Greeley, J. Rossmeisl, J. K. Nørskov, *Catal. Lett.* **2011**, *141*, 909.
[10] M. Shao, A. Peles, K. Shoemaker, *Nano Lett.* **2011**, *11*, 3714.
[11] P. Strasser, *Science* **2015**, *349*, 379.
[12] J. K. Nørskov, J. Rossmeisl, A. Logadottir, L. Lindqvist, J. R. Kitchin, T. Bligaard, H. Jónsson, *J. Phys. Chem. B* **2004**, *108*, 17886.
[13] V. Stamenkovic, B. S. Mun, K. J. J. Mayrhofer, P. N. Ross, N. M. Markovic, J. Rossmeisl, J. Greeley, J. K. Nørskov, *Angew. Chem.* **2006**, *118*, 2963.
[14] J. K. Nørskov, T. Bligaard, J. Rossmeisl, C. H. Christensen, *Nat. Chem.* **2009**, *1*, 37.
[15] N. Seriani, W. Pompe, L. C. Ciacchi, *J. Phys. Chem. B* **2006**, *110*, 14860.
[16] D. Fantauzzi, S. Krick Calderón, J. E. Mueller, M. Grabau, C. Papp, H.-P. Steinrück, T. P. Senftle, A. C. T. van Duin, T. Jacob, *Angew. Chem., Int. Ed.* **2017**, *56*, 2594.
[17] T. P. Senftle, R. J. Meyer, M. J. Janik, A. C. T. van Duin, *J. Chem. Phys.* **2013**, *139*, 044109.
[18] T. P. Senftle, A. C. T. van Duin, M. J. Janik, *Catal. Commun.* **2014**, *52*, 72.
[19] Software for Chemistry & Materials (SCM), "ReaxFF 2017," http://www.scm.com (accessed: November 2019).
[20] S.-T. Lin, M. Blanco, W. A. Goddard, *J. Chem. Phys.* **2003**, *119*, 11792.
[21] T. Jacob, *J. Electroanal. Chem.* **2007**, *607*, 158.
[22] D. Fantauzzi, J. Bandlow, L. Sabo, J. E. Mueller, A. C. T. van Duin, T. Jacob, *Phys. Chem. Chem. Phys.* **2014**, *16*, 23118.
[23] D. Fantauzzi, J. E. Mueller, L. Sabo, A. C. T. van Duin, T. Jacob, *ChemPhysChem* **2015**, *16*, 2797.
[24] Y. Wen, H. Fang, Z. Zhu, S. Sun, *Phys. Lett. A* **2009**, *373*, 272.
[25] Y. Wen, H. Fang, Z. Zhu, S. Sun, *Phys. Lett. A* **2009**, *373*, 1800.
[26] R. Huang, Y.-H. Wen, Z.-Z. Zhu, S.-G. Sun, *J. Mater. Chem.* **2011**, *21*, 11578.
[27] "Cohesive Energy | The Elements Handbook at KnowledgeDoor," http://www.knowledgedoor.com/2/elements_handbook/cohesive_energy.html (accessed: November 2019).
[28] S. G. Lambie, G. R. Weal, C. E. Blackmore, R. E. Palmer, A. L. Garden, *Nanoscale Adv.* **2019**, *1*, 2416.
[29] T. P. Senftle, M. J. Janik, A. C. T. van Duin, *J. Phys. Chem. C* **2014**, *118*, 4967.
[30] K. Wang, H. Wu, M. Ge, W. Xi, J. Luo, *Mater. Charact.* **2018**, *145*, 246.
[31] G. A. Kimmel, N. G. Petrik, Z. Dohnálek, B. D. Kay, *Phys. Rev. Lett.* **2005**, *95*, 166102.
[32] H.-Y. Park, S. H. Ahn, S.-K. Kim, H.-J. Kim, D. Henkensmeier, J. Y. Kim, S. J. Yoo, J. H. Jang, *J. Electrochem. Soc.* **2016**, *163*, F210.
[33] A. Vegas, *Inorganic 3D Structures*, Springer-Verlag, Berlin Heidelberg **2011**.
[34] G. L. Dimas Rivera, *PhD Thesis*, Universidad Autónoma de Nuevo León, San Nicolás de los Garza, Mexico **2015**.
[35] A. Dreuw, L. S. Cederbaum, *Chem. Rev.* **2002**, *102*, 181.
[36] E. Guilminot, A. Corcella, F. Charlot, F. Maillard, M. Chatenet, *J. Electrochem. Soc.* **2007**, *154*, B96.
[37] "aradi/nanocut," https://bitbucket.org/aradi/nanocut (accessed: November 2019).
[38] A. C. T. van Duin, S. Dasgupta, F. Lorant, W. A. Goddard, *J. Phys. Chem. A* **2001**, *105*, 9396.
[39] K. Chenoweth, A. C. T. van Duin, W. A. Goddard, *J. Phys. Chem. A* **2008**, *112*, 1040.
[40] G. Kresse, J. Hafner, *Phys. Rev. B* **1993**, *47*, 558.
[41] G. Kresse, J. Hafner, *Phys. Rev. B* **1994**, *49*, 14251.
[42] G. Kresse, J. Furthmüller, *Phys. Rev. B* **1996**, *54*, 11169.
[43] G. Kresse, J. Furthmüller, *Comput. Mater. Sci.* **1996**, *6*, 15.
[44] G. Kresse, D. Joubert, *Phys. Rev. B* **1999**, *59*, 1758.
[45] J. P. Perdew, K. Burke, M. Ernzerhof, *Phys. Rev. Lett.* **1996**, *77*, 3865.
[46] D. Gunceler, K. Letchworth-Weaver, R. Sundararaman, K. A. Schwarz, T. A. Arias, *Modell. Simul. Mater. Sci. Eng.* **2013**, *21*, 074005.
[47] K. Mathew, R. Sundararaman, K. Letchworth-Weaver, T. A. Arias, R. G. Hennig, *J. Chem. Phys.* **2014**, *140*, 084106.
[48] K. Mathew, R. G. Hennig, *ArXiv160103346 Cond-Mat* **2016**.
[49] M. Van den Bossche, E. Skúlason, C. Rose-Petruck, H. Jónsson, *J. Phys. Chem. C* **2019**, *123*, 4116.
[50] F. Neese, *Wiley Interdiscip. Rev.: Comput. Mol. Sci.* **2012**, *2*, 73.
[51] F. Weigend, R. Ahlrichs, *Phys. Chem. Chem. Phys.* **2005**, *7*, 3297.
[52] F. Weigend, *Phys. Chem. Chem. Phys.* **2006**, *8*, 1057.
[53] D. Andrae, U. Häußermann, M. Dolg, H. Stoll, H. Preuß, *Theor. Chim. Acta* **1990**, *77*, 123.
[54] A. V. Marenich, C. J. Cramer, D. G. Truhlar, *J. Phys. Chem. B* **2009**, *113*, 6378.
[55] W. Humphrey, A. Dalke, K. Schulten, *J. Mol. Graphics* **1996**, *14*, 33.

NANO MICRO small

Supporting Information

for *Small*, DOI: 10.1002/smll.201905159

Simulations of the Oxidation and Degradation of Platinum Electrocatalysts

Björn Kirchhoff, Laura Braunwarth, Christoph Jung, Hannes Jónsson, Donato Fantauzzi, and Timo Jacob**

Supporting Information

Simulations of the Oxidation and Degradation of Platinum Electrocatalysts

*Björn Kirchhoff, Laura Braunwarth, Christoph Jung, Hannes Jónsson, Donato Fantauzzi, and Timo Jacob**

1) Reproduction of formation energy results by Lambie *et al*. with ReaxFF

The formation energy of icosahedral, cuboctahedral, and decahedral nanoparticle structures between 53 and 315 atoms were calculated using ReaxFF. Structures were obtained from Lambie and co-workers[28] and reoptimized in the ReaxFF framework before energy evaluation. The formation energy E_F is calculated according to Equation 1 as

$$E_F = \frac{E_{tot}^{system} - N_{Pt} \cdot g_{Pt}}{N_{Pt}^{\frac{2}{3}}}, \#1$$

where E_{tot}^{system} is the total DFT or ReaxFF energy of the system, N_{Pt} is the number Pt atoms in the system, and g_{Pt} is the cohesive energy of *fcc*-Pt ($g_{Pt}^{DFT} = 6.11\ eV/atom$,[28] $g_{Pt}^{ReaxFF} = 5.72\ eV/atom$, $g_{Pt}^{exp.} = 5.82\ eV/atom$[27]).

Figure S1 compares the VASP-DFT results from Lambie *et al.* with trends obtained with our ReaxFF force field and ADF v2017.106.

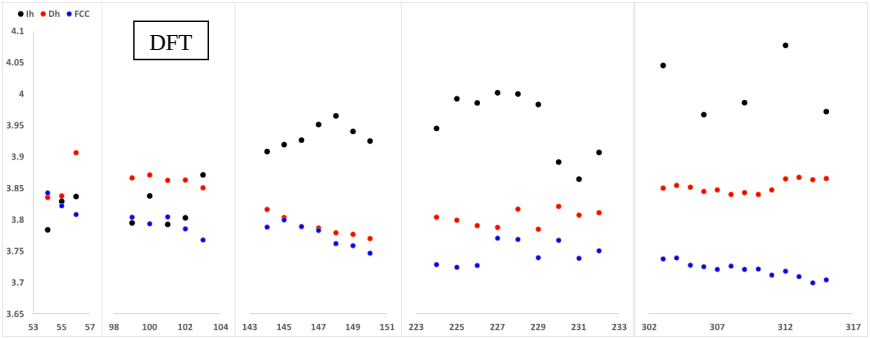

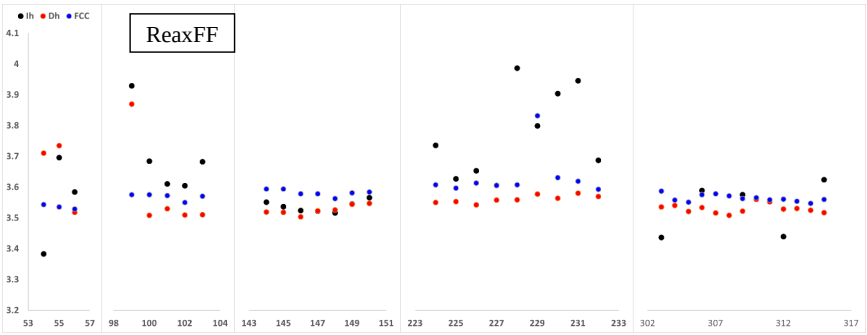

Figure S1. Comparison of DFT[28] (top) and ReaxFF formation energy trends for icosahedral (Ih, black), decahedral (Dh, red), and cuboctahedral (FCC, blue) Pt clusters between 53 and 315 atoms.

The observed differences between ReaxFF and DFT can be related to the description of Pt–Pt interactions in the force field, which are governed by two-body terms. While two-body terms can provide a good description for small systems being dominated by direct neighbour interactions as well as extended facets where long-range ordering is prevalent, deviations are expected for medium-sized clusters being strongly influenced by next-nearest-neighbour interactions.

2) Overview of GCMC structures for UHV conditions

Figure S2 gives an overview over the oxidation process at UHV (p_O = 10^{-10} mbar) conditions. NAP (p_O = 1 mbar) conditions are presented in the main manuscript.

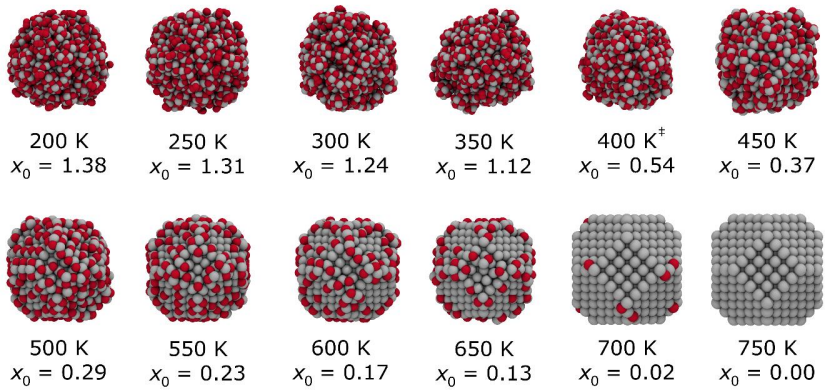

Figure S2. Thermodynamic minimum-energy structures obtained in ReaxFF-GCMC simulations at UHV (p_O = 10^{-10} mbar) conditions. x_O: oxygen-to-platinum ratio.

3) Electrochemical phase diagrams for 2-4 nm cuboctahedral particles

Figure S3 presents electrochemical phase diagrams of 2, 3, and 4 nm cuboctahedral nanoparticles constructed using the EAITD methodology. Unlike in **Figure 4**, entropic and solvation contributions are not taken into account.

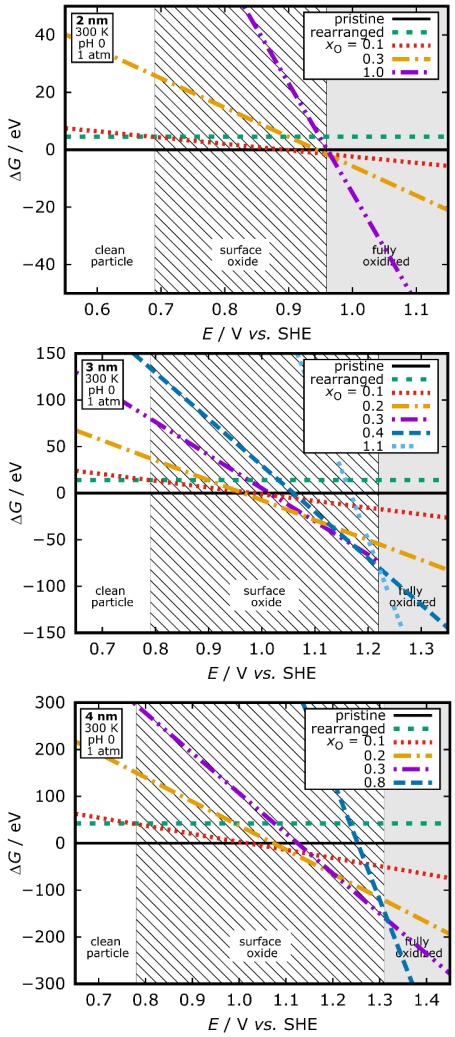

Figure S3. Electrochemical phase diagrams for 2, 3 and 4 nm cuboctahedral nanoparticles (in this sequence from top to bottom). Entropic and solvation contributions are not taken into account.

4) Structural comparison of Pt_6O_8 and Pt_3O_4

Table S1. Comparison of key bond lengths r and bond angles θ for the Pt_6O_8 cluster and Pt_3O_4 crystal structure from ReaxFF and DFT-PBE. The $[Pt_6O_8]^{4-}$ DFT-PBE was relaxed using an implicit solvent model (CPCM-SMD). Note that ReaxFF cannot perform calculations using explicit charges. It is notable that using ReaxFF, two different types of Pt-Pt and Pt-O bonds are present in Pt_3O_4, while all bonds are homogenous in Pt_3O_4. Only one type of Pt-O bond is found in Pt_3O_4 at the PBE level. This structural inaccuracy of Pt_3O_4 with ReaxFF likely corresponds to the too low formation energy reported in the original force field publication.[22]

	$[Pt_6O_8]$ ReaxFF	$[Pt_6O_8]^{4-}$ DFT-PBE	Pt_3O_4 ReaxFF	Pt_3O_4 DFT-PBE
$r_{Pt\text{-}Pt}$	2.92 Å	2.78 Å	2.81 Å, 3.42 Å	2.82 Å, 3.46 Å
$\theta_{Pt<Pt<Pt}$	60 °	60 °	49 °	48 °
$r_{Pt\text{-}O}$	2.03 Å	2.13 Å	2.00 Å, 1.76 Å	2.00 Å
$\theta_{Pt<O<Pt}$	83 °	82 °	120 °	120 °
$r_{O\text{-}O}$	2.69 Å	2.93 Å	2.75 Å, 3.0 Å	2.82 Å

XYZ coordinates of the structure evaluated here are presented at the end of this SI.

5) Charge distribution analysis of structures containing the Pt_6O_8 motif

The ReaxFF partial charge distribution of a nanoparticle structure containing the Pt_6O_8 motif is analysed in order to reveal its chemical nature. To this end, ReaxFF partial charge distributions of 3 nm spherical particles cut from PtO, α-PtO_2, β-PtO_2, and Pt_3O_4 cells are obtained and the distribution maxima from these structures are used to "calibrate" the analysis procedure, see **Figure S4**. We found oxygen partial charges to be most reliable to identify the

nature of the oxide structure. **Figure 5** shows the partial oxygen charge density plot for a structure containing the Pt_6O_8 motif; calibration bands are shown with dotted lines.

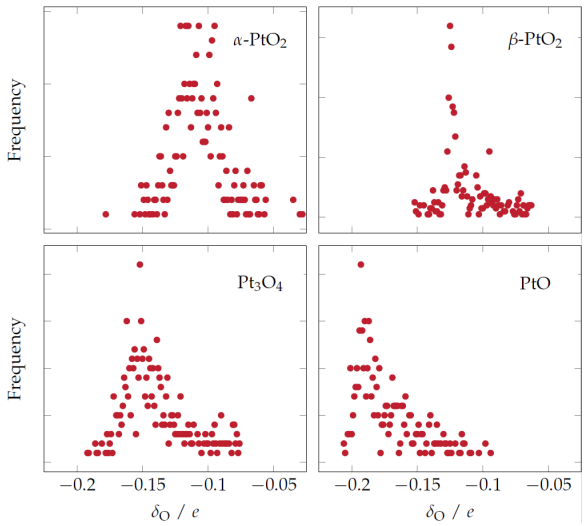

Figure S4. Partial oxygen charge distribution plots for 3 nm spherical particles cut from bulk PtO, α-PtO_2, β-PtO_2, and Pt_3O_4 cells and relaxed within the ReaxFF framework.

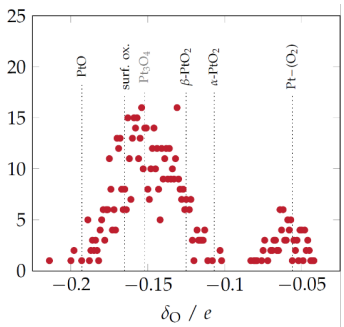

Figure S5. Partial oxygen charge distribution plot of a fully oxidized structure containing the Pt_6O_8 motif. Dotted lines indicate distribution maxima from "calibration" runs, see **Figure S4**.

6) DFT calculations on $[Pt_6O_8]^n$ (n = 0, -2, -4, -6)

Molecular DFT-PBE calculations with ORCA were carried out to obtain formation energy values for $[Pt_6O_8]^n$ (n = 0, -2, -4, -6) in various spin states in the gas phase as well as using an implicit water solvent model. Results in **Table S2** reveal that while $^1[Pt_6O_8]^{4-}$, as suggested by Vegas, is indeed most stable when including implicit solvation with E_F = -44.3 eV, $^3[Pt_6O_8]^{2-}$ is more stable in the gas phase with E_F = -29.7 eV (*vs.* -16.8 eV for $^1[Pt_6O_8]^{4-}$). This is not surprising since multiply-charged anions have low stability in the gas phase[35] and thus, trends from the implicit solvent calculation are more significant. Besides demonstrating high stability of this structure, this result also suggests that $[Pt_6O_8]^{4-}$ is easily stabilized when dissolved in water. It is therefore reasonable to assume that $[Pt_6O_8]^{4-}$ anions are highly mobile in aqueous solutions. Due to the problematic nature of calculating single atom reference energy values such as ^{3}Pt using DFT, which is needed when estimating E_F, we repeated this study using periodic DFT calculations where E_F is calculated with respect to the more reliable cohesive energy of the *fcc*-Pt crystal, g_{Pt}. This way, E_F of $[Pt_6O_8]^{4-}$ is found to be -5.3 eV using the same PBE functional. By invoking an implicit water solvent model, E_F decreases to -13.0 eV. The VASP gas phase E_F is consistent with the -7.5 eV obtained in ReaxFF for the same process, especially given the already highlighted disparity in the description of the Pt_3O_4 phase.

Table S2. Energy of formation E_{form} for $[Pt_6O_8]^n$ (n = 0, -2, -4, -6) from the elements $^3O_2$ and ^{3}Pt as calculated with the molecular ORCA code. Results from gas phase an implicit solvent (CPCM-SMD water) are presented.

$[Pt_6O_8]^n$ n =	$E_{\mathrm{form}}^{\mathrm{gas}} / eV$	$E_{\mathrm{form}}^{\mathrm{solv}} / eV$

0	Singlet: -25.87 eV Triplet: -25.93 eV Quintuplet: -25.93 eV	Singlet: -25.98 eV Triplet: -26.03 eV Quintuplet: -26.09 eV
-2	Singlet: -29.57 eV Triplet: -29.68 eV Quintuplet: -28.99 eV	Singlet: -36.37 eV Triplet: -36.46 eV
-4	Singlet: -16.80 eV Triplet: -15.87 eV	Singlet: -44.25 eV Triplet: *did not converge*
-6	Singlet: 11.70 eV Triplet: *11.40 eV* [1]	Singlet: *did not converge*
[1] Cluster is destroyed during optimization; does not converge.		

7) Constrained MD Simulation of Pt_6O_8 Detachment in Presence of Explicit Water

A constrained MD simulation is performed on fully oxidized cuboctahedral nanoparticle featuring an exposed Pt_6O_8 cluster on its surface in a simulation box with explicit water molecules (shown partly in **Figure S6**) to study the total energy change upon detachment of the Pt_6O_8 cluster. To this end, the water box containing the oxidized nanoparticle is pre-

equilibrated using an NVT ensemble (300 K, 400,000 iterations) until changes in the total energy and temperature are converged. A bond constraint is employed which forces the Pt_6O_8 cluster away from its host particle is then applied for 100,000 iterations at 300 K. Afterwards, the system containing the detached Pt_6O_8 cluster is equilibrated again for 200,000 iterations without the bond constraint. In **Figure S6**, detachment is observed at *ca*. 12,500 fs. After this point, the total energy of the simulation decreases, indicating overall stabilization of the system. The bond constraint is turned off after *ca*. 25,000 iterations. Comparing the average total energy of the system beyond this point with the average total energy of the pre-equilibrated system, we estimate the detachment to be exothermic by 11-12 eV.

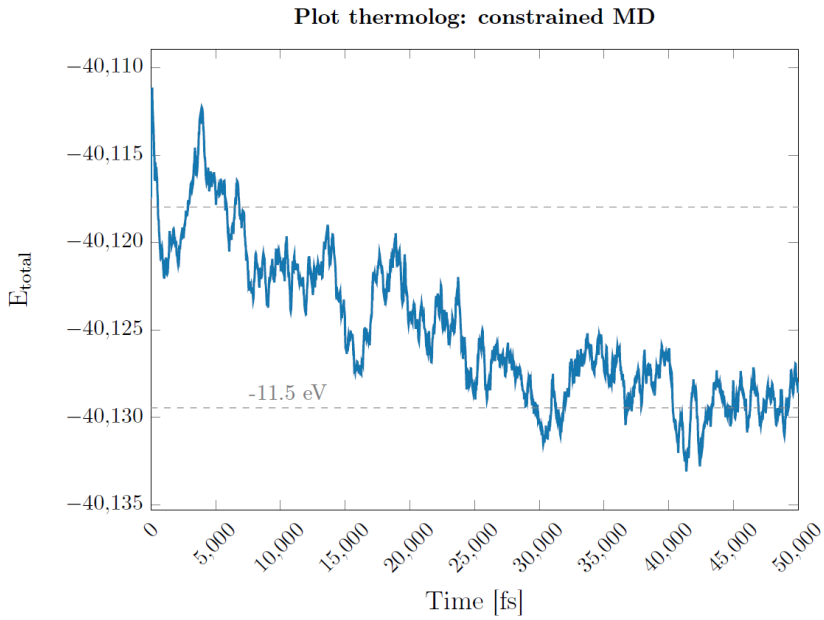

Figure S6. Total energy of a constrained MD simulation of a Pt_6O_8 cluster detaching from a fully oxidized cuboctahedral nanoparticle as a function of simulation time. Detachment of the Pt_6O_8 cluster is observed at *ca.* 12,500 fs. The bond constraint was turned off at *ca*. 25,000 fs.

8) Optimized ReaxFF lattice parameters for Pt and Pt oxides

Table S3. Optimised lattice parameters for Pt and Pt oxides used for ReaxFF calculations. SG: spacegroup.

Structure	SG	*a* / Å	*b* / Å	*c* / Å	*α*	*β*	*γ*
Pt	$Fm\bar{3}m$	3.94737	3.94737	3.94737	90.0	90.0	90.0
α-PtO_2	$P\bar{3}m1$	3.16017	3.16017	4.75548	90.0	90.0	120.0
β-PtO_2	$Pnnm$	4.58390	4.63850	3.23600	90.0	90.0	90.0
Pt_3O_4	$Pm\bar{3}n$	5.71200	5.71200	5.71200	90.0	90.0	90.0
PtO	$P42/mmc$	3.25468	3.25468	5.33397	90.0	90.0	90.0

9) Note on reproducibility with newer versions of SCM's ADF software

The present results were obtained using ADF-ReaxFF version 2017.106. We were unable to reproduce GCMC results with any version later than 2017.109; with newer version, for particles larger than 2 nm, the simulation will converge before complete oxidation of the particles occurs and the Pt_6O_8 motif is not observed. However, if structures generated with version 2017.106 are used as input for energy calculations with the most recent version available to us (2018.106), the same total energy values are obtained. We are therefore convinced that the reported observations are consistent but that the internal driving force that advances the calculation beyond local minima configurations is different in newer versions. Groups looking to use this methodology should be aware of this version conflict.

10) Optimized structures of the Pt_6O_8 cluster and a Pt_3O_4 crystal

```
14
      Pt3O4 - ReaxFF (cell in A and °) 5.71   5.71   5.71  90.00  90.00  90.00
Pt      1.35781   -0.05810    2.73009
Pt      4.26928   -0.02823    2.89594
Pt      2.73024    1.35786   -0.05778
Pt      2.89577    4.26918   -0.02858
Pt     -0.05800    2.73040    1.35780
Pt     -0.02836    2.89566    4.26930
O       1.40499    1.40575    1.40606
O       4.39105    3.95231    1.24419
O       3.95251    1.24471    4.39150
O       1.24555    4.39107    3.95216
O       4.22113    4.22027    4.22001
O       1.23461    1.67425    4.38270
O       1.67398    4.38215    1.23419
O       4.38144    1.23471    1.67443

14
      Pt6O8 - ReaxFF
```

```
Pt  24.01562  26.78372  25.17560
Pt  24.66008  24.58947  26.98978
Pt  26.05341  23.21040  24.82688
Pt  26.79013  25.94704  25.52642
Pt  25.40887  25.40458  23.01263
Pt  23.27886  24.04703  24.47593
O   25.75794  27.04424  24.16189
O   26.59722  24.18694  26.52448
O   25.27046  26.51356  26.75144
O   22.98422  25.27637  26.06754
O   23.47166  25.80720  23.47800
O   24.79851  23.48059  23.25093
O   27.08482  24.71762  23.93493
O   24.31110  22.94980  25.84048


14
      Pt3O4 - ReaxFF (cell in A and °) 5.65 5.65 5.65 90 90 90
Pt       2.82240096       1.41120048       0.00000000
Pt       2.82240096       4.23360144       0.00000000
Pt       0.00000000       2.82240096       4.23360144
Pt       0.00000000       2.82240096       1.41120048
Pt       4.23360144       0.00000000       2.82240096
Pt       1.41120048       0.00000000       2.82240096
O       4.23360144       1.41120048       1.41120048
O       1.41120048       1.41120048       4.23360144
O       1.41120048       4.23360144       1.41120048
O       4.23360144       4.23360144       4.23360144
O       1.41120048       4.23360144       4.23360144
O       4.23360144       4.23360144       1.41120048
O       1.41120048       1.41120048       1.41120048
O       4.23360144       1.41120048       4.23360144


14
      Pt6O8 - DFT-PBE (ORCA 4.0, def2-TZVP, singlet, charged 4-, H2O CPCM+SMD
implicit solvation)
Pt  50.49758028914566     -3.80100866950718     22.18187848873570
Pt  51.06358781112112     -5.90768242798125     23.94947372016069
Pt  52.48856956463806     -7.22691121257054     21.92116351120363
Pt  53.15616886764747     -4.59018157645059     22.61953425755314
Pt  51.92230819453316     -5.11992541915873     20.15388129872868
Pt  49.82979081809933     -6.43746288292181     21.48360458844192
O   52.30513320935937     -3.27336984117127     21.16469098217943
O   53.14150163781537     -6.38683137012759     23.77782075181563
O   51.66993547843564     -3.85598920274480     23.96971615092557
O   49.20999087165207     -5.22124251726794     23.13024709284414
O   49.84507421241861     -4.63973771961862     20.32543941148871
O   51.31582703455984     -7.17188765362676     20.13416840753220
O   53.77588750885248     -5.80641337201712     20.97334655947683
O   50.68009450172165     -7.75423613483578     22.93799477891374
```

Publication II

Accuracy Assessment of Density Functionals for the Oxygen Reduction Reaction on Doped Graphenes

B. Kirchhoff, A. Ivanov, E. Skúlason, T. Jacob, D. Fantauzzi, H. Jónsson*

Author contributions: Aleksei Ivanov performed PZ-SIC calculations. Björn Kirchhoff performed all other calculations and data analysis and wrote the initial manuscript draft. Egill Skúlason, Timo Jacob, Donato Fantauzzi, and Hannes Jónsson supervised the project. Egill Skúlason, Timo Jacob, and Hannes Jónsson contributed writing revisions. Submitted to *Journal of Chemical Theory and Computation.*

Assessment of the Accuracy of Density Functionals for Calculating Oxygen Reduction Reaction on Nitrogen Doped Graphene

Björn Kirchhoff,[†,‡] Aleksei Ivanov,[†] Egill Skúlason,[¶] Timo Jacob,[‡,§,‖] Donato Fantauzzi,[†] and Hannes Jónsson[*,†]

†*Science Institute and Faculty of Physical Sciences, University of Iceland, VR-III, Hjarðarhagi 2, 107 Reykjavík, Iceland*

‡*Institute of Electrochemistry, Ulm University, Albert-Einstein-Allee 47, 89081 Ulm, Germany*

¶*Science Institute and Faculty of Industrial Engineering, Mechanical Engineering and Computer Science, University of Iceland, Hjarðarhagi 2, 107 Reykjavík, Iceland*

§*Helmholtz-Institute Ulm (HIU) Electrochemical Energy Storage, Helmholtz-Straße 16, 89081 Ulm, Germany*

‖*Karlsruhe Institute of Technology (KIT), P.O. Box 3640, 76021 Karlsruhe, Germany*

E-mail: hj@hi.is

Abstract

Experimental studies of the oxygen reduction reaction (ORR) at nitrogen doped graphene electrodes have reported a remarkably low overpotential, on the order of 0.5 V, similar to Pt based electrodes. Theoretical calculations using density functional theory have lent support for this claim. However, other measurements have indicated that transition metal impurities are actually responsible for the ORR activity, thereby

raising questions about the reliability of both the experiments and the calculations. In order to assess the accuracy of the theoretical calculations, various generalized gradient approximation (GGA), meta-GGA and hybrid functionals are employed here and calibrated against high-level wave function based coupled cluster calculations (CCSD(T)) of the overpotential as well as self-interaction corrected density functional calculations and published quantum Monte Carlo calculations of O adatom binding to graphene. The PBE0 and HSE06 hybrid functionals are found to give more accurate results than the GGA and meta-GGA functionals, as would be expected, and for low dopant concentration, 3.1%, the overpotential is calculated to be 1.0 V. The GGA and meta-GGA functionals give a lower estimate by as much as 0.4 V. When the dopant concentration is doubled, the overpotential calculated with hybrid functionals drops, while it increases in GGA functional calculations. The opposite trends result from different potential determining steps, the *OOH species being of central importance in the hybrid functional calculations while the reduction of *O determines the overpotential obtained in GGA and meta-GGA calculations. The results presented here are mainly based on calculations of periodic representations of the system, but a comparison is also made with molecular flake models which are found to give erratic results due to finite size effects and geometric distortions during energy minimization. The presence of the electrolyte has not been taken into account explicitly in the calculations presented here, but is estimated to be important for definitive calculations of the overpotential.

1 Introduction

Doped graphene has attracted attention over the past decade as a metal-free catalyst [1–3] and is being explored as a possible replacement for expensive and rare platinum group metals for the oxygen reduction reaction (ORR) in fuel cells.[4] Qu *et al.* synthesized a few-layer nitrogen-doped graphene (NG) by chemical vapor deposition on a SiO_2/Ni substrate and used it as the cathode in ORR experiments. They reported an onset potential similar to commercial platinum catalysts under alkaline conditions and better resistance to methanol

and CO poisoning, as well as good cycling stability.[5] Since then, several experimental studies have reported on high ORR activity in NG as has been reviewed by Wang *et al.*[6] and Zhang *et al.*[1] Generally, NG is reported to catalyze the $4\,e^-$ ORR mechanism at similar or slightly lower catalytic activity than Pt under alkaline conditions while having higher durability.

The possible influence of transition metal impurities on the catalytic activity measured for NG is, however, a subject of ongoing debate. Some widely used preparation methods[7,8] are based on a permanganate oxidant and the Mn atoms can be present in the product even after washing.[9] Extreme conditions have in some cases been used to reduce the amount of metal residue and this has been found to result in reduced ORR activity.[10] NG synthesized under explicitly metal-free conditions has been reported to give higher ORR overpotential.[11]

Theoretical studies of ORR on NG have been conducted using various approaches. Classical dynamics simulations with energy and atomic forces estimated using electron density functional theory (DFT) have been used to study the relative stability of the various intermediates in ORR as well as free energy barriers for the reaction steps.[12–14] The first theoretical estimate of the overpotential was presented by Studt[15] using the thermochemical model (TCM).[16] There, the overpotential, η_{TCM} , is estimated from the free energy of the intermediates and the computational hydrogen electrode. Using the BEFF-vdW functional,[17] which is of the generalized gradient approximation (GGA) functional form, Studt obtained a value of $\eta_{\mathrm{TCM}} = 0.72$ V for NG with a dopant concentration of 6.2% and identified the potential determining step to involve reduction of *O adatom, but pointed out that solvation effects need to be taken into account in order to obtain a more reliable estimate.[15] We note that the TCM also does not include kinetic effects, *i.e.* the free energy barriers of the elementary reaction steps.[18] Reda *et al.* later carried out an extensive study using the same functional and method to estimate η_{TCM} for a range of dopant concentrations and to assess the effect of solvation by including ice-like layers of water molecules.[19] Using another functional of the GGA form, the PBE functional,[20] Li *et al.* reported a lower value for the onset potential, 0.45 V, from an extrapolation of calculated results for N-doped nanoribbon models.[21] Gísla-

son and Skúlason[22] obtained a η_{TCM} a value of 0.57 V for the overpotential using the RPBE functional,[23] a version of the PBE functional adjusted to give adsorption energy in better agreement with experimental measurements. Other calculations using the PBE functional have reported even lower values for the overpotential, such as 0.48 V for a model containing a cluster of three N dopants.[24]

The above studies were carried out using periodic, infinite-sheet or ribbon models of the system, but some other studies have used calculations of finite, molecular flake models to estimate the overpotential of ORR on NG. These studies have invariably been carried out with hybrid density functionals where some fraction of exact exchange is included in the functional form. These functionals are generally considered to give more accurate results than GGA functionals. Using the B3LYP hybrid functional,[25,26] Zhang and Xia calculated the overpotential for a flake model with a Stone-Wales defect,[27] and in a combined experimental and theoretical study, Jiao *et al.* reported η_{TCM} values for graphene doped with various types of atoms (N, B, P, S, O).[28] They found that B-doped graphene exhibits similarly good ORR performance as NG with η_{TCM} values similar to a commercial Pt catalyst.

The theoretical results discussed briefly above essentially fall into two classes, namely calculations of extended, periodic models of the system using energy functionals of the GGA form, or hybrid energy functional calculations of finite, molecular-like models. Apparently, both approaches give similarly good results indicating that NG can have ORR overpotential close to that of Pt catalysts. This could be interpreted as an indication that GGA and hybrid functionals are equally applicable to these studies and that periodic and finite models of the system give equivalent results. This is suprising since benchmark diffusion Monte Carlo simulations of the binding of an O adatom on a periodic model of graphene have shown significant errors in the binding energy obtained from GGA functionals.[29] Janesko *et al.* expanded on this benchmark study[30] by testing also meta-GGA and hybrid functionals, showing that hybrid functionals are significantly more accurate, especially the PBE0[31,32] and HSE06[33] functionals. The question, therefore, arises how the overpotential for ORR

predicted by hybrid functionals for periodic model systems of NG compare with the values previously obtained using GGA functionals, and whether the finite, flake models of NG give similar results as the extended, periodic models.

This article reports on a comprehensive study of various DFT functionals for calculating the overpotential for ORR on NG using both periodic as well as finite models. First, benchmark calculations of oxygen adsorption on undoped graphene are performed with a set of DFT functionals as well as explicitly self-interaction corrected GGA functional and the results compared with the diffusion Monte Carlo results. Secondly, η_{TCM} values for ORR on NG are reported for the various DFT functionals and both periodic and finite model systems. A remarkably large range of values is obtained, indicating what level of theory is needed to obtain best estimates of the overpotential within the TCM approximation. The effect of solvation remains the largest uncertainity, as discussed in the context of several different estimates.

2 Methodology

The calculations of the periodic representation of the system are carried out using a plane wave basis set with an energy cutoff of 600 eV to represent valence electrons and the projector-augmented wave (PAW) method[34,35] used to account for the effect of inner electrons. The energy functionals used in this study include the GGA functionals PBE,[20] BEEF-vdw,[17] as well as the meta-GGA functionals TPSS,[36] SCAN,[37] and hybrid functionals PBE0,[31,32] HSE06,[33] and B3LYP.[25,26] For BEEF-vdW, the implementation by Klimeš *et al.* was used.[38,39] If not stated otherwise, the simulation cell includes a 32-atom representation of the graphene and is constructed using lattice parameters (see Table S1) obtained from a C_4 graphite bulk cell ($P6_3/mmc$ spacegroup) optimized using a converged $11 \times 11 \times 3$ k-point grid. Wave functions are self-consistently optimized until the energy in subsequent iterations changes by less than 10^{-6} eV. Atomic coordinates are optimized until forces drop below 10^{-2} eV Å^{-1}. Gaussian-

type finite temperature smearing is used to speed up convergence. The smearing width is chosen so that the electronic entropy remains below 1 meV. Real-space evaluation of the projection operators is used to speed up calculations of larger systems, using a precision of 10^{-3} eV atom^{-1}. This scheme is also used with the isolated molecules to ensure consistency. The periodic images are separated by 14 Å of vacuum and a dipole correction is applied perpendicular to the slab. Omnidirectional dipole correction is used in the calculations of isolated molecules. The calculations are performed with the Vienna *ab initio* simulation package (VASP) version 5.4.4.[40–43]

DFT calculations of the finite model systems, *i.e.* the flakes, are carried out using the PBE and PBE0 density functionals. Furthermore, a high-level wave function based approach, the coupled-cluster singles doubles and perturbative triples (CCSD(T)) method, is used to test the accuracy. The domain-based local pair natural orbital (DLPNO) approximation[44–48] is used to reduce the computational effort of CCSD(T) calculations and a complete basis set extrapolation scheme[49–51] with the cc-pVDZ and cc-pVTZ[52] basis sets is used to reduce the basis set error. The def2-TZVP triple-ζ basis set is used[53] in the DFT calculations and the RIJCOSX[54] approximation applied to speed up the exact exchange part in hybrid DFT and DLPNO-CCSD(T) calculations. The def2/J[55] auxiliary basis set is used there. The cc-pVTZ/C[56] auxiliary basis set is additionally used with DLPNO-CCSD(T) calculations. The calculations are performed using ORCA software version 4.0.1.[57,58]

The test calculations on oxygen adsorption on undoped graphene are performed using a rhombic 4×4 supercell with 32 atoms (G32), as illustrated in figure 1. Comparison is made with high-level diffusion Monte Carlo (DMC) results reported by Hsing *et al.* with atomic coordinates provided by the authors. To ensure compatibility with the DMC calculations, calculations are carried out using the $M(0.5, 0)$ special k-point, but converged $\boldsymbol{k}$ grid calculations are also carried out with a $5 \times 5 \times 1$ Γ-centered grid. The lowest energy site for the oxygen adatom is the bridge position and the on-top site is significantly higher in energy. Calculations focus on the energy difference between the two configurations.

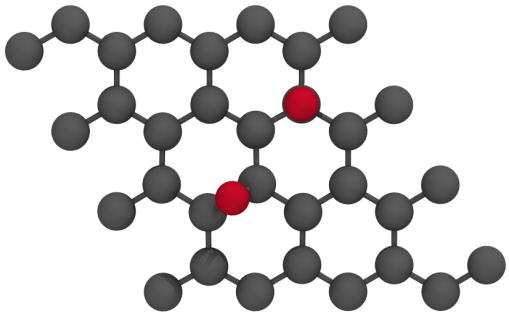

Figure 1: The 4x4 graphene simulation cell and location of the O-adatom at bridge and on-top sites.

In order to gain further insight into the limitations of the accuracy of the GGA functionals, an explicit self-interaction correction as proposed by Perdew and Zunger[59] (PZ-SIC) is applied to the PBE functional in the calculations of the O-adatom configurations. The calculations make use of a real-space grid representation of the valence electrons and PAW for inner electrons as implemented in the GPAW software version 20.1.0.[60] A grid mesh of 0.15 Å is used and direct minimization over complex orbitals is carried out.[61–63] As has been established previously from atomization and band gap studies, the PZ-SIC is scaled by a half.[64]

The free energy of reaction intermediates of ORR on NG is calculated using the 32-atom orthogonal simulation cell subject to periodic boundary conditions, with either one (gN1-G32) or two (gN2-G32) graphitic N dopants included, see figures 2 and 3. The resulting dopant concentration is 3.1% and 6.2%. This supercell is found to be large enough to obtain adsorption energy of ORR intermediates *O, *OH, and *OOH (see figure S1) unaffected by interaction with periodic images at the lower doping level. A $4 \times 4 \times 1$ Monkhorst-Pack[65] k-point grid and 400 eV energy cutoff are found to give converged results (see table S2 and figure S2). SCAN requires a denser FFT integration grid than the other functionals as has

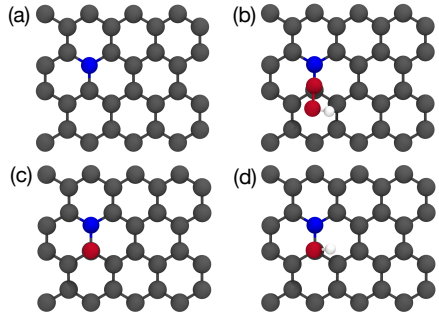

Figure 2: Simulation cell of the 3.1% N-doped graphene (**a**) and relaxed structures of the oxygen reduction reaction intermediates: *OOH (**b**), *O (**c**), and *OH (**d**). N atoms blue, O atoms red, H atoms white, C atoms gray.

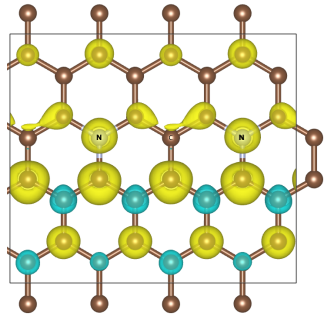

Figure 3: Simulation cell of the 6.2% N-doped graphene calculated using the HSE06 functional. The system has a small net magnetization moment at this level of theory, but not when a GGA or meta-GGA functional are used. The spin-up and spin-down densities are colored differently and the two N dopant atoms are marked. Periodic images of some of the atoms are shown in addition to those within the simulation cell.

been reported previously.[66] To speed up the optimization of the atomic coordinates in the hybrid functional calculations, a k-point reduction scheme for the exact exchange step is used, reducing it to the Γ point only. For a representative test system, the adsorption energy error introduced by this approximation is found to be $0.006 - 0.008$ eV (see Table S3). Final

total energy results are obtained using the full k-point grid.

Zero point energy and vibrational entropy contributions are calculated from Γ point phonon calculations within the harmonic approximation using four displacements of 0.015 Å per degree of freedom. The graphene backbone is constrained in these calculations to reduce computational effort. For a representative test system and the PBE functional, the error introduced by this approximation is found to translate to an increase of η_{TCM} by 0.04 V (see Tables S4 and S5). For phonon calculations using hybrid functionals, the same exact exchange k-point reduction scheme is used as for the energy minimization.

Potential-dependent free energy diagrams at pH 0 are constructed using the TCM.[16,18] From the free energy for each intermediate x, the reaction free energy is calculated as

$$G^x_{\mathrm{ads}}(U) = E^x_{\mathrm{el}} + E^x_{\mathrm{ZPE}} - TS^x_{\mathrm{vib}} + neU\,, \tag{1}$$

with E^x_{el} being the total energy of intermediate x, E^x_{ZPE} the zero-point energy correction, TS^x_{vib} the entropy correction evaluated at $T = 298.15$ K, and neU describing the effect of the potential where n is the number of electrons transferred during step x. Adsorption free energy values are calculated using gas-phase H_2O and H_2 as reference, for which entropy contributions are obtained from the NIST-JANAF Thermochemical Tables.[67] By varying U in (1), an estimate of the onset potential is obtained as the point at which all reaction steps first become downhill. For an ideal ORR catalyst, this point would occur at 1.23 V. Non-ideal systems deviate from this and η_{TCM} is obtained as the difference between 1.23 V and the calculated onset potential. See the Supporting Information for more details.

2.1 Test of functionals: O-adatom on graphene

In order to test the accuracy of the various DFT functionals, a comparison is made with the published DMC results of Hsing *et al.* for the binding of an O adatom to graphene.[29] The results are summarized in table 1. Here, the difference in total energy at the two sites for the

O adatom, on-top and bridge, $\Delta E = E_{\mathrm{tot}}^{\mathrm{top}} - E_{\mathrm{tot}}^{\mathrm{bridge}}$, is reported. This measure ensures that

Table 1: Calculated energy difference $\Delta E = E_{\mathrm{tot}}^{\mathrm{top}} - E_{\mathrm{tot}}^{\mathrm{bridge}}$ between on-top and bridge sites of an O adatom on graphene using various DFT functionals, self-interaction corrected PBE and diffusion Monte Carlo. For the M point results, the relative deviation with respect to diffusion Monte Carlo results is given in brackets.

	ΔE / eV		
Method	M point[a]	5×5×1 grid[b]	optimized[c]
DMC	1.36[d]	–	–
SIC	1.47 (+8 %)	–	–
PBE0	1.29 (-5 %)	1.10	1.09
HSE06	1.28 (-6 %)	1.10	1.10
B3LYP	0.99 (-27 %)	0.80	0.80
TPSS	0.97 (-29 %)	0.78	0.79
SCAN	0.92 (-32 %)	0.96	0.92
PBE	0.92 (-32 %)	0.75	0.75
BEEF-vdW	0.82 (-40 %)	0.65	0.63 ± 0.20[e]

[a] M point evaluated for atom coordinates provided by Hsing *et al.*[29]
[b] $5 \times 5 \times 1$ $\boldsymbol{k}$ grid evaluated for atom coordinates provided by Hsing *et al.*[29]
[c] $5 \times 5 \times 1$ $\boldsymbol{k}$ grid evaluated for atom coordinates optimized using the respective density functional.
[d] Value obtained from $M(0.5, 0)$ point DMC calculation.
[e] Standard deviation based on an ensemble size of 2000.

the different density functionals are compared exclusively based on their description of the electronic structure of the graphene-oxygen system, eliminating contributions from the O atom reference that can be problematic in DFT calculations.[68,69] The DMC results of Hsing *et al.* were obtained for the special $M = (0.5, 0)$ k-point only. The values in column "M point" in table 1 are obtained using this k-point and the same atom coordinates as used by Hsing *et al.*

The hybrid functionals PBE0 and HSE06 give results that are closest to the DMC values, with deviations of only 5 and 6%, respectively. These functionals differ only be the inclusion

of screening in HSE06. A 27% lower value with respect to DMC is obtained with the B3LYP hybrid functional. These results are in agreement with those of Janesko *et al.*[30] The GGA functionals, PBE and BEEF-vdW, give results that differ significantly from the DMC results and the results obtained with the two meta-GGA functionals, TPSS (29%) and SCAN (32%), have similar errors.

The reason for the shortcoming of the GGA and meta-GGA functionals in this calculation can be traced to the self-interaction error that is introduced in Kohn-Sham functionals that only depend on the total electron density. The explicitly self-interaction corrected PBE functional gives an energy difference that is close to but even a bit higher than the DMC results, with 8% deviation.

The BEEF-vdW functional includes van der Waals interaction and several calculations were additionally carried out to assess the importance of this contribution. Results obtained using the SCAN-rVV10[70] and DFT-D3BJ[71,72] with PBE and HSE06[73] are given in table S6. The addition of van der Waals interaction does not change the calculated energy difference significantly. The good performance of the self-interaction corrected PBE as well as the PBE0 and HSE06 hybrid functionals indicates that the dominant source of error in the GGA and meta-GGA calculations is due to the self-interaction.

The DMC calculations are limited to just one k-point and do not include structure relaxation. The effect of these two limitations is studied using the DFT functionals. First, the influence of the k-point grid is investigated. To this end, ΔE is recalculated with the previously used density functionals on a $5\times5\times1$ k-point grid on the same geometries used by Hsing and co-workers for DMC. While the ΔE values obtained this way cannot be directly compared to DMC, any changes in the relative sequence of functionals will reveal possible dependencies on the k-point sampling. Results of this test are summarized in column "$5\times5\times1$ grid" in table 1. The SIC method is omitted from hereon since the current implementation only supports single k-point calculations. While the obtained ΔE values are overall lower by *ca.* 0.2 eV compared to the M point results, the relative ordering of results is consistent

between M point and full k-point grid calculations. The only outlier is SCAN, which, using the 5×5×1 k-point grid, produces a significantly higher ΔE value than all other meta-GGA and GGA functionals as well as B3LYP. Note however that SCAN requires a denser FFT grid than the other functionals for convergence of the M point calculation. The numerical sensitivity of SCAN has been reported on in the past.[66] The PBE result is identical to the value published by Hsing and *et al.*[29] and the overall trend is in agreement with the sequence published by Janesko and co-workers.[30] Note that the values Janesko *et al.* report are overall larger by 0.2–0.3 eV, which the group attributes to the use of an LCAO instead of a plane-wave basis set.[30]

Secondly, the influence of the relaxation of the atomic configuration on the binding energy difference is investigated. So far, all ΔE calculations were performed using atomic configurations provided by Hsing and co-workers used for DMC calculations. Since different density functionals will produce different equilibrium lattice parameters, it is possible that this approach could introduce a form of lattice strain, leading to biased results. For this test, the atomic configurations and cell parameters of each system are therefore relaxed with each density functional using a $5 \times 5 \times 1$ k-point grid. Optimal graphite lattice parameters are obtained for each functional and are listed in table S1. The ΔE values obtained in this test are presented in column "optimized" in table 1. No significant differences are found compared to column "$5 \times 5 \times 1$ grid", with only a small discrepancy observed for SCAN. These results suggest that using the same geometry throughout the M point benchmark is inconsequential to the benchmark results. This conclusion also implies that for this material class, it is a suitable simulation approach to relax geometries at the GGA level and obtain accurate total energy values using a higher-level method.

The BEEF-vdW functional has an error estimate built in to indicate what range of values can be expected from any reasonable parametrization of the GGA functional form. The one standard deviation error bar obtained with an ensemble size of 2000 for the binding energy difference is quite large, 0.2 eV, corresponding to ± 30 %.

3 Results

Results obtained for periodic models of doped graphene are presented first and then results obtained using finite, flake-like models.

3.1 A. Periodic with 3.1% and 6.2% doping

The ORR overpotential for the periodic models of NG are calculated with the same set of density functionals used in the test against the DMC results for the O adatom on graphene. Given the good performance there, HSE06 is herein used as the best estimate for the overpotential and as the baseline for comparison. The periodic model systems of NG contain 32 atoms in the simulation cell and a dopant concentration of 3.1% (gN1-G32p) as illustrated in figure 2 and 6.2% (gN2-G32p) as illustrated in figure 3. These concentration values are within the 1 to 10% range reported for experimentally studied materials.[6] The calculated values of the adsorption energy for the various ORR intermediates are converged with respect to system size in the low concentration model (see figure S1).

The calculated free energy of the intermediates in the $4e^-$ ORR reaction path is shown in figure S3 for the lower dopant concentration and in figure 4 for the higher dopant concentration. The onset potential, U_o, that makes the potential determining step flat in free energy is determined for each case, and from that the overpotential is estimated as $\eta_{\mathrm{TCM}} = 1.23$ V - U_o. For the lower dopant concentration, a large range of values is obtained and a correlation between the value of the estimated overpotential and the binding energy difference of the O adatom is noted. This is illustrated in figure 5 which shows the calculated η_{TCM} values for each functional as a function of the ΔE values from column 'optimized' in table 1.

The onset potential is limited by the formation of *OOH in all cases for the lower dopant concentration. The hybrid functionals, PBE0 and HSE06, produce the highest η_{TCM} values of *ca.* 1.0 V. B3LYP produces a η_{TCM} similar to the HSE06 reference value despite showing larger deviations from the DMC results on the calculations of the *O binding energy

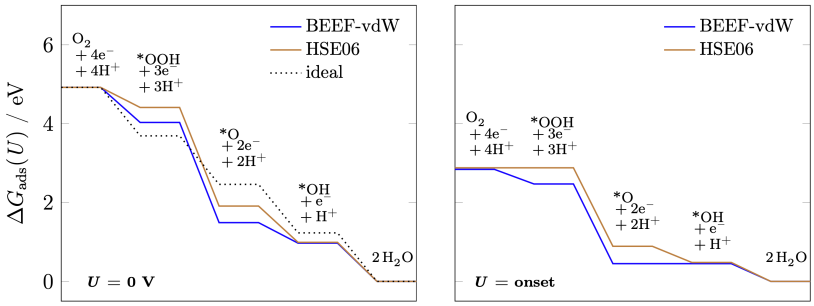

Figure 4: Calculated free energy for the oxygen reduction reaction on graphene with 6.2% N-dopant concentration. Left: at zero voltage. Right: at voltage giving as flat free energy profile as possible without any step being uphill. For the BEEF-vdW this voltage is 0.52 V corresponding to $\eta_{\mathrm{TCM}} = 0.71$ V and the reduction of *O is the potential determining step (as for the other GGA functionals), while for the HSE06 this voltage is 0.51 V corresponding to $\eta_{\mathrm{TCM}} = 0.72$ V and the reduction of O_2 to form *OOH is the potential determining step.

difference. This is a result of B3LYP producing *OH and *OOH free energy values similar to PBE0 and HSE06 while a larger deviation is observed for the free energy of the *O intermediate. Since ORR onset potential on this particular model system is limited by the *OOH formation step, the η_{TCM} obtained with B3LYP is in good agreement with PBE0 and HSE06.

The results obtained with PBE, TPSS, and SCAN functionals are found to be similar, analogous to the calculations of the *O binding energy difference. Compared to PBE0/HSE06, they underestimate η_{TCM} by 0.2–0.4 V. The BEEF-vdW functional underestimates η_{TCM} by *ca.* 0.4 V. The vertical error bars for BEEF-vdW in figure 5 indicate the uncertainty of η_{TCM} based on the standard deviation of the free energy values used to calculate η_{TCM}, obtained from an ensemble size of 2000 functionals. The error bars span a wide range of values, between 0.2–1.0 V. Note that PBE-D3 gives an almost identical η_{TCM} value as BEEF-vdW, indicating that the observed difference between BEEF-vdW and PBE is likely due to the added dispersion energy. Based on these results and the earlier benchmark, inclusion of exact exchange in hybrid functionals appears to be necessary to obtain accurate TCM results

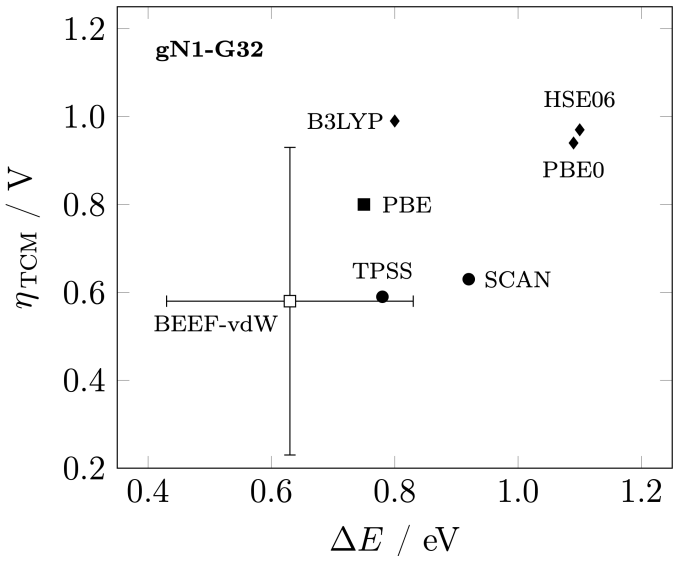

Figure 5: Thermochemical overpotentials η_{TCM} for 3.1% N-doped graphene calculated using various DFT functionals vs. the binding energy difference for the O adatom, ΔE, from column "optimized" in table 1. The general trend is that functionals giving a more accurate estimate of ΔE give higher values of the onset potential η_{TCM} . GGA: squares; meta-GGA: circles; hybrid functionals: diamonds.

for graphene-based materials. Care should be taken in the choice of functional if correct description of the *O intermediate is crucial; there, the B3LYP functional is less accurate. The η_{TCM} value of *ca.* 1.0 V obtained with the HSE06 functional is significantly higher than values published previously, as discussed above in the introduction.

When the dopant concentration is doubled to 6.2% the electronic structure of NG calculated with HSE06 shows interesting features. The calculated spin density is illustrated in figure 3 and shows non-zero net magnetization as well. This is in agreement with experiments which show that certain dopant cluster arrangements lead to a ferromagnetic ground state with non-zero magnetization.[74] However, in the GGA calculations, no net magnetic moment is obtained. This result indicates that GGA functionals fail to describe some fundamental

aspects of the electronic structure of this material.

Using the HSE06 functional, the binding strength of all ORR intermediates increases when the dopant concentration is doubled, with the largest increase obtained for *O. This leads to a decrease of η_{TCM} to 0.72 V, with *OOH reduction still remaining the potential determining step. In the calculations using PBE and BEEF-vdW, the potential determining step is the reduction of *O. The hybrid functionals and GGA functionals, therefore, give quite different trends for ORR when the dopant concentration is 6.2% even though the estimated overpotential is quite similar.

3.2 B. Finite flake models

Calculated η_{TCM} for finite model systems similar to those used in several previous studies[27,28,75,76] are shown in figure 6. In particular, the calculations are performed for a 54-atomic NG flake akin to the model used by Jiao and co-workers[28] (see figure S6) where the dopant concentration is 2.4 %. Using the PBE0 functional, a η_{TCM} value of 0.62 V is obtained. These results are noteworthy because the η_{TCM} values obtained this way are significantly lower than results for the periodic model systems at 3.1 % dopant concentration (0.62 V *vs.* 0.94 V with PBE0). Results from the periodic and molecular flake models are, therefore, not consistent since in the periodic case, a trend was established relating increasing dopant concentration to lower η_{TCM} values. Furthermore, the size of the periodic model is shown to be converged with regards to the adsorption energy values of ORR intermediates as shown in the figure S1. Reducing the dopant concentration of the periodic model system does not change the obtained η_{TCM} value. In the following, two potential causes of this deviation between molecular and periodic model systems are investigated in more detail, finite size effects and geometric distortion of the flake models.

To study the influence of finite size effects in more detail, adsorption energy calculations of ORR intermediates are performed using the PBE and PBE0 functionals on a set of hydrogen-terminated models generated from the periodic size convergence study shown in figure 6.

These models therefore retain the atomic configurations of the periodic structures. Only the hydrogen atoms are allowed to relax during the calculations. Figure 6 **a** shows the obtained adsorption energy trends as a function of the flake size. Since all the flake models contain

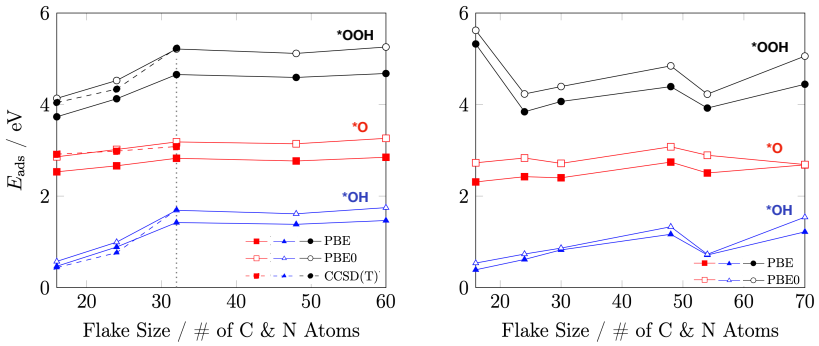

Figure 6: Adsorption energy of the *O, *OH and *OOH for flakes containing one N atom as a function of the total number of atoms in the flake. Left: Flakes shaped as the simulation cell used in the periodic calculations but capped with hydrogen atoms. The atomic coordinates are fixed as in the relaxed periodic configurations except that the capping hydrogen atoms are allowed to relax. High-level, wave function based DLPNO-CCSD(T) calculations show that the PBE0 functional gives more accurate results than PBE. Right: Round or diamond-shaped flakes where all atom coordinates are allowed to change as the energy is minimized.

one N atom, the dopant concentration decreases as a function of the flake size. In order to test the accuracy of the DFT functionals, high level wave function based calculations are performed and treated as benchmark results. DLPNO-CCSD(T) calculations are performed for flakes of up to 32 atoms. The results confirm the PBE0 functional to be most accurate for this application. The flakes in this set show similar convergence behavior to the periodic models but admolecules are overall less strongly bound compared to the periodic calculations with HSE06. This decreased binding strength results in a very high η_{TCM} value of *ca.* 1.7 V in case of the converged 32-atomic model. It is suggested that this deviation is a result of finite size effects modifying the adsorption energetics. Note that the different choice of basis set can influence this comparison as well but the difference between LCAO and PW showcased by Janesko and co-workers[30] is not large enough to fully account for the *ca.* 1 eV

increase in adsorption energy of the *OOH intermediate on the flake model compared to the periodic calculation.

The second set of calculations is performed on round and diamond-shaped molecular flakes of increasing size. They are not generated from periodic models and the atomic coordinates are not constrained in any way. These models also contain only one dopant atom. Strong deformation of the flakes is observed during energy minimzation, see figure S10. Adsorption energy values as a function of the flake size are shown in figure 6 **b**. Unlike for the flake models derived from periodic configurations of the atoms, no obvious convergence trend is observed with regards to the flake size. Adsorption energy values fluctuate by as much as 0.8 eV up to a flake size of 70 C & N atoms, at which point hybrid calculations start to become too computationally demanding. Notably, the 54 atom flake, which was used to calculate the η_{TCM} values at the start of this section, shows strong binding of ORR intermediates compared to the flakes derived from periodic models and therefore produces a small η_{TCM}. Overall, the results show that geometric distortions of the flakes affect the calculated adsorption energy in unpredictable ways.

Lastly, η_{TCM} values are calculated for these two sets of finite NG models and the results are shown in Figure 7. Free energy diagrams are shown in figures S8 and S9. For this

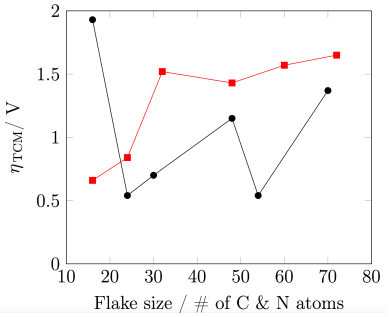

Figure 7: Estimated η_{TCM} for round and diamond-shaped flakes allowed to fully relax during calculations and flakes with fixed geometry generated from (relaxed) periodic models that are capped with hydrogen atoms.

comparison, only the electronic ground state energy values are considered since ZPE and entropic contributions do not change the trends. The η_{TCM} trends in figure 7 directly correspond to changes of the *OOH adsorption energy values in figure 6. This relationship is a result of *OOH formation being the potential determining step in all the models. It is noteworthy that for the round and diamond-shaped systems, which are not generated from periodic systems, the flakes with 24 and 54 C and N atoms give rise to the lowest η_{TCM}. These two models are round whereas the others are diamond shaped, see figure S6. The shape of the model therefore seems to influence its thermochemistry significantly. This does not appear to be the case for the models generated from periodic models, even though the periodic models presented in the size convergence study (see figure S1) also vary in their aspect ratio.

4 Discussion

In this study, the accuracy of various density functionals is assessed for adsorption of oxygen-containing adspecies on graphene-based materials. The thermochemical overpotentials η_{TCM} for the associative $4e^-$ ORR mechanism on a periodic NG model system are calculated with GGA, meta-GGA and hybrid density functionals. Results indicate that GGA functionals underestimate η_{TCM} by up to 0.4 V when the dopant concentration is low, 3.1%. The hybrid PBE0 and HSE06 functionals which have been shown to give more accurate estimates of the binding of an O adatom on pure graphene as compared to DMC results, give a larger estimate of the overpotential, of 1.0 V. The meta-GGA functionals, TPSS and SCAN, give values of the overpotential that are similar to the ones obtained from GGA functionals. Bayesian error estimation with the BEEF-vdW functional produces a large uncertainty of $\Delta\eta_{\mathrm{TCM}} \approx 0.8$ V indicating that the GGA functional form is unreliable. It should be noted, however, that this error estimate does not take into account systematic errors in the GGA functional form, such as the self-interaction error, which is shown here to be responsible

for the shortcomings of GGA in calculations of the O adatom binding on graphene. The *OOH intermediate can be further stabilized by increasing the dopant concentration, which decreases η_{TCM} obtained by HSE06 to 0.72 V. This trend is opposite to the GGA results where the reduction of *O becomes the potential determining step. The trends obtained with GGA functionals can therefore be quite different from the trends obtained with hybrid functionals for this reaction.

It is clear from these studies that hybrid functionals give more accurate results than GGA or meta-GGA functionals. The main uncertainty that remains is the effect of solvation, *i.e.* the presence of the aqueous electrolyte and in particular hydrogen bonding of the admolecules with water molecules. Various different estimates of the shift in free energy of ORR intermediates due to the presence of water have been presented in the literature. The classical dynamics simulations of Yu *et al.*[14] give a lowering of the binding free energy of all the intermediates by about 0.5 eV, but the calculations of Reda *et al.*[19] using ice layers indicate a lowering of 0.18 eV for *OOH and *OH and about twice as much for *O. Such contributions from solvation can change the estimated η_{TCM} significantly. If the free energy of *OOH is lowered by 0.2 eV, the η_{TCM} obtained from calculations where the formation of *OOH is the potential determining step is reduced by 0.2 V. For example, the η_{TCM} obtained from the HSE06 functional becomes *ca.* 0.8 V for the 3.1% doping concentration.

Similarly, for the higher dopant concentration of 6.2 %, the η_{TCM} value obtained with HSE06 is reduced from 0.72 V to 0.54 V, which is in the same range as commercial Pt catalysts. Figure S4 shows free energy diagrams with and without solvation contributions for the lower dopant concentration, where the solvation effect estimated by Reda *et al.* is applied.

Ultimately, extensive sampling of solvent configurations around the adsorbate taking into account the electrochemical environment is required to refine the calculated estimates of the overpotential in ORR. Furthermore, the effect of free energy barriers in the elementary steps may need to be taken into account instead of just the thermodynamics of the intermediates.

The simulations of electrochemical systems is a challenging but rapidly advancing field and further development of the simulation methodology will in the future make more accurate estimates of the electrochemical overpotential possible.

Lastly, doped molecular flakes are investigated. The η_{TCM} from flake models which retain the atomic configuration of a periodic model system is larger than 1.0 V, indicating that quantum size effects strongly decrease adsorption strength for all ORR intermediates. However, for a set of typical round and diamond-shaped flakes, strong geometric distortion during relaxation is observed. This leads to erratic jumps in the adsorption energetics of ORR intermediates for different flake sizes and shapes.

Further research using hybrid DFT functionals is required to explore the debated adsorption mode of O_2 and kinetic aspects of ORR on NG. Edge-effects, the influence of geometric distortions like the Stone-Wales defect, and the activity of B-doped graphene models should be re-investigated using periodic model systems and the HSE06 functional to confirm or correct previously published trends. Finally, solvation contributions, which are found to affect adsorption free energy values significantly, need to be obtained using rigorous sampling of solvent configurations and the explicit electrode potential needs to be taken into account.

Acknowledgement

This work was supported by the Icelandic Research Fund. BK thanks the University of Iceland Research Fund for a doctoral fellowship. Dr. Cheng-Rong Hsing and Prof. Mei-Yin Chou are acknowledged for providing graphene geometries and Dr. Yan Jiao is acknowledged for providing graphene flake geometries used in their respective studies. Dr. Maxime Van den Bossche is thanked for fruitful discussions. The calculations were performed at the Icelandic Research High Performance Computing center at the University of Iceland.

Supporting Information Available

Data on adsorption energy calculations, vibrational frequencies and resulting free energy corrections, as well as a list of all adsorption configurations for ORR intermediates can be found in the Supporting Information.

References

(1) Zhang, J.; Xia, Z.; Dai, L. Carbon-based electrocatalysts for advanced energy conversion and storage. *Sci. Adv.* **2015**, *1*, e1500564.

(2) Hu, C.; Dai, L. Carbon-Based Metal-Free Catalysts for Electrocatalysis beyond the ORR. **2016**, *55*, 11736–11758.

(3) Sturala, J.; Luxa, J.; Pumera, M.; Sofer, Z. Chemistry of Graphene Derivatives: Synthesis, Applications, and Perspectives. **2018**, *24*, 5992–6006.

(4) Ge, X.; Sumboja, A.; Wuu, D.; An, T.; Li, B.; Goh, F. W. T.; Hor, T. S. A.; Zong, Y.; Liu, Z. Oxygen Reduction in Alkaline Media: From Mechanisms to Recent Advances of Catalysts. *ACS Catal.* **2015**, *5*, 4643–4667.

(5) Qu, L.; Liu, Y.; Baek, J.-B.; Dai, L. Nitrogen-Doped Graphene as Efficient Metal-Free Electrocatalyst for Oxygen Reduction in Fuel Cells. *ACS Nano* **2010**, *4*, 1321–1326.

(6) Wang, H.; Maiyalagan, T.; Wang, X. Review on Recent Progress in Nitrogen-Doped Graphene: Synthesis, Characterization, and Its Potential Applications. *ACS Catal.* **2012**, *2*, 781–794.

(7) Hummers, W. S.; Offeman, R. E. Preparation of Graphitic Oxide. *J. Am. Chem. Soc.* **1958**, *80*, 1339–1339.

(8) Marcano, D. C.; Kosynkin, D. V.; Berlin, J. M.; Sinitskii, A.; Sun, Z.; Slesarev, A.; Alemany, L. B.; Lu, W.; Tour, J. M. Improved Synthesis of Graphene Oxide. *ACS Nano* **2010**, *4*, 4806–4814.

(9) Wang, L.; Ambrosi, A.; Pumera, M. "Metal-Free" Catalytic Oxygen Reduction Reaction on Heteroatom-Doped Graphene is Caused by Trace Metal Impurities. *Angew. Chem. Int. Ed.* **2013**, *52*, 13818–13821.

(10) Ambrosi, A.; Chua, C. K.; Khezri, B.; Sofer, Z.; Webster, R. D.; Pumera, M. Chemically reduced graphene contains inherent metallic impurities present in parent natural and synthetic graphite. *PNAS* **2012**, *109*, 12899–12904.

(11) Masa, J.; Zhao, A.; Xia, W.; Sun, Z.; Mei, B.; Muhler, M.; Schuhmann, W. Trace metal residues promote the activity of supposedly metal-free nitrogen-modified carbon catalysts for the oxygen reduction reaction. *Electrochem. Comm.* **2013**, *34*, 113–116.

(12) Ikeda, T.; Boero, M.; Huang, S.-F.; Terakura, K.; Oshima, M.; Ozaki, J.-i. Carbon Alloy Catalysts: Active Sites for Oxygen Reduction Reaction. *J. Phys. Chem. C* **2008**, *112*, 14706–14709.

(13) Okamoto, Y. First-principles molecular dynamics simulation of O2 reduction on nitrogen-doped carbon. *Appl. Surf. Sci.* **2009**, *256*, 335–341.

(14) Yu, L.; Pan, X.; Cao, X.; Hu, P.; Bao, X. Oxygen reduction reaction mechanism on nitrogen-doped graphene: A density functional theory study. *J. Catal.* **2011**, *282*, 183–190.

(15) Studt, F. The Oxygen Reduction Reaction on Nitrogen-Doped Graphene. *Catal. Lett.* **2013**, *143*, 58–60.

(16) Nørskov, J. K.; Rossmeisl, J.; Logadottir, A.; Lindqvist, L.; Kitchin, J. R.; Bligaard, T.;

Jónsson, H. Origin of the Overpotential for Oxygen Reduction at a Fuel-Cell Cathode. *J. Phys. Chem. B* **2004**, *108*, 17886–17892.

(17) Wellendorff, J.; Lundgaard, K. T.; Møgelhøj, A.; Petzold, V.; Landis, D. D.; Nørskov, J. K.; Bligaard, T.; Jacobsen, K. W. Density functionals for surface science: Exchange-correlation model development with Bayesian error estimation. *Phys. Rev. B* **2012**, *85*, 235149.

(18) Skúlason, E.; Jónsson, H. Atomic scale simulations of heterogeneous electrocatalysis: recent advances. *Advances in Physics X* **2017**, *84*, 481.

(19) Reda, M.; Hansen, H. A.; Vegge, T. DFT study of stabilization effects on N-doped graphene for ORR catalysis. *Catal. Today* **2018**, *312*, 118–125.

(20) Perdew, J. P.; Burke, K.; Ernzerhof, M. Generalized Gradient Approximation Made Simple. *Phys. Rev. Lett.* **1996**, *77*, 3865–3868.

(21) Li, M.; Zhang, L.; Xu, Q.; Niu, J.; Xia, Z. N-doped graphene as catalysts for oxygen reduction and oxygen evolution reactions: Theoretical considerations. *J. Catal.* **2014**, *314*, 66–72.

(22) Gíslason, P. M.; Skúlason, E. Catalytic trends of nitrogen doped carbon nanotubes for oxygen reduction reaction. *Nanoscale* **2019**, *11*, 18683–18690.

(23) Hammer, B.; Hansen, L. B.; Nørskov, J. K. Improved adsorption energetics within density-functional theory using revised Perdew-Burke-Ernzerhof functionals. *Phys. Rev. B* **1999**, *59*, 7413–7421.

(24) Sinthika, S.; Waghmare, U. V.; Thapa, R. Structural and Electronic Descriptors of Catalytic Activity of Graphene-Based Materials: First-Principles Theoretical Analysis. *Small* **2018**, *14*, 1703609.

(25) Stephens, P. J.; Devlin, F. J.; Chabalowski, C. F.; Frisch, M. J. Ab Initio Calculation of Vibrational Absorption and Circular Dichroism Spectra Using Density Functional Force Fields. *J. Phys. Chem.* **1994**, *98*, 11623–11627.

(26) Kim, K.; Jordan, K. D. Comparison of Density Functional and MP2 Calculations on the Water Monomer and Dimer. *J. Phys. Chem.* **1994**, *98*, 10089–10094.

(27) Zhang, L.; Xia, Z. Mechanisms of Oxygen Reduction Reaction on Nitrogen-Doped Graphene for Fuel Cells. *J. Phys. Chem. C* **2011**, *115*, 11170–11176.

(28) Jiao, Y.; Zheng, Y.; Jaroniec, M.; Qiao, S. Z. Origin of the Electrocatalytic Oxygen Reduction Activity of Graphene-Based Catalysts: A Roadmap to Achieve the Best Performance. *J. Am. Chem. Soc.* **2014**, *136*, 4394–4403.

(29) Hsing, C. R.; Wei, C. M.; Chou, M. Y. Quantum Monte Carlo investigations of adsorption energetics on graphene. *J. Phys. Condens. Matter* **2012**, *24*, 395002.

(30) Janesko, B. G.; Barone, V.; Brothers, E. N. Accurate Surface Chemistry beyond the Generalized Gradient Approximation: Illustrations for Graphene Adatoms. *J. Chem. Theory Comput.* **2013**, *9*, 4853–4859.

(31) Perdew, J. P.; Ernzerhof, M.; Burke, K. Rationale for mixing exact exchange with density functional approximations. *J. Chem. Phys.* **1996**, *105*, 9982–9985.

(32) Adamo, C.; Barone, V. Toward reliable density functional methods without adjustable parameters: The PBE0 model. *J. Chem. Phys.* **1999**, *110*, 6158–6170.

(33) Krukau, A. V.; Vydrov, O. A.; Izmaylov, A. F.; Scuseria, G. E. Influence of the exchange screening parameter on the performance of screened hybrid functionals. *J. Chem. Phys.* **2006**, *125*, 224106.

(34) Blöchl, P. E. Projector augmented-wave method. *Phys. Rev. B* **1994**, *50*, 17953–17979.

(35) Kresse, G.; Joubert, D. From ultrasoft pseudopotentials to the projector augmented-wave method. *Phys. Rev. B* **1999**, *59*, 1758–1775.

(36) Furche, F.; Perdew, J. P. The performance of semilocal and hybrid density functionals in 3d transition-metal chemistry. *J. Chem. Phys.* **2006**, *124*, 044103.

(37) Sun, J.; Ruzsinszky, A.; Perdew, J. Strongly Constrained and Appropriately Normed Semilocal Density Functional. *Phys. Rev. Lett.* **2015**, *115*, 036402.

(38) Klimeš, J.; Bowler, D. R.; Michaelides, A. Chemical accuracy for the van der Waals density functional. *J. Phys.: Condens. Matter* **2010**, *22*, 022201.

(39) Klimeš, J.; Bowler, D. R.; Michaelides, A. Van der Waals density functionals applied to solids. *Phys. Rev. B* **2011**, *83*, 195131.

(40) Kresse, G.; Hafner, J. Ab initio molecular dynamics for liquid metals. *Phys. Rev. B* **1993**, *47*, 558–561.

(41) Kresse, G.; Hafner, J. Ab initio molecular-dynamics simulation of the liquid-metal–amorphous-semiconductor transition in germanium. *Phys. Rev. B* **1994**, *49*, 14251–14269.

(42) Kresse, G.; Furthmüller, J. Efficiency of ab-initio total energy calculations for metals and semiconductors using a plane-wave basis set. *Comput. Mater. Sci.* **1996**, *6*, 15–50.

(43) Kresse, G.; Furthmüller, J. Efficient iterative schemes for ab initio total-energy calculations using a plane-wave basis set. *Phys. Rev. B* **1996**, *54*, 11169–11186.

(44) Pinski, P.; Riplinger, C.; Valeev, E. F.; Neese, F. Sparse maps—A systematic infrastructure for reduced-scaling electronic structure methods. I. An efficient and simple linear scaling local MP2 method that uses an intermediate basis of pair natural orbitals. *J. Chem. Phys.* **2015**, *143*, 034108.

(45) Riplinger, C.; Pinski, P.; Becker, U.; Valeev, E. F.; Neese, F. Sparse maps—A systematic infrastructure for reduced-scaling electronic structure methods. II. Linear scaling domain based pair natural orbital coupled cluster theory. *J. Chem. Phys.* **2016**, *144*, 024109.

(46) Guo, Y.; Sivalingam, K.; Valeev, E. F.; Neese, F. SparseMaps—A systematic infrastructure for reduced-scaling electronic structure methods. III. Linear-scaling multireference domain-based pair natural orbital N-electron valence perturbation theory. *J. Chem. Phys.* **2016**, *144*, 094111.

(47) Pavošević, F.; Pinski, P.; Riplinger, C.; Neese, F.; Valeev, E. F. SparseMaps—A systematic infrastructure for reduced-scaling electronic structure methods. IV. Linear-scaling second-order explicitly correlated energy with pair natural orbitals. *J. Chem. Phys.* **2016**, *144*, 144109.

(48) Pavošević, F.; Peng, C.; Pinski, P.; Riplinger, C.; Neese, F.; Valeev, E. F. SparseMaps—A systematic infrastructure for reduced scaling electronic structure methods. V. Linear scaling explicitly correlated coupled-cluster method with pair natural orbitals. *J. Chem. Phys.* **2017**, *146*, 174108.

(49) Zhong, S.; Barnes, E. C.; Petersson, G. A. Uniformly convergent n-tuple-zeta augmented polarized (nZaP) basis sets for complete basis set extrapolations. I. Self-consistent field energies. *J. Chem. Phys.* **2008**, *129*, 184116.

(50) Neese, F.; Valeev, E. F. Revisiting the Atomic Natural Orbital Approach for Basis Sets: Robust Systematic Basis Sets for Explicitly Correlated and Conventional Correlated ab initio Methods? *J. Chem. Theory Comput.* **2011**, *7*, 33–43.

(51) Helgaker, T.; Klopper, W.; Koch, H.; Noga, J. Basis-set convergence of correlated calculations on water. *J. Chem. Phys.* **1997**, *106*, 9639–9646.

(52) Dunning, T. H. Gaussian basis sets for use in correlated molecular calculations. I. The atoms boron through neon and hydrogen. *J. Chem. Phys.* **1989**, *90*, 1007–1023.

(53) Weigend, F.; Ahlrichs, R. Balanced basis sets of split valence, triple zeta valence and quadruple zeta valence quality for H to Rn: Design and assessment of accuracy. *Phys. Chem. Chem. Phys.* **2005**, *7*, 3297–3305.

(54) Kossmann, S.; Neese, F. Efficient Structure Optimization with Second-Order Many-Body Perturbation Theory: The RIJCOSX-MP2 Method. *J. Chem. Theory Comput.* **2010**, *6*, 2325–2338.

(55) Weigend, F. Hartree–Fock exchange fitting basis sets for H to Rn †. *J. Comput. Chem.* **2008**, *29*, 167–175.

(56) Weigend, F.; Köhn, A.; Hättig, C. Efficient use of the correlation consistent basis sets in resolution of the identity MP2 calculations. *J. Chem. Phys.* **2002**, *116*, 3175–3183.

(57) Neese, F. The ORCA program system. *Wiley Interdiscip. Rev. Comput. Mol. Sci.* **2012**, *2*, 73–78.

(58) Neese, F. Software update: the ORCA program system, version 4.0. *Wiley Interdiscip. Rev. Comput. Mol. Sci.* **2018**, *8*, e1327.

(59) Perdew, J. P.; Zunger, A. Self-interaction correction to density-functional approximations for many-electron systems. *Phys. Rev. B* **1981**, *23*, 5048–5079.

(60) Enkovaara, J.; Rostgaard, C.; Mortensen, J. J.; Chen, J.; Du\lak, M.; Ferrighi, L.; Gavnholt, J.; Glinsvad, C.; Haikola, V.; Hansen, H. A.; Kristoffersen, H. H.; Kuisma, M.; Larsen, A. H.; Lehtovaara, L.; Ljungberg, M.; Lopez-Acevedo, O.; Moses, P. G.; Ojanen, J.; Olsen, T.; Petzold, V.; Romero, N. A.; Stausholm-Møller, J.; Strange, M.; Tritsaris, G. A.; Vanin, M.; Walter, M.; Hammer, B.; Häkkinen, H.; Madsen, G. K. H.; Nieminen, R. M.; Nørskov, J. K.; Puska, M.; Rantala, T. T.; Schiøtz, J.;

Thygesen, K. S.; Jacobsen, K. W. Electronic structure calculations with GPAW: a real-space implementation of the projector augmented-wave method. *J. Phys. Condens. Matter* **2010**, *22*, 253202.

(61) Klüpfel, S.; Klüpfel, P.; Jónsson, H. Importance of complex orbitals in calculating the self-interaction-corrected ground state of atoms. *Phys. Rev. A* **2011**, *84*, 050501.

(62) Lehtola, S.; Jónsson, H. Unitary Optimization of Localized Molecular Orbitals. *J. Chem. Theory Comput.* **2013**, *9*, 5365–5372.

(63) Lehtola, S.; Jónsson, E. O.; Jónsson, H. Effect of Complex-Valued Optimal Orbitals on Atomization Energies with the Perdew–Zunger Self-Interaction Correction to Density Functional Theory. *J. Chem. Theory Comput.* **2016**, *12*, 4296–4302.

(64) Klüpfel, S.; Klüpfel, P.; Jónsson, H. The effect of the Perdew-Zunger self-interaction correction to density functionals on the energetics of small molecules. *J. Chem. Phys.* **2012**, *137*, 124102.

(65) Monkhorst, H. J. Special points for Brillouin-zone integrations. *Phys. Rev. B* **1976**, *13*, 5188–5192.

(66) Brandenburg, J. G.; Bates, J. E.; Sun, J.; Perdew, J. P. Benchmark tests of a strongly constrained semilocal functional with a long-range dispersion correction. *Phys. Rev. B* **2016**, *94*, 115144.

(67) Chase, Jr., M. W. NIST-JANAF Thermochemical Tables, 4th ed. *J. Phys. Chem. Ref. Data* **1998**, *Monograph 9*, 1–1951.

(68) Klüpfel, S.; Klüpfel, P.; Jónsson, H. The effect of the Perdew-Zunger self-interaction correction to density functionals on the energetics of small molecules. *J. Chem. Phys.* **2012**, *137*, 124102.

(69) Blöchl, P. E. First-principles calculations of defects in oxygen-deficient silica exposed to hydrogen. *Phys. Rev. B* **2000**, *62*, 6158–6179.

(70) Peng, H.; Yang, Z.-H.; Perdew, J. P.; Sun, J. Versatile van der Waals Density Functional Based on a Meta-Generalized Gradient Approximation. *Phys. Rev. X* **2016**, *6*, 041005.

(71) Grimme, S.; Antony, J.; Ehrlich, S.; Krieg, H. A consistent and accurate ab initio parametrization of density functional dispersion correction (DFT-D) for the 94 elements H-Pu. *J. Chem. Phys* **2010**, *132*, 154104.

(72) Grimme, S.; Ehrlich, S.; Goerigk, L. Effect of the damping function in dispersion corrected density functional theory. *J. Comput. Chem.* **2011**, *32*, 1456–1465.

(73) Moellmann, J.; Grimme, S. DFT-D3 Study of Some Molecular Crystals. *J. Phys. Chem. C* **2014**, *118*, 7615–7621.

(74) Błoński, P.; Tuček, J.; Sofer, Z.; Mazánek, V.; Petr, M.; Pumera, M.; Otyepka, M.; Zbořil, R. Doping with Graphitic Nitrogen Triggers Ferromagnetism in Graphene. *J. Am. Chem. Soc.* **2017**, *139*, 3171–3180.

(75) Sidik, R. A.; Anderson, A. B.; Subramanian, N. P.; Kumaraguru, S. P.; Popov, B. N. O $_2$ Reduction on Graphite and Nitrogen-Doped Graphite: Experiment and Theory. *J. Phys. Chem. B* **2006**, *110*, 1787–1793.

(76) Zhang, L.; Niu, J.; Dai, L.; Xia, Z. Effect of Microstructure of Nitrogen-Doped Graphene on Oxygen Reduction Activity in Fuel Cells. *Langmuir* **2012**, *28*, 7542–7550.

Graphical TOC Entry

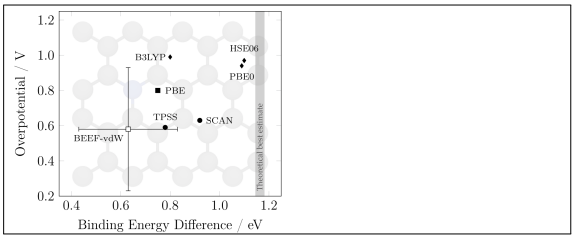

Calculated overpotential for ORR on 3.1% N doped graphene using various energy functionals as a function of the calculated energy difference of oxygen adatom at on-top site and bridge site. The best estimate of the binding energy difference obtained from quantum Monte Carlo simulations is indicated with a gray area. A standard deviation error bar obtained for both quantities using the BEEF-vdW functional are also shown.

Supporting Information for:

Accuracy Assessment of Density Functionals for the Oxygen Reduction Reaction on Doped Graphenes

Björn Kirchhoff,[†,‡] Aleksei Ivanov,[†] Egill Skúlason,[¶] Timo Jacob,[‡,§,‖] Donato Fantauzzi,[†] and Hannes Jónsson[*,†]

†*Science Institute and Faculty of Physical Sciences, University of Iceland, VR-III, Hjarðarhagi 2, 107 Reykjavík, Iceland*

‡*Institute of Electrochemistry, Ulm University, Albert-Einstein-Allee 47, 89081 Ulm, Germany*

¶*Science Institute and Faculty of Industrial Engineering, Mechanical Engineering and Computer Science, University of Iceland, VR-III, Hjarðarhagi 2, 107 Reykjavík, Iceland*

§*Helmholtz-Institute Ulm (HIU) Electrochemical Energy Storage, Helmholtz-Straße 16, 89081 Ulm, Germany*

‖*Karlsruhe Institute of Technology (KIT), P.O. Box 3640, 76021 Karlsruhe, Germany*

E-mail: hj@hi.is

Table 1: C–C distances ($d_{\mathrm{C–C}}$) and interlayer distances d_{layers} of $P6_3/mmc$ graphite bulk cells optimized at the respective level of theory compared to experimental values.

Position	$d_{\mathrm{C–C}}$ / Å	d_{layers} / Å
Experimental[1,2]	1.420	3.335
PBE	1.424	3.929
PBE-D3	1.423	3.343
BEEF-vdW	1.423	3.630
TPSS	1.423	4.380
SCAN	1.416	3.441
SCAN-rVV10	1.416	3.343
PBE0	1.414	4.520
HSE06	1.415	3.766
HSE06-D3	1.414	3.351
B3LYP	1.419	3.922

1 Optimized cell parameters

2 Supercell size convergence study

Supercell size convergence for Nitrogen-doped graphene (NG, Figure 1). Supercells always included one graphitic dopant; the dopant concentration therefore is not static. All supercells were converged with respect to the $\boldsymbol{k}$ grid before evaluation. Note that HSE06 values are obtained using the $\boldsymbol{k}$ grid reduction scheme for the exact exchange (EE) step outlined in the main manuscript. Also, adsorption energy values given here may vary from the final reported values since they were obtained with less strict precision parameters. The NG model seems to require a 32 atomic cell in particular for converged *OH results.

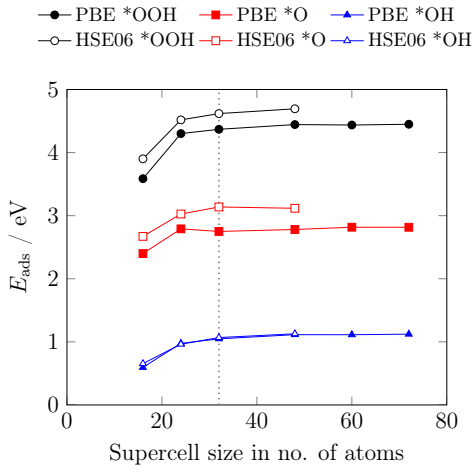

Figure 1: Supercell size convergence study for cells containing 1 graphitic Nitrogen atom at the PBE and HSE06 level, with the latter using the $\boldsymbol{k}$ point reduction scheme outlined in main MS.

3 $\boldsymbol{k}$ Grid convergence of η_{TCM}

We investigate the dependence of the thermodynamic reaction overpotentials η_{TCM} with respect to the $\boldsymbol{k}$ point grid for the PBE, SCAN, and HSE06 density functional approximations. The calculation parameters are the same as for the final reported values in the main manuscript. HSE06 values reported here used the full $\boldsymbol{k}$ grid for the HF step. Table 2 reports values for NG. Note that $\boldsymbol{k}$ grid convergence with SCAN difficult, showing decreasing η_{TCM}

Table 2: $\boldsymbol{k}$ grid convergence study for thermodynamic reaction overpotentials η_{TCM} on gN1-G32 in V.

	η_{TCM}			
Functional	$3\times3\times1$	$4\times4\times1$	$5\times5\times1$	$7\times7\times1$
PBE	0.84	—	0.80	0.81
SCAN	0.64	—	0.63	0.54
HSE06	1.03	0.98	0.97	—

up to the dense $7 \times 7 \times 1$ grid.

4 Plane wave energy cutoff convergence

The plane wave energy cutoff criterion is governed by the ENCUT tag in VASP input files. Figure 2 reports convergence of the total energy of the gN1-G32 model at the full HSE06 level.

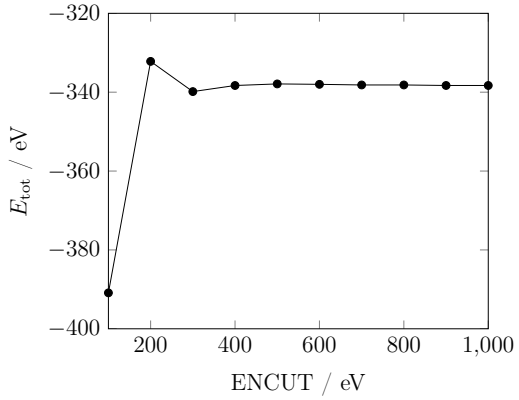

Figure 2: ENCUT convergence for the total energy of adsorbate-free gN1-G32 at the HSE06 level, using single-point calculations on relaxed geometry and a $5 \times 5 \times 1$ $\boldsymbol{k}$ grid.

5 Error estimation: exact exchange $\boldsymbol{k}$ point reduction scheme for hybrid DFT geometries

We evaluate the error introduced by the EE $\boldsymbol{k}$ point reduction scheme for hybrid calculations presented in and used throughout the main manuscript. Table 3 compares (purely electronic) adsorption energy values for HSE06 obtained by a) geometry optimization using the $\boldsymbol{k}$ reduction scheme and final single-point energy evaluation on the full grid (denoted HSE06*) and b) both geometry relaxation and final single-point energies on the full grid. We used

Table 3: Comparison of total electronic energy values obtained via the HF $\boldsymbol{k}$ point reduction scheme for geometry optimizations (HSE06*) and by full optimization at the HSE06 level (HSE06).

System	$E_{\mathrm{tot}}^{\mathrm{HSE06*}}$ / eV	$E_{\mathrm{tot}}^{\mathrm{HSE06}}$ / eV	ΔE_{tot} / eV
clean NG sheet	-334.8969	-334.9058	-0.0089
*O	-342.3237	-342.3298	-0.0062
*OH	-347.3367	-347.3434	-0.0067
*OOH	-353.4844	-353.4927	-0.0083

a $4 \times 4 \times 1$ $\boldsymbol{k}$ grid and an energy cutoff of 500 eV for this comparison. Note that the full optimization is extremely computationally demanding, making denser $\boldsymbol{k}$ grids unreasonable to use. The introduced error is *ca.* 0.01 eV, which is noticeable but overall one magnitude lower than that introduced by other factors such as the choice of functional.

6 Error estimation: constrained geometry *vs.* full phonon calculation

Tables 4 and 5 list the electronic energy values, free energy corrections and final adsorption free energy values obtained using constrained phonon calculations (backbone constrained, considered only contributions from the adsorbate) and a full phonon calculation (including contributions from the backbone) at the PBE level. Calculation of the adsorption free

Table 4: Thermodynamic corrections from constrained phonon calculation.

System	E_{tot} / eV	E_{ZPE} / eV	$T \cdot \Delta S$ / eV	G_{tot} / eV	G_{ads} / eV
gN1-G32	-293.464	—	—	—	—
*O	-298.163	0.083	0.049	-298.129	2.499
*OH	-303.274	0.392	0.062	-302.944	0.936
*OOH	-307.427	0.466	0.149	-307.110	3.933

energies used H_2O (-13.669 eV) and H_2 (-6.506 eV) as reference in both cases. When OP_T

Table 5: Thermodynamic corrections from full phonon calculation.

System	E_{tot} / eV	E_{ZPE} / eV	$T \cdot \Delta S$ / eV	G_{tot} / eV	G_{ads} / eV
gN1-G32	-293.464	5.288	0.394	-288.570	—
*O	-298.163	5.392	0.442	-293.213	2.521
*OH	-303.274	5.734	0.438	-297.978	1.008
*OOH	-307.427	5.811	0.509	-302.125	4.024

is calculated from these values, the disparity amounts to 0.04 V (0.29 V for the constrained *vs.* 0.33 V for the unconstrained calculation). We therefore suggest that the reported overpotentials are slightly underestimated throughout the manuscript as a result of this approximation.

7 Calculation of potential-dependent free energy diagrams

Free energy diagrams were constructed according to the method by Nørskov and co-workers.[3–5] The Standard Hydrogen Electrode (SHE) is defined so that

$$\mathrm{H_{2(g)}} \longleftrightarrow 2\,(\mathrm{H^{+}_{(aq)}} + \mathrm{e^{-}}) \tag{1}$$

holds true, which corresponds to reaction conditions of pH 0 in solution, $\mathrm{H_2}$ pressure of 1 bar, and room temperature (298.15 K). This allows to define the following reactions (2)–(4) to be in equilibrium at an electrode potential of $U = 0$,

$$2\,\mathrm{H_2O} + {}^{*} \quad \longleftrightarrow \quad {}^{*}\mathrm{OOH} + \frac{3}{2}\mathrm{H_2} \tag{2}$$

$$\mathrm{H_2O} + {}^{*} \quad \longleftrightarrow \quad {}^{*}\mathrm{OH} + \frac{1}{2}\mathrm{H_2} \tag{3}$$

$$\mathrm{H_2O} + {}^{*} \quad \longleftrightarrow \quad {}^{*}\mathrm{O} + \mathrm{H_2}\ , \tag{4}$$

whereby * denotes the lowest-energy adsorption position on the NG backbone. Within this approximation, the references are defined with respect to gas phase H_2 and H_2O, thus avoiding calculation of the notoriously difficult $^3O_2$ molecule or the radical $^{\cdot}OH$ and $^{\cdot}OOH$ species in isolation.

Assuming the associative pathway, the individual steps of the catalytic $4e^-$ ORR pathway on NG can therefore be defined, given in Equations (5) to (8), as

$$O_2 + {}^* + H^+ + e^- \longrightarrow {}^*OOH \tag{5}$$

$${}^*OOH + H^+ + e^- \longrightarrow {}^*O + H_2O \tag{6}$$

$${}^*O + H^+ + e^- \longrightarrow {}^*OH \tag{7}$$

$${}^*OH + H^+ + e^- \longrightarrow H_2O + {}^* \tag{8}$$

Thus, the following equations for the potential-dependent adsorption Gibbs free energies $\Delta G(U)$ of each reaction step[3] can be derived:

$$\Delta G_{OOH}(U) = (G_{OOH} + 2\,G_{H_2O}) - (G_{clean} + 3\,G_{H^+}) - 3\,eU \tag{9}$$

$$\Delta G_{O}(U) = (G_{O} + G_{H_2O}) - (G_{clean} + 2\,G_{H^+}) - 2\,eU \tag{10}$$

$$\Delta G_{OH}(U) = (G_{OH} + G_{H_2O}) - (G_{clean} + G_{H^+}) - eU \tag{11}$$

$$\tag{12}$$

Gibbs free energy results are calculated as $G_x(U_0) = E_x + E_{ZPE} + T \cdot S_x$, with the total SCF energy from DFT calculations E_x, zero-point energy E_{ZPE} and the entropic correction $T \cdot S_x$ at room temperature $T = 298.15K$ and pH 0 calculated from harmonic vibrational frequency analysis.

8 Free energy diagrams

Free energy diagrams at 0 V and at the onset and at the ORR onset potential are constructed for the PBE, BEEF-vdW, TPSS, SCAN, PBE0, HSE06, and B3LYP functionals, see Figure 3.

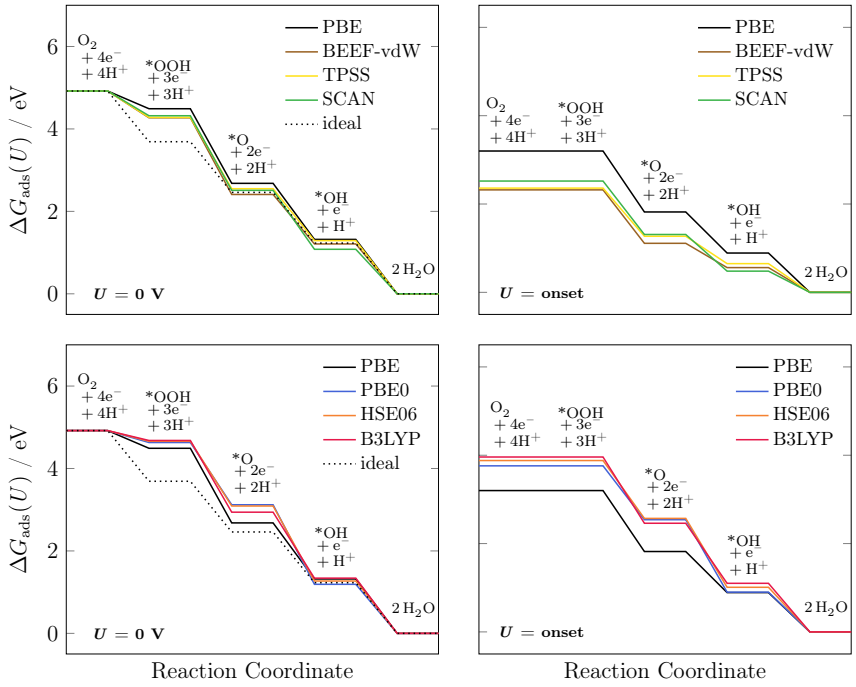

Figure 3: Free energy diagrams for gN1-G32 at 0 V (left) and at the onset electrode potential (right) obtained using GGA and meta-GGA functionals (top) as well as PBE and hybrid functionals (bottom). The ideal ORR catalyst with a free energy change of 1.23 V at each reaction step is shown as a dashed line.

9 Influence of dispersion correction

Table 6: Calculated total energy difference $\Delta E = E_{\mathrm{tot}}^{\mathrm{top}} - E_{\mathrm{tot}}^{\mathrm{bridge}}$ of graphene sheets with top- and bridge-bound adatoms, using various DFT functionals, SIC, and DMC. For M point results, the relative deviation with respect to DMC is given in brackets. This table contains additional values for dispersion-corrected functionals not given in the main manuscript. Dispersion correction is found to play an insignificant role.

	ΔE_{D} / eV				
Method	Hsing[6,a]	M point[b]	full $\boldsymbol{k}$ grid[c]	opt. + full $\boldsymbol{k}$ grid[d]	Janesko[7,e]
DMC	1.360	–	–	–	–
SIC	–	1.47 (+8 %)	–	–	–
PBE0	–	1.29 (-5 %)	1.10	1.09	–
HSE06	–	1.28 (-6 %)	1.10	1.10	1.31
HSE06-D3	–	1.26 (-7 %)	1.26	1.05	–
B3LYP	–	0.99 (-27 %)	0.80	0.80	1.10
TPSS	–	0.97 (-29 %)	0.78	0.79	0.93
SCAN-rVV10	–	0.941 (-31 %)	0.959	0.923	–
SCAN	–	0.92 (-32 %)	0.96	0.92	–
PBE	0.74	0.92 (-32 %)	0.75	0.75	0.91
PBE-D3	–	0.91 (-33 %)	0.72	0.72	–
BEEF-vdW	–	0.82 (-40 %)	0.65	0.63 ± 0.20[f]	–

[a] M point evaluated for geometries provided by Hsing *et al.*[6]
[b] $5 \times 5 \times 1$ $\boldsymbol{k}$ grid evaluated for geometries provided by Hsing *et al.*[6]
[c] $5 \times 5 \times 1$ $\boldsymbol{k}$ grid evaluated for geometries optimized using the respective density functional.
[d] Value obtained from $M(0.5, 0)$ point DMC calculation.
[e] Standard deviation based on an ensemble size of 2000.

10 Reda *et al.* solvation contribution reproduction with HSE06

To complete the thermodynamic description of the models presented in this study, the influence of solvation on the stability of the ORR intermediates is considered. To this end, the influence of a single layer of 8 H_2O molecules (corresponds to $\theta = \frac{2}{3}$ monolayer) on the binding energy of the adsorbate is assessed. A single layer of water was recently found to give converged solvation energy results in a study by Reda *et al.* on a similar NG model system.[8] The solvation stabilizations obtained from the HSE06 functional in these calculations are summarized in Table 7. Figure 4 compares the resulting free energy diagrams to

Table 7: Solvation stabilization by 8 explicit H_2O molecules for ORR intermediates on NG. Negative values indicate stabilization.

	ΔE_{solv} / eV
Intermediate	gN1-G32p
*O	-0.38
*OH	-0.12
*OOH	-0.14

gas phase results from gN1-G32p. Inclusion of solvation stabilization in the free energy description presented above will lead to a reduction of the thermochemical overpotentials from 0.97 to 0.82 V. This is exclusively due to stabilization of the *OOH intermediate whose free energy governs the onset potential. Note that the *O intermediate experiences significant stabilization as well which could be significant for systems where the *O intermediate is the bottleneck step.

11 Illustrations of flake models

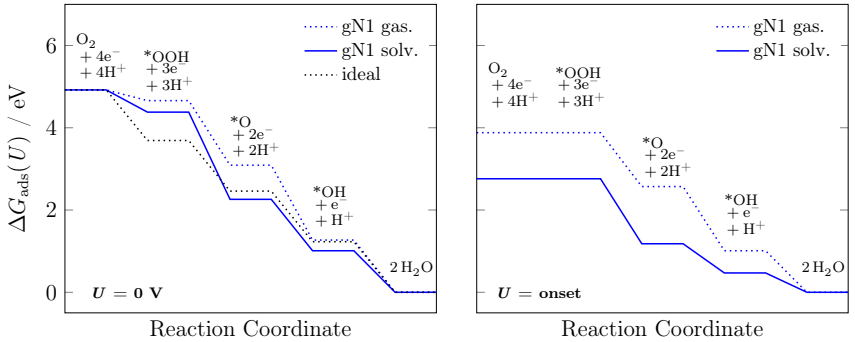

Figure 4: Free energy diagrams for gN1-G32p blue at 0V (left) and the onset electrode potential (right) obtained with HSE06. Gas.: pure gas phase values; solv.: including solvation correction from 8 explicit H_2O molecules.

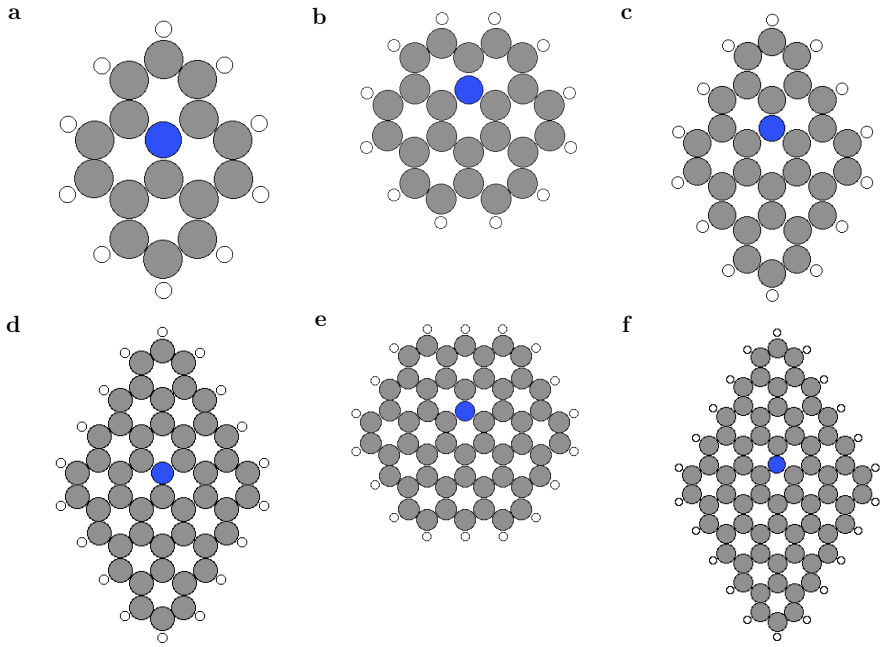

Figure 5: Illustration of unconstrained flake models with **a** 16, **b** 24, **c** 30, **d** 48, **e** 54, and **f** 70 C and N atoms.

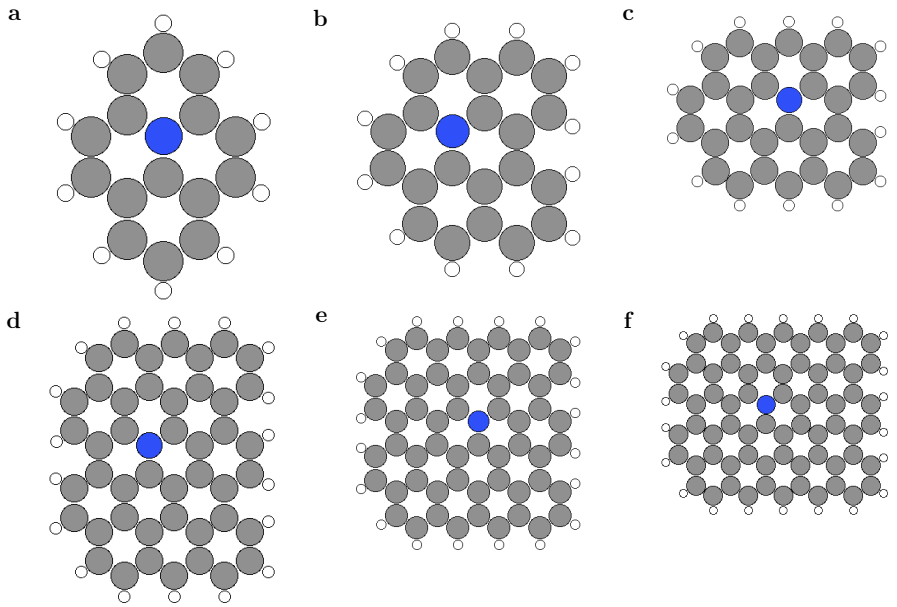

Figure 6: Illustration of flake models generated from periodic structures with **a** 16, **b** 24, **c** 32, **d** 48, **e** 60, and **f** 72 C and N atoms.

12 Free energy diagrams for flake models

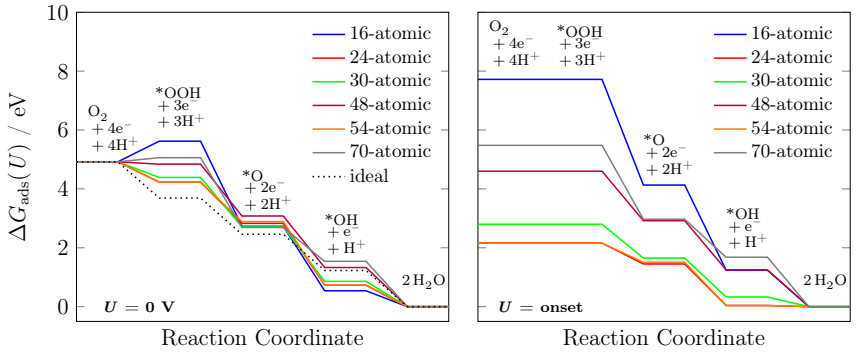

Figure 7: Free energy diagrams for round and diamond shaped flakes that are allowed to fully relax during the calculations.

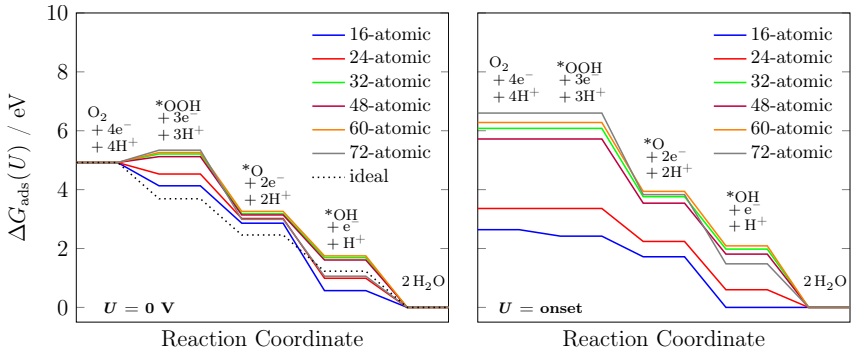

Figure 8: Free energy diagrams for flakes generated from periodic models and capped with hydrogen atoms. Only the hydrogen atoms are allowed to relax during the calculation while the C/N backbone is kept rigid in the atomic configuration of the periodic model system.

13 Deformation of unconstrained flake models

Unconstrained molecular flake models show strong deformation when adatoms are being placed on the surface and the structure is relaxed, see Figure 9.

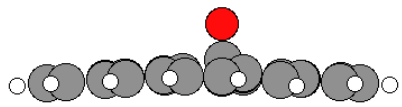

Figure 9: Exemplary illustration of deformation of a molecular flake model (30 atoms) after geometry relaxation in the presence of an O adatom.

References

(1) Cooper, D. R.; D'Anjou, B.; Ghattamaneni, N.; Harack, B.; Hilke, M.; Horth, A.; Majlis, N.; Massicotte, M.; Vandsburger, L.; Whiteway, E.; Yu, V. Experimental Review of Graphene. *ISRN Condens. Matter Phys.* **2012**, *2012*, 1–56.

(2) Delhaes, P. *Graphite and Precursors*; CRC Press, 2014.

(3) Nørskov, J. K.; Rossmeisl, J.; Logadottir, A.; Lindqvist, L.; Kitchin, J. R.; Bligaard, T.; Jónsson, H. Origin of the Overpotential for Oxygen Reduction at a Fuel-Cell Cathode. *J. Phys. Chem. B* **2004**, *108*, 17886–17892.

(4) Lima, F. H. B.; Zhang, J.; Shao, M. H.; Sasaki, K.; Vukmirovic, M. B.; Ticianelli, E. A.; Adzic, R. R. Catalytic Activity-d-Band Center Correlation for the O2 Reduction Reaction on Platinum in Alkaline Solutions. *J. Phys. Chem. C* **2007**, *111*, 404–410.

(5) Shao, M.; Liu, P.; Zhang, J.; Adzic, R. Origin of Enhanced Activity in Palladium Alloy Electrocatalysts for Oxygen Reduction Reaction. *J. Phys. Chem. B* **2007**, *111*, 6772–6775.

(6) Hsing, C. R.; Wei, C. M.; Chou, M. Y. Quantum Monte Carlo investigations of adsorption energetics on graphene. *J. Phys. Condens. Matter* **2012**, *24*, 395002.

(7) Janesko, B. G.; Barone, V.; Brothers, E. N. Accurate Surface Chemistry beyond the Generalized Gradient Approximation: Illustrations for Graphene Adatoms. *J. Chem. Theory Comput.* **2013**, *9*, 4853–4859.

(8) Reda, M.; Hansen, H. A.; Vegge, T. DFT study of stabilization effects on N-doped graphene for ORR catalysis. *Catal. Today* **2018**, *312*, 118–125.

Publication III

Flexible QM/MM Partitioning Algorithm based on Elastic Collisions of Molecules in Inner and Outer Regions

B. Kirchhoff, E. Ö. Jónsson, A. O. Dohn, T. Jacob, H. Jónsson*

Author contributions: Björn Kirchhoff programmed the SAFIRES code, performed all simulations and data analysis, and wrote the initial manuscript draft. Elvar Jónsson contributed mathematical notation to the manuscript. Asmus Dohn programmed the FIRES code used for comparison to SAFIRES. Elvar Jónsson, Asmus Dohn, Timo Jacob, and Hannes Jónsson supervised the project and contributed writing revisions. Submitted to *Journal of Chemical Theory and Computation.* Preprint available: arXiv:2103.16342 [physics].

Elastic Collision Based Dynamic Partitioning Scheme for Hybrid Simulations

Björn Kirchhoff,[†] Elvar Örn Jónsson,[†] Asmus Ougaard Dohn,[†,‡] Timo Jacob,[¶,§,‖] and Hannes Jónsson[*,†]

[†]*Science Institute and Faculty of Physical Sciences, University of Iceland, VR-III, 107 Reykjavík, Iceland.*

[‡]*Technical University of Denmark, Lyngby, Denmark.*

[¶]*Institute of Electrochemistry, Ulm University, Albert-Einstein-Allee 47, 89081 Ulm, Germany.*

[§]*Helmholtz-Institute Ulm (HIU) Electrochemical Energy Storage, Helmholtz-Straße 16, 89081 Ulm, Germany.*

[‖]*Karlsruhe Institute of Technology (KIT), P.O. Box 3640, 76021 Karlsruhe, Germany.*

E-mail: hj@hi.is

Abstract

In hybrid simulations, such as the QM/MM approach, the system is partitioned into regions that are treated at different levels of theory. The key question then becomes how to evaluate the interactions between particles on opposite sides of the boundary. One approach is to place the boundary in such a way that particles near the boundary on both sides are of the same type, thus simplifying the evaluation of the interactions. If mobile particles are present, such as solvent molecules, and particles are allowed to cross the boundary, the conservation of energy and atomic forces is problematic unless the computational effort is increased significantly. By preventing particles from

crossing the boundary but allowing the boundary to be flexible, an accurate estimate of average thermodynamic properties is obtained in principle as illustrated by the flexible inner region ensemble separator (FIRES) method [C. Rowley and B. Roux, J. Chem. Theory Comput. 8, 3526 (2012)]. In FIRES, a harmonic restraint is applied to particles near the boundary so they can cross the boundary to some extent resulting in anomalies in the particle density. Here, a constraint approach is presented where particles instantaneously scatter from the boundary. This scattering-adapted FIRES (SAFIRES) implementation makes use of a variable-time-step propagation algorithm where the time step is scaled automatically to identify the moment a collision should occur. If the length of the time step is kept constant, this propagator reduces to a regular Langevin dynamics algorithm, and to the velocity Verlet algorithm for conservative dynamics if the friction coefficient is set to zero. Correct average ensemble statistics are obtained as demonstrated in simulations where, for testing purposes, the particles in the two regions are treated at the same level of theory, namely a homogeneous Lennard-Jones (LJ) liquid and liquid water based on the TIP4P potential function. In order to illustrate this approach in solid-liquid interface simulations, a LJ liquid in contact with the surface of a crystal is also simulated. The simulations using SAFIRES are shown to reproduce the unconstrained reference simulations without significant deviations in the particle density and the dynamics are shown to conserve energy when coupling to the heat bath is turned off.

1 Introduction

With the advent of and widespread access to high-performance computing resources over the past decades, computational methods have become increasingly important in predicting material properties and chemical reaction mechanisms. However, the desire to correctly describe processes at interfaces has been straining the limits of standard computational methods based on density functional theory (DFT). The solid-liquid interface is of particular interest but has proven troublesome because solvents — and especially water — often

take part in reactions rather than acting as neutral bystanders.[1–3] The influence of solvation can alter reaction behavior significantly[4–7] and can even cause structural changes in, for example, a catalyst through solvent-induced rearrangement.[8–11] Correct description of solvent interactions is often crucial when trying to understand complex natural phenomena such as the water splitting reaction in photosystem II[12] or substrate binding in protein active sites.[13] Solvation energy contributions have also been shown to significantly affect free energy trends and energy barriers of reaction intermediates on (homogeneous or heterogeneous) catalyst models, making correct description of solvation contributions an important ingredient in the computational analysis of reaction mechanisms and for deriving rational catalyst optimization strategies.

Ideally, solvent molecules should be present in computational models of such systems. Unfortunately, only a few solvent molecules can be included in DFT calculations due to rapidly increasing computational effort as system size is increased. Furthermore, DFT calculations of static solvent molecule arrangements obtained by optimization[14–16] only serve as an approximation as the influence of the liquid phase is not properly taken into account. Dynamics simulations where atomic forces are obtained from electronic structure calculations can, in principle, be used to obtain reliable solvation energy contributions from statistical averaging but are too computationally demanding, both in terms of the system size and the length of the time that needs to be simulated, for routine application.

Various methods exist that attempt to make the effect of solvation accessible in a more computationally efficient manner. Therein, the implicit solvation method constitutes the most common approach. Here, the solvent is represented as a homogeneous medium based on key bulk properties such as the permittivity. However, implicit solvation models do not describe important short range electronic and chemical interactions such as hydrogen bonding and electron or proton transfer reactions. The inclusion of an implicit solvent often does not improve the accuracy of the calculated results and typically does not provide close agreement with experimentally measured solvation energy.[17–20]

The embedded solvation approach, where a few solvent molecules are explicitly represented near the reaction center while the rest of the solvent is treated implicitly, can significantly improve results while remaining computationally efficient.[21–23] However, the number of included explicit solvent molecules requires careful optimization. Enough explicit molecules should be used to model the desired interactions accurately but the inclusion of too many molecules can lead to problems.[24]

Lastly, hybrid simulation methods can be used to calculate solvation effects in a computationally efficient way. In hybrid simulations, the simulation box is divided into coupled regions that are treated at different levels of theory. A prominent example of this approach is the QM/MM method.[25–29] Here, the solute and a few solvent molecules are calculated using accurate and computationally demanding electronic structure methods while the majority of the solvent molecules is computed using a potential function. This scheme makes it possible to carry out molecular dynamics (MD) or Monte Carlo (MC) simulations including thousands of solvent molecules with sufficient sampling of the phase space to properly include solvation effects.

A crucial aspect of any hybrid simulation scheme is the description of the boundary between the inner and outer regions. Several different approaches exist for the implementation of such a boundary with the goal of causing as little disturbance to the system as possible. In adaptive hybrid methods, particles are allowed to move from one region to the other.[30–38] However, this approach leads to discontinuities if the description of a particle is switched abruptly as it crosses the boundary. Additional calculations of all permutations of particles in terms of the two theoretical descriptions in a buffer region around the boundary can be used to statistically smooth out these discontinuities.[38] But, this corrective process greatly increases the computational effort.

Restrictive methods constitute another approach to the boundary in hybrid simulations. In 2012, Rowley and Roux introduced a restrictive boundary scheme called the Flexible Inner Region Ensemble Separator (FIRES).[39] In FIRES, particles are confined to their originally

assigned region using a penalty potential energy term that is activated whenever a particle crosses the boundary. The boundary is dynamically defined by the outermost particle in the inner region. In combination with the requirement that all particles near the boundary on either side need to be identical, FIRES can be shown to recover correct average thermodynamic properties of the system despite the presence of the boundary.[39,40] However, continuity of trajectories is lost due to the artificial redirection of particles at the boundary. FIRES is computationally efficient because, unlike the adaptive methods, the level of theory used to describe the particles never changes and therefore, no discontinuities are introduced in the energy and atomic forces. FIRES has, for example, been used in benchmark calculations of dissolved Zn and Mg[41] ions and to calculate the solvation of a transition state of a nucleophilic carbonyl reaction.[42]

The penalty potential energy term used in the Rowley-Roux implementation is actually an approximation to the FIRES premise, as the mathematical formalism implies instantaneous redirection at the boundary. An accumulation of particles can occur at the boundary in FIRES simulations, as reported by Bulo *et al.*. An analogous accumulation is observed for hybrid simulations with a static, hard sphere boundary.[43]

Aside from FIRES, other boundary-based methods have been developed, in particular the Boundary Based on Exchange Symmetry (BEST) method[44,45] and the Boundary Constraint with Correction (BCC) method.[46] In BEST, the separating potential is constructed by calculating a penalty function that is unity for a separated particle pair and approaches zero as the particle configuration becomes more undesirable, *i.e.* as particles travel further into the opposite region.[44,45] The bias function is then obtained as the product of penalty functions of all permutations of particle pairs; hence, the reference to exchange symmetry. However, since particle pairs that are unproblematic (*i.e.* in different regions) do not contribute significantly to the bias function, Shiga and Masia find that construction of the bias function can be simplified by only taking into account single or double exchanges of the particle pairs with penalty functions closest to zero. An updated version of BEST, entitled

QUEST, has been introduced and shown to give good results.[47]

The BCC method utilizes the Fermi function to create a bias potential inspired by BEST to separate particles into the two regions.[46] As the authors remark, the basic premise behind boundary-based methods — instantaneous redirection at the boundary — cannot be achieved using a potential energy penalty. The BCC method therefore attempts to rectify the statistical error related to the accumulation of molecules at the boundary, mentioned above, by performing an additional set of calculations to remove contributions of the bias potential from thermodynamic properties of the erroneous configurations. This approach thereby adds additional computational overhead to the simulations.

In the method presented here, particles are scattered instantaneously from the boundary. We refer to the method as Scattering-Adapted FIRES (SAFIRES). Analogous to other boundary-based methods, the boundary between the inner and outer region is defined dynamically by the outermost particle in the inner region. To enforce the boundary SAFIRES uses an elastic collision scheme. This instantaneous approach to particle redirection however necessitates that time steps are variable during the simulation so that collisions occur when the involved particles are located exactly on the boundary. Therefore, fractional time steps are calculated on-the-fly as conflicts arise and a new variable-time-step propagation algorithm for the dynamics is introduced. The new propagator reduces to the Vanden-Eijnden–Ciccotti algorithm for Langevin dynamics[48] if the time step is kept constant and further reduces to the velocity Verlet algorithm if the friction coefficient is set to zero. Atomic forces are only updated at full time step intervals in order to retain the temporal consistency of the calculation and to satisfy time-reversibility of the Taylor expressions that the propagation algorithm is derived from. SAFIRES dynamics conserve energy if the coupling to the heat bath is turned off. Figure 1 illustrates the SAFIRES approach for a solute/solvent and a liquid/solid systems in a schematic way.

The article is organized as follows: section 2 describes the implementation of SAFIRES for a spherical boundary centered on a fixed solute. Therein, subsection 2.1 gives an overview

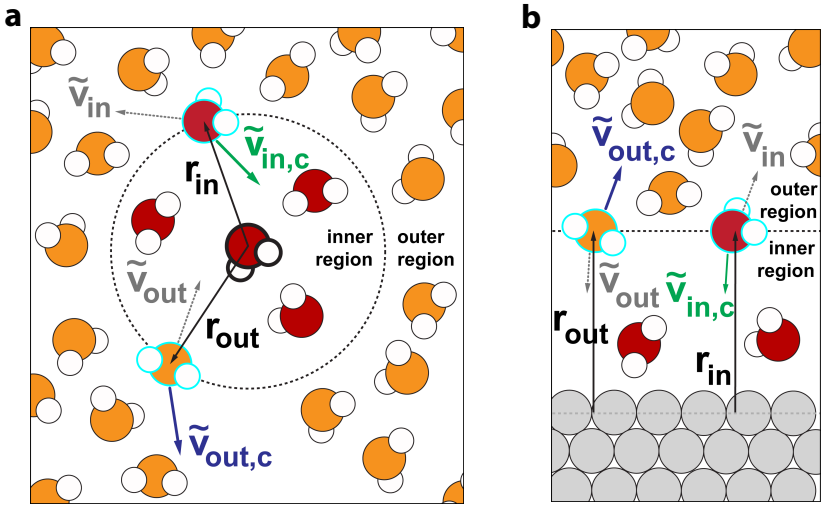

Figure 1: Illustration of the SAFIRES approach for a molecular (**a**) and a liquid/solid interface (**b**) with water. The flexible boundary is shown as a dotted black circle or line. Molecules in the inner region are shown in red, while those in the outer region are shown in orange. The solid surface is shown in grey. **r**: vector connecting the solute (**a**) or a plane parallel to the surface (**b**) to the particles in the inner (in) and outer (out) region. The gray $\tilde{\mathbf{v}}$ vectors represent the initial velocity of the molecule in the inner (in) and outer (out) region before the collision. The vectors $\tilde{\mathbf{v}}_c$ represent the velocity vectors of the molecule in the inner (green) and outer (blue) region after the elastic collision.

of the SAFIRES algorithm, subsection 2.2 presents the time propagation algorithm where fractional time steps are incorporated to find the exact point of collision, subsection 2.3 describes the binary elastic collision at the boundary, and subsection 2.4 discusses the possibility that multiple collisions need to be performed in a single time step. Section 3 describes the implementation of SAFIRES for a planar boundary, used for example in liquid/solid simulations. Section 4 discusses the method in the context of polyatomic molecules where the focus is on the center of mass of each molecule. Section 5 describes the systems simulated where the two regions are described at the same level of theory in order to have a clear reference to judge the accuracy of the results. Section 6 presents the results obtained for a Lennard-Jones (LJ) liquid where one of the atoms is treated as a 'solute' (subsection 6.1), and liquid water described with the TIP4P potential function where the 'solute' is one of the water molecules (subsection 6.2). A simulation of a liquid/solid interface using LJ potential is described in subsection 6.3. Calculated distribution functions are used in all cases to evaluate the ability of the method to reproduce the average structural features of unconstrained simulations. A comparison is, furthermore, made with results of simulations using FIRES. The article concludes with discussion and conclusion sections.

2 Spherical boundary

2.1 Overview of the algorithm

The key steps in the algorithm for detecting and resolving an instance where a particle from the outer region attempts to enter the inner region is depicted schematically in figure 2(a) for a model system with a molecular solute and a spherical boundary between the regions. For simplicity, it is assumed here that the system consists of an atomic liquid and a fixed solute. The algorithm for a liquid of polyatomic molecules is presented in section 4. The algorithm for liquid/solid interface, where the boundary is a two-dimensional plane, is largely the same with some simplifications as outlined in Section 3.

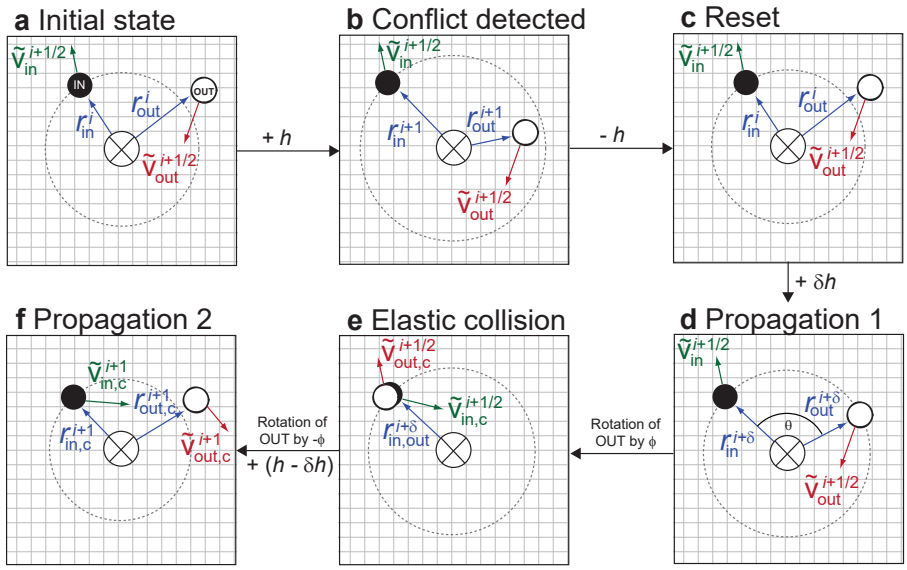

Figure 2: Schematic overview of the steps involved in the identification and resolution of an instance where a particle from the outer region attempts to enter the inner region. The superscript indicates the time step. $\mathbf{r}_{\text{in}}$ and $\mathbf{r}_{\text{out}}$ give the position of an inner and an outer region particle with respect to the fixed solvent particle. The radius of the boundary is the length of $\mathbf{r}_{\text{in}}$. $\tilde{\mathbf{v}}$ denotes particle velocity that includes random components from the Langevin equation of motion. **a:** The initial, conflict-free state of the system. **b:** After the particles have moved according to one full time step, h, the outer region particle has moved into the inner region. **c:** The particles are then moved to the previous conflict-free state. **d:** A fractional time step δh is found that moves the two particles right to the boundary. **e:** Then, $\mathbf{r}_{\text{out}}$ is rotated to coincide with $\mathbf{r}_{\text{in}}$ and $\tilde{\mathbf{v}}_{\text{out}}$ is rotated in the same way, followed by a binary elastic collision where velocity components normal to the boundary surface are exchanged. The subscript c is added to vectors that have been modified by the collision. **f:** After the collision and rotation of $\mathbf{r}_{\text{out}}$ and $\tilde{\mathbf{v}}_{\text{out}}$ back, the position of the particles is updated for the remainder of the time step $h(1-\delta)$. If no outer region particle is inside the boundary, the force on the particles is evaluated and the velocity updated.

At the start of a simulation of the dynamics, three sets of indices are assigned to the atoms. The first, s, identifies the solute particle, that defines the origin of the boundary. A second set of indices, S_{in}, identifies the particles in the inner region. The outermost particle in this region determines the radius of the boundary, r_b. The rest of the particles must be at a larger distance from the solute and are assigned to the outer region and to the third set,

S_{out}, which identifies the outer particles.

The time propagation algorithm for Langevin dynamics makes use of a basic time step h and given current position of the particles, $\mathbf{r}^i$, with respect to a fixed solute, corresponding to time ih, the force acting on the particles is evaluated and an update of the velocity made to give $\mathbf{v}^{i+1/2}$. At the start of a new iteration, $i+1$, the coordinates of the particles are updated to $\mathbf{r}^{i+1}$ and the radius of the spherical boundary, r_b, evaluated as the distance from the solute to the outermost inner region particle, as indicated in figure 2(a)

$$r_b = || \mathbf{r}_{\alpha_b}^{i+1} || = \max || \mathbf{r}_{\alpha}^{i+1} || \quad \forall \alpha \in S_{\text{in}}, \tag{1}$$

were α_b is the index for the outermost inner region particle. A check is then carried out whether any of the particles in the outer region are within the boundary, *i.e.* are at a smaller distance from the solute than r_b. Possibly, this includes more than one particle and the set of such particles is denoted by S'_{out}

$$S'_{\text{out}} = \left\{ \beta : || \mathbf{r}_{\beta}{}^{i+1} || < r_b \quad \forall \beta \in S_{\text{out}} \right\} . \tag{2}$$

If no such conflict is detected, *i.e.* $S'_{\text{out}} = \emptyset$, the force acting on the particles is evaluated at the new positions of the particles and the velocity updated to complete the iteration.

If, however, a conflict is detected (as shown in figure 2(b)), the simulation is reverted to the previous position of the particles (figure 2(c)) and a fractional time step δh,where $0 < \delta < 1$, is found such that no outer region particle is inside the boundary and the closest one is right on the boundary, *i.e.*

$$\min || \mathbf{r}_{\beta}^{i+\delta} || = r_b \quad \forall \beta \in S'_{\text{out}}. \tag{3}$$

A propagation of the particle coordinates over a partial time step is then performed. The method for determining the value of δ is presented in section 2.2.

The partial propagation leads to particle positions indicated in figure 2(d). The vector giving the location of the outer region particle that is located on the boundary, denoted by index β_b, is then rotated so as to coincide with the location of the inner region particle, α_b, that defines the radius of the boundary at this point in time. The corresponding velocity vector, $\mathbf{V}_{\beta_b}^{1+1/2}$, is rotated in the same way. Then, an elastic collision is performed between this pair of particles resulting in an exchange of the components of the velocity vectors normal to the boundary, as indicated in figure 2(e). This step is described in section 2.3. After the collision has been performed, the position vector of the outer region particle is rotated back to the original position and its new velocity vector rotated in the same way.

Lastly, the system is propagated by the remaining fractional time step $(1-\delta)h$ required to complete a regular time step h, see figure 2(f) to give particle positions $\mathbf{r}^{i+1}$. The subscript c on the position and velocity vectors indicates that they have been modified by an elastic collision.

After the second fractional time step, the boundary is updated based on the new particle positions and another check for conflicts is performed. This updates both the index α_b and the set S'_{out} since, having resolved the first boundary crossing, some of the other conflicts detected earlier may also have been resolved and new conflicts may, furthermore, have occurred. If an additional conflict is detected, the steps depicted in figure 2(c)-(f) are repeated as discussed in Section 2.4.

After a conflict free state of the system has been reached, the iteration is completed and the time will then have evolved by a full time step. A new iteration started.

2.2 Time evolution including fractional step

The time evolution of the system is described by the discretized Langevin equation of motion. The coordinates of all n particles in the system at time step i are given by the $3n$ dimensional vector $\mathbf{R}^i$. The corresponding velocity vector is $\mathbf{V}^i$ and the force divided by the particle mass

is vector $\mathbf{F}(\mathbf{R}^i)$. The iterative Langevin propagator used here can be written as[48]

$$\begin{aligned}
\mathbf{V}^{i+\frac{1}{2}} &= \mathbf{V}^i + \frac{1}{2}h\mathbf{F}(\mathbf{R}^i) - \frac{1}{2}h\gamma\mathbf{V}^i + \frac{1}{2}\sigma\sqrt{h}\mathbf{\Sigma}^i \\
&- \frac{1}{8}h^2\gamma\left(\mathbf{F}(\mathbf{R}^i) - \gamma\mathbf{V}^i\right) - \frac{1}{4}h^{\frac{3}{2}}\gamma\left(\frac{1}{2}\mathbf{\Sigma}^i + \frac{\sigma}{\sqrt{3}}\mathbf{\Lambda}^i\right) \qquad (4) \\
\mathbf{R}^{i+1} &= \mathbf{R}^i + h\mathbf{V}^{i+\frac{1}{2}} + h^{\frac{3}{2}}\frac{\sigma}{2\sqrt{3}}\mathbf{\Lambda}^i \qquad (5) \\
\mathbf{V}^{i+1} &= \mathbf{V}^{i+\frac{1}{2}} + \frac{1}{2}h\mathbf{F}(\mathbf{R}^{i+1}) - \frac{1}{2}h\gamma\mathbf{V}^{i+\frac{1}{2}} + \frac{\sigma}{2}\sqrt{h}\mathbf{\Sigma}^i \\
&- \frac{1}{8}h^2\gamma\left(\mathbf{F}(\mathbf{R}^{i+1}) - \gamma\mathbf{V}^{i+\frac{1}{2}}\right) - \frac{1}{4}h^{\frac{3}{2}}\gamma\sigma\left(\frac{1}{2}\mathbf{\Sigma}^i + \frac{1}{\sqrt{3}}\mathbf{\Lambda}^i\right) \qquad (6)
\end{aligned}$$

where the coupling to a heat bath at temperature T is specified by

$$\sigma = \sqrt{2T\gamma/m}, \qquad (7)$$

with m being particle mass, γ the thermostat friction coefficient, and $\mathbf{\Sigma}$ and $\mathbf{\Lambda}$ being $3n$-dimensional vectors with elements drawn from covariant Gaussian distributions that are randomized at the start of each iteration i.

As discussed above, the time propagation may need to be split up into partial time steps in order to resolve instances where an outer region particle attempts to enter the inner region. The time propagation is then split into two time intervals — first a propagation that brings one of the outer particles to the boundary followed by a binary collision and then a completion of the time step. Forces are only evaluated again after a full time step has been completed and the location of the particles is consistent with the inner/outer region separation. Therefore, equation (6) is performed only after all conflicts have been resolved. Only equations (4)-(5) need to be considered for the resolution of conflicts in particle locations. Resolution of such issues requires no additional evaluations of the force and therefore involves insignificant additional computational effort in typical simulations.

It has been shown that iterative algorithms for Langevin dynamics can become numerically unstable for variable time steps.[49] The algorithm presented here seeks to avoid this

pitfall and satisfy the time reversibility of the Taylor expressions the propagator is derived from by updating all components in equation (4) and the third term in equation (5) based on full time steps. Equation (5) is rewritten to separate the part of the velocity vector that comes from the deterministic part of the equation of motion, $\mathbf{V}$, and the full velocity vector, $\tilde{\mathbf{V}}$, that includes the random component corresponding to interaction with the heat bath as

$$\tilde{\mathbf{V}}^{i+\frac{1}{2}} = \mathbf{V}^{i+\frac{1}{2}} + h^{\frac{1}{2}}\frac{\sigma}{2\sqrt{3}}\mathbf{\Lambda}^i \tag{8}$$

$$\mathbf{R}^{i+1} = \mathbf{R}^i + h\tilde{\mathbf{V}}^{i+\frac{1}{2}} \tag{9}$$

so the update of the coordinates in equation (9) becomes linear in the time step h.

After updating the coordinates to $\mathbf{R}^{i+1}$ as described above, the outermost inner particle, α_b, is identified and the condition of equation (2) checked. For all elements β in S'_{out} the fractional time that brings outer particles to the boundary needs to be found. Denoting the particle positions with respect to the solute as $\mathbf{R}^i_{s,\alpha \text{ or } \beta} = \mathbf{R}^i_{\alpha \text{ or } \beta} - \mathbf{R}^i_s$ the positions of the conflicting atom coordinates satisfy at the point of collision

$$||\mathbf{R}^{i+\delta}_{s,\alpha_b}|| \stackrel{!}{=} ||\mathbf{R}^{i+\delta}_{s,\beta}|| \quad \forall\beta \in S'_{\text{out}}. \tag{10}$$

Using equation (10) in combination with equation (9) leads to

$$||\mathbf{R}^i_{s,\alpha_b} + h'_\beta\tilde{\mathbf{V}}^{i+1/2}_{\alpha_b}|| = ||\mathbf{R}^i_{s,\beta} + h'_\beta\tilde{\mathbf{V}}^{i+1/2}_{\beta}|| \quad \forall\beta \in S'_{\text{out}}. \tag{11}$$

This is solved analytically for the partial time step, h'_β, required to propagate each conflicting in/out particle pair to the same distance from the solute

$$h'^2_\beta \underbrace{\left((\tilde{\mathbf{V}}^{i+1/2}_{\alpha_b})^2 - (\tilde{\mathbf{V}}^{i+1/2}_{\beta})^2\right)}_{=a} + h'_\beta \underbrace{2\left(\mathbf{R}^i_{s,\alpha_b}\cdot\tilde{\mathbf{V}}^{i+1/2}_{\alpha_b} - \mathbf{R}^i_{s,\beta}\cdot\tilde{\mathbf{V}}^{i+1/2}_{\beta}\right)}_{=b} + \underbrace{\left((\mathbf{R}^i_{s,\alpha_b})^2 - (\mathbf{R}^i_{s,\beta})^2\right)}_{=c} = 0 \tag{12}$$

$$h'_\beta = \frac{-b \pm \sqrt{b^2 - 4ac}}{2a}\,. \tag{13}$$

The relevant solution is the smallest value of h'_β as it corresponds to the earliest attempt of an outer particle to cross the boundary. This particle is denoted with index β_b. The coordinates are then updated according to

$$\mathbf{R}^{i+\delta} = \mathbf{R}^i + h'_{\beta_b}\tilde{\mathbf{V}}^{i+1/2}\,, \tag{14}$$

where $h'_{\beta_b} = \delta h$ so that inner particle α_b and outer particle β_b are at equal distance from the solute. This is depicted in figure 2(d). Note that a real-valued and positive solution $h' \leq h$ is always guaranteed since $h > 0$ and $(\mathbf{R}^i_{s,\alpha_b})^2 < (\mathbf{R}^i_{s,\beta})^2$.

2.3 Elastic collision

Once a conflict has been detected and the fractional time step propagation has been performed in such a way that the outermost inner particle, α_b, and the innermost outer particle, β_b, are both at the boundary, the velocities of these particles need to be redirected in order to prevent the outer region particle from reaching the inner region. This redirection is achieved through a binary elastic collision between the conflicting particles and results in an exchange of the components of the velocities normal to the boundary.

In the case of Langevin dynamics the velocity vectors $\tilde{\mathbf{v}}^{i+1/2}_{\text{in}} = \tilde{\mathbf{V}}^{i+1/2}_{\alpha_b}$ and $\tilde{\mathbf{v}}^{i+1/2}_{\text{out}} = \tilde{\mathbf{V}}^{i+1/2}_{\beta_b}$ containing the random component are considered. If coupling to the bath is turned off and the iterative time propagation algorithm reduces to the velocity Verlet algorithm, they include just the deterministic component of the velocity. In the following the time step index i is omitted for simplicity.

In order to induce the collision, the position vector of the outer particle, β_b is rotated to coincide with that of the inner particle, α_b. The position vectors of the two atoms with respect to the solute are $\mathbf{r}_{\text{in}} = \mathbf{R}_{\alpha_b} - \mathbf{R}_s$ and $\mathbf{r}_{\text{out}} = \mathbf{R}_{\beta_b} - \mathbf{R}_s$ and the angle ϕ between the

vectors is given based on the four-quadrant inverse tangent[50]

$$\phi = \arctan\left(||\mathbf{r}_{\mathrm{in,s}} \times \mathbf{r}_{\mathrm{out,s}}||, (\mathbf{r}_{\mathrm{in,s}} \cdot \mathbf{r}_{\mathrm{out,s}})\right). \tag{15}$$

The rotational axis is

$$\mathbf{c} = \frac{\mathbf{r}_{\mathrm{in}} \times \mathbf{r}_{\mathrm{out}}}{||\mathbf{r}_{\mathrm{in}} \times \mathbf{r}_{\mathrm{out}}||} \tag{16}$$

and the rotation is performed with the Euler-Rodrigues form of the rotational matrix $X(\mathbf{c}, \phi)$ (see equation (S1)). This gives

$$\mathbf{r}_{\mathrm{in}}^T = \mathbf{r}_{\mathrm{out}}^{\mathrm{rot},T} = X(\mathbf{c}, \phi)\mathbf{r}_{\mathrm{out}}^T \tag{17}$$

where the superscript T denotes transpose. Similarly, the velocity vector of the outer particle is rotated in the same way

$$\tilde{\mathbf{v}}_{\mathrm{out}}^{\mathrm{rot},T} = X(\mathbf{c}, \phi)\tilde{\mathbf{v}}_{\mathrm{out}}^T. \tag{18}$$

A binary elastic collision is then performed between the two particles according to

$$\boldsymbol{\Delta}\tilde{\mathbf{v}}_{\mathrm{out}}^{\prime\,\mathrm{rot}} = -\boldsymbol{\Delta}\tilde{\mathbf{v}}_{\mathrm{in}}^{\prime} = -\frac{((\tilde{\mathbf{v}}_{\mathrm{out}}^{\mathrm{rot}} - \tilde{\mathbf{v}}_{\mathrm{in}}) \cdot \mathbf{r}_{\mathrm{in}})\ \mathbf{r}_{\mathrm{in}}}{||\mathbf{r}_{\mathrm{in}}||^2} \tag{19}$$

where the components normal to the boundary are exchanged. The vectors $\boldsymbol{\Delta}\tilde{\mathbf{v}}_{\mathrm{out}}^{\prime\,\mathrm{rot}}$ and $\boldsymbol{\Delta}\tilde{\mathbf{v}}_{\mathrm{in}}^{\prime}$ represent the change to the outer and inner particle velocities as a result of the elastic collision. The equations do not include the mass dependent prefactor $2m_{\mathrm{in\ or\ out}}/(m_{\mathrm{in}}+m_{\mathrm{out}})$ which is always equal to unity here since the particles in the inner and outer region near the boundary are identical. This also applies to molecules which are treated as pseudo-particles, see section 4.

After the collision between the two conflicting particles, $\boldsymbol{\Delta}\tilde{\mathbf{v}}_{\mathrm{out}}^{\prime\,\mathrm{rot}}$ is rotated in a way that

brings the position of the outer particle back to the original position

$$\Delta\tilde{\mathbf{v}}'_{\text{out}} = X(\mathbf{c}, -\phi)\Delta\tilde{\mathbf{v}}'^{\,\text{rot}}_{\text{out}} \tag{20}$$

and the velocity is updated such that

$$\tilde{\mathbf{V}}^{i+1/2}_{c,\alpha_b} = \tilde{\mathbf{v}}_{\text{in}} + \Delta\tilde{\mathbf{v}}'_{\text{in}} \quad \text{and} \quad \tilde{\mathbf{V}}^{i+1/2}_{c,\beta_b} = \tilde{\mathbf{v}}_{\text{out}} + \Delta\tilde{\mathbf{v}}'_{\text{out}}. \tag{21}$$

The coordinates of the particles are updated for the remainder of the time step as

$$\mathbf{R}^{i+1}_c = \mathbf{R}^{i+\delta} + (h - h')\tilde{\mathbf{V}}^{i+1/2}_{\text{c}}\,. \tag{22}$$

At this stage the updated coordinates are checked for additional conflicts, first by updating the boundary radius, equation (3), resulting in an update of α_b, followed by a check whether any outer particles have crossed the new boundary, equation (2), resulting in an update of S'_{out}. Resolution of multiple boundary conflicts within the same time step are discussed in section 2.4.

If no additional conflicts are detected for $\mathbf{R}^{i+1}_c$, a calculation of the force is carried out, $\mathbf{F}(\mathbf{R}^{i+1})$, and the velocity vectors are updated to $\mathbf{V}^{i+1}$ according to equation (6), using $\mathbf{V}^{i+\frac{1}{2}}_{\text{c}}$. This completes the update of all vectors for time step i+1.

2.4 Multiple conflicts

Multiple conflicts in the same time step do not add significant complexity. The same procedure is applied as outlined in the preceding section, using the updated $\mathbf{R}^{i+\delta}$ and $\tilde{\mathbf{V}}^{i+1/2}_{\text{c}}$ vectors as a starting point. A new partial time step, $h'' \leq (h - h')$, is solved for using equations (10)–(13) where the vector $\mathbf{R}^{i+\delta}_s = \mathbf{R}^{i+\delta} - \mathbf{R}_s$ is now used in equation (11). If one or more incidence of an outer particle entering the inner region is identified, the shortest time for such an event is calculated and the corresponding fractional time step ϵh found that

brings the outermost inner particle to the boundary. The position of the particles is then

$$\mathbf{R}^{i+\delta+\epsilon} = \mathbf{R}^{i+\delta} + h''\tilde{\mathbf{V}}_{\mathrm{c}}^{i+1/2} \tag{23}$$

and an elastic collision is again performed to correct the velocity $\tilde{\mathbf{V}}_{\mathrm{c}}^{i+1/2}$.

This process of resolving multiple conflicts and solving for partial time steps in smaller and smaller remaining time intervals can in principle be continued indefinitely. However, in the calculations that have been carried out and are presented in Section 6 it rarely happens that more than one conflict occurs in a single time step, even if multiple outer particles are identified as entering the inner region through equation (2). The resolution of the first such event often results in the resolution of other possible conflicts within the same time step due to the change in the trajectory of the outermost particle in the inner region, α_{b}.

3 Planar boundary

In the case of a planar boundary, as for a liquid/solid interface simulation, the method is somewhat simpler. Given an orthorhombic left-handed Cartesian coordinate system with origin $O = (0, 0, 0)$ and periodicity along the x- and y-axis, an xy-plane boundary is located at the inner region particle with the largest z-coordinate

$$r_z^b = \max(\mathbf{R}_{z,\alpha}^{i+1}) \;\; \forall \alpha \in S_{\mathrm{in}} \tag{24}$$

and the check for conflicts is

$$S'_{\mathrm{out}} = \left\{ \beta : \; \mathbf{R}_{z,\beta}^{i+1} < r_z^b \;\; \forall \beta \in S_{\mathrm{out}} \right\} . \tag{25}$$

If one or more conflict is detected, the partial time step required to propagate the various outer region particles in S'_{out} to the boundary is then solved for according to

$$\mathbf{R}^{i+\delta}_{z,\alpha_b} \stackrel{!}{=} \mathbf{R}^{i+\delta}_{z,\beta} \quad \forall \beta \in S'_{\text{out}}\,, \tag{26}$$

where α_b is the index for the particle with largest value of z, resulting in the condition

$$\mathbf{R}^{i}_{z,\alpha_b} + h'_\beta \tilde{\mathbf{V}}^{i+1/2}_{z,\alpha_b} = \mathbf{R}^{i}_{z,\beta} + h'_\beta \tilde{\mathbf{V}}^{i+1/2}_{z,\beta} \quad \forall \beta \in S'_{\text{out}} \tag{27}$$

for the partial time steps that bring an outer region particle to the boundary.

The collision between an outer region particle that attempts to enter the inner region with the inner region particle that defines the location of the boundary results in an exchange of the z-components of the velocity vectors. The exchange is

$$\boldsymbol{\Delta}\tilde{\mathbf{v}}'_{z,\text{out}} = -\boldsymbol{\Delta}\tilde{\mathbf{v}}'_{z,\text{in}} = \tilde{\mathbf{v}}_{z,\text{in}} - \tilde{\mathbf{v}}_{z,\text{out}} \tag{28}$$

followed by an update of the velocity vectors and the coordinates in an analogous manner as described in the preceding sections for a spherical boundary.

Conceptually, the outer particle is shifted in (x, y) location to the same coordinates as the inner region particle defining the boundary, but no rotation of vector is required in this case and each collision conserves momentum as well as energy.

4 Polyatomic molecules

When polyatomic molecules are involved, the algorithm focuses on the center of mass of each molecule. Effectively, a molecule is considered as a pseudo-particle and conflicts are identified as the center of mass of an outer region molecule attempts to enter the inner region. Water molecules are taken here as an example. In the case of a system of n_{mol} rigid water

molecules the position and velocity vectors are $3n_{\text{mol}}$-dimensional

$$\mathbf{R}^i_{\text{cm}} = \left\{ \sum_{a \in S_{\text{mol}}} m_a \mathbf{R}^i_a / M \quad \forall S_{\text{mol}} \in S \right\} \tag{29}$$

$$\mathbf{V}^i_{\text{cm}} = \left\{ \sum_{a \in S_{\text{mol}}} m_a \mathbf{V}^i_a / M \quad \forall S_{\text{mol}} \in S \right\} \tag{30}$$

where the subset $S_{\text{mol}} = \{\text{O}, \text{H}_1, \text{H}_2\}$ indexes the atoms of each molecule in the set S of all atom indices and m_a are the masses of the atoms and M is the total mass of a molecule. The force vector is

$$\mathbf{F}_{\text{cm}}(\mathbf{R}^i_{\text{cm}}) = \left\{ \sum_{a \in S_{\text{mol}}} m_a \mathbf{F}(\mathbf{R}^i_a) / M \quad \forall S_{\text{mol}} \in S \right\} . \tag{31}$$

Additionally, for the Langevin integrator the random variable vector fields transform as

$$\mathbf{\Sigma}^i_{\text{cm}} = \left\{ \sum_{a \in S_{\text{mol}}} \sqrt{m_a}\ \mathbf{\Sigma}^i_a \,/\, M \quad \forall S_{\text{mol}} \in S \right\} \tag{32}$$

and similarly for $\mathbf{\Lambda}^i_{\text{cm}}$. The square root dependence of the per-atom mass-weighing follows from the multiplicative factor σ defined in equation (7). The velocity of the center of mass, $\tilde{\mathbf{V}}^i_{\text{cm}}$, is evaluated using equation (8).

The checks for conflicts, equations (2)-(3), and fractional time step evaluations, equations (11)-(13), are based on center of mass coordinates of the molecules to identify conflicting in/out pseudo-particle pair indices α_b and β_b, as well as index sets $S^{\alpha_b}_{\text{mol}} = \{\alpha^{\text{O}}_b, \alpha^{\text{H}_1}_b, \alpha^{\text{H}_2}_b\}$ and $S^{\beta_b}_{\text{mol}} = \{\beta^{\text{O}}_b, \beta^{\text{H}_1}_b, \beta^{\text{H}_2}_b\}$. That is, for a conflicting in/out pseudo-particle pair, the molecular indices and corresponding atomic indices are identified.

The elastic collisions as described in Section 2.3, result in an exchange of the velocity of the center of mass of the two molecules, but does not affect the velocity of the atoms relative to the center of mass. For example, given conflicting pseudo-particle pairs and corresponding velocity $\tilde{\mathbf{v}}^{i+1/2}_{\text{cm,in}} = \tilde{\mathbf{V}}^{i+1/2}_{\text{cm},\alpha_b}$ and $\tilde{\mathbf{v}}^{i+1/2}_{\text{cm,out}} = \tilde{\mathbf{V}}^{i+1/2}_{\text{cm},\beta_b}$ the resulting changes $\mathbf{\Delta}\tilde{\mathbf{v}}'^{\,\text{rot}}_{\text{cm,out}}$ and $\mathbf{\Delta}\tilde{\mathbf{v}}'_{\text{cm,in}}$

affect the velocity of the center of mass. After rotation of the velocity vector for the center of mass of the outer molecule – to give $\boldsymbol{\Delta}\tilde{\mathbf{v}}'_{\mathrm{cm,out}}$ – the changes in the velocity components need to be redistributed to the individual atoms of each molecule

$$\tilde{\mathbf{V}}_{c,\alpha}^{i+1/2} = \left(\tilde{\mathbf{V}}_{\alpha}^{i+1/2} + \boldsymbol{\Delta}\tilde{\mathbf{v}}'_{\mathrm{cm,in}}\right) \forall \alpha \in S_{\mathrm{mol}}^{\alpha_b},$$

and

$$\tilde{\mathbf{V}}_{c,\beta}^{i+1/2} = \left(\tilde{\mathbf{V}}_{\beta}^{i+1/2} + \boldsymbol{\Delta}\tilde{\mathbf{v}}'_{\mathrm{cm,out}}\right) \forall \beta \in S_{\mathrm{mol}}^{\beta_b} \tag{33}$$

This method of redistribution of the change in velocity redirects the molecule as a whole without affecting other degrees of freedom, such as rotation, and is compatible with with constraints on the shape of the molecule in simulations with, for example, rattle.[51]

5 Simulated systems

For testing purposes, the systems simulated here are such that the inner and outer region are treated at the same level of theory. The reference system is then well known and rigorous comparison can be made. The goal is to ensure that the partitioning of the system into an inner and outer region does not introduce any artificial effects.

Simulations are first of all performed for systems of atoms interacting via the LJ potential using parameter values and temperature to mimic liquid argon ($\sigma = 3.4$ Å, $\epsilon = 120\ k_{\mathrm{B}}$, $\rho = 1.374$ g cm^{-3}, $T = 94.4$ K).[52] The systems are equilibrated over 1 ns of NVT ensemble Langevin dynamics using a time step of 1 fs. The distribution functions $g(r)$ and $g(z)$ are then sampled every 0.1 ps for a total of 1 ns using the same time step and either the Langevin (NVT) or velocity Verlet (NVE) propagator (the latter to test energy conservation).

The simulation of the LJ liquid involved 512 atoms with 25 of them assigned to the inner region, including the fixed central particle (the 'solute'). In the simulation of the liquid/solid interface, three layers of 16 atoms represent the FCC crystal with (111) orientation.[53] These

atoms are kept immobile during the simulation. The inner region contains either 16 or 32 movable atoms, while the outer region contains 122 or 96 atoms.

Simulations of water make use of the TIP4P potential function.[54] The system is equilibrated over 250 ps in an NVT ensemble using the Langevin propagator with a time step of 2 fs and a friction coefficient of 0.01. The $g(r)$ is then sampled every 1 ps for a total of 20 ns, using an NVT ensemble and the Langevin propagator with a time step of 0.5 fs. A friction coefficient of 0.05 is used. The first 20 ps of each parallel run are discarded before sampling. Rattle constraints are used to fix bond lengths and bond angles of the water molecules.[51] The inner region contains 14 molecules, including the fixed, central molecule (the 'solute').

All pair distributions are sampled using the VMD software.[55] SAFIRES and FIRES are implemented within the Python-based framework of the Atomic Simulation Environment (ASE).[56] A force constant of $k_{\mathrm{FIRES}} = 500$ kcal A^{-2} is used in the FIRES calculations.

6 Results

6.1 Lennard-Jones liquid

Figure 3 depicts a cross section of the LJ liquid with different colors for the solute (pink), particles in the inner region (blue), and particles in the outer region (grey). Both inner and outer region are calculated using the same LJ potential.

Using this model system, energy conservation of the SAFIRES algorithm is tested for NVE velocity Verlet dynamics according to the approach presented by Allen and Tildesley.[57] It is found that energy conservation with SAFIRES is significantly improved over that in FIRES, see figure S1.

Next, the influence of the ensemble separator on the simulation is quantified. To this end, the $g(r)$ is calculated from 1 ns of NVE velocity Verlet dynamics each. The velocity Verlet integrator is used over the Langevin integrator to keep the first test as simple as possible and to monitor energy conservation. Only pairs involving the solute are included in the sampling

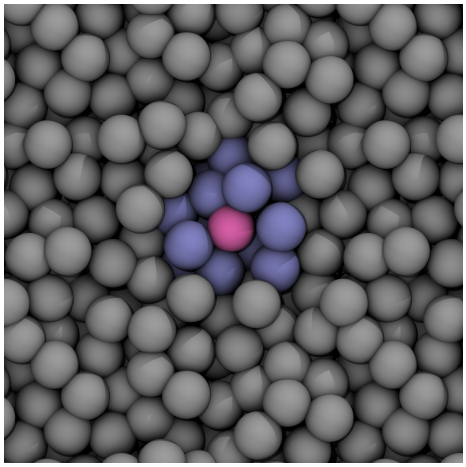

Figure 3: Cross section illustration of the LJ liquid. Pink: fixed solute atom. Blue: atoms in the inner region. Grey: atoms in the outer region.

so that $r = 0$ indicates the position of the solute. This requires longer trajectories to obtain reliable statistics but makes it possible to produce statistics on the location of the boundary and evaluate its influence on the $g(r)$. The $g(r)$ for an unconstrained reference simulation as well as for simulations with SAFIRES and FIRES are shown in figure 4. Also shown in figure 4 are normalized probability distributions for the location of the FIRES and SAFIRES boundaries.

SAFIRES reproduces the unconstrained $g(r)$ without significant deviations. Notably, FIRES introduces accumulation artifacts around the location of the boundary. For a LJ liquid with lower density, the boundary location distributions as well as the artifact around the boundary observed with FIRES broaden see figure S2.

6.2 Liquid water

Results of a simulation of water using the TIP4P potential function are shown in figure 5. The shape of the water molecules is kept fixed using the rattle constraint algorithm for bond lengths and bond angle. The radial distribution function $g(r)$ obtained with SAFIRES is

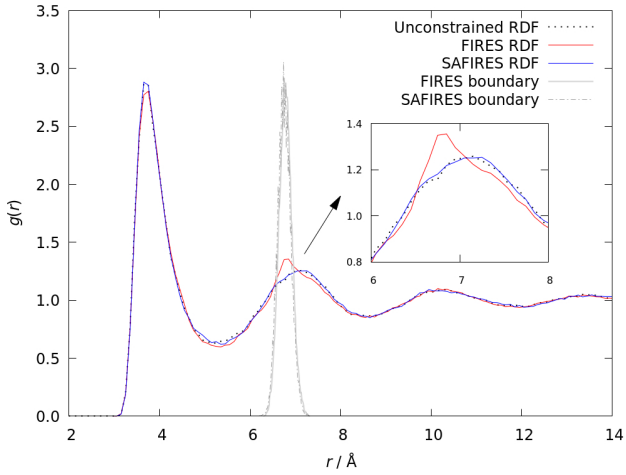

Figure 4: Radial distribution function, $g(r)$, of a LJ liquid. The pair distances sampled are between a fixed central LJ particle (the 'solute') and the surrounding particles. Black dotted: reference calculation without any partitioning into inner and outer regions. Blue: Results of a simulation with SAFIRES. Red: Results of a simulation with FIRES. Dashed light grey: normalized probability distribution of the SAFIRES boundary location. Dark grey: normalized probability distribution of the location of the FIRES boundary.

compared with that of a reference calculation where the system is not partitioned into an inner and outer region. As can be seen from the figure, the agreement is good and there is no sign of artificial features in the SAFIRES results due to the boundary between the two regions. Results of simulations with FIRES are also shown where there is clear enhancement of density at the boundary. These results for liquid water are analogous to the results obtained for the LJ liquid in figure 4. The SAFIRES algorithm is, therefore, shown to work well for molecules as well as atomic systems.

6.3 Liquid/solid interface

To illustrate the applicability of the method for surface science problems, a LJ liquid using argon parameters is placed in a simulation cell with an FCC crystal surface represented by three layers with (111) orientation. The location of the atoms in the crystal is fixed. Figure

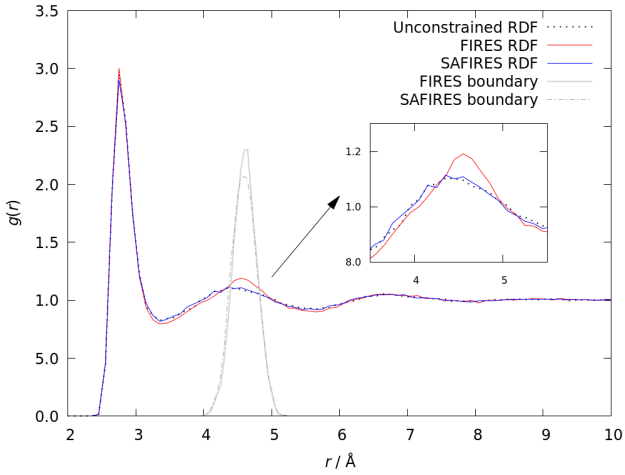

Figure 5: Radial distribution function, $g(r)$, for water using the TIP4P potential function. Pairs are sampled between a fixed central water molecule ('solute') and the surrounding water molecules. Black dotted line: unconstrained reference calculation. Blue: Results obtained with SAFIRES. Red: Results obtained with FIRES. Dashed light grey and dark grey: normalized probability distribution for the location of the SAFIRES and FIRES boundary, respectively.

6 illustrates the model system. The vacuum region above this asymmetric surface slab used

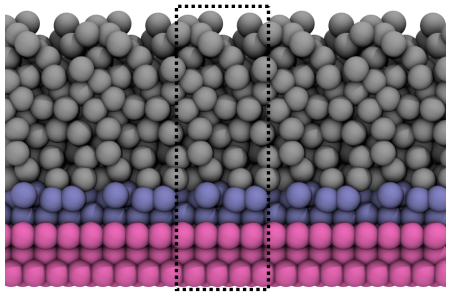

Figure 6: Side view of a crystal surface in contact with liquid simulated using Lennard-Jones potential function. Pink: frozen (111) layers in the face centered cubic crystal. Blue: atoms free to move in the inner region. Grey: atoms in the outer region. A dotted line indicates the simulation box. The vacuum region separating periodic images in the z direction is omitted for clarity.

to avoid interaction with the next periodic image in z direction is not shown.

The probability distribution $g(z)$ is calculated from 1 ns of NVE ensemble velocity Verlet dynamics using this model. Pairs are calculated between the z values of an xy-plane located in the top layer of the surface and of the particles that constitute the liquid. In this way, the origin of the abscissa in figure 7 coincides with the top layer of the surface. Figure 7 shows the resulting $g(z)$ of an unconstrained simulation and of two simulations using SAFIRES, one simulation with 16 LJ particles in the inner region (corresponding to one layer in the crystal) and another simulation with 32 movable particles in the inner region. Simulations

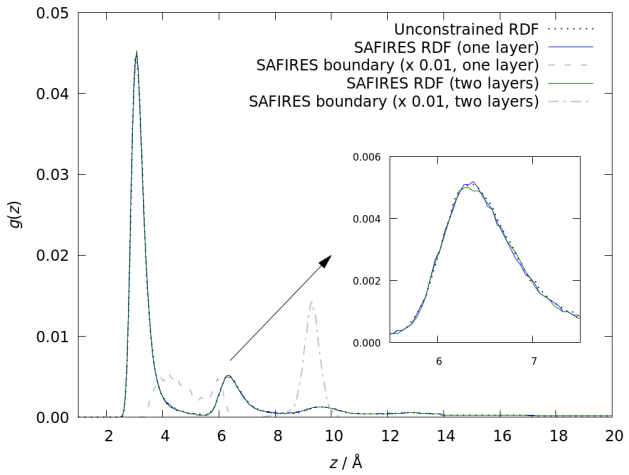

Figure 7: Probability distribution function, $g(z)$, for a LJ liquid in contact with the (111) surface of a face centered cubic crystal of frozen atoms, 16 atoms per layer subject to periodic boundary conditions in the $x-y$ plane. Pair distances are sampled between an x-y plane located in the outermost layer of the crystal and the movable atoms that constitute the liquid. Black dotted line: reference calculation where the system is not partitioned into inner and outer region. Blue: results of a SAFIRES simulation. Grey dashed line and dashed-dotted line: probability distributions for the location of the SAFIRES boundary when 16 movable and 32 atoms are included in the inner region, resp.

using the SAFIRES algorithm reproduce the reference results without significant deviations, both in case of 16 or 32 movable atoms within the inner region. This indicates robustness of the method with respect to the way inner and outer regions are defined.

In case of the simulation with 32 movable atoms in the inner region, the normalized probability distribution of the SAFIRES boundary is slightly broadened and less symmetric compared to the liquid presented in figure 4. This difference in shape is a result of the generally lower density of the liquid in this case as it can expand into the vacuum.

For the simulation with 16 movable atoms in the inner region, the normalized probability distribution of the SAFIRES boundary is significantly broadened as a result of interface effects. The movable LJ atoms near the crystal surface are significantly more ordered than the remaining liquid. This leads to larger distance on average between these atoms and atoms further away from the surface and broadening of the boundary location distribution in the z direction.

7 Discussion

The results presented here show no indication that simulations using SAFIRES introduce artifacts in the probability distribution of the particles. The previous implementation of this type of approach, FIRES, with a harmonic restraint at the boundary, however, does introduce peaks in the density of particles at the boundary. The observed improvement by SAFIRES is due to the instantaneous resolution of boundary conflicts. In FIRES, particles are subject to a spring force when passing the boundary, accelerating them either away or towards the solute. This means, they spend some time in the region they do not belong to, being first decelerated and then accelerated again in the opposite direction. The spring force approach, therefore, leads to an accumulation of particles near the boundary. The effect depends on density. A smaller peak in the $g(r)$ is observed at lower particle density (see Supporting Information). This means that the artifact can potentially be obfuscated under certain simulation conditions, as speculated by Bulo and co-workers.[43]

The SAFIRES algorithm described above is based on binary elastic collisions between the outer region particle that attempts to enter the inner region and the outermost inner region

particle that defines the location of the boundary. Alternatively, such boundary conflicts could be resolved as collisions of the particles with the boundary acting as a hard wall. The changes in the velocity vectors, $\boldsymbol{\Delta}\tilde{\mathbf{v}}$, would then be calculated as

$$\boldsymbol{\Delta}\tilde{\mathbf{v}}'_{\text{in}} = -2 \left(\tilde{\mathbf{v}}_{\text{in}} \cdot \frac{\mathbf{r}_{\text{in}}}{||\mathbf{r}_{\text{in}}||} \right) \frac{\mathbf{r}_{\text{in}}}{||\mathbf{r}_{\text{in}}||} \tag{34}$$

$$\boldsymbol{\Delta}\tilde{\mathbf{v}}'_{\text{out}} = -2 \left(\tilde{\mathbf{v}}_{\text{out}} \cdot \frac{\mathbf{r}_{\text{out}}}{||\mathbf{r}_{\text{out}}||} \right) \frac{\mathbf{r}_{\text{out}}}{||\mathbf{r}_{\text{out}}||} \,. \tag{35}$$

The change in the velocity vectors for such a hard wall collision corresponds to subtraction of twice the normal component with respect to the surface tangent. The rotation of the outer particle position and velocity vectors into the reference frame of the inner particle is not required in this case (equations (16) and (20)), thus simplifying procedure. In this approach, it is not necessary to redirect inner region particles that already travel towards the solute and outer region particles that already travel away from the solute. SAFIRES determines if redirection is required by checking the following conditions based on the scalar products:

$$\tilde{\mathbf{v}}_{\text{in}} \cdot \frac{\mathbf{r}_{\text{in}}}{||\mathbf{r}_{\text{in}}||} > 0 \tag{36}$$

$$\tilde{\mathbf{v}}_{\text{out}} \cdot \frac{\mathbf{r}_{\text{out}}}{||\mathbf{r}_{\text{out}}||} < 0 \,. \tag{37}$$

This approach also gives distribution functions in good agreement with the reference results where no boundary is introduced, as shown in the Supporting Information.

Figures S4–S6 compare the $g(r)$ of unconstrained reference simulations with results obtained using elastic collisions with the boundary treated as a hard wall, instead of binary collisions. Sampling is carried out for a total of 1, 2, or 3 ns. Figures S4–S6 show that this implementation requires longer sampling time until a $g(r)$ is obtained that accurately reproduces the unconstrained reference simulation, indicating that the binary collision implementation is more efficient.

While the solute has been kept fixed here, the more general approach of this algorithm

would include a moving solute. The binary collision scheme is simpler in that case. For the planar boundary in liquid/solid simulation this approach would also not conserve momentum as does the binary collision approach.

While the test simulations presented here have made use of simple interaction potentials, there is no technical problem in applying the approach in more advanced description of the fluid phase, such as functions that include polarizability and self-consistent calculation of the electrostatics of the inner and outer regions.[58,59] Future development and application of SAFIRES is anticipated in simulations of electrochemistry where calculations that include explicitly the effect of applied voltage have so far included the effect of the dielectric in a limited way, if at all.

SAFIRES will be made available as part of the open source ASE software.

8 Conclusions

An algorithm is presented for the boundary in hybrid simulations where the system is separated into two subsystems treated at different levels of theory. The boundary is flexible in terms of location but restrictive in that particles cannot cross it. Correct average ensemble statistics are obtained under two conditions: (i) the particles near the boundary on both sides are of the same type, and (ii) the position of the boundary moves with the outermost particle in the inner region. Particles in the outer region attempting to cross the boundary are instantaneously redirected by an elastic binary collision with the outermost particle in the inner region. A variable-time-step propagator for Langevin dynamics is presented where the time of collision is identified and partial time step taken to the point of collision and again after the collision to complete a full time step. The algorithm conserves energy if the coupling to the heat bath is turned off and in the case of liquid/solid interface simulations it also conserves the total momentum of moving particles.

In simulations of a LJ liquid with a solute, liquid water with a TIP4P potential function

and a LJ liquid in contact with a crystal surface, where for testing purposes the inner and outer region particles are treated at the same level of theory, the method reproduces well probability distribution functions obtained from unconstrained simulations, without any enhancement or reduction of density of particles near the boundary.

Acknowledgement

BK thanks the University of Iceland Research Fund for a Ph.D. fellowship. The work was furthermore supported by the Icelandic Research Fund (grants 174582-053 and 196279-051) and by the DFG (German Science Foundation) through the Collaborative Research Center SFB-1316 as well as the cluster of excellence POLiS (project ID 390874152). The calculations were performed using resources provided by the Icelandic Research High Performance Computing (IRHPC) facility at the University of Iceland.

Supporting Information Available

The results of the energy conservation test, a $g(r)$ of an LJ liquid of lower density, the $g(r)$ of an LJ liquid sampled using an NVT ensemble, a comparison of the reflective and momentum-exchange-based implementations of SAFIRES, and pseudocode of the SAFIRES algorithm are presented in the electronic Supporting Information.

References

(1) Qvortrup, K.; Petersen, R. G.; Dohn, A. O.; Møller, K. B.; Nielsen, T. E. Solvent-Controlled Chemoselectivity in the Photolytic Release of Hydroxamic Acids and Carboxamides from Solid Support. *Org. Lett.* **2017**, *19*, 3263–3266.

(2) Kitanosono, T.; Masuda, K.; Xu, P.; Kobayashi, S. Catalytic Organic Reactions in Water toward Sustainable Society. *Chem. Rev.* **2018**, *118*, 679–746.

(3) Dohn, A. O.; Kjær, K. S.; Harlang, T. B.; Canton, S. E.; Nielsen, M. M.; Møller, K. B. Electron Transfer and Solvent-Mediated Electronic Localization in Molecular Photocatalysis. *Inorg. Chem.* **2016**, *55*, 10637–10644.

(4) Gould, N. S.; Li, S.; Cho, H. J.; Landfield, H.; Caratzoulas, S.; Vlachos, D.; Bai, P.; Xu, B. Understanding solvent effects on adsorption and protonation in porous catalysts. *Nat. Commun.* **2020**, *11*, 1060.

(5) Mellmer, M. A.; Sanpitakseree, C.; Demir, B.; Bai, P.; Ma, K.; Neurock, M.; Dumesic, J. A. Solvent-enabled control of reactivity for liquid-phase reactions of biomass-derived compounds. *Nat. Catal.* **2018**, *1*, 199–207.

(6) Román-Leshkov, Y.; Chheda, J. N.; Dumesic, J. A. Phase Modifiers Promote Efficient Production of Hydroxymethylfurfural from Fructose. *Science* **2006**, *312*, 1933–1937.

(7) Rossin, A.; Kovács, G.; Ujaque, G.; Lledós, A.; Joó, F. The Active Role of the Water Solvent in the Regioselective CO Hydrogenation of Unsaturated Aldehydes by [RuH2(mtppms)x] in Basic Media. *Organometallics* **2006**, *25*, 5010–5023.

(8) Dohn, A. O.; Jónsson, E. Ö.; Kjær, K. S.; van Driel, T. B.; Nielsen, M. M.; Jacobsen, K. W.; Henriksen, N. E.; Møller, K. B. Direct Dynamics Studies of a Binuclear Metal Complex in Solution: The Interplay Between Vibrational Relaxation, Coherence, and Solvent Effects. *J. Phys. Chem. Lett.* **2014**, *5*, 2414–2418.

(9) Warzok, U.; Marianski, M.; Hoffmann, W.; Turunen, L.; Rissanen, K.; Pagel, K.; A. Schalley, C. Surprising solvent-induced structural rearrangements in large [NI + N] halogen-bonded supramolecular capsules: an ion mobility-mass spectrometry study. *Chem. Sci.* **2018**, *9*, 8343–8351.

(10) Yang, K.; Chen, X.; Zheng, Z.; Wan, J.; Feng, M.; Yu, Y. Solvent-induced surface disorder and doping-induced lattice distortion in anatase TiO2 nanocrystals for enhanced photoreversible color switching. *J. Mater. Chem. A* **2019**, *7*, 3863–3873.

(11) Levi, G.; Biasin, E.; Dohn, A. O.; Jónsson, H. On the interplay of solvent and conformational effects in simulated excited-state dynamics of a copper phenanthroline photosensitizer. *Phys. Chem. Chem. Phys.* **2020**, *22*, 748–757.

(12) Hodel, F. H.; Luber, S. Redox-Inert Cations Enhancing Water Oxidation Activity: The Crucial Role of Flexibility. *ACS Catal.* **2016**, *6*, 6750–6761.

(13) Abel, R.; Young, T.; Farid, R.; Berne, B. J.; Friesner, R. A. Role of the Active-Site Solvent in the Thermodynamics of Factor Xa Ligand Binding. *J. Am. Chem. Soc.* **2008**, *130*, 2817–2831.

(14) Burnham, C. J.; English, N. J. Crystal Structure Prediction via Basin-Hopping Global Optimization Employing Tiny Periodic Simulation Cells, with Application to Water–Ice. *J. Chem. Theory Comput.* **2019**, *15*, 3889–3900.

(15) Zhang, J.; Dolg, M. Global optimization of clusters of rigid molecules using the artificial bee colony algorithm. *Phys. Chem. Chem. Phys.* **2016**, *18*, 3003–3010.

(16) Reda, M.; Hansen, H. A.; Vegge, T. DFT study of stabilization effects on N-doped graphene for ORR catalysis. *Catal. Today* **2018**, *312*, 118–125.

(17) Heenen, H. H.; Gauthier, J. A.; Kristoffersen, H. H.; Ludwig, T.; Chan, K. Solvation at metal/water interfaces: An ab initio molecular dynamics benchmark of common computational approaches. *J. Chem. Phys.* **2020**, *152*, 144703.

(18) E. Skyner, R.; L. McDonagh, J.; R. Groom, C.; Mourik, T. v.; O. Mitchell, J. B. A review of methods for the calculation of solution free energies and the modelling of systems in solution. *Phys. Chem. Chem. Phys.* **2015**, *17*, 6174–6191.

(19) Gray, C. M.; Saravanan, K.; Wang, G.; Keith, J. A. Quantifying solvation energies at solid/liquid interfaces using continuum solvation methods. *Mol. Simul.* **2017**, *43*, 420–427.

(20) Zhang, J.; Zhang, H.; Wu, T.; Wang, Q.; van der Spoel, D. Comparison of Implicit and Explicit Solvent Models for the Calculation of Solvation Free Energy in Organic Solvents. *J. Chem. Theory Comput.* **2017**, *13*, 1034–1043.

(21) Garcia-Ratés, M.; García-Muelas, R.; López, N. Solvation Effects on Methanol Decomposition on Pd(111), Pt(111), and Ru(0001). *J. Phys. Chem. C* **2017**, *121*, 13803–13809.

(22) Van den Bossche, M.; Skúlason, E.; Rose-Petruck, C.; Jónsson, H. Assessment of Constant-Potential Implicit Solvation Calculations of Electrochemical Energy Barriers for H2 Evolution on Pt. *J. Phys. Chem. C* **2019**, *123*, 4116–4124.

(23) Basdogan, Y.; Maldonado, A. M.; Keith, J. A. Advances and challenges in modeling solvated reaction mechanisms for renewable fuels and chemicals. *Wiley Interdiscip. Rev. Comput. Mol. Sci.* **2020**, *10*, e1446.

(24) Basdogan, Y.; Groenenboom, M. C.; Henderson, E.; De, S.; Rempe, S. B.; Keith, J. A. Machine Learning-Guided Approach for Studying Solvation Environments. *J. Chem. Theory Comput.* **2020**, *16*, 633–642.

(25) Warshel, A.; Levitt, M. Theoretical studies of enzymic reactions: Dielectric, electrostatic and steric stabilization of the carbonium ion in the reaction of lysozyme. *J. Mol. Biol.* **1976**, *103*, 227–249.

(26) Thole, B. T.; van Duijnen, P. T. On the quantum mechanical treatment of solvent effects. *Theor. Chim. Acta* **1980**, *55*, 307–318.

(27) Field, M. J.; Bash, P. A.; Karplus, M. A combined quantum mechanical and molecular mechanical potential for molecular dynamics simulations. *J. Comp. Chem.* **1990**, *11*, 700–733.

(28) Dohn, A. O.; Jónsson, E. O.; Levi, G.; Mortensen, J. J.; Lopez-Acevedo, O.; Thygesen, K. S.; Jacobsen, K. W.; Ulstrup, J.; Henriksen, N. E.; Møller, K. B.; Jónsson, H. Grid-Based Projector Augmented Wave (GPAW) Implementation of Quantum Mechanics/Molecular Mechanics (QM/MM) Electrostatic Embedding and Application to a Solvated Diplatinum Complex. *Journal of Chemical Theory and Computation* **2017**, *13*, 6010–6022.

(29) Dohn, A. O. Multiscale electrostatic embedding simulations for modeling structure and dynamics of molecules in solution: A tutorial review. *Int. J. Quant. Chem. n/a*, e26343.

(30) Waller, M. P.; Kumbhar, S.; Yang, J. A Density-Based Adaptive Quantum Mechanical/Molecular Mechanical Method. *ChemPhysChem* **2014**, *15*, 3218–3225.

(31) Bernstein, N.; Várnai, C.; Solt, I.; Winfield, S. A.; Payne, M. C.; Simon, I.; Fuxreiter, M.; Csányi, G. QM/MM simulation of liquid water with an adaptive quantum region. *Phys. Chem. Chem. Phys.* **2012**, *14*, 646–656.

(32) Heyden, A.; Lin, H.; Truhlar, D. G. Adaptive Partitioning in Combined Quantum Mechanical and Molecular Mechanical Calculations of Potential Energy Functions for Multiscale Simulations. *J. Phys. Chem. B* **2007**, *111*, 2231–2241.

(33) Pezeshki, S.; Lin, H. Adaptive-Partitioning QM/MM for Molecular Dynamics Simulations: 4. Proton Hopping in Bulk Water. *J. Chem. Theory Comput.* **2015**, *11*, 2398–2411.

(34) Bulo, R. E.; Ensing, B.; Sikkema, J.; Visscher, L. Toward a Practical Method for Adaptive QM/MM Simulations. *J. Chem. Theory Comput.* **2009**, *5*, 2212–2221.

(35) Field, M. J. An Algorithm for Adaptive QC/MM Simulations. *J. Chem. Theory Comput.* **2017**, *13*, 2342–2351.

(36) Watanabe, H. C.; Kubař, T.; Elstner, M. Size-Consistent Multipartitioning QM/MM: A Stable and Efficient Adaptive QM/MM Method. *J. Chem. Theory Comput.* **2014**, *10*, 4242–4252.

(37) Watanabe, H. C. Improvement of performance, stability and continuity by modified size-consistent multipartitioning quantum mechanical/molecular mechanical method. *Molecules* **2018**, *23*, 1882.

(38) Watanabe, H. C.; Cui, Q. Quantitative Analysis of QM/MM Boundary Artifacts and Correction in Adaptive QM/MM Simulations. *J. Chem. Theory Comput.* **2019**, *15*, 3917–3928.

(39) Rowley, C. N.; Roux, B. The Solvation Structure of Na^+ and K^+ in Liquid Water Determined from High Level *ab Initio* Molecular Dynamics Simulations. *J. Chem. Theory Comput.* **2012**, *8*, 3526–3535.

(40) Beglov, D.; Roux, B. Finite representation of an infinite bulk system: Solvent boundary potential for computer simulations. *J. Chem. Phys.* **1994**, *100*, 9050–9063.

(41) Lu, X.; Gaus, M.; Elstner, M.; Cui, Q. Parametrization of DFTB3/3OB for Magnesium and Zinc for Chemical and Biological Applications. *J. Phys. Chem. B* **2015**, *119*, 1062–1082.

(42) Boereboom, J. M.; Fleurat-Lessard, P.; Bulo, R. E. Explicit Solvation Matters: Performance of QM/MM Solvation Models in Nucleophilic Addition. *J. Chem. Theory Comput.* **2018**, *14*, 1841–1852.

(43) Bulo, R. E.; Michel, C.; Fleurat-Lessard, P.; Sautet, P. Multiscale Modeling of Chemistry in Water: Are We There Yet? *J. Chem. Theory Comput.* **2013**, *9*, 5567–5577.

(44) Shiga, M.; Masia, M. Boundary based on exchange symmetry theory for multilevel simulations. I. Basic theory. *J. Chem. Phys.* **2013**, *139*, 044120.

(45) Shiga, M.; Masia, M. Erratum: "Boundary based on exchange symmetry theory for multilevel simulations. I. Basic theory" [J. Chem. Phys. 139, 044120 (2013)]. *J. Chem. Phys.* **2013**, *139*, 119901.

(46) Takahashi, H.; Kambe, H.; Morita, A. A simple and effective solution to the constrained QM/MM simulations. *J. Chem. Phys.* **2018**, *148*, 134119.

(47) Shiga, M.; Masia, M. Quasi-boundary based on exchange symmetry theory for multilevel simulations. *Mol. Simul.* **2015**, *41*, 827–831.

(48) Vanden-Eijnden, E.; Ciccotti, G. Second-order integrators for Langevin equations with holonomic constraints. *Chem. Phys. Lett.* **2006**, *429*, 310–316.

(49) Skeel, R. D. Variable step size destabilizes the Störmer/leapfrog/verlet method. *BIT Numer. Math.* **1993**, *33*, 172–175.

(50) Vincenty, T. Direct and Inverse Solutions of Geodesics on the Ellipsoid with Application of Nested Equations. *Surv. Rev.* **1975**, *23*, 88–93.

(51) Andersen, H. C. Rattle: A "velocity" version of the shake algorithm for molecular dynamics calculations. *J. Comp. Phys.* **1983**, *52*, 24–34.

(52) Rahman, A. Correlations in the Motion of Atoms in Liquid Argon. *Phys. Rev.* **1964**, *136*, A405–A411.

(53) Barrett, C. S.; Meyer, L. The Crystal Structures of Argon and Its Alloys. Low Temperature Physics LT9. Boston, MA, 1965; pp 1085–1088.

(54) Abascal, J. L. F.; Vega, C. A general purpose model for the condensed phases of water: TIP4P/2005. *J. Chem. Phys.* **2005**, *123*, 234505.

(55) Humphrey, W.; Dalke, A.; Schulten, K. VMD: Visual molecular dynamics. *J. Mol. Graph.* **1996**, *14*, 33–38.

(56) Larsen, A. H.; Mortensen, J. J.; Blomqvist, J.; Castelli, I. E.; Christensen, R.; Dulak, M.; Friis, J.; Groves, M. N.; Hammer, B.; Hargus, C.; Hermes, E. D.; Jennings, P. C.; Jensen, P. B.; Kermode, J.; Kitchin, J. R.; Kolsbjerg, E. L.; Kubal, J.; Kaasbjerg, K.; Lysgaard, S.; Maronsson, J. B.; Maxson, T.; Olsen, T.; Pastewka, L.; Peterson, A.; Rostgaard, C.; Schiøtz, J.; Schütt, O.; Strange, M.; Thygesen, K. S.; Vegge, T.; Vilhelmsen, L.; Walter, M.; Zeng, Z.; Jacobsen, K. W. The atomic simulation environment—a Python library for working with atoms. *J. Phys.: Condens. Matter* **2017**, *29*, 273002.

(57) Allen, M. P.; Tildesley, D. J. *Computer simulation of liquids*, second edition ed.; Oxford University Press: Oxford, United Kingdom, 2017.

(58) Jónsson, E. Ö.; Dohn, A. O.; Jónsson, H. Polarizable Embedding with a Transferable H2O Potential Function I: Formulation and Tests on Dimer. *J. Chem. Theory Comput.* **2019**, *15*, 6562–6577.

(59) Dohn, A. O.; Jónsson, E. Ö.; Jónsson, H. Polarizable Embedding with a Transferable H2O Potential Function II: Application to (H2O)n Clusters and Liquid Water. *J. Chem. Theory Comput.* **2019**, *15*, 6578–6587.

Graphical TOC Entry

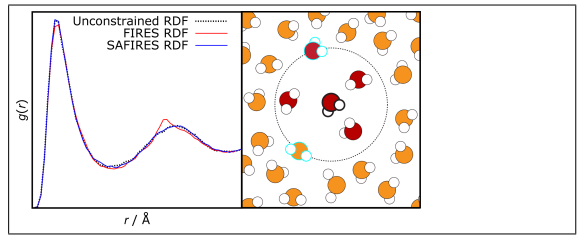

Supplementary Information:

Elastic Collision Based Dynamic Partitioning Scheme for Hybrid Simulations

Björn Kirchhoff,[†] Elvar Örn Jónsson,[†] Asmus Ougaard Dohn,[†,‡] Timo Jacob,[¶,§,‖] and Hannes Jónsson[*,†]

†*Science Institute and Faculty of Physical Sciences, University of Iceland, VR-III, 107 Reykjavík, Iceland.*

‡*Technical University of Denmark, Lyngby, Denmark.*

¶*Institute of Electrochemistry, Ulm University, Albert-Einstein-Allee 47, 89081 Ulm, Germany.*

§*Helmholtz-Institute Ulm (HIU) Electrochemical Energy Storage, Helmholtz-Straße 16, 89081 Ulm, Germany.*

‖*Karlsruhe Institute of Technology (KIT), P.O. Box 3640, 76021 Karlsruhe, Germany.*

E-mail: hj@hi.is

1 Euler-Rodrigues rotational matrix

The rotational matrix used in this work is of the Euler-Rodrigues form,

$$X(\mathbf{c},\phi) = \begin{vmatrix} e^2+f^2-g^2-h^2 & 2(fg-eh) & 2(fh+eg) \\ 2(fg+eh) & e^2+g^2-f^2-h^2 & 2(gh-ef) \\ 2(fh-eg) & 2(gh+ef) & e^2+h^2-f^2-g^2 \end{vmatrix}, \tag{S1}$$

with $e = \cos(\phi/2)$ and $(f,g,h) = -\mathbf{c}\sin(\phi/2)$, where ϕ is the rotational angle calculated in equation (18) and $\mathbf{c}$ is the rotational axis calculated in equation (20).

2 Energy conservation test

Energy conservation is tested with the LJ liquid model system (σ = 3.4 Å, ϵ = 120 k_B, ρ = 1.374 g cm^{-3}, T = 94.4 K) shown in Figure 3, using the Verlocity-Verlet propagator (*NVE* ensemble) and time steps between 0.25 and 10 fs for a total of 100 ps according to the scheme proposed by Allen and Tildesley.[1] Results for each time step are averaged over 5 runs from different starting images. The obtained energy conservation trends are shown in Figure S1. The calculated RMS energy fluctuation trends indicate that energy conservation is improved using SAFIRES over FIRES.

3 Lennard-Jones Liquid at lower density

To illustrate the effect of varying density on the position and width of the FIRES and SAFIRES boundary location probability distribution, the simulation illustrated in Figure 3 of the main manuscript is repeated using a lower density of the LJ liquid ($\rho = 1.100$ g cm^{-3} *vs.* $\rho = 1.374$ g cm^{-3}). The resulting $g(r)$ for a FIRES simulation, a SAFIRES simulation, and an unconstrained reference simulation are shown in Figure S2. The $g(r)$ are sampled every 0.1 ps over 1 ns using a timestep of 1 fs and the argon LJ parameters outlined in the

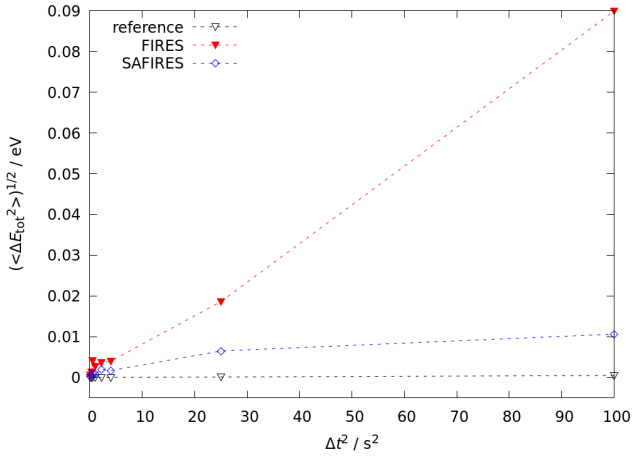

Fig. S 1: Energy conservation test for unconstrained reference simulations (black empty triangles), simulations using the FIRES boundary method (red filled triangles) and simulations using the SAFIRES boundary method (blue empty diamonds) on the basis of the LJ liquid model system presented in Figure 3.

computational section of the main manuscript.

4 Lennard-Jones Liquid, *NVT* ensemble

The LJ liquid model system depicted in Figure 3 ($\sigma = 3.4$ Å, $\epsilon = 120$ k_B, $\rho = 1.374$ g cm^{-3}) is simulated using an NVT ensemble and the Langevin propagator. A friction coefficient of 0.05 is used to achieve the thermostat target temperature of 94.4 K. Figure S 3 displays the resulting $g(r)$ of an unconstrained reference simulation as well as for simulations using FIRES and SAFIRES. The $g(r)$ are sampled every 0.1 ps over 1 ns using a timestep of 1 fs.

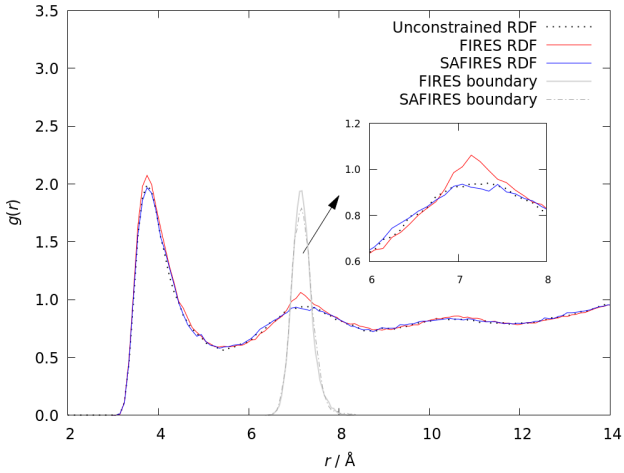

Fig. S 2: $g(r)$ of a LJ liquid using argon parameters. Black dashed line: reference simulation without any ensemble separation; red: simulation using FIRES boundary method; blue: simulation using SAFIRES boundary method; dashed light grey: probability distribution of the FIRES boundary location; dark grey: probability distribution of the SAFIRES boundary location. This example uses a lower density of the liquid ($\rho = 1.100$ g cm^{-3}) than the example in the main manuscript.

5 Comparison of different methods for boundary conflict resolution

The LJ liquid model system depicted in Figure 3 ($\sigma = 3.4$ Å, $\epsilon = 120$ k_B, $\rho = 1.374$ g cm^{-3}) is simulated using an *NVE* ensemble and the velocity Verlet propagator. Figures S 4–6 display the resulting $g(r)$ of unconstrained reference simulations as well as for simulations using SAFIRES using two different methods, namely (i) boundary conflict resolution via elastic collisions including momentum exchange of the conflicting inner/outer particle pair and (ii) resolution via elastic collisions with the boundary treated as a hard wall. The $g(r)$ are sampled every 0.1 ps over 1–3 ns using a timestep of 1 fs. It appears that the elastic collision based implementation of SAFIRES requires less overall simulation time to closely reproduce the unconstrained calculation compared to the reflective implementation.

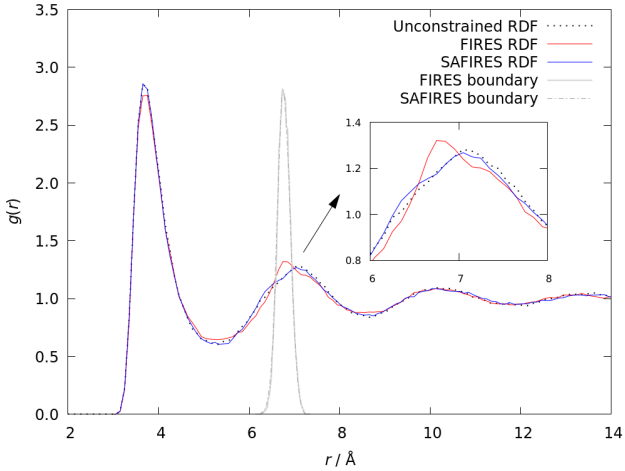

Fig. S 3: $g(r)$ of a LJ liquid using argon parameters. NVT ensemble. Black dashed line: reference simulation without any ensemble separation; red: simulation using FIRES boundary method; blue: simulation using SAFIRES boundary method; dashed light grey: probability distribution of the FIRES boundary location; dark grey: probability distribution of the SAFIRES boundary location.

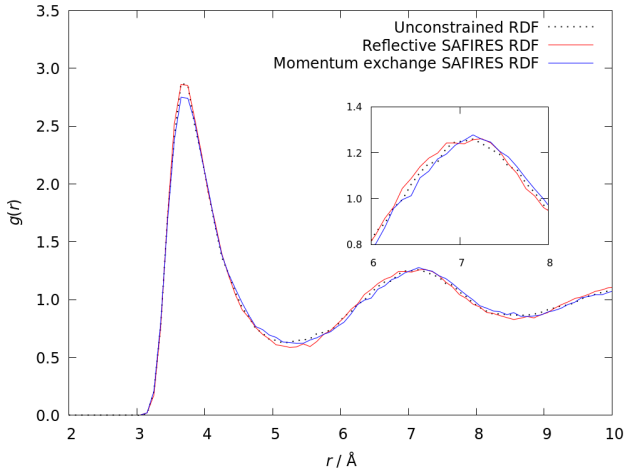

Fig. S 4: $g(r)$ of a LJ liquid using argon parameters. *NVE* ensemble sampled every 100 ps over 1 ns. Black dotted line: reference simulation without any ensemble separation; red: simulation using SAFIRES where boundary conflicts are resolved via elastic collisions between the conflicting inner/outer particle pair; blue: simulation using SAFIRES where boundary conflicts are resolved via elastic collisions of the particles with the boundary treated as a hard wall.

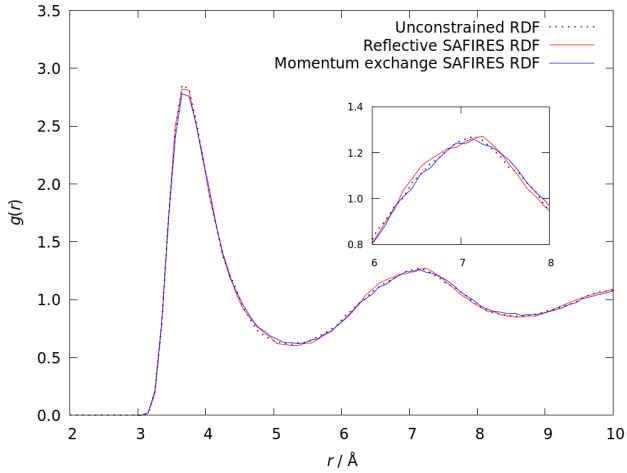

Fig. S 5: $g(r)$ of a LJ liquid using argon parameters. *NVE* ensemble sampled every 100 ps over 2 ns. Black dotted line: reference simulation without any ensemble separation; red: simulation using SAFIRES where boundary conflicts are resolved via elastic collisions between the conflicting inner/outer particle pair; blue: simulation using SAFIRES where boundary conflicts are resolved via elastic collisions of the particles with the boundary treated as a hard wall.

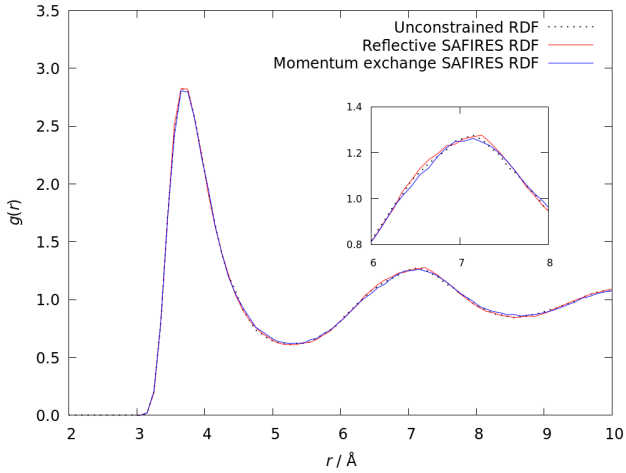

Fig. S 6: $g(r)$ of a LJ liquid using argon parameters. *NVE* ensemble sampled every 100 ps over 3 ns. Black dotted line: reference simulation without any ensemble separation; red: simulation using SAFIRES where boundary conflicts are resolved via elastic collisions between the conflicting inner/outer particle pair; blue: simulation using SAFIRES where boundary conflicts are resolved via elastic collisions of the particles with the boundary treated as a hard wall.

6 SAFIRES pseudocode

atoms: MD output array containing properties and calculation results for all atoms.

previous_atoms: *atoms* array from a previous iteration.

Δt: default time step of the MD simulation.

Δt_{rem}: float used to keep track of fractional time steps.

recent: array used to remember the particle pair that recently collided.

Langevin equation as implemented in ASE:

$$\begin{aligned} v' &= v + \frac{1}{2}\,\Delta t\; F - \frac{1}{2}\,\Delta t\;\gamma\; v + \frac{1}{2}\,\sqrt{\Delta t}\;\sigma\;\xi \\ &- \frac{1}{8}\,\Delta t^2\;\gamma\,(F - \gamma\; v) - \frac{1}{4}\,\Delta t^{\frac{3}{2}}\;\gamma\;\sigma\left(\frac{1}{2}\;\gamma + \frac{1}{\sqrt{3}}\;\eta\right) \qquad \text{(S2)} \\ x' &= x + \Delta t\; v' + \Delta t^{\frac{3}{2}}\;\sigma\;\frac{1}{2\sqrt{3}}\;\eta \qquad \text{(S3)} \\ \text{Where: } \sigma &= \sqrt{\frac{2\;T\;\gamma}{m}} \qquad \text{(S4)} \end{aligned}$$

x: array of position vectors for each atom.

m: array of masses for each atom.

v: array of velocity vectors for each atom.

F: array of force vectors for each atom.

T: simulation temperature.

γ: Langevin friction coefficient.

ξ, η: array of random force vectors for atom x.

Algorithm 1: check($atoms$, $recheck$=False)

Result: Find conflicts (outer atom inside inner area) and coordinate their resolution.

for *inner atom in atoms* **do**
  calculate distance d_{inner} to solute;
end
set d_{thresh} = largest calculated d_{inner} value;
set i_{thresh} = index of inner atom corresponding to largest d_{inner};

$conflicts$ = array();
for *outer atom in atoms* **do**
  d_{outer} = distance of outer atom to solute;
  if $d_{outer} \leq d_{thresh}$ **then**
    i_{outer} = index of outer atom;
    if *(i_{outer}, i_{thresh}) != recent* **then**
      Δt_{new} = **extrapolate**(i_{outer}, i_{thresh});
      add array(i_{outer}, idx_{thresh}, Δt_{new}) to $conflicts$;
    end
  end
end

if *length(conflicts) > 0* **then**
  choose array(i_{outer}, i_{thresh}, Δt_{new}) from $conflicts$ that contains the smallest Δt_{new} value;
  $atoms = previous\_atoms$;
  propagate($atoms$, Δt_{new}, $halfstep = 1$, $recheck$);
  collide(i_{outer}, i_{thresh});
  $recent$ = array(i_{outer}, i_{thresh});
  $previous\_atoms = atoms$;
  if $\Delta t_{rem} == 0$ **then**
    $\Delta t_{\mathrm{rem}} = \Delta t - \Delta t_{\mathrm{new}}$;
  else
    $\Delta t_{\mathrm{rem}} = \Delta t_{\mathrm{rem}} - \Delta t_{\mathrm{new}}$;
  end
  propagate($atoms$, Δt_{rem}, $halfstep = 2$, $recheck$);
  check($atoms$, $recheck$=True);
else
  $previous\_atoms$ = atoms;
  $\Delta t_{\mathrm{rem}} = 0$;
  $recent$ = empty;
end

Algorithm 2: extrapolate(i_{outer}, i_{thresh}, *recheck*)

Result: Extrapolate the timestep required to propagate the conflicting inner and outer particles to the same distance wrt. the solute.

Update x, v, F, ξ, η, m from *atoms*;

if *recheck == False* **then**

  for *x in array*(i_{outer}, i_{thresh}) **do**

    $\sigma_x = \sqrt{2\ T\ \gamma\ /\ m_x}$;

    $e_x = \Delta t\ (F_x - \gamma\ v_x)\ /\ 2 + \sqrt{\Delta t}\ \sigma_x\ \xi_x\ /\ 2$
    $\quad -\Delta t^2\ \gamma\ (F_x - \gamma\ v_x)\ /\ 8 - \Delta t^{\frac{3}{2}}\ \gamma\ \sigma_x\ (\xi_x\ /\ 2 + \eta_x\ /\ \sqrt{3})\ /\ 4$;

    $f_x = \Delta t^{\frac{1}{2}}\ \sigma_x\ \eta_x\ /\ (2\sqrt{3})$;

  end

end

if *recheck==True* **then**

  $e = 0$;

  $f = 0$;

end

$v'_{outer} = v_{i_{outer}} = v_{outer} + e_{outer} + f_{outer}$;

$v'_{inner} = v_{i_{thresh}} = v_{inner} + f_{inner} + e_{inner}$;

$c_0 = \langle r_{outer}, r_{outer} \rangle - \langle r_{inner}, r_{inner} \rangle$;

$c_1 = 2\,\langle r_{outer}, v'_{outer} \rangle - 2\,\langle r_{inner}, v'_{inner} \rangle$;

$c_2 = \langle v'_{outer}, v'_{outer} \rangle - \langle v'_{inner}, v'_{inner} \rangle$;

results = array();

for *root in* ($c_2\ x^2 + c_1\ x + c_0 = 0$) **do**

  if *real(root) == True AND root* > 0 *AND root* $<= \Delta t$ **then**

    save *root* in *results*;

  end

end

return smallest value in *results* as Δt_{new};

Algorithm 3: propagate($atoms$, Δt_{new}, $halfstep$, $recheck$)

Result: Propagate atoms using a Langevin style propagator. Both halfsteps can be propagated separately.

Update x, v, F, ξ, η, m from $atoms$;

if $recheck == False$ **then**

$\sigma = \sqrt{2\ T\ \gamma\ /\ m}$;

$e = \Delta t\ (F - \gamma\ v)\ /\ 2 + \sqrt{\Delta t}\ \sigma\ \xi\ /\ 2$
$\quad -\Delta t^2\ \gamma\ (F - \gamma\ v)\ /\ 8 - \Delta t^{\frac{3}{2}}\ \gamma\ \sigma\ (\xi\ /\ 2 + \eta\ /\ \sqrt{3})\ /\ 4$;

$f = \Delta t^{\frac{1}{2}}\ \sigma\ \eta\ /\ (2\sqrt{3})$;

end

if $recheck == True$ **then**

$e = 0$;

$f = 0$;

end

if $halfstep == 1$ **then**

$v' = v + e$;

$x' = x + \Delta t_{new}\ (v' + f)$;

overwrite atomic positions in $atoms$ with x';

$v'' = (x' - x - \Delta t_{new}\ f)/\Delta t_{new}$;

end

if $halfstep == 2$ **then**

$x' = x + \Delta t_{new}\ v$;

overwrite atomic positions in $atoms$ with x';

$v' = (x' - x)/\Delta t_{new}$;

calculate new forces $\rightarrow F = F_{\mathrm{new}}$;

re-calculate e with F_{new} (see above);

$v'' = v' + e$;

end

update atomic velocities in $atoms$ with v'';

Algorithm 4: collide(idx_{outer}, idx_{inner})

Result: Perform a fully elastic collision between the conflicting inner and a outer atoms.

r_{outer}, r_{inner}: distance vector from solute to *inner*, *outer*.

m_{outer}, m_{inner}: atomic mass of *inner*, *outer*.

v_{outer}, v_{inner}: velocity vector of *inner*, *outer*.

$\theta = arctan2\left(\frac{r_{outer} \times r_{inner}}{|r_{outer} \times r_{inner}|}, \langle r_{outer}, r_{inner} \rangle\right)$;

$n = \frac{r_{outer} \times r_{inner}}{|r_{outer} \times r_{inner}|}$;

$a = \cos(\theta)$;

$b, c, d = -n \ \sin(\theta)$;

$$X^{\text{rot}} = \begin{bmatrix} a^2+b^2-c^2-d^2 & 2(bc+ad) & 2(bd-ac) \\ 2(bc-ad) & a^2+c^2-b^2-d^2 & 2(cd+ab) \\ 2(bd+ac) & 2(cd-ab) & a^2+d^2-b^2-c^2 \end{bmatrix};$$

$r^{\text{rot}}_{outer} = \left\langle X^{\text{rot}}(\theta), r_{outer} \right\rangle$;

$v^{\text{rot}}_{outer} = \left\langle X^{\text{rot}}(\theta), v_{outer} \right\rangle$;

$M = m_{outer} + m_{inner}$;

$v_{12} = v^{\text{rot}}_{outer} - v_{inner}$;

$\Delta v^{\text{rot, post}}_{outer} = \frac{-2m_{inner}}{M} \ \frac{\langle v_{12}, r_{inner} \rangle \cdot r_{inner}}{|r_{inner}|^2}$;

$\Delta v^{\text{post}}_{inner} = \frac{2m_{outer}}{M} \ \frac{\langle v_{inner}, r_{inner} \rangle \cdot r_{inner}}{|r_{inner}|^2}$;

$\Delta v^{\text{post}}_{outer} = \left\langle X^{\text{rot}}(2\pi - \theta), \Delta v^{\text{rot, post}}_{outer} \right\rangle$;

apply new velocities to *atoms*;

References

(1) Allen, M. P.; Tildesley, D. J. *Computer simulation of liquids*, second edition ed.; Oxford University Press: Oxford, United Kingdom, 2017.